Durham E-Theses

Atomistic simulation of biaxial liquid crystals and mixtures of liquid crystals

Pelaez Laguno, Jorge

Atomistic Simulation of Biaxial Liquid Crystals and Mixtures of Liquid Crystals

Jorge Peláez Laguno

Department of Chemistry

Durham University

March 2007

Submitted in the partial fulfilment of the requirements for the degree of

Doctor of Philosophy

Abstract

Atomistic Simulation of Biaxial Liquid Crystals and Mixtures of Liquid Crystals

Jorge Peláez Laguno

In this thesis molecular dynamics (MD) simulations at a fully-atomistic level have been undertaken to study the biaxiality and the structure of the liquid crystalline phase formed by the *para*-heptylbenzoate diester of 2,5-bis-(p-hydroxyphenyl)-1,3,4-oxadiazole (ODBP-Ph-C_7), which is a bent-core mesogen. This has been the first time the transition between isotropic and liquid crystalline phases has been achieved using a fully atomistic (all-atom) potential. Simulations at five different temperatures covering the nematic range of ODBP-Ph-C_7 have been undertaken to study the temperature dependence of the biaxial ordering. Ferroelectric domains have been observed in all the systems. Simulations started from the biaxial nematic phase have been performed with the partial charges turned off to study the influence of the electrostatic interactions on the behaviour of the system. A system composed of ODBP-Ph-C_7 and the deuterated molecule hexamethylbenzoate-d_{10} (HMB) has also been simulated to check the validity of the ^{2}H NMR method, which is often employed to study biaxiality.

MD simulations at a fully-atomistic level have been also performed for the mixture of liquid crystals E7, commercialized by Merck. The nematic phase for this mixture is grown from an isotropic phase using an fully atomistic (all-atom) potential, and in order to study the temperature dependence of the order parameter simulations at six different temperatures covering the nematic range have been performed. The internal structure of the mixture, alongside some of its material properties such as rotational viscosity and flexoelectric coefficients have been studied.

Finally, *ab initio* calculations involving several molecular fragments which are components of some of the most common mesogens have been carried out to calculate torsional energies of key dihedral angles. Subsequently, torsional energies have been fitted using a Fourier series expansion to obtain torsional parameters for an atomistic force field. These will be used in future atomistic simulations of liquid crystals.

Declaration

The work in this thesis is based on research carried out at Durham University. The material contained in this thesis has not previously been submitted for any other degree at Durham University or any other institution. The research within this thesis has been conducted by the author unless indicated otherwise.

The copyright of this thesis rests with the author. No quotations from it should be published without the author's prior consent and information derived from it should be acknowledged.

<div align="center">

Jorge Peláez Laguno

March 2007

</div>

Acknowledgments

Bueno, y estos últimos agradecimientos van para la gente sin la que, aunque no hayan estado aquí personalmente o no tengan nada que ver con la química, esta tesis no sería hoy una realidad. Gracias a toda la "tropa gufi" por las cantidades industriales de apoyo mostradas, especialmente a Alfonso, por estar al otro lado del cable duranate estos tres años y pico. Quiero agradecer especialmente a toda mi familia, quienes han aguantado todas las "miserias" (carros y carretas) inherentes a un doctorado durante estos tres años y pico.

En un aparte tambien quiero dar gracias a mi novia Carmen, por estar a buenas y a malas en la distancia y la proximidad todo este tiempo (y el que queda, espero).

Contents

List of Figures

List of Tables

Chapter 1

Introduction to Liquid Crystals

1.1   Origin of Liquid Crystals

Traditionally the difference between the crystalline solid phase and the isotropic liquid phase has been characterized by the differences in orientational and positional order of the molecules. In crystals, both are maintained at long range, whereas in the isotropic liquid neither of them are maintained at long range, although they can exist at short range.

At the end of 1800's the Austrian botanist Reinitzer noticed, while he was investigating cholesteric acetates and benzoates that, between the crystalline and liquid phases, there was a temperature interval where the compound remained in a sort of cloudy fluid state [1]. After this, the cholesterol derivatives melted completely producing a totally normal liquid. After his discovery he contacted Lehmann, who started a survey about the phenomena and concluded that crystals could exist in such a phase that they seemed to be liquid [2]. Further studies revealed that what Lehmann termed "liquid crystal" is an intermediate phase between the crystal phase and the isotropic liquid, characterized by long range orientational order in one dimension and either positional order in one or two dimensions or no long range positional order at all.

1.2 Types of Liquid Crystals

Liquid Crystals can be separated into two different classes, thermotropic and ly-otropic. The former, in which the molecules studied in this project are included, is characterized by a phase transition between the crystalline and the liquid crystalline phase caused exclusively by a change in temperature. The latter is characterized because the transition between phases can also occur due to a change in the concentration, i.e. due to the action of a solvent.

Thermotropic Liquid Crystals

Traditionally, thermotropic liquid crystals are mainly formed of two different types of mesogens (i.e., molecules with the capacity of forming liquid crystalline phases): calamitics and discotics. However, in the last ten years, a new type of molecule has been introduced in this classification with the synthesis of bent-core mesogens.

Calamitic liquid crystals have a main axis which gives them an elongated shape (hence they are also known as rod-shaped). They are composed of aliphatic chains and a rigid core, which is formed of at least one aromatic ring (if not several), such as phenyl or pyrimidine, which may be linked by functional groups such as acetate or ether. The location of the rigid cores within the molecule may be either in the extremes or in the centre of the molecule. In the latter case, two aliphatic chains are bonded to opposite sides of the central core, forming a rod. In the former case a single aliphatic chain is bonded to the rigid core. Although the biaxial nematic phase had been predicted for low molecular weight nematogens a long time ago [3], and there were many false claims for experimental discovery [4, 5], nobody was able to prove their existence of such a phase experimentally, until two very recent papers [6, 7].

Discotic liquid crystals are formed by mesogenic molecules which are gathered in disc-like structures. A significant number of them are derivatives of molecules such as terphenes. The typical structure of the discotic molecules is defined by a

(a)   (b)   (c)
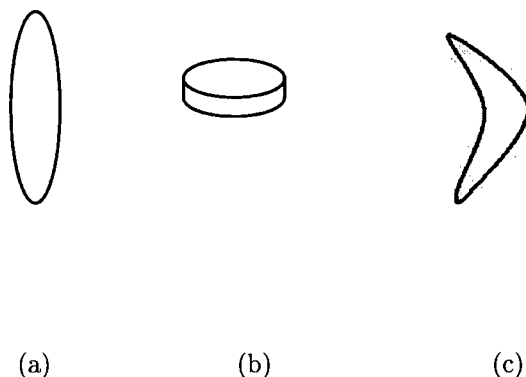
Figure 1.1: Schematic representation of three different types of thermotropic liquid crystals: (a) calamitic, (b) discotic and (c) bent-core.

central rigid aromatic core, formed by several aromatic rings, and several aliphatic chains linked to the rigid core in order to confer flexibility to the molecule.

As mentioned above, in the past few years a new type of thermotropic liquid crystal has emerged with the bent-core molecules. This consist of a V-shaped central rigid core, with an aliphatic chain bonded to each side, forming a banana shaped molecule. A possible variant to the banana shaped molecules, albeit not so popular, is the hockey-stick type of mesogens, with a single aliphatic chain bonded to the central core. Several different names have been given to the bent-core thermotropic liquid crystals, amongst which are "banana shaped", "boomerang shaped", etc. Although initially the bent-core molecules were considered as a type of calamitic liquid crystal, several characteristic features suggested that they constituted a group on their own, especially in what concerns the novel phases formed by this type of mesogens. This point will be subsequently discussed.

Lyotropic Liquid Crystals

Lyotropic liquid crystals are composed of amphiphilic molecules. In polar solvents, these are gathered forming different structures, as micelles (coloids) or bilayers, with their polar head groups orientated toward the solvent and the apolar

aliphatic chains orientated toward each other. At higher concentrations, the micelles are the constituents of the liquid crystalline phase. The lyotropic mesogens can create different mesophases, depending on the different types of molecular arrangements. These can be lamellar (from sheets), hexagonal (from rod-shaped micelles), cubic (from spherical micelles), nematic, gel and intermediate phases. For a further discussion see [8].

          (a)   (b)
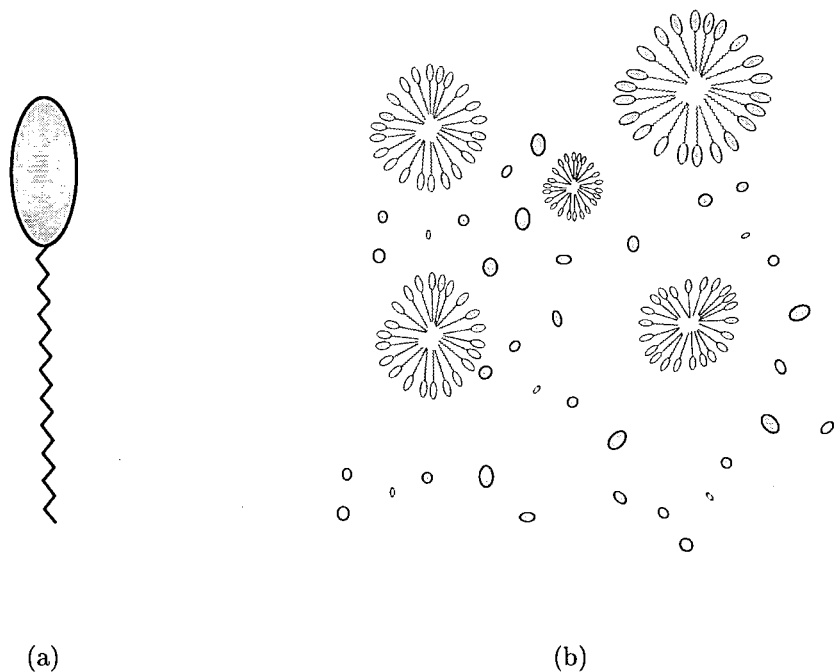
Figure 1.2: Schematic representation of a lyotropic mesogen (a) and a micellar phase (b).

Polymeric and Dendritic Liquid Crystals

Polymeric liquid crystals are formed of mesogenic units attached to each other through a polymeric chain. The mesogenic units are normally standard thermotropic calamitic nematogens. This type of liquid crystal are able to form different liquid crystal phases, such as uniaxial [9–11], biaxial [12–14] nematic and several smectic C phases.

Dendritic liquid crystal are formed on the same basis as the polymeric liquid crystal, although in this case the mesogenic units are connected in such a way that they form a dendrimer [15–20]. This is disposed as a spiderweb, with a central core and different branches spreading out from it. Subsequently, the branches fork to give a new set of branches (or a new generation), in this way, after several generations the branches form a three dimensional tree structure.
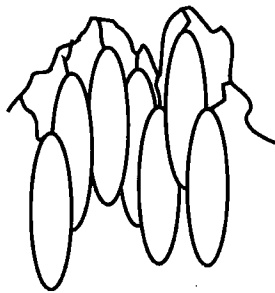
Figure 1.3: Schematic representation of a polymeric liquid crystal.

1.3 Types of Thermotropic Liquid Crystalline Phases

The first classification of different liquid crystalline phases was carried out by G. Friedel [21]. Friedel disliked the term liquid crystal and used the term mesogen instead, as molecules which are able to form mesophase. The prefix *meso* comes from Greek and means middle. Therefore, Friedel interpreted liquid crystalline phases as intermediate phases between the isotropic phase, where neither orientational or transitional order exist at long range and the crystalline one, where both orientational and transitional order exist.

Nematic Phases

The nematic phase is characterized by a long range orientational order. This might occur in just one dimension, forming the uniaxial nematic phase, or in three dimensions, forming the biaxial nematic phase. The latter has been observed very rarely, mainly in lyotropic and polymeric liquid crystals [12–14, 22], although quite recently it has also been detected in thermotropic liquid crystals [6, 23–25]. Further discussion on this phase will take place in subsequent chapters. In the case of calamitic and bent-core mesogens, the uniaxial nematic phase onset takes place when the main axis of the molecules (i.e., the one running along the spine of the molecules) aligns parallel to a common direction, known as the director. In the case of the discotic molecules the alignment occurs amongst the axes normal to the plane where the rigid-core of the molecule is contained (see figure 1.4). In the uniaxial nematic phase mesogenic molecules are aligned with respect to a common director vector over long distances. Hence, the nematic phase differs from the isotropic one in the fact that in the latter orientational order can only exist at short range, between nearest neighbour molecules. The degree of alignment is measured by means of an order parameter, as will be explained in section 1.4.

Smectic Phases

All smectic mesophases have the common characteristic that their molecules are stacked in layers. Smectic phases occur amongst calamitic and bent-core molecules. However, the way in which the molecules are positioned in layers lead to different subclasses of smectic liquid crystalline phases. A possible subclassification can be achieved by attending to the orientation of the molecular long axis with respect to the layer planes. According to this, smectic mesophases can be subdivided in orthogonal (for instance, SmA) and tilted (for instance, SmC) phases (see figure 1.5). In the former the long molecular long axis remains perpendicular to the layer plane, whereas in the latter it is tilted. Moreover there are some mesophases which
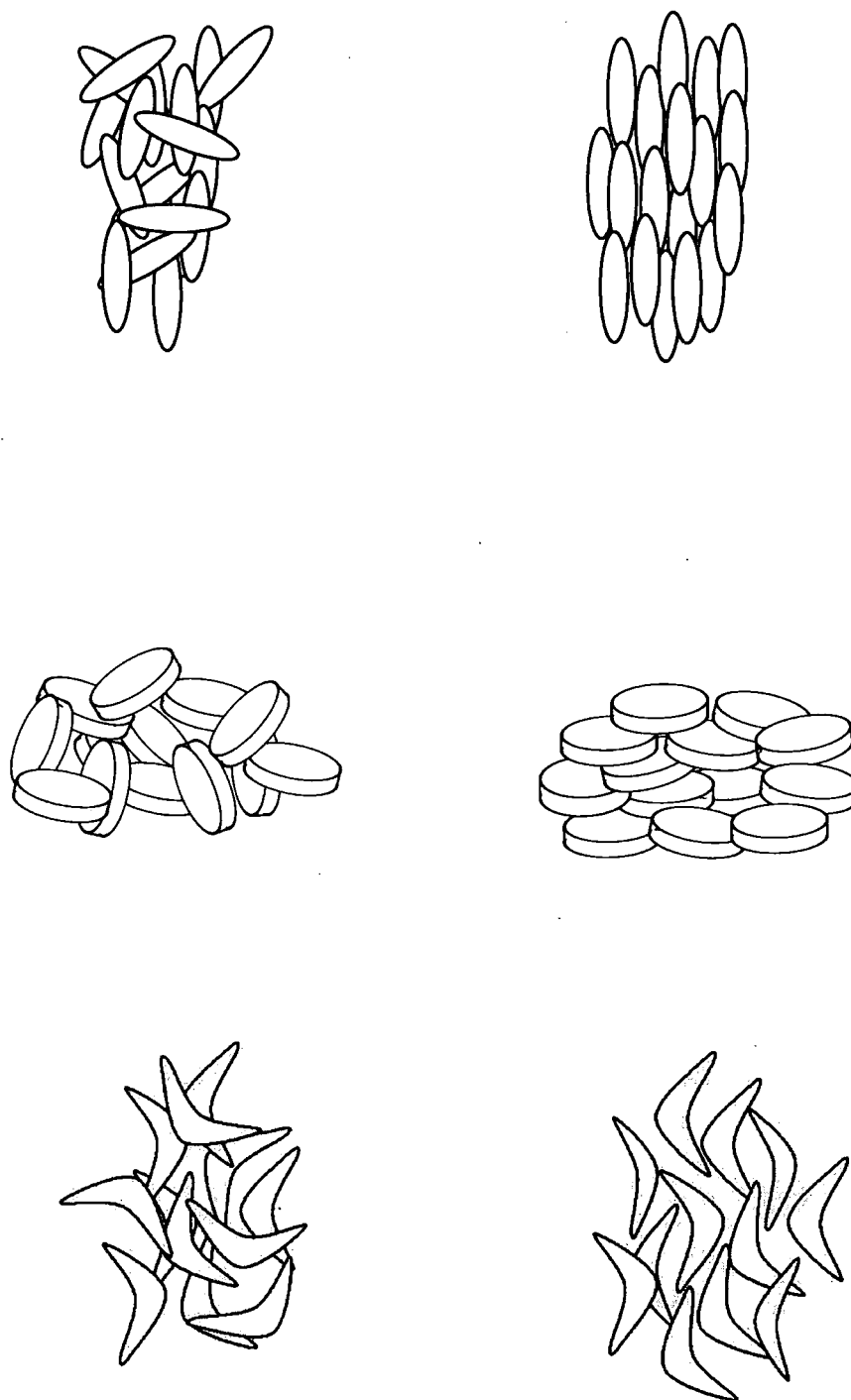
Figure 1.4: Differences between the isotropic (left) and nematic (right) phases formed by calamitic (top), discotic (middle) and bent-core (bottom) mesogens.

have local hexagonal order, such as SmB.

In the last ten years many different smectic phases formed by bent-core molecules have been characterized. A new nomenclature has been applied to these smectic phases according to the particular features they exhibit, such as biaxiality and ferroelectric and anti-ferroelectric behaviour. For a comprehensive review on the topic see ref. [26]. Thus a capital "B" followed by a numerical suffix determines the different types of "banana" phases. Examples are given in 1.5.

(a)   (b)

(c)   (d)
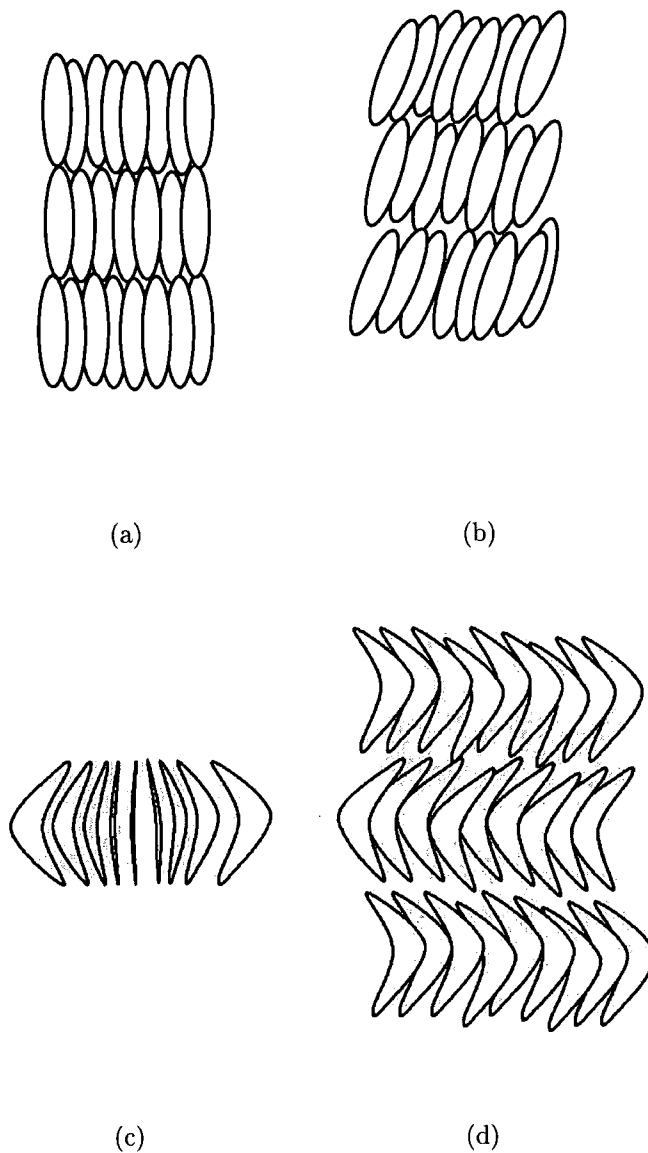
Figure 1.5: Schematic representation of some smectic phases formed by calamitic mesogens and bent-core ones: (a) SmA, (b) SmC, (c) B_7 and (d) B_2.

Columnar Phases

Columnar phases may be consider as the equivalent of smectic phases but for discotic molecules. In a columnar phase, the mesogens stack on top of each other as though they were coins. The columns created in such a way tend to pack forming a hexagonal arrangement (see figure 1.6).
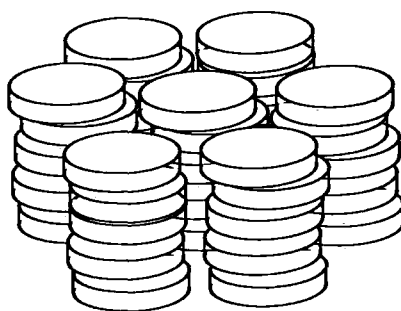
Figure 1.6: Schematic representation of a columnar phase formed by discotic mesogens.

Chiral Nematic Phases

The chiral nematic phase, originally named cholesteric phase, arises from the presence of chiral molecules in a nematic phase. The chirality of the molecules is transmitted to the bulk phase, forcing the director to undergo a helical twist in space, about an axis perpendicular to the long axes of the mesogens (see figure 1.7).

1.4 Order Parameter

In order to make possible the measurement of the degree of order existing in a liquid crystal bulk system, an order parameter must be calculated. This is a way of
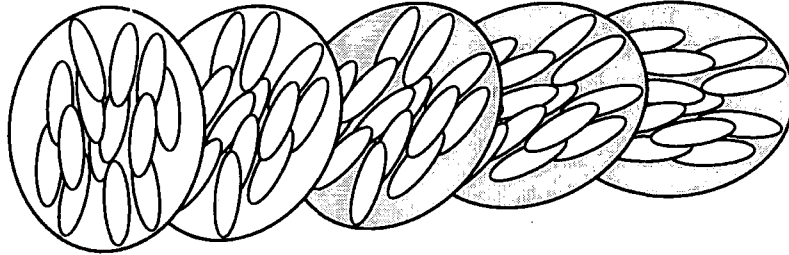
Figure 1.7: Schematic representation of a chiral nematic phase. The diagram shows the molecular order at different positions along a line perpendicular to the director.

measuring the average alignment of the long molecular axis (in a mono axial liquid crystal) with the ensemble director.

The search for a vector representing the long axis of each molecule is carried out with the diagonalisation of the inertia tensor matrix for each molecule [27]

$$I_{\alpha\beta} = \sum_i m_i (s_i^2 \delta_{\alpha\beta} - s_{i\alpha} s_{i\beta}), \tag{1.1}$$

$$\delta_{\alpha\beta} = \begin{cases} 0 \text{ if } \alpha \neq \beta \\ 1 \text{ if } \alpha = \beta \end{cases}, \tag{1.2}$$

where m_i is the mass in atom i and s_i are the atomic distance vectors with respect to the molecule center of mass and $\alpha, \beta = x, y, z$. The long axis vector is defined as the eigenvector associated with the smallest eigenvalue in the inertia tensor matrix. However, this is not the only way of characterizing the orientation of molecules. This can be also represented by the orientation of the molecular dipole moment (if present) or by vectors defining the shape of the molecules.

To calculate the director for the ensemble it is necessary to diagonalize the or-

dering tensor

$$Q_{\alpha\beta} = \frac{1}{N} \sum_{j=1}^{N} \frac{3}{2} a_{j\alpha} a_{j\beta} - \frac{1}{2} \delta_{\alpha\beta}; \qquad (1.3)$$

where N represents the number of molecules, a_j the molecular long axis for the molecule j and the subscripts α, β represents the coordinates x, y and z of the long axis and $\delta_{\alpha\beta}$ is the same as the one in equation 1.2. The value of the director vector (usually denoted as **n**) is given by the eigenvector associated with the largest eigenvalue of Q.

The uniaxial order parameter, S_2, can be associated with the largest eigenvector of Q. It can also be obtained from the expression

$$S_2 = < P_2 \cos(\mathbf{n}.\mathbf{a}) > = < P_2 \cos\theta >, \qquad (1.4)$$

where P_2 is the second rank Legendre polynomial, θ is the angle between the molecular long axis **a** and the director **n** and the angular brackets show the average over all the molecules within the ensemble.

1.5 Scope of this Thesis

This thesis can be divided in four principal blocks with a main feature in common: the atomistic simulation of liquid crystals. The first block is formed by chapters 2 and 3. The former introduce different simulation techniques, making particular stress on molecular dynamics, which has been used throughout this thesis. In chapter three the phenomenon of biaxiality is introduced, alongside bent-core liquid crystals. In the second block (constituting chapters 4 and 5) atomistic simulation of low-weight thermotropic bent-core liquid crystal are described. The aim of this simulation was to reproduce the biaxial nematic phase which has been recently been claimed to be produced by the *para*-heptylbenzoate diester of 2,5-bis(p-

hydroxyphenyl)-1,3,4-oxadiazole (ODBP-Ph-C$_7$) [23]. A wide spectrum of temperatures covering all the nematic range have been simulated, and an isotropic phase has been quenched into a nematic phase. Moreover, the experimental system used in the determination of the biaxial phase using ^{2}H NMR (normally considered as the ultimate proof in the characterization of biaxial nematic phases [28]) has been also reproduced. The latter required incorporation of a probe molecule hexamethylbenzene into a bulk system of ODBP-Ph-C$_7$.

The second block of results covers chapters 6 and 7. Atomistic simulations of the commercial mixture of liquid crystals E7 have been undertaken in order to determine the structure of the nematic phase formed by such a mixture, as well as the existing correlations between different types of molecules. Subsequently, the results obtained in the atomistic simulations have been used to calculate the rotational viscosity and the flexoelectricity coefficients of the mixture.

Last, but not least, the third block of results constitutes a single chapter. In chapter 8 quantum mechanical calculations at an *ab initio* level have been performed using the density functional theory with the aim of calculating torsional energies in different molecules which are components of most of the mesogens. The torsional energies are subsequently employed in the parametrization of atomistic force field parameters which can be used in the future in further atomistic simulations of liquid crystals.

Chapter 2

Computer Simulation

2.1 Introduction

Computer simulations have their origin back in 1953, when a very simplistic model including few hundreds of molecules formed of two dimensional hard discs were simulated using a *Metropolis Monte Carlo* technique [29]. However, the first molecular dynamics simulation had to wait until four years later. Alder and Wainwright used this technique to simulate a sytem formed of hard spheres [30, 31].

Albeit the first models used in molecular simulations were extremely simplistic and idealized, subsequent more complicated models have been elucidated with the aim of producing more realistic simulations. Lennard-Jones potentials and later Gay-Berne potentials describe the interaction between single particles in a more accurate way than the hard models used to run the first simulations. Likewise, atomistic simulations run using parameters calculated with the state-of-the-art *ab initio* methods provide a description of the molecular interactions, which are far more realistic than single particle molecular potentials.

The importance of molecular simulation dwells in the fact that it fills the gap existing between theory and experiment. Moreover, it provides the chance to achieve results which are out of reach for both theory and experiment. Molecular simulation can be used with a wide range of intentions. In the field of theoretical science it has been widely used to corroborate different hypothesis and theories. Besides, molecular simulation makes possible the reproduction of experiments that might

13

be unfeasible in the laboratory for different reasons, for instance due to extreme conditions of pressure and temperature. Another main advantage is given by the capacity of molecular simulation to reproduce particular systems at a microscopic level, taking account of molecular interactions, something that is rather complicated to carry out experimentally.

Nevertheless, there are also drawbacks to mention in the use of molecular simulation. Unfortunately, the quality of the simulation depends on the model used, as well as in the parameters employed to define the interactions between particles. Simplistic models do not allow a faithful reproduction of a real system, and more detailed models, such as atomistic ones, are computationally very expensive and thus both the system size and the time period simulated are limited. However, the continuous development of new and more powerful processors and the the gathering of these into clusters and supercomputers allow the use of parallel simulations. The latter provides great expectations for the future.

The different time scales required to simulate different types of molecular motions represent another issue in the simulation process. Hence different techniques have to be employed to tackle different types of motion.

Subsequently, a brief review of simulation models and different techniques for molecular simulation will be presented. For more detailed reviews of simulation related specifically to liquid crystalline systems see references [32, 33].

2.2 Simulation Models

2.2.1 Single Site Models

Single site models are the simplest existing for atoms and molecules. However, because of their simplicity, they are relatively easy to simulate and can be used for systems formed from a large number of particles.

Single site models involve a unique set of coordinates to define the position and (in the case of an anisotropic site) the interaction of the molecules. This concerns the centres of mass of the molecules. However, the form of the interaction potential may vary greatly between different models.

The most basic single site model is the spin one. In this model the molecules are merely represented by the position of the centres of mass as a fixed lattice and a vector defining the orientation of the molecule. Adjacent spins then interact through a well-defined pair potential, which represents the molecular interaction. No excluded volume is included in this model.

The use of a sphere as an approximate representation of an atom or a molecule constitutes a more complicated model than the one described above, albeit still very simplistic. Here, continuous coordinates are used to define the position of the particle and typically the interaction potential introduces an excluded volume interaction. Spheres have a completely isotropic shape, thus they can not adopt a preferred orientation. This makes them useless to model liquid crystal behaviour on their own, although latterly it will be explained how they can take part in more complicated models which are suitable for liquid crystals. However, they have been widely used in the simulation of isotropic fluids [34].

Spherocylinders (figure 2.1) provide a convenient way of including orientational dependence into a single site model. These models are represented by a centre of mass vector, an orientation vector u_i a radius D and an additional, L/D, representing the ratio between the molecular length and diameter.

Some anisotropic models have additional parameters in order to decrease their symmetry, thus becoming biaxial. A model proposed by Allen [35] used hard ellipsoids to simulate biaxial platelets, so as to be able to produce biaxial phases (see figure 2.1).

Finally, single site models can also use ellipsoids in order to represent molecules. As with spherocylinders, this type of model has the advantage of possessing an anisotropic shape, which allows molecules to adopt different orientations with respect to each other, as shown in figure 2.2. As a consequence this type of model is also useful for liquid crystalline phases. The shape anisotropy for an ellipsoid is given by

$$\chi = \frac{\left(\sigma_e/\sigma_s\right)^2 - 1}{\left(\sigma_e/\sigma_s\right)^2 + 1}, \tag{2.1}$$

where σ_s and σ_e are the side-to-side and end-to-end separations for two touching molecules. The fact that the final shape of the ellipsoid is closer to a calamitic or
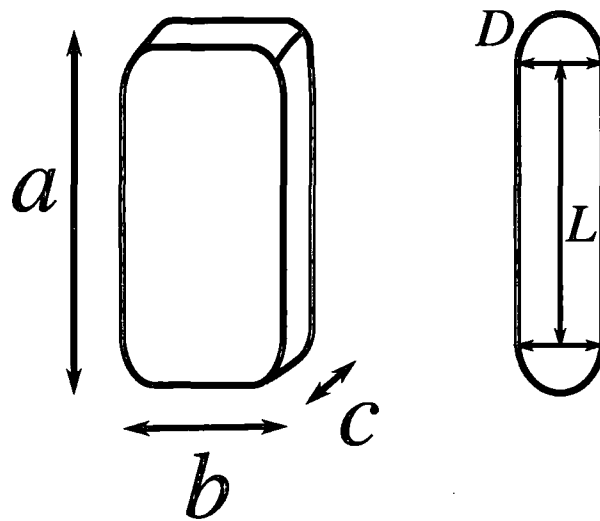
Figure 2.1: Diagram showing a biaxial ellipsoid (left) and a spherocylinder (right). In the case of the former three parameters, a, b and c are given in order to define the anisotropic shape. The latter is symmetric about its axis of revolution, and its shape is defined by the length (L) and the diameter (D).

a discotic mesogen depends upon these two parameters. For the rod-like ellipsoids $\sigma_e > \sigma_s$, whereas for the disk-like ellipsoids the relation is the opposite way around.
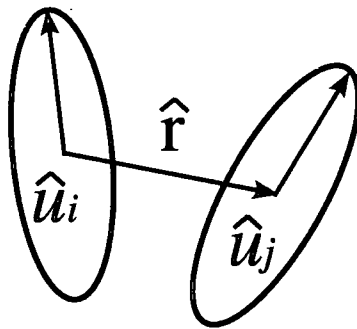
Figure 2.2: Two ellipsoids with orientations given by the unit vectors $\hat{u}_i$ and $\hat{u}_j$ and with a relative position with respect to each other given by the unit vector $\hat{r}$.

2.2.2 Atomistic Models

In atomistic models the representation of a molecule is accomplished by considering every single atom within the molecule (*all-atom* atomistic model) or every heavy atom except for the hydrogens (*united atom* model).

Atomistic models (ref. [36–39]) have both advantages and drawbacks with respect to the single-site models. The main advantage dwells in their capacity to represent molecular conformations.

However, this type of model also presents an important disadvantage: its high degree of complexity makes it extremely time consuming, since interactions between all the atoms within the system are to be taken into account. An atomistic model is represented in figure 2.3 (a).

2.2.3 Coarse Grain Models

Coarse grain models are intended to achieve a good compromise between the simplistic but fast single-site models and the detailed but time consuming atomistic models. To do so, in this atoms which form a defined component of a molecule (i.e.,

a phenyl ring or an aliphatic chain) are grouped into a single site (for instance, a sphere or a spherocylinder), and represented by one of the single-site models described above (see figure 2.3). Subsequently these single sites are bonded together in order to form a more complex molecule. This type of model is particularly useful to describe macromolecules such as dendrimers or polymeric liquid crystals [40–45].
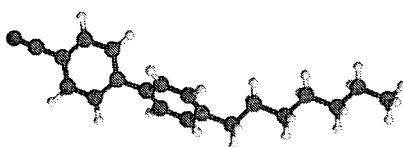
(a)
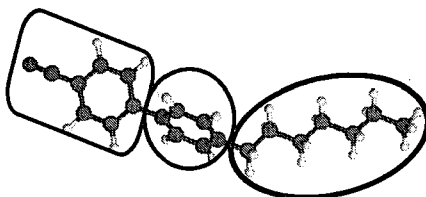
(b)

Figure 2.3: Atomistic model (a) and a possible coarse grain model (b) of the mesogen 7CB.

2.3   Potentials

Potentials represent the different interactions existing between two particles. In addition to the different models of particles described above, there are also different types of potentials, running from the most simplistic hard walls to the most sophisticated force fields.

2.3.1   Hard Potentials

Hard potentials constitute the most simplistic potential used for molecular simulation. They present the big advantage of being fast and easy to implement. However, they represent a rather simplified model for real molecular interactions. Hard potentials can be purely repulsive or can be combined with an attractive well. A hard wall potential can be represented by:

$$V(r) = \begin{cases} 0 \text{ if } r > r_0 \\ \infty \text{ if } r \leq r_0 \end{cases}, \qquad (2.2)$$

where r_0 is the threshold inter-particle distance and r is the actual inter-particle distance. The overlapping between molecules is characterized by an infinite energy and thus forbidden. The square well potential, parallel to the hard wall, has discrete values. However, an attractive term is included for certain intermolecular distances:

$$V(r) = \begin{cases} \infty \text{ if } r \leq r_1 \\ \varepsilon \text{ if } r_1 < r < r_2 \\ 0 \text{ if } r \geq r_2 \end{cases}, \qquad (2.3)$$

where ε represents the well depth. Once the threshold of r_1 is overcome, there is a sharp increment of the energy from a negative to infinite energy, becoming suddenly a repulsive potential. The pair potential with respect to the intermolecular distance r is represented in figure 2.4 (b).

The potentials described above have been used to represent intermolecular interactions in simulations of hard ellipsoids [46] and hard spherocylinders [47]. Such models are capable of showing a nematic phase (ellipsoids and spherocylinders) and

smectic A and smectic B phases (spherocylinders only) [48].
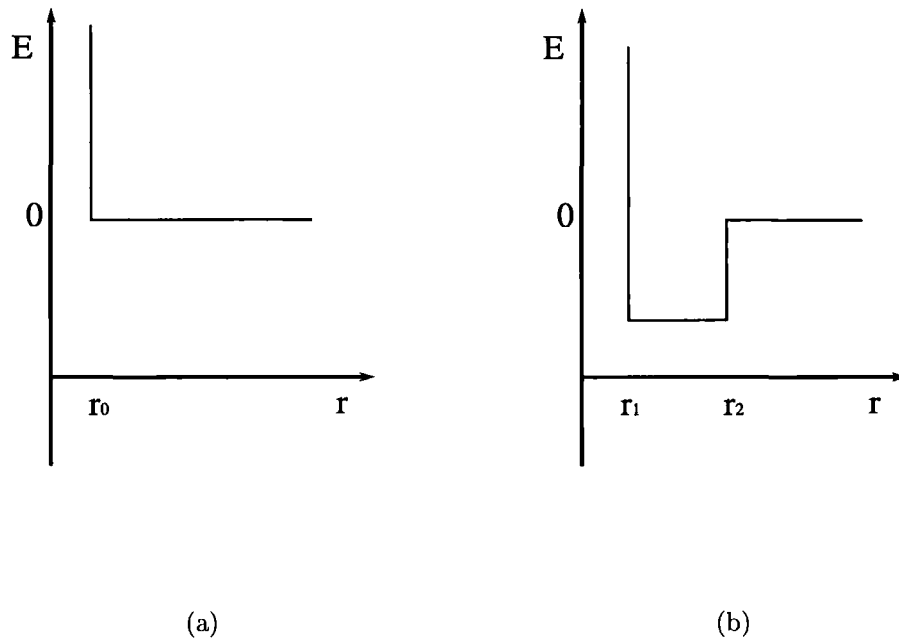
Figure 2.4: Representation of the hard wall (a) and hard well (b) potentials.

2.3.2 Soft Potentials

Unlike hard potentials, soft potentials do not have discrete values. Instead, they are represented by a continuous function, an example of which is shown in figure 2.5. This demands more complicated expressions than those used for hard potentials, increasing the time required to run the simulations.

Both purely repulsive and attractive soft potentials are possible. The former is shown in figure 2.5 (a), whereas the latter is shown in figure 2.5 (b). In the case of the attractive potentials, the well depth is often given by the parameter ε.

The Lennard-Jones Potential

The Lennard Jones potential is one of the most popular amongst the soft potentials. It is mainly formed of two terms, an attractive and a repulsive one

(a)   (b)
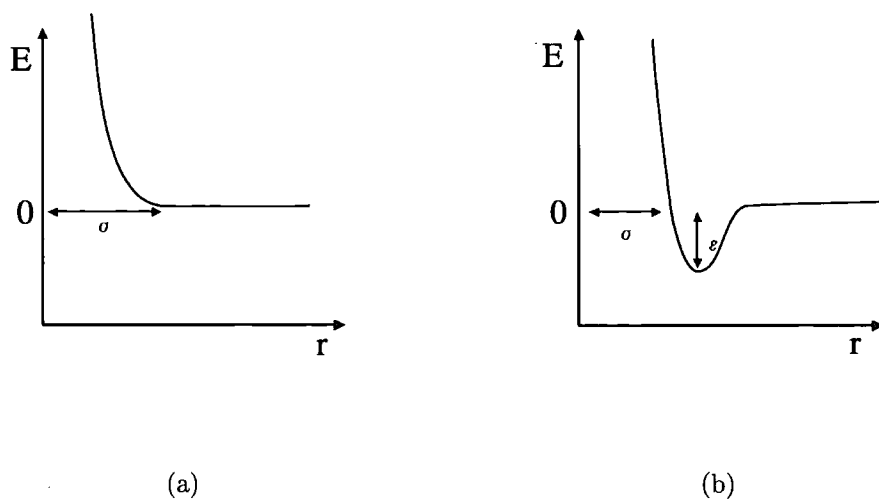
Figure 2.5: Representation of soft repulsive (a) and attractive (Lennard-Jones type) (b) potentials where r is the interparticle distance.

$$V_{LJ} = 4\epsilon_{ij} \left[\left(\frac{\sigma_{ij}}{r} \right)^{12} - \left(\frac{\sigma_{ij}}{r} \right)^{6} \right], \tag{2.4}$$

where ϵ is the well depth and σ is the inter-particle distance at which the potential equals zero. In the Lennard-Jones potential [49], both parameters σ and ϵ are constant and their value depends on the particles involved in the interaction.

The Lennard-Jones potential is isotropic and therefore no preferred orientation can be accounted. A representation of the Lennard-Jones potential can be appreciated in figure 2.5 (b).

The Gay-Berne Potential

The Gay-Berne potential [50] is an anisotropic potential because certain molecular orientations are energetically more favoured than others, as can be gathered from figure 2.6. The Gay-Berne potential is represented by a formula which includes anisotropic attraction and repulsion (eq.2.4). The equation for the Gay-Berne potential is given by

$$V_{GB}\left(\hat{r}, \hat{u}_1, \hat{u}_2\right) = 4\epsilon \left[\left(\frac{\sigma_0}{r - \sigma\left(\hat{r}, \hat{u}_1, \hat{u}_2\right) + \sigma_0} \right)^{12} + \left(\frac{\sigma_0}{r - \sigma\left(\hat{r}, \hat{u}_1, \hat{u}_2\right) + \sigma_0} \right)^{6} \right],$$

$$(2.5)$$

where the well depth is given by

$$\epsilon = \epsilon_0 \epsilon \left(\hat{u}_1, \hat{u}_2\right)^{\nu} \epsilon' \left(\hat{r}, \hat{u}_1, \hat{u}_2\right)^{\mu}. \tag{2.6}$$

In equation 2.6, $\epsilon\left(\hat{u}_1, \hat{u}_2\right)$ is given by

$$\epsilon\left(\hat{u}_1, \hat{u}_2\right) = \left[1 - \chi^2 \left(\hat{u}_1 \cdot \hat{u}_2\right)^2\right]^{-\frac{1}{2}}, \tag{2.7}$$

where χ is the shape anisotropy defined in 2.1 and $\epsilon'\left(\hat{r}, \hat{u}_1, \hat{u}_2\right)$ is given by

$$\epsilon'\left(\hat{r}, \hat{u}_1, \hat{u}_2\right) = 1 - \left(\frac{\chi'}{2}\right) \left[\frac{\left(\hat{r} \cdot \hat{u}_1 + \hat{r} \cdot \hat{u}_2\right)^2}{1 + \chi'\left(\hat{u}_1 \cdot \hat{u}_2\right)} + \frac{\left(\hat{r} \cdot \hat{u}_1 - \hat{r} \cdot \hat{u}_2\right)^2}{1 - \chi'\left(\hat{u}_1 \cdot \hat{u}_2\right)} \right], \tag{2.8}$$

where χ' is given by

$$\chi' = \frac{\left[1 - \left(\frac{\epsilon_e}{\epsilon_s}\right)^{\frac{1}{\mu}}\right]}{\left[1 + \left(\frac{\epsilon_e}{\epsilon_s}\right)^{\frac{1}{\mu}}\right]}. \tag{2.9}$$

For the sake of simplicity, it is rather common to define χ and χ' in terms of the ratios $\kappa = \sigma_e/\sigma_s$ and $\kappa' = \epsilon_e/\epsilon_s$. Hence χ and χ' read

$$\chi = \left(\frac{\kappa^2 - 1}{\kappa^2 + 1}\right) \tag{2.10}$$

$$\chi' = \left(\frac{\kappa'^{\frac{1}{\mu}} - 1}{\kappa'^{\frac{1}{\mu}} + 1}\right). \tag{2.11}$$

The anisotropic contact distance $\sigma\left(\hat{r}, \hat{u}_1, \hat{u}_2\right)$ is given by

$$\sigma\left(\hat{r}, \hat{u}_1, \hat{u}_2\right) = \sigma_0 \left\{ 1 - \frac{\chi}{2} \left[\frac{\left(\hat{r} \cdot \hat{u}_1 + \hat{r} \cdot \hat{u}_2\right)^2}{1 + \chi\left(\hat{u}_1 \cdot \hat{u}_2\right)} + \frac{\left(\hat{r} \cdot \hat{u}_1 - \hat{r} \cdot \hat{u}_2\right)^2}{1 - \chi\left(\hat{u}_1 \cdot \hat{u}_2\right)} \right] \right\}^{-\frac{1}{2}}, \tag{2.12}$$

where $\hat{r}$ is the unit vector representing the orientation of the vector existing between the centres of mass of the two molecules, and $\hat{u}_1$ and $\hat{u}_2$ are the unit vectors representing the molecular orientations, as shown in figure 2.2. σ is the intermolecular distance at which the attractive and repulsive energies counteract each other, resulting in the potential equally zero. The Gay-Berne potential is probably the most popular soft-non-spherical potential presently in existence [51–55].

(a)   (b)
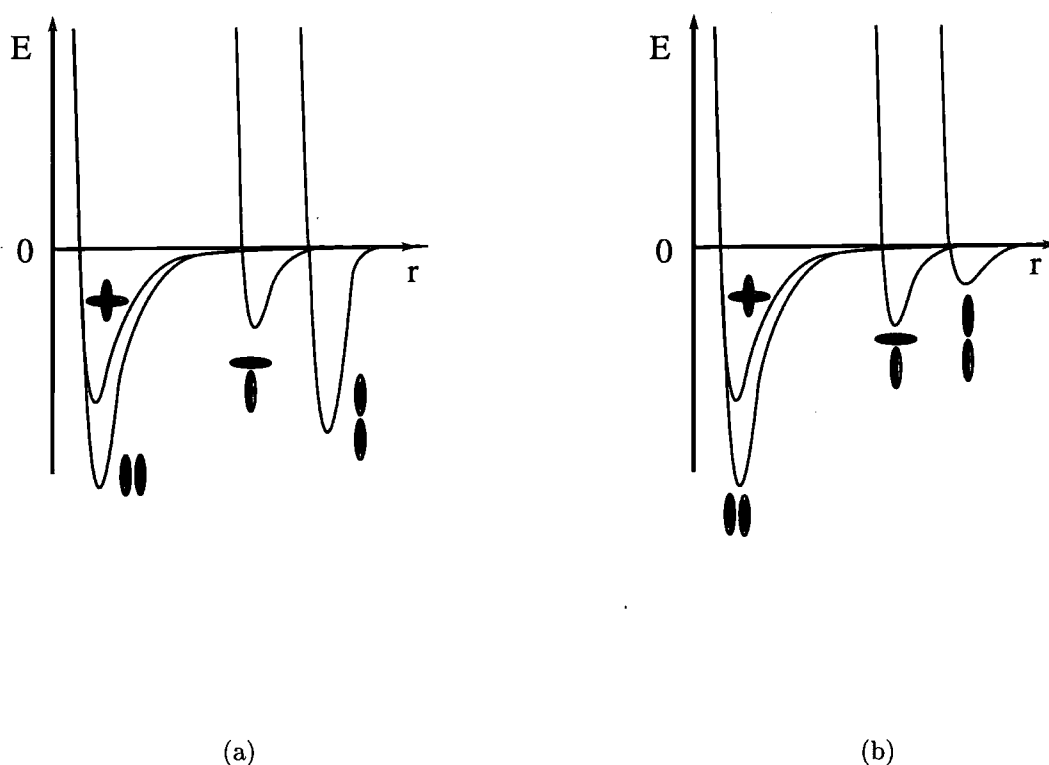
Figure 2.6: Representation of Gay-Berne potentials where different pairwise orientations have different energies, constituting an anisotropic potential.

2.3.3   Force Fields

A type of potential that has become widely used in chemistry is a "molecular force field". These have been developed to take into account the intermolecular and in-

tramolecular interactions for each atom in the system. There is not a unique functional form for the force field. Instead, its form depends on the accuracy required.

$$E = \underbrace{\sum E_{bonds} + \sum E_{angles} + \sum E_{dihedrals}}_{Intermolecular\ Interactions} + \underbrace{\sum E_{coulomb} + \sum E_{vdw}}_{Intramolecular\ Interactions}. \qquad (2.13)$$

Equation 2.13 gives the atomistic force field which will be used throughout this work. In it, bond stretching, angle bending and dihedral angle torsions are taken into account within the intramolecular terms. The two former terms are treated as harmonic, that is, the potential is proportional to the separation of the atoms from their equilibrium position. A harmonic potential arises from taking a Taylor expansion of the full potential truncated at the second term

$$E_{bond} = \sum_{bonds} \frac{1}{2} k_{bond}(l - l_0)^2, \qquad (2.14)$$

$$E_{angle} = \sum_{angles} \frac{1}{2} k_{angle}(\theta - \theta_0)^2. \qquad (2.15)$$

In equation 2.14 k_{bond} represents the harmonic force constant, l_0 represents the reference bond length and l the actual one. In equation 2.15, k_{angle} represents the angle bending force constant and θ and θ_0 represent the actual and the reference bond angles, respectively.

By contrast, the torsional energy can not be treated in this way, since the dihedral angle is not specified relative to an equilibrium position but is able to rotate with a 360^0 periodicity. Therefore it is more appropriate to develop it as a Fourier expansion

$$E_{dihedral} = \sum_{dihedrals} \sum_{n} V_n \cos(1 + (n\phi - \delta_n)) \qquad (2.16)$$

$$\delta_n = \begin{cases} 0^0 \text{ if } n = \text{odd} \\ 180^0 \text{ if } n = \text{even} \end{cases}, \qquad (2.17)$$

where n is the number of terms in which the expansion is carried out. Usually this number is never bigger than 6. V_n are the torsional rotational force constants and ϕ is the current torsional angle. δ_n are the phase angles and adopt the values specified in equation 2.17.

In the intermolecular part of the force field equation, there are two terms included: one dealing with the electrostatic (coulombic) interactions, and another dealing with the rest of long term interactions (van der Waals interactions). The former are normally represented by

$$E_{elec} = \sum_{i,j} \frac{1}{4\pi\epsilon_0} \frac{q_i q_j}{r_{ij}}, \qquad (2.18)$$

where r_{ij} is the inter-atomic distance and q_i are the atomic charges. Equation 2.18 does not include the interaction between atoms with a common bond or angle.

Regarding the van der Waals interaction, different expressions are adopted depending on the type of model simulated. In case of an atomistic model, these interactions are normally represented by a Lennard-Jones potential (eq. 2.4). However, in the case of coarse grained models; it is very common that different types of molecular models are combined in order to represent a molecule, as shown in figure 2.3 (b) [45, 56]. Therefore, for these cases a combination of Lennard-Jones and Gay-Berne potentials are used to deal with the site-to-site interactions. In this case, the van der Waals component of the potential reads

$$E_{vdW} = \sum_{LJ} E_{LJ-LJ} + \sum_{GB} E_{GB-GB} + \sum_{GB-LJ} E_{LJ-GB}. \qquad (2.19)$$

2.4   Simulation Techniques

2.4.1   Molecular Mechanics

Molecular mechanics is a technique which, by means of classical mechanics, tries to find the minimum energy structure of a certain molecule [57,58]. Molecules are represented by a group of nuclei linked by harmonic forces, whereas the electronic movements are neglected. Molecular mechanics is also considered an empirical method, since most of the parameters used as force constants in the force field come from experimental data. Normally the molecules treated with molecular mechanics are isolated in the gas phase. Therefore the first step is to choose a draft structure from which to start the simulation. An energy minimization is then carried out. There are several different methods to carry out this task, such as the steepest descent method or methods which employ the second derivative (Newton-Raphson method etc [57, 59]). Each method uses an iterative procedure in which bond distances, angles and dihedral are changed in a series of steps. The methods continue until a global minimum is reached.

Molecular mechanics is a very desirable technique due to its simplicity. In general, it is used to find conformational energies in isolated molecules, especially in those where extension is not very large. However, for larger molecules, it is very likely that multiple potential energy minima will be found. Multiple minima appear when there is more than one conformation in the molecule capable of supporting the minimum energy in the molecule. Sometimes not all the minima have the same energy. In those cases, the energy minima are divided into the global minimum, which is the minimum with the lowest energy, and local minima, which are the rest.

2.4.2   Molecular Dynamics

This technique consists of solving the Newton equations of motion for a determined group of particles. It uses the well known relation

$$m\mathbf{a} = \mathbf{F}, \tag{2.20}$$

where the force $\mathbf{F}$ can be calculated by means of the expression

$$\mathbf{F} = -\nabla V(r), \tag{2.21}$$

$V(r)$ being the potential. Usually given by a force field, although it can be any type of potential used to describe the interactions among the molecules.

Equation 2.20 can also be written as

$$m\frac{\partial^2 \mathbf{r}}{\partial t^2} = \mathbf{F}. \tag{2.22}$$

By integrating this equation, it is possible to know the evolution of the system with respect to the time. Depending on the type of model used, this can be composed of molecules or atoms.

Integration of the equations of motion is typically carried out by means of finite difference methods. In these, the system is given a set of initial positions, velocities and accelerations at time t and the finite difference algorithm is used to advance these quantities forward to a time $t+\delta t$, where δt is known as the time step. The smaller δt is, the bigger the accuracy obtained but also the longer the simulation run lasts. Therefore a compromise between accuracy and simulation time must be reached.

The Verlet Algorithm

Several finite difference algorithms have been designed (see ref. [60]). The requirements that must be fulfilled are rapidity, small memory requirement, time-

reversibility and capable to deal with long δt, satisfying the conservation momenta law and being easy to program.

The algorithm presented by Verlet [61] turns out to be a very suitable one. It is made up from Taylor expansions

$$r(t + \delta t) = r(t) + \delta t \, v(t) + \left(\frac{1}{2} \right) \delta t^2 \, a(t) + ... \tag{2.23}$$

$$r(t - \delta t) = r(t) - \delta t \, v(t) + \left(\frac{1}{2} \right) \delta t^2 \, a(t) - ... \tag{2.24}$$

By adding equation 2.23 to equation 2.24, the Verlet algorithm, independent for coordinates is obtained:

$$r(t + \delta t) = 2r(t) - r(t - \delta t) + \delta t^2 a(t). \tag{2.25}$$

Nevertheless, as the velocity is required for the calculation of the kinetic energy, it can be obtained from the expression:

$$v(t) = \frac{r(t + \delta t) - r(t - \delta t)}{2\delta t}. \tag{2.26}$$

However, the Verlet algorithm also has its disadvantages. In order to obtain expression 2.25, a small figure is added to a big one, which is likely to produce errors. Also, the way this algorithm deals with the velocity is not very practical. Hence a new algorithm, was proposed to tackle these drawbacks. This is called the leap-frog algorithm [62, 63]:

$$r(t + \delta t) = r(t) + \delta t \, v(t + \frac{1}{2}\delta t), \tag{2.27}$$

where the velocity, leaps over the coordinates in order to produce the next $\frac{1}{2}\delta t$ values

$$v(t + \frac{1}{2}\delta t) = v(t - \frac{1}{2}\delta t) + \delta t \, a(t). \tag{2.28}$$

Apart from these algorithms, many other have been proposed, such as the velocity Verlet or those proposed for the predictor-corrector method [60].

Barostats and Thermostats

So far we have taken for granted that the energy, number of molecules and volume of our ensemble are keep constant, thus we are dealing with the micro-canonical ensemble. However, since most of the experiments carried out in the laboratory happen at constant pressure and temperature, it might be interesting to change the micro-canonical ensemble for the isothermal-isobaric ensemble. To do this there are different methods (see ref. [64]). The Berendsen method [65] consists of using a rescaling parameter, which modifies the volume of the cell by a factor of μ and the coordinates of the atomic particles by a factor of $\mu^{\frac{1}{3}}$ in order to obtain the desired pressure. The formula for the rescaling parameter is

$$\mu = 1 - \frac{\beta \Delta t}{3\tau_p}(P - P_0), \tag{2.29}$$

for an isotropic variation of the cell size, where β is the isothermal compressibility and τ_p is time constant, P is the current pressure and P_0 is the desired pressure. If an anisotropic variation is needed, a rescaling tensor is required.

For keeping the temperatures constant, the velocity of the particles are modified, since the the temperature is related to the average kinetic energy, and this is dependent on the velocity. The velocity rescaling parameter λ has the form

$$\lambda = 1 + \frac{\Delta t}{\tau_T}\left(\frac{T_0}{T} - 1\right). \tag{2.30}$$

2.4.3 Monte Carlo Technique

One way of obtaining the value of a certain observable is a time average, as occurs in molecular dynamics; but this is not the only one. In the Monte Carlo technique, an observable is obtained as an average over different configurations: an ensemble

average.

In the Monte Carlo method, in its crudest version; different configurations are generated by making random changes to the coordinates and then a statistical weight proportional to the Boltzmann factor is assigned to them.

In the importance sampling method the configurations are generated according to a probability distribution proportional to the Boltzmann factor and then accepted configurations are equally taken into account in the final averages.

In the Metropolis Monte Carlo method, configurations will occur with the correct Boltzmann weight and therefore the correct statistical average is obtained after a series of configurations has been generated. The way in which the contributing configurations are chosen in the Metropolis Monte Carlo Method is explained below. One particle is randomly chosen from the ensemble with an energy given by E_n. Its position is modified within a determinate region of the space, and the potential for that configuration is recalculated, giving E_m. If this potential is smaller than the former one (i.e., $E_m < E_n$), the movement is accepted and the new configuration for the ensemble is taken in account for the total average. If the potential is bigger than the former one (i.e., $E_m > E_n$), the movement may be accepted with a probability given by

$$\wp = \exp\left(\frac{-\delta E_{mn}}{k_B T}\right), \tag{2.31}$$

where $\delta E_{mn} = E_n - E_m$. In practice this means that a random number from an interval between 0 to 1 is produced. If this is smaller than $\wp$ then the movement is accepted, if not, the movement is rejected and the ensemble goes back to the former configuration, contributing again to the total average.

2.5 Periodic Boundary Conditions

It is obvious that the interactions between particles in the center of the cluster are different from those on the surface, since the former are completely surrounded

by neighbour particles whereas the latter are in contact with the other molecules only on one side. It is obvious as well that all the ensembles must be limited in the number of particles, since it is impossible to compute an infinite number of particles. Thus the following problem is presented to us: how can we handle particles placed at the boundaries? The answer is to employ periodic boundary conditions.

By using the periodic boundary conditions, the ensemble studied is surrounded by images of itself. In this way, the particles placed on the right side of the ensemble interact with those of the left side of one of its images and those placed in the upper side interact with those placed in the bottom of the image above.

If the translational movement in which particles are involved move them out of the box, let us say, through the left boundary, automatically the equivalent particle of the right image will penetrate into the ensemble through the right boundary. In this way the number of particles is kept constant within the ensemble.

It is important to remark that a cut-off must normally be applied to the non-bonded interactions. This consists of limiting the range of non-bonded interactions to a certain distance. This never must be larger than half the length of the periodic box, since otherwise a molecule could interact with itself across the boundary conditions.

2.6 Data Analysis

2.6.1 Orientational Distribution Function

The orientational distribution function (ODF) produces a probability distribution of the molecular orientation. This is given by the angle between an unit vector defining the orientation of a molecule and the director vector.

This distribution can be expanded in terms of Legendre polynomials over even terms in l,
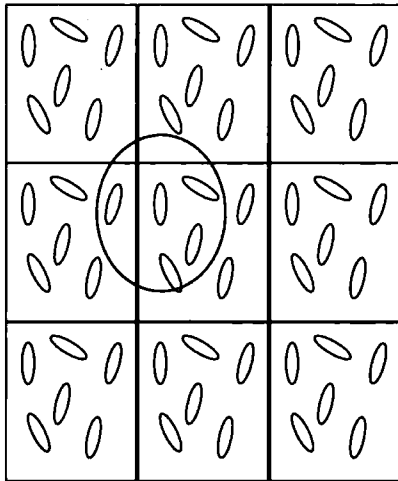
Figure 2.7: Periodic Boundary Conditions. The simulation box (central box) is surrounded by its periodic images. The circle radius is equal to half of the box side, and represents the maximum allowed cutoff for this system.

$$f\left(\cos\theta\right) = \sum_l c_l P_l\left(\cos\theta\right) = \sum_l \frac{2l+1}{2}\bar{P}_l P_l\left(\cos\theta\right), \qquad (2.32)$$

where the coefficients $\bar{P}_l$ are the order parameters. Therefore, for a nematic phase in a system with absence of any type of ferroelectricity, very populated states for $\cos\theta \sim \pm 1$ are to be expected. By contrast, in the case of an isotropic phase, a homogeneous distribution formed by a flat line is the pattern produced by the ODF.

2.6.2 Radial Distribution Functions

The radial distribution function (RDF) provides the probability of finding two particles i and j, at a distance r from each other. This function is given by the formula

$$g(r) = \frac{V}{N^2}\left\langle \sum_i^N \sum_{j\neq i}^N \delta(r - r_{ij}) \right\rangle, \qquad (2.33)$$

where δ is the Dirac delta function, r_{ij} is the vector existing between the centres of mass of particles i and j and V and N are the volume of the system and the number of sites, respectively.

The radial distribution function can be measured in three dimensions or just in one. For a liquid crystal an useful distinction between two different RDFs can be made. If the measurement is accomplished along the direction of the director vector the distribution function becomes $g_\parallel(r)$, whereas if the measurement of the distribution is accomplished perpendicular to the director vector, this becomes $g_\perp(r)$.

The use of $g_\parallel(r)$ is particularly interesting for characterization of smectic phases. In that case, the function produces a sinusoidal pattern, whereas if the system is in the nematic or isotropic phase, it produces a flat line.

2.6.3 Orientational Correlation Functions

In systems formed of isotropic molecules, orientational correlation functions provide useful information. These set of functions produce the correlation between the pairwise orientation of the molecules as a function of the intermolecular distance, and averaged over all the molecules within the ensemble. The general formula of these functions is

$$g_l(r) = \langle P_l \left(\cos \phi_{ij} \right) \rangle_{r-\delta r, r+\delta r}, \; l = 1, 2, \tag{2.34}$$

where ϕ_{ij} represents the angle between the axes of the molecules i and j.

Two of these functions are particularly interesting in the study of the liquid crystalline phases. For $l = 1$, $g_1(r)$ determines the pairwise correlation existing between molecular dipoles. In this way, it is possible to discriminate between non-ferroelectric, ferroelectric or antiferroelectric phases. For $l = 2$, $g_2(r)$ provides the pairwise correlation between the orientation of two molecules, regardless of their dipole orientation.

Chapter 3

Biaxiality

3.1 Introduction

Biaxial liquid crystals were predicted for the first time by Freiser in 1970 [3]. His theory stated that certain types of molecules are able to produce a biaxial nematic phase from the isotropic phase through a second order phase transition. A biaxial nematic phase occurs when orientational order exists at long range in more than one direction within the system. Latterly, Freiser's theory was proved in lyotropic [22] and polymeric [12–14] liquid crystals. Nonetheless, this innovative phase remained elusive for low-weight thermotropic liquid crystals for more than thirty years, despite the large number of studies which attempted to find it. A brief summary of them will be made later on. As far as simulation is concerned there have been a large number of models employed, raising from particle based potentials to lattice models. The shape assigned to the molecules was also modified on several occasions, raising from a lozenge shape to a boomerang shape.

Recently, Madsen *et al.* [23] announced the first successful syntheses of a thermotropic biaxial mesogen. This finding was subsequently corroborated by X-ray diffraction studies [6]. Thanks to the combination of a banana shape and a very strong dipole the molecule was claimed to maintain a bidirectional orientational order. Subsequent to this discovery a new molecule with the same characteristics but a totally different morphology was created by Merkel *et al.* [24]. Subsequent experimental evidence of phase biaxiality was provided using ^{2}H NMR spectroscopy [25].

This molecule was constituted by a siloxane core with four calamitic mesogens attached in a tetrahedral fashion.

3.2 Molecular Design of Thermotropic Biaxial and Bent-Core Liquid Crystals

3.2.1 Thermotropic Biaxial Liquid Crystals

Molecular biaxiality has been described as the deviation from the cylindrical shape in a molecule [66, 67]. Ferrarini *et al.* [68] proposed a mathematical method to quantify molecular biaxiality using the parameter λ

$$\lambda = \frac{\left(\frac{3}{2}\right)^{\frac{1}{2}} L\left(B - W\right)}{\left\{L\left(B + W\right) - 2BW\right\}},\tag{3.1}$$

where L, B and W are the molecular length, breadth and width respectively.

Freisier predicted that a type of molecule with a biaxial molecular shape in between calamitic and discotic would form a biaxial phase trough a second order phase transition from the isotropic phase [3]. Subsequent theoretical works corroborated his theory and developed new and complementary theories within a relatively short period of time [69–71]. However, it was not until ten years later that the first biaxial nematic phase was found in a lyotropic system [22], and six more years were required until a biaxial nematic phase formed by a thermotropic mesogen was claimed [72]. In that case, the design of the mesogen was conceived so that the molecular shape was in between a calamitic and a discotic, following Freiser's theory mentioned above. With this purpose an oblate and a prolate mesogen were merged into a single molecule. This provided the molecule with molecular biaxiality as can be seen in figure 3.1. The assumption of the phase biaxiality of the system was based on its optical texture. Several announcements of biaxial nematic phases followed in subsequent years (fig.3.2, ref. [73]; fig. 3.3, ref. [74]). Again the synthesis of these materials had the target of a molecular shape in between calamitic and discotic. Incidentally, V (see figure 3.3) was the first thermotropic mesogen studied using the ^{2}H NMR technique to prove its biaxial phase. This technique is considered as

the most reliable experimental technique to determined biaxial phases [28] and will be described in a subsequent section (3.5.2). Nevertheless, no evidence of a biaxial phase was found. The next molecule tested using ^{2}H NMR was II (see fig. 3.2). No evidence of biaxial phase was found. A new attempt to characterize the biaxial phase using this technique was made on I [75] (see fig. 3.1) with the same result as in previous occasions. Nevertheless, the reliability of ^{2}H NMR was proved [76] when it assured the biaxiality of a lyotropic nematic phase derived from the one found by Yu and Saupe [77].
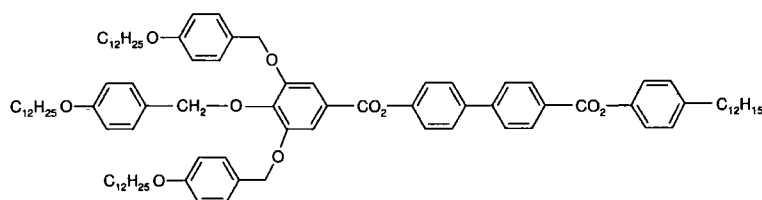
I

Figure 3.1: Candidate to form a biaxial phase by Malthete *et al.* [72].

Chandrasekhar made a new attempt [78] (see III in figure 3.2) linking two discotic molecules to the extremes of a rigid calamitic mesogen formed from three phenyl rings. Praefcke also carried out a new attempt [79] (see IV in figure 3.3) by linking two discotic molecules through a flexible aliphatic chain. Fletcher *et al.* [80] synthesized a molecule formed by two moieties, one discotic and the other one calamitic, in a new attempt to achieve the molecular conditions required to form a biaxial phase, (see VI in figure 3.4). A last attempt was performed by Omnes [81] (see VII in figure 3.4), providing the molecule with an electric dipole. Unfortunately, none of them has succeeded in producing a biaxial phase.
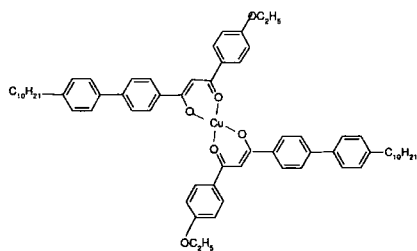
II
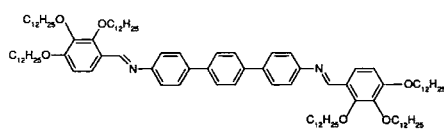
III

Figure 3.2: Chandrasekhar *et al.* attempts to synthesize a biaxial thermotropic molecule II [73] and III [78].
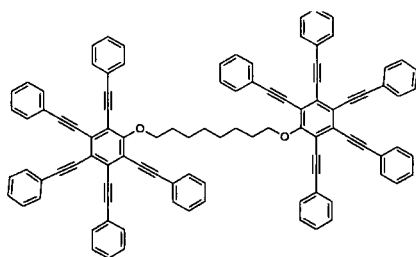
IV
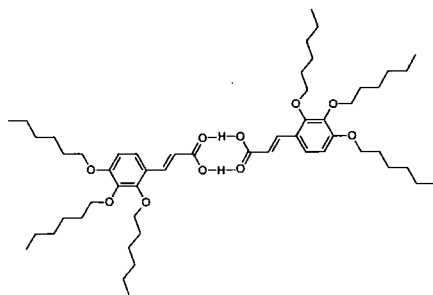
V

Figure 3.3: Praefckel suggestions to recreate a biaxial phase IV [79] and V [74].

VI   VII
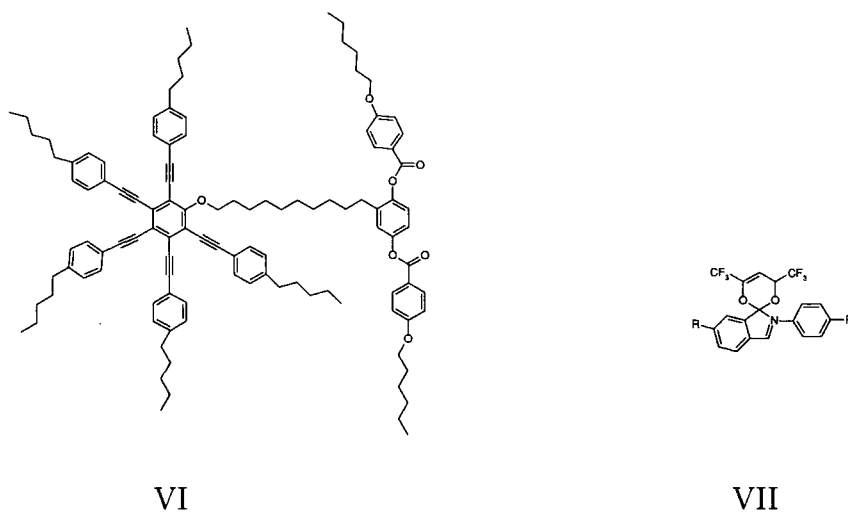
Figure 3.4: Candidates to produce biaxial phase by Fletcher *et al.* (VI [80]) and Omnes *et al.* (VII [81]).

3.2.2   Bent-Core Liquid Crystal Molecules

In the past decade there has been increasing interest in bent-core mesogens. Before the possibility of obtaining a low-weight thermotropic biaxial liquid crystal was considered, bent-core molecules were synthesized for the sake of the interest alone, because of the numerous and novel smectic phases they formed. The molecular structure of banana shaped molecules can be sketched using three main components. The first of these components is the central bent-core, which is responsible for providing the molecule with its characteristic boomerang shape. Several different structures have been used in order to open or narrow the angle formed by the two arms in the molecule. Examples include phenyl rings, terphenyls, naphtalenes, etc (see figure 3.5). Rigid arms (see figure 3.7), formed by aromatic rings and linking groups can be considered the second component of molecular structure. The linking groups constitute a bridge between aromatic rings and also between the other components of the molecule (see figure 3.6). The interactions established amongst the aromatic rings of the arms of the molecule are responsible for the liquid crystalline behaviour. The aromatic rings in the arms of the molecules are, above all, phenyl rings (polysubstituted, monosubstituted or not substituted at all), although it is also possible to find examples of the use of aromatic rings such as pyridines or

pyrimidines. Finally, a third component is the aliphatic chain, a common feature in all the mesogens. This is responsible for conferring flexibility to the mesogen. The length of the chain differs considerably between different molecules. For two excellent reviews on the topic see [26,82].
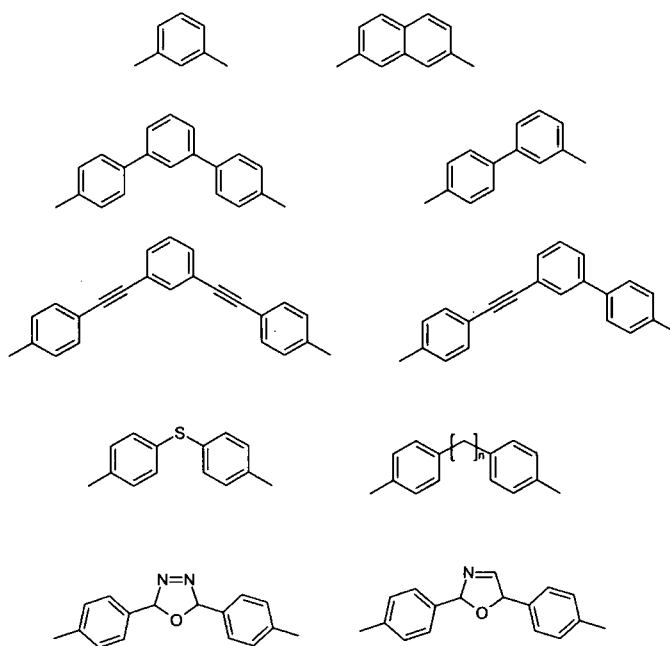
Figure 3.5: Different rigid banana-shaped bent-cores.
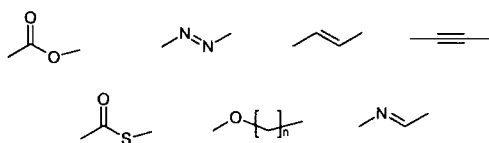
Figure 3.6: Most common linking groups in a bent-core mesogen.
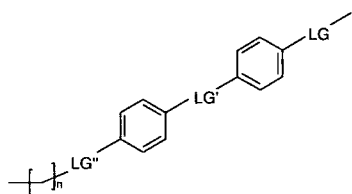
Figure 3.7: Example of the rigid part of the arm of a typical bent-core molecule. LG represents the linking groups.

3.3 Successful Thermotropic Biaxial Liquid Crystals

After thirty four years of pursuing a biaxial nematic phase produced by thermotropic liquid crystals, this was finally found in a system formed by a thermotropic liquid crystalline side chain polymer [13, 14]. In the same year, ^{2}H NMR evidence of a biaxial phase was found in two different low weight thermotropic liquid crystals, producing a revolution in the field of liquid crystals. These two molecules are not correlated in structure whatsoever, and the mechanisms triggering the onset of the biaxial phase are probably different in them. The first one was a bent-core molecule named ODBP-Ph-C$_7$ (see figure 3.8) presented by Madsen *et al.* [23]. The inter-arm angle was estimated in $\sim 140^0$ and it has a transverse dipole moment of ~ 4 D [6]. These two characteristics (molecular shape and molecular dipole) are most probably crucial to the formation of a biaxial nematic phase, as will be demonstrated in chapter 4. ODBP-Ph-C$_7$ forms very viscous systems and the liquid crystalline phase only exists at very high temperatures, as can be gathered from figure 3.8. The above mentioned high temperatures made the experimental measurement of the order parameters using the ^{2}H NMR almost unfeasible, causing serious doubts about the validity of the phase. However, the biaxiality of the liquid crystal phase was subsequently corroborated by X-ray diffraction [6]. Nevertheless, the mechanism responsible for the onset of the biaxial phase still remained elusive.

$$\text{I} \xrightarrow{495\,\text{K}} \text{N} \xrightarrow{446\,\text{K}} \text{SmX} \xrightarrow{439\,\text{K}} \text{SmY} \xrightarrow{421\,\text{K}} \text{K}$$
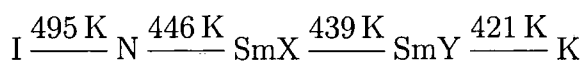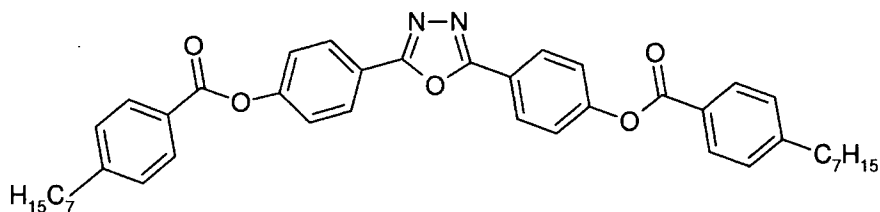
Figure 3.8: Chemical structure of ODBP-Ph-C_7 (top) and transition temperature between different phases of the molecule ODBP-Ph-C_7 (bottom).

The second molecule which succeeded in producing a biaxial phase was a organo-siloxane tetrapode [24], which had four mesogenic units appended laterally to its central core. The internal structure of this molecule is completely different from the one of ODBP-Ph-C_7. Infrared techniques were employed to provide evidence of biaxiality, alongside the ^{2}H NMR spectrum. In this case, the most probable reason for the existence of phase biaxiality was pointed out by the authors as the incapability of the mesogenic units to rotate freely about their longitudinal axes, due to their lateral attachment to the siloxane core through a flexible aliphatic chain. This would force the mesogenic components of the molecule to remain ordered in two dimensions, along their longitudinal axes and parallel to the lateral bond to the flexible chain, hence producing phase biaxiality in the system.

3.4   Simulation Models of Biaxial and Bent-Core Liquid Crystals

3.4.1   Biaxial Models

As mentioned before, there have been several attempts to simulate a biaxial liquid crystalline phase. With this aim several different models have been proposed, going

from the most modest ones, such as lattice models, to more sophisticated ones, for instance biaxial Gay-Berne models.

The first attempt to simulate a biaxial liquid crystal was carried out by Hashim *et al.* [83] in 1985. In that occasion, a mixture formed from a calamitic mesogen acting as a solvent and a biaxial particle playing the role of solute was represented by a cubic lattice model. The molar fraction of the solute was only 0.05. This proportion solute / solvent was deliberately chosen in an attempt to reproduce NMR studies of solute ordering. The distribution of the solute in the lattice prevented two solute particles from being nearest neighbours. An anisotropic molecular interaction was represented by a soft potential. Two different potentials were used depending on the type of molecular interaction. For the solvent-solvent (uniaxial) interaction a potential based on the relative orientation of the molecular long axes was used (eq. 3.2), whereas for the solute-solvent interaction a biaxial attractive potential was implemented (eq. 3.3).

$$U_{ij}^{11} = -\varepsilon^{11}\frac{(3\mathbf{w}_i \cdot \mathbf{w}_j - 1)}{2} \tag{3.2}$$

$$U_{ij}^{12} = -\left\{ \varepsilon_{2,0}^{12}\frac{(3\mathbf{w}_i \cdot \mathbf{w}_j - 1)}{2} + \varepsilon_{2,2}^{12}\left(\frac{3}{2}\right)^{\frac{1}{2}}\left[(\mathbf{w}_i \cdot \mathbf{v}_j)^2 - (\mathbf{w}_i \cdot \mathbf{u}_j)^2\right] \right\}, \tag{3.3}$$

where ε^{11} is a positive constant determining the strength of the interaction between solvent particles, $\varepsilon_{2,m}^{12}$ is a irreducible spherical tensor which determines the strength of the solute-solvent interaction, $\mathbf{w}$ is the unit vector representing the symmetry axis of the solvent. The orientation of the solute was represented by the three unit vectors $\mathbf{u}$, $\mathbf{v}$ and $\mathbf{w}$. The subscripts i, j are used to represent two different particles, and the superscripts $1, 2$ represent the different types of interactions (solvent-solvent and solute-solvent).

The final result of the simulation produced a system with a moderate biaxial order parameter of approximately 0.2. It also stated a correlation between the biaxial and the uniaxial order parameters.

Ten years later another lattice model also based on an attractive potential was

proposed by Biscarini *et al.* [67]. The target of this work was to map the phase diagrams for a biaxial molecule. In this case, the system was entirely formed of a single type of particles. A second rank attractive pair potential was designed based on the orientational correlation between molecules. These were basically represented by three molecular axis or "spins". Different degrees of molecular biaxiality (i.e., the deviation from the cylindrical molecular symmetry) were tested. Four different order parameters, based on a second rank tensor, were calculated to characterize the biaxial phase

$$\langle P_2 \rangle = \langle R_{00}^2 \rangle = \frac{3}{2} \langle \cos^2 \beta \rangle - \frac{1}{2}, \tag{3.4}$$

$$\langle R_{02}^2 \rangle = \sqrt{\frac{3}{8}} \langle \sin^2 \beta \cos 2\gamma \rangle, \tag{3.5}$$

$$\langle R_{20}^2 \rangle = \sqrt{\frac{3}{8}} \langle \sin^2 \beta \cos 2\alpha \rangle, \tag{3.6}$$

$$\langle R_{22}^2 \rangle = \left\langle \frac{1}{4} \left(\cos^2 \beta + 1 \right) \cos 2\alpha \cos 2\gamma - \frac{1}{2} \cos \beta \sin 2\alpha \sin 2\gamma \right\rangle, \tag{3.7}$$

where α, β, γ are the Euler angles. In addition, a biaxial phase parameter η representing the one calculated in the ^{2}H NMR experiments:

$$\eta = \sqrt{6} \langle D_{20}^2 \rangle / \langle P_2 \rangle \tag{3.8}$$

was used. Here, $\langle D_{20}^2 \rangle$ represents one of the Wigner functions [84] symmetry-adapted of the D_{2h} group.

The molecular biaxiality given by λ was responsible for the quantification of the deviation of the molecular shape from the cylindrical symmetry. Hence $\lambda = \frac{1}{\sqrt{6}}$ marks the boundary between the prolate and the oblate shape. A phase diagram of the temperature against the molecular biaxiality λ showed that the Landau tricritical point corresponding to the isotropic - biaxial nematic phase a second order transition was observed for $\lambda = 0.48$. Uniaxial calamitic and discotic nematic phases were successfully reproduced as well, with first order isotropic-nematic transitions. A

maximum value of 0.5 was achieved for the biaxial order parameter, $\langle R_{22}^2 \rangle$, whereas the values registered for $\langle R_{20}^2 \rangle$ and $\langle R_{02}^2 \rangle$ where greater than 0.1. A maximum value of 0.1 was obtained for $\langle P_2 \rangle$. Nevertheless, the results for the biaxial parameter η were not totally consistent with the experimental results, since its value was higher for molecules lacking biaxiality ($\eta = 0.5$ for $\lambda = 0$) than for those with a substantial degree of biaxiality ($\eta \simeq 0.2$ for $\lambda = 0.2, 0.3$).

The introduction of translational degrees of freedom in the first off-lattice models created to simulate biaxial molecules constituted a step forward in the simulation of biaxial liquid crystals. The first of these models was introduced by M. Allen in 1990 [35]. Monte Carlo simulations were performed in order to reproduce a biaxial phase. A hard ellipsoid was used to represent a biaxial body. This was shaped using the three molecular parameters: a, b and c, representing the molecular length, breadth and width respectively. The ratios between these parameters were used to control the biaxial shape of the molecular model: c/a, which was fixed to 10, and b/a, which adopted several different values (1.259, 1.585, 6.310 and 7.943).

This work neglected two of the four order parameters exposed above ($\langle R_{20}^2 \rangle$ and $\langle R_{02}^2 \rangle$) due to their small value, and focused on the other two ($\langle R_{00}^2 \rangle$ and $\langle R_{22}^2 \rangle$). Allen derived an expression for the latter two based on Cartesian coordinates rather than on Euler angles:

$$\langle R_{00}^2 \rangle = Q_{00}^2 = \langle Z \cdot Q^{zz} \cdot Z \rangle, \tag{3.9}$$

$$\langle R_{22}^2 \rangle = Q_{22}^2 = \frac{1}{3} \langle X \cdot Q^{xx} \cdot X + Y \cdot Q^{yy} \cdot Y - X \cdot Q^{yy} \cdot X - Y \cdot Q^{xx} \cdot Y \rangle, \tag{3.10}$$

where X, Y, Z are the director vectors along the x, y and z directions. Q^{AA} is the second rank ordering tensor

$$Q_{\alpha\beta}^{aa} = \frac{1}{N} \sum_{i=1}^{N} \left(\frac{3}{2} \mathbf{a}_{i\alpha} \mathbf{a}_{i\beta} - \frac{1}{2} \delta_{\alpha\beta} \right), \tag{3.11}$$

where $\mathbf{a}$ represents a unit vector along the x, y or z molecular axes, i represents

each one of the N molecules in the system and $\alpha, \beta = 1, 2, 3$.

Hence, Q_{00}^2 (see eq. 3.9) represents the uniaxial order parameter and Q_{22}^2 (see eq. 3.10) represents the biaxial order parameter. This notation will be used throughout all the present thesis, and both Q_{00}^2 and Q_{22}^2 will be calculated in numerous occasions in subsequent chapters.

Allen [35] performed simulations covering the whole density range within a typical liquid crystalline phase, in order to generate the phase diagrams of the system. The attempt succeeded in reproducing isotropic, discotic nematic, calamitic nematic and biaxial phases. However, the phase transition between such phases was not perfectly mapped due to limitations in the system size and the computation time. A latter work by Camp and Allen [85] tried to repair this problem by tracing the phase coexistence line using a Gibbs-Duhem integration of the coexistent pressure with respect to the molecular biaxiality. In this case the isotropic-discotic nematic and the isotropic-calamitic nematic first order transition are considerably weakened by the introduction of a biaxial character in the molecule. However, no conclusive poof of the second order transition between the isotropic phase and the biaxial nematic was obtained. The system used to represent the biaxial mesogens was similar to the one used in the previous work by Allen [35], and therefore the molecules were also represented by hard ellipsoids.

Biaxial liquid crystals have also been described using more complex models. Sarman [86] created a biaxial body by merging nine discotic Gay-Berne ellipsoids at a distance of $\sigma/2$, which produced a molecular length-breadth-width ratio of $5 : 1 : 0.4$. He removed the attractive part of the Gay-Berne potential to create a short-range intermolecular interaction. This model successfully produced a biaxial nematic phase. Nevertheless, since the motivation of the model was to study the application of an algorithm to constrain the director angular velocity, no further investigations on the biaxial phase or phase transitions were carried out. However, in a subsequent paper [87], Sarman studied the onset of the biaxial phase using this model and the influence of molecular biaxiality on it. On this occasion the model was adapted to have length-breadth-width ratios of $4.5 : 1 : 0.4$, $5 : 1 : 0.4$, $5.5 : 1 : 0.4$ and $6 : 1 : 0.4$.

Uniaxial and biaxial order parameters were defined according to ref. [35]. As the system was compressed and the reduced density (n^*) increased, discotic nematic phases were achieved for the two first models. However, the increase of n^* caused the onset of calamitic nematic phases for the last two models. After further compression the four models produced biaxial nematic phases. In all the cases, the isotropic-uniaxial transitions were first order and the uniaxial nematic-biaxial nematic transition were second order.
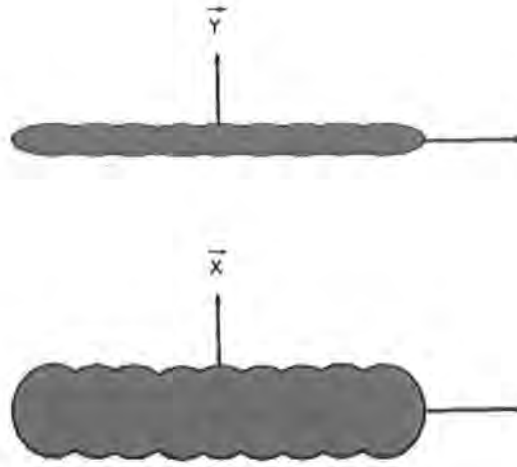
Figure 3.9: Representation of the biaxial model proposed by Sarman.

A different Gay-Berne off-lattice model was proposed by Berardi and Zannoni [88], consisting of soft ellipsoids. The way molecular biaxiality was defined differed significantly from that proposed by Ferrarini *et al.* [68], in equation 3.1. Berardi and Zannoni used two different parameters to define molecular biaxiality: the shape biaxiality (λ_σ) and the interaction biaxiality (λ_ϵ)

$$\lambda_\sigma = \sqrt{\frac{3}{2}} \frac{\sigma_x - \sigma_y}{2\sigma_z - \sigma_x - \sigma_y}, \tag{3.12}$$

$$\lambda_\epsilon = \sqrt{\frac{3}{2}} \frac{\epsilon_x - \epsilon_y}{2\epsilon_z - \epsilon_x - \epsilon_y}, \tag{3.13}$$

where σ_x, σ_y and σ_z are the axes of the ellipsoid and ϵ_x, ϵ_y and ϵ_z are proportional

to the well depths for the *side-to-side*, *face-to-face* and *end-to-end* interactions of the molecule. Positive values of λ_ϵ favour *face-to-face* interactions while negative ones favoured *side-to-side* interactions. Different simulations were performed for different biaxial parameters sets $(\lambda_\sigma, \lambda_\epsilon)$ in a wide range of reduced temperatures $(T^* = 1.5 - 4.0)$. For positive shape and interaction biaxialities, *face-to-face* stacking was favoured, resulting in the formation of biaxial layers. However, negative λ_ϵ produced a biaxial nematic phase in a wide range of T^*.

Finally, a different type of model has been able to reproduce a biaxial phase [89]. In this case, a lattice model representing mesogens formed from two different moieties, one calamitic and the other discotic, linked to each other through a flexible spacer. The latter is represented by an internal effective torsional potential derived from a Lebwohl-Lasher potential [90]

$$U_{ij} = \varepsilon P_2 \left(\cos \beta_{ij} \right) = \varepsilon P_2 \left(\mathbf{u}_i \cdot \mathbf{u}_j \right), \tag{3.14}$$

where $\mathbf{u}$ is a unit vector representing the orientation of a particle at the site i (or j), β_{ij} is the angle between these vectors and P_2 is the second Legendre function. The strength of the torsional angle is controlled by the parameter ε_a^*. Positive values of ε_a^* result in a perpendicular relative orientation of the two moieties, whereas negative values of ε_a^* produce parallel relative orientation. For $\varepsilon_a^* = 0$, the torsional angle is allowed to rotate freely.

Each site on the cubic lattice interacts only with its nearest neighbours. The inter-site interactions are also represented by a potential derived from the Lebwohl-Lasher potential. The inter-site interactions are controlled by the parameter ε^*. When $\varepsilon^* < 1$ the parallel alignment between calamitic mesogenic units from different sites is more favoured. When $\varepsilon^* > 1$ it is the parallel alignment between discotic subunits from different sites which is more favoured. When $\varepsilon^* = 1$ the parallel relative orientations of rod-rod and disc-disc are equally favoured.

Simulations at different reduced temperatures (T^*) were performed for different sets of ε_a^*, ε^*. When the internal torsional angle was kept fixed at 90^0 there is a second order isotropic-nematic biaxial transition for $\varepsilon^* = 1$ as T^* is decreased. The reduction of the rigidity of the perpendicular internal torsional angle does not

introduce significant changes. No changes are appreciated either when the maximal flexibility is allowed in the relative orientation of the mesogenic units. However, for negative values of ε_a^* (parallel orientation of the main axis of the two moieties preferred) the isotropic-biaxial nematic transition become strongly first order when T^* is decreased (for $\varepsilon^* = 1$). In addition, the calamitic nematic phase is destabilized.

3.4.2 Banana Models

Interest in bent-core molecules has increased in recent years, in part due to the ability exhibited by this group of mesogens to produce smectic phases with yet unknown properties and structures. Also the characteristics of this kind of molecules makes them magnificent candidates to become thermotropic biaxial liquid crystals. Therefore, several models have been implemented to reproduce the above mentioned smectic phases and the phase biaxiality formed by banana-like molecules. Some of these models have merely relied on short range excluded volume interactions to reproduce biaxial phases. However, other models have added long range electrostatic interactions. Both cases are subsequently reviewed.

Non-Polar Models

One of the advantages of creating bent-core models dwells in the fact that even if no electrostatic interactions are considered in the simulation, i.e. no electric dipole is present in the model, a steric dipole is always present due to the banana shape. This theoretically allows the simulation of polar ferroelectric and antiferroelectric phases without considering long range electrostatic interactions.

A first attempt to reproduce mesophases of bent-core molecules was accomplished by Camp et al. [91] by elaborating a model based on purely repulsive interactions. To do so two spherocylinders were bonded end-to-end forming each one of the arms of a banana-shaped molecule. Seven different inter-arm angles ϕ were studied in the simulation ($\phi = 180^0, 170^0, 160^0, 150^0, 120^0, 108^0$ and 90^0). For all but one, corresponding to 108^0, the spherocylinders length-to-diameter ratio was $L/D = 2$. For $\phi = 180^0$ this ratio was modified to $L/D = 9.5$. This has its motivation in the fact that the Landau bicritical point had been previously predicted for $\phi = 108^0$ at the

limit of infinitely thin rods [92]. None of the simulated ϕ values produced biaxial orientational order in a fluid phase. For $\phi = 180^0, 170^0, 160^0$, the isotropic phase evolved into an uniaxial nematic one as the density was increased. Afterwards, uniaxial nematic-smectic and smectic-crystal transitions were registered. Smaller ϕ values destabilized the smectic phase, and therefore the mesogens formed a crystalline phase immediately after the nematic phase. This crystalline phase was biaxial. For even smaller inter-arm angles ($\phi = 60^0, 90^0$), no spontaneously ordered phases were found.

However, a mechanically stable biaxial phase was found for simulations performed with molecular shape parameters $\phi = 108^0$ and $L/D = 9.5$, when the initial configuration of the system was pre-set to biaxial. Nonetheless, no isotropic-nematic biaxial or uniaxial nematic-biaxial nematic transitions were registered.

Lansac et al. [93] produced a complete phase diagram of the reduced pressure against the inter-arm angle, ϕ, based on a spherocylinder model similar to the one explained above. However, the spherocylinder dimensions were different ($L/D = 5$). At low pressures the common phase found for all different ϕ was the isotropic liquid (I). At higher pressure a uniaxial nematic phase (N) was observed for $\phi > 135^0$. By contrast for $\phi < 135^0$, smectic A phases showing an interlayer antiferroelectric polar order (SmAP$_A$) is exhibited in the phase diagram. At even larger densities, SmAP$_A$ becomes a crystalline phase with antiferroelectric order (XP$_A$). There is a phase transition from the N into the SmAP$_A$ phase for $135^0 < \phi < 165^0$, while for $\phi > 165^0$ the N phase becomes a normal SmA phase. For even larger densities columnar and crystalline phases are observed for large ϕ. Therefore this work suggested that the magnitude of the inter-arm angle is a crucial factor in the formation of liquid crystalline phases. Wider ϕ values stabilize the N phase whereas narrower ϕ values stabilize more structured phases, such as the SmAP$_A$. It can also be inferred that excluded volume interactions are not sufficient to cause the onset of a biaxial nematic phase in a bent-core system.

The latter assumption fostered the creation of new bent-core models which accounts for the attractive interactions as well as for the repulsive. Memmer [94] proposed a model based on two ellipsoids represented by a Gay-Berne potential and
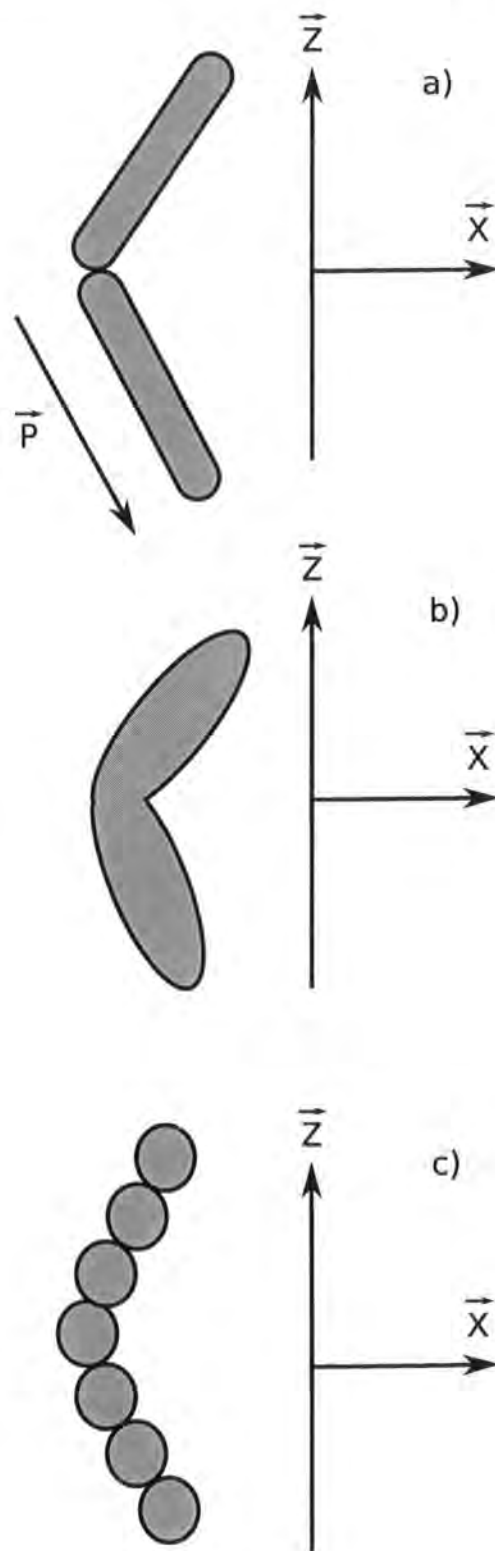
Figure 3.10: Bent core models based on two spherocylinders (a), two ellipsoids (b) and tangential spheres (c).

linked in the same way as the two spherocylinders in the models explained above. The inter-arm angle in his model was given a fixed value ($\phi = 140^0$). No Q^2_{22} values were presented but instead data for Q^2_{00} was provided for both the longitudinal and the transversal molecular axes ($\overrightarrow{Z}$ and $\overrightarrow{X}$ axis respectively, according to fig. 3.10). Different transitions were found between the isotropic-nematic phases and between the nematic-SmAP$_A$. In the nematic phase Q^2_{00} along the $\overrightarrow{Z}$ axis was ≈ 0.6 whereas the same value along the $\overrightarrow{X}$ axis was ≈ 0.2. This order, albeit larger than zero, is a collateral effect of the molecular long axis alignment for a finite sized system, and thus represents the molecular biaxiality, rather than the phase one. The nematic phase was claimed to be twisted nematic.

A similar model based on two ellipsoids represented by a Gay-Berne potential was proposed by Johnston *et al.* [95]. In this particular case, a set of five different inter-arm angles was simulated ($\phi = 180^0, 170^0, 160^0, 140^0$ and 130^0), producing different results. The rod-like model with $\phi = 180^0$ produced the phase transitions $I \rightarrow N \rightarrow SmX \rightarrow SmB$. The reduced temperature (T^*) decreases from left to right, and SmX refers to a non-identified smectic phase and SmB to an hexatic smectic phase. After introducing a small degree of biaxiality in the molecule the scheme of the phase transitions varies, since there is no $I \rightarrow N$ transition and the systems quenches directly to a SmA phase from the isotropic phase. After this, at lower T^*, the system goes into a SmB phase. On increasing the molecular biaxiality by introducing the transformation to $\phi = 160^0$, the phase transition scheme is newly altered, registering the changes: $I \rightarrow N \rightarrow SmA \rightarrow Sm\overline{B}$, where $Sm\overline{B}$ represents a tilted non-chiral SmB phase. The presence of smectic phases disappear as the inter-arm angle was reduced to $\phi = 140^0$. In this case a twisted grain boundary (TGB) was exhibited by the system when T^* decreases. This was expected since in the model proposed by Memmer a uniaxial twisted nematic phase was found for the same inter-arm angle. No ordered phases were found for $\phi < 130^0$.

More recently, Bates and Luckhurst [96] have carry out a comprehensive study of the phase diagrams of different models considering different inter-arm angles as well as different symmetries between the two parts of the dimer. For accomplishing this task they used a lattice model in which molecules interacted with the six next

nearest neighbours. The interactions were represented by a modified Lebwohl-Lasher potential [90]. Interesting results suggested that a Landau point was observed for an optimum inter-arm angle of 109.47^0. Hence, this model has been able to successfully reproduce the formation of a biaxial nematic phase by a bent-core mesogen. In addition, in this work new methods for measuring the biaxiality were introduced. In order to provide a quantitative measure of the biaxiality, they calculated the biaxial parameter η with the same equation used in ^{2}H NMR experiments. Here though, molecular axes were used rather than the quadrupole tensor calculated with the quadrupole momenta along the C-^{2}H bonds

$$\eta = \frac{(q_{yy} - q_{xx})}{q_{zz}}, \tag{3.15}$$

where, for ^{2}H NMR, q_{xx}, q_{yy} and q_{zz} represent the principal components of the second rank quadrupole tensor. These are chosen so that the condition $|q_{zz}| > |q_{yy}| > |q_{xx}|$ [28] is met. During the simulation, the values of the second rank quadrupole tensor have been substituted by the values of the second rank ordering tensor (eq., calculated with the eq. 3.11). These were calculated using the orientation of the molecule given by a vector along the arms of the molecule. This has been labeled as axis $\overrightarrow{P}$ in figure 3.10 (a). The authors concluded that this was the best of all the molecular axes to determine the biaxial parameter. This method will also be used to determine the biaxial phase not only considering the $\overrightarrow{P}$ axis but also other molecular axes throughout ongoing chapters of this thesis.

Apart from the models formed by two dimers, other models have recreated the shape of a bent-core molecule by rigidly bonding several different spheres. This model has been used by Xu and co-workers [97]. For that particular simulation seven different spheres were bonded together forming a V-shaped body with $\phi = 140^0$. There were no intramolecular interactions and the intermolecular ones were described in terms of a truncated Lennard-Jones potential of the Weeks-Chandler-Andersen type [98]. The cut-off imposed in the inter-sphere distance assured that no long-range interactions were taken into account and therefore this potential was transformed to a short ranged one. Through this model it was possible to obtain a chiral crystalline phase and a SmA phase. A model similar to the one described

above has also been used by Dewar and Camp [99] to study the effect of the variation of ϕ in liquid crystalline phases. Thus, the molecular inter-arm angle adopted three different values ($\phi = 180^0, 160^0, 140^0$). In the case of $\phi = 160^0$, three different phases could be observed: I, N and $Sm\overline{B}$. However, no biaxiality could be appreciated in any of them. For the inter-arm angle $\phi = 140^0$, no nematic phase could be monitored and there was no evidence of biaxiality in the liquid crystal phases obtained.

Polar Models

Since most real bent-core molecules have a dipole moment in their structure, it could be suggested that introducing this feature in the simulation models is necessary if realistic mesophases are to be reproduced. However, this task is not trivial and few groups have tackled this challenge.

Johnston and coworkers [100] have developed a model based on a prior one [101] with an added transversal dipole across the centre of the molecule. In common with their previous work, several different inter-arm angles were tested using this model ($\phi = 170^0, 160^0, 140^0$ and 110^0). The addition of long range molecular interactions in this model stabilized the more structured phases in detriment to the most fluid ones (i.e. smectic phases to the detriment of nematic ones). For $\phi = 170^0$ and 160^0 the I phase suffered a transition into the SmA phase directly. Further decreases in temperature had different effects for each one of the inter-arm angles. For $\phi = 170^0$ the SmA phase transformed into a $Sm\overline{B}$ and, eventually, into a tilted biaxial SmB phase with polar ferroelectric order ($Sm\overline{B}_bP_F$). For $\phi = 160^0$, the SmA phase transformed into a tilted biaxial SmB phase with polar antiferroelectric order ($Sm\overline{B}_bP_{AF}$). In both cases the tilted structure has a synclinic arrangement. By decreasing the inter-arm angle to 140^0 the transition I $\rightarrow$ SmAP$_{AF}$ was observed. This system shows biaxiality in the same way as previous polar systems did. For the narrowest inter-arm angle no ordered phase was found. This results show clearly that although the electrostatic interactions stabilize the smectic phases, they also play a crucial role in controlling the onset of the biaxiality.

Another innovative model was simulated by Orlandi *et al.* [102]. In fig. 3.11 it is possible to appreciate that three ellipsoids have been put together in order to create

a bent shape model. In this occasion, the inter-arm angle remained fixed at 120^0. A transverse dipole moment was tested (fig. 3.11 a), and a pair of dipoles located in different parts of the molecule (fig. 3.11 b and c) were also studied. Several ordered phases were found in the simulations performed using this particular model, which is in contrast with the model studied by Johnston and coworkers [100]. Although the longitudinal director vector did not register any tilted angle with respect to the layer normal, the phase biaxiality was certainly present ($Q_{22}^2 = 0.38$). The same SmB phase was found when the transverse electric dipole was substituted by two lateral dipoles located in the centres of the two lateral ellipsoids (fig.3.11 b). The sequence of phase transitions occurred as follows: I $\rightarrow$ N $\rightarrow$ SmA $\rightarrow$ SmB$_b$P$_{AF}$ as T^* decreased. Hence, the hexatic smectic phase proved to be biaxial again ($Q_{22}^2 = 0.36$). Nevertheless no biaxial nematic phase was found. Finally, the results obtained by changing the position of the dipoles (fig.3.11 c) produced the results: I $\rightarrow$ N $\rightarrow$ Sm$\overline{\text{B}}$ as T^* decreased. The nematic phase was, once again, uniaxial and the biaxiality of the smectic phase was more moderated than in the two previous occasions ($Q_{22}^2 = 0.16$). It is noteworthy that the decrease in the phase biaxiality is associated with the disappearance of the polar order in the phase. Therefore the results also suggest that the concept of biaxiality is intimately connected to the polar order in the phase.

3.5 Experimental Characterization of the Biaxial Phase

Biaxiality can be a confusing concept. A molecule can have a biaxial shape (molecular biaxiality) but still be totally incapable of forming a biaxial phase. The accomplishment of the latter is known as the phase biaxiality. By convention, the biaxial phase is produced when a molecular property or observable represented by a symmetric and traceless second rank tensor has different values in each one of its principal values. By contrast, in the uniaxial phase just one of the principal values differs from the other two, which are equal. This assumption is behind most of the experimental techniques developed to determine phase biaxiality. Moreover, the determination of the biaxial phase in molecular simulation is also based on it.
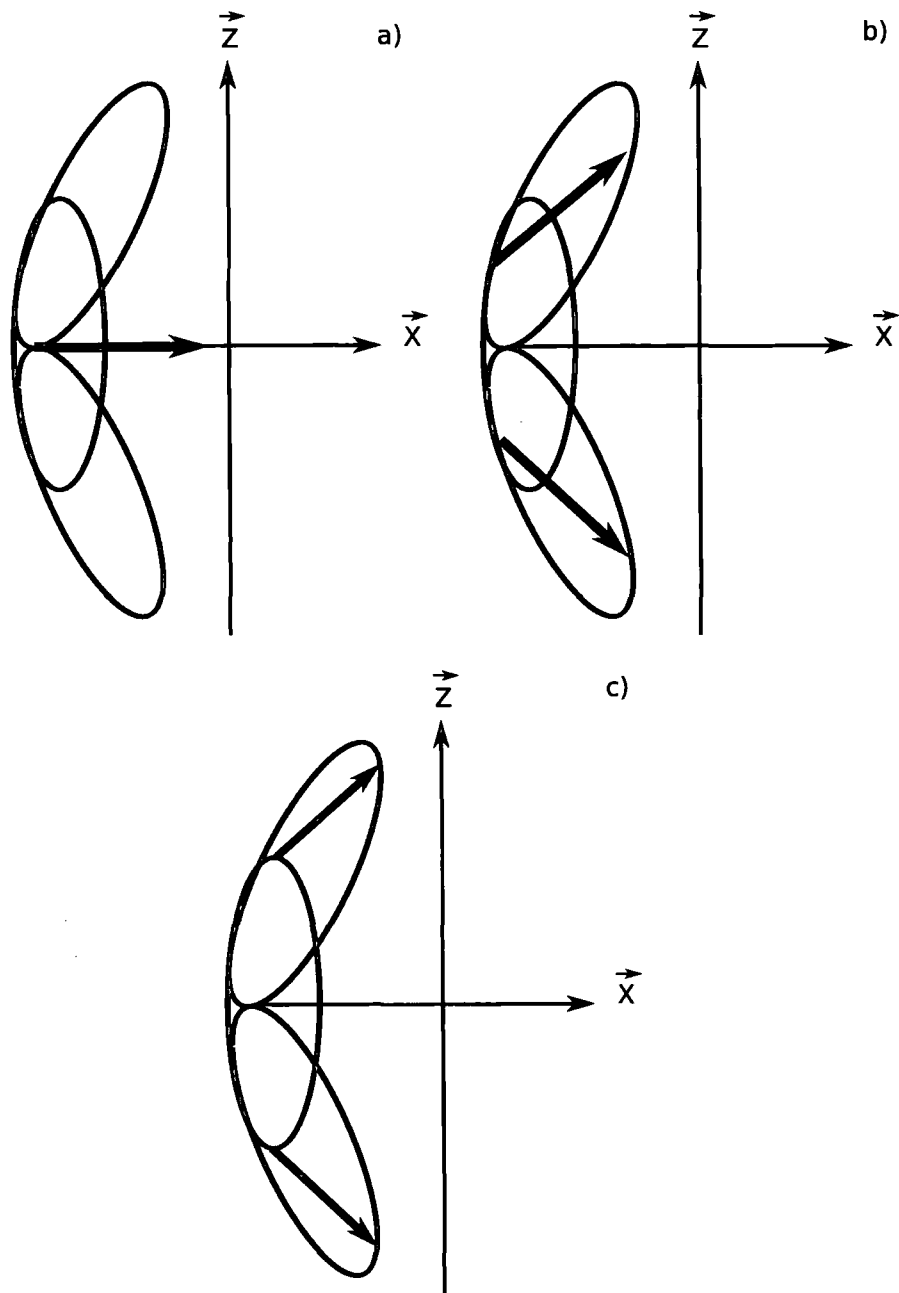
Figure 3.11: Bent-core molecule models formed from three ellipsoids with (a) a single transversal dipole, (b) two oblique dipoles located in the centre of the external ellipsoids and (c) two oblique dipoles located at the extremes of the central ellipsoid. The dipole moments are represented by thick arrows.

Some of these techniques will be briefly described. Below further references to these techniques will be made in further chapters.

3.5.1   Conoscopy

In conoscopy the observable involved in the determination of the phase biaxiality is the refractive index. To perform an experiment it is necessary to set the mesogens in a monodomain. With this purpose the sample is confined in a cell between two electrodes. When a potential is applied an alignment between the nematic director vector $\overrightarrow{l}$ and the direction of the electric field is produced. The walls of the cell are disposed in such a manner that in the case that more than one director vector exists, such as $\overrightarrow{m}$, this will align parallel to the wall due to surface interactions. When the sample is observed in a microscopy using polarized light, the patterns produced by uniaxial and biaxial phases are different and characteristic. In the former a cross-shaped pattern is formed, whereas in the latter the cross is bisected in two boomerang-like curves, which are placed opposite each other (see figure 3.12).

Unfortunately, it has been shown that sometimes in an uniaxial phase the main director vector $\overrightarrow{l}$ can be tilted with respect to the cell walls due to surface interactions. This produces a pattern equal to the one in a biaxial phase, leading to erroneous conclusions regarding the type of phase present. This case has been frequently described in the literature [73, 74, 103].

3.5.2   Deuterium Nuclear Magnetic Resonance (^{2}H NMR)

Deuterium nuclear magnetic resonance has proved itself to be a robust technique in the determination of biaxial nematic phases. However, this technique presents many practical difficulties. The presence of a deuterated position in the molecule is necessary to produce a spectrum. The arduousness of synthetic procedures to achieve this is frequently the motivation for introducing deuterated probe molecules which align with the mesogens in the system, adapting their orientation.

When a ^{2}H NMR spectrum is taken from a nematic, two peaks corresponding to a doublet appear. The splitting between these two peaks depends on the angle
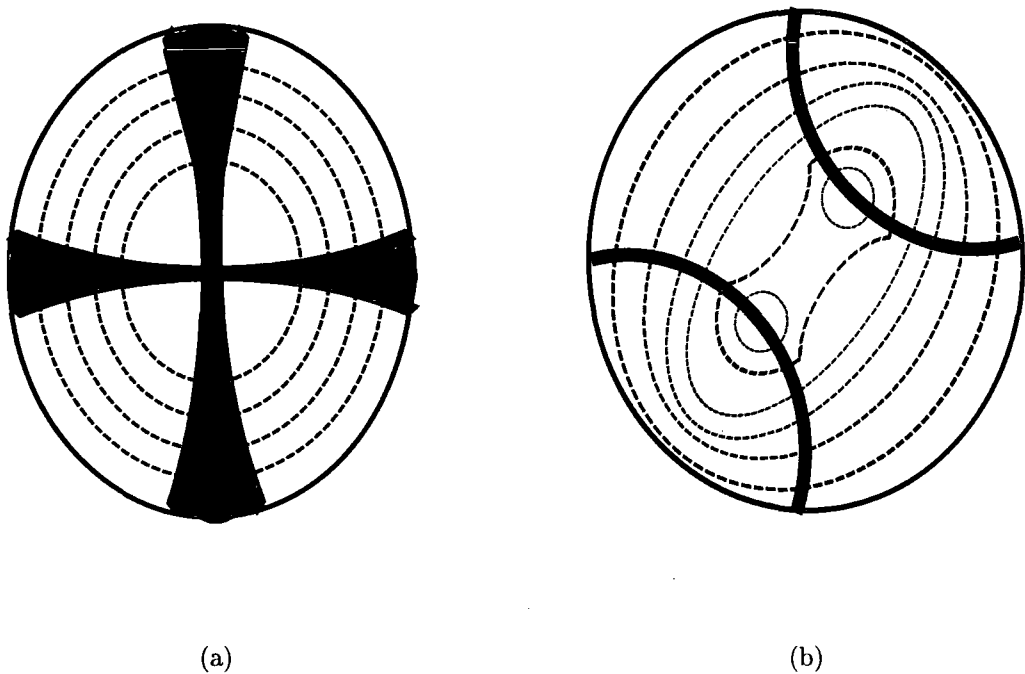
Figure 3.12: Schematic representation of conoscopies for (a) a uniaxial nematic and (b) a biaxial nematic.

(β) between the director vector and the direction of the applied magnetic field $\vec{B}$. The value of the splitting is a maximum when the director and $\vec{B}$ are parallel, and minimum when the angle between director vector and field is equal to the magic number 54^0.

In the particular case of an uniaxial phase, the ratio between the maximum and minimum splitting is 2 : 1. By contrast, when the sample is biaxial this ratio differs from 2 : 1, being either larger or smaller. This fact makes it possible to use the technique to qualitatively prove the presence of a biaxial phase.

Nonetheless, this technique does not totally lack problems. The nematic director vector always tends to align parallel to the magnetic field, and therefore it is difficult to measure different angles between them. To tackle this problem the sample is spun about an axis perpendicular to the magnetic field. Since $\vec{B}$ is in the plane where the sample lays, a random orientation of the director with the field direction is achieved at each moment, and therefore the final spectrum results in an average of all possible orientations between the director and field (see figure 3.5.2).

This technique has been extremely useful to unmask uniaxial phases which originally had been mistaken for biaxial ones by other experiments, as exposed above.
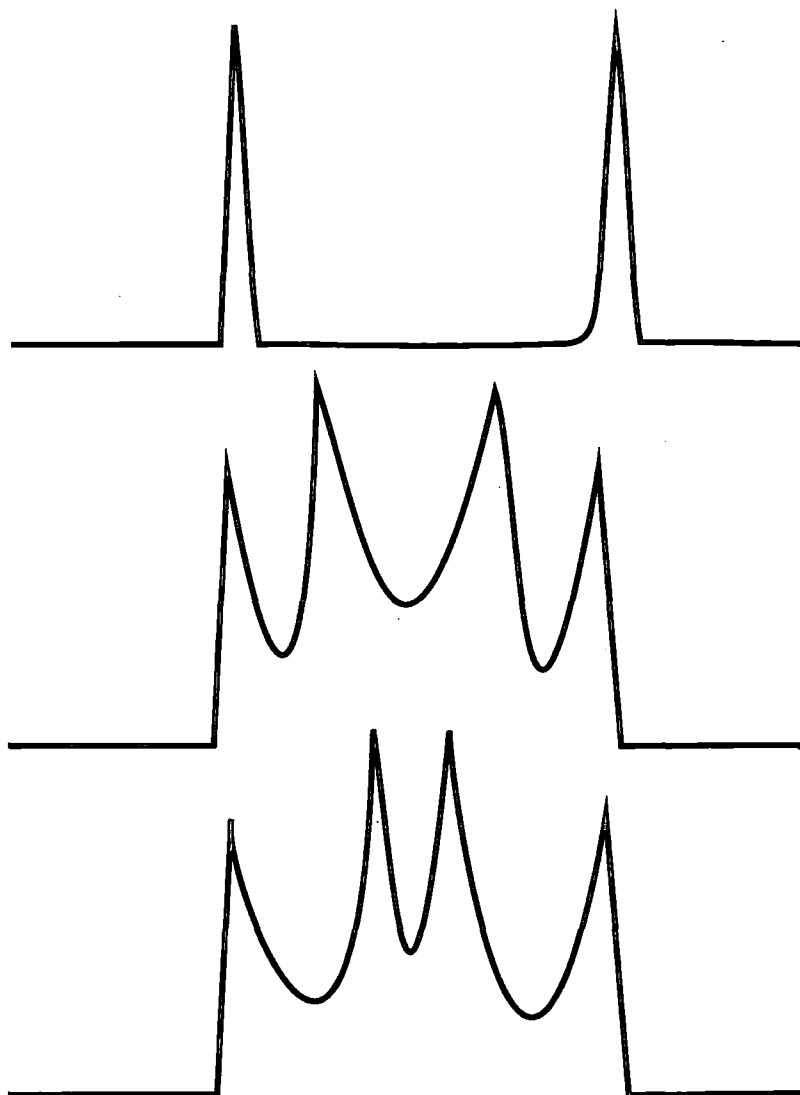
Figure 3.13: ^{2}H NMR of a deutered probe molecule in a nematic phase for a static sample (top), in a nematic phase for the spinning sample (middle) and in a biaxial phase for the spinning sample (bottom).

3.5.3 X-Ray Diffraction

X-ray diffraction techniques have also been widely used in order to characterize liquid crystalline phases [6, 104–106]. An example of some of the possible patterns obtained for different liquid crystalline phases is shown in figure 3.14. Two different zones are to be differentiated in the diffraction data. The external or wide angle

zone shows the order and orientation of the molecules at short range, whereas the small angle or internal zone shows long range orientational and translational order. The fact that short range correlation is exhibited by wide angle diffractions occurs as a consequence of the diffraction patterns being measured in reciprocal space. Diffraction patterns show order in two dimensions: one parallel to the main director vector, represented by $\parallel \overrightarrow{n}$ in figure 3.14 and one perpendicular to the main director vector, and represented by $\perp \overrightarrow{n}$. Nevertheless, in the case of the biaxial phase there is more than one director vector. The directions parallel to the director representing the order of the long axes of the molecules is labeled $\overrightarrow{n}_{long ax.}$, whereas the direction parallel to the director given by the short axes of the molecules is labeled $\overrightarrow{n}_{short ax.}$ (see fig. 3.14 (b)).

The diffuse peaks observed in the wide angle area in all the diagrams in figures 3.14, 3.15 and 3.16 are typical of liquid phases. In a purely crystalline environment the peaks are highly defined. It is possible to notice at short range that there is no orientational order along the long axis. This is due to the fact that the diffraction patterns showed in the wide angle zone do not occur at enough long range to cover the length of two molecules, and therefore only local order (i.e., the one existing between nearest neighbours) is represented.

However, the small angle region is different for each liquid crystalline phase. In a uniaxial nematic phase (see fig. 3.14 (a)), it is possible to observe two diffuse peaks along the coordinate axis $\parallel \overrightarrow{n}$. The fact that the peaks are diffuse is indicative of orientational order but not translational one. By contrast, translational order can be appreciated in figure 3.14 (c), where the diffraction pattern of a SmA phase is shown. The distance between layers can be gathered from the distance between the diffraction peaks along $\parallel \overrightarrow{n}$.

In the case of SmC phases, different X-ray diffraction patterns may be obtained, depending on the type of the alignment of the phase. In figure 3.15 patterns belonging to two different types of SmC phases are shown, alongside the diagrams representing the corresponding phases. The distances between layers can be obtained in the same way as explained above for the SmA phase, while the tilt angle can be obtained by measuring the angle between the diffraction peaks and the merid-

(a)   (b)
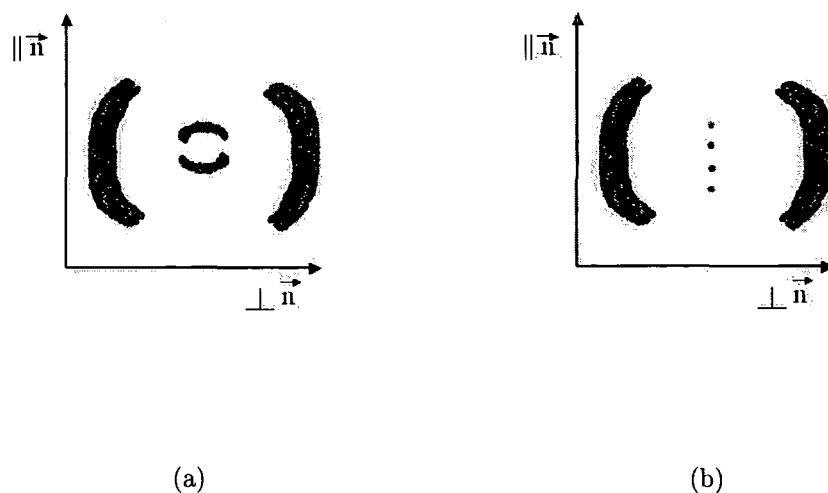
Figure 3.14: Schematic representation of the diffraction patterns of different liquid crystalline phases. Uniaxial nematic phase (a) and smectic A phase (b).

ian axis. When the tilting occurs in a single direction (fig. 3.15 (a)), a single pair of peaks is observed, whereas when the tilting occurs in two directions, two pairs of peaks can be appreciated (fig. 3.15 (b)).

Figure 3.16 (a) represents the biaxial nematic phase produced by the bent-core molecule ODBP-Ph-C_7 [6], whereas figure 3.16 (b) shows the pattern obtained in the border between a uniaxial nematic phase and a SmC phase when cybotactic groups (i.e., small local domains with a SmC order) have been formed. It is noteworthy to notice that both figures are rather similar. However, Kumar et al. have proved that major differences exist between them [6]. In the case of the cybotactic groups, the interlayer distance is smaller than the molecular length, whereas in the case of the biaxial phase, the intermolecular distance reported was ~ 44 Å, approximately the same as the molecular length. Thus the molecules exhibit no tilting. Moreover, the pattern shown in 3.16 (b) can only be registered in narrow temperature intervals, due to the fact that cybotactic groups are formed in the pre-transitional state between nematic and SmC phases. However, the diffraction pattern shown in figure 3.16 (a) was obtained in the whole nematic range. Aside from that, after the nematic-SmC phase transition was fully accomplished, the diffraction pattern produced by ODBP-Ph-C_7 showed a single pair of peaks (similar to that shown in 3.15 (a)), and
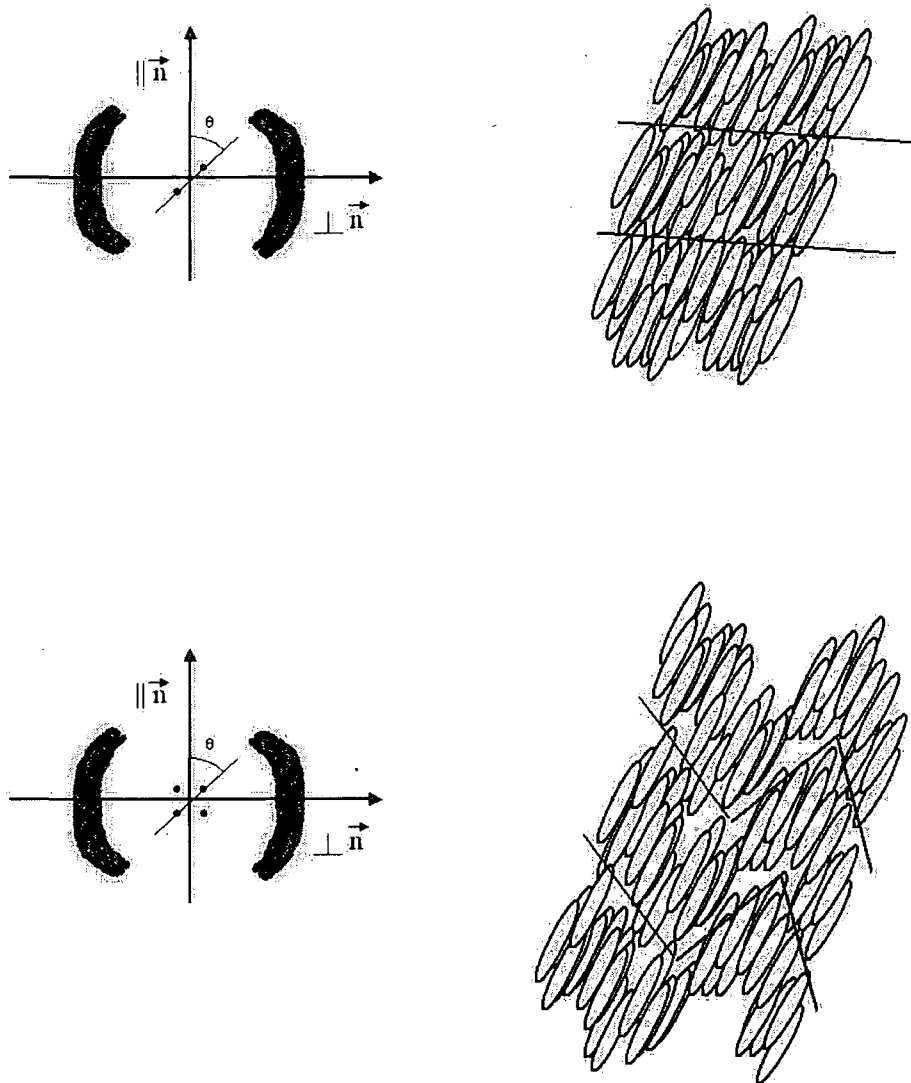
Figure 3.15: Diffraction patterns corresponding to two different types of SmC phases (right) and diagram of the type of phases represented (left). θ represents the angle between the director and the layer normal.

on reversing into the nematic phase the same four-peak pattern appeared again.

$\| \vec{n}$ long ax.

$\| \vec{n}$

$\| \vec{n}$ short ax.

$\perp \vec{n}$

(a)   (b)
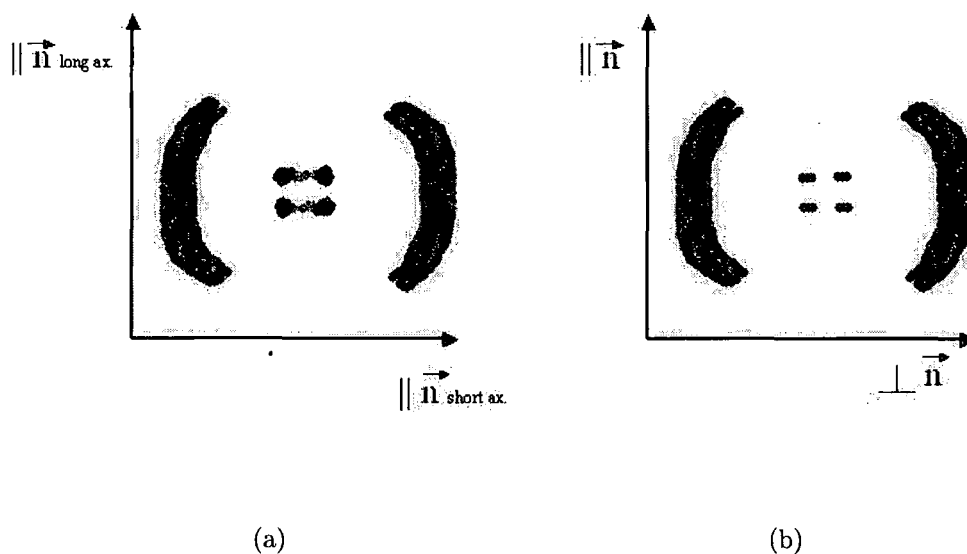
Figure 3.16: Schematic representation of the diffraction patterns obtained from (a) a biaxial phase and (b) a uniaxial phase in the transition region with a SmC phase with cybotactic groups existing in the sample.The main director is aligned vertically in both diagrams. In (a) the short axis director is aligned horizontally.

3.6   Criteria in the Definition of Molecular Orientation

The orientation of the molecule ODBP-Ph-C_7 has been defined based on three different criteria. One of them has been based on the axes of inertia calculated by means of the inertia tensor (eq. 1.1), as explained in section 1.4. A different criterion was based on the calculation of the three internal molecular axes using different sets of vectors, with the origin in the centre of the oxadiazole ring and the extremes in different parts of the mesogenic arms (see table 3.1). The longitudinal molecular axes (or molecular long axes) were calculated subtracting the vector of one of the arms to the vector of the other for all the different sets, as shown in figure 3.17, whereas the transverse molecular axes (or short molecular axes) was calculated adding the vector of one of the arms to the vector of the other one for all the different vector

sets (see figure 3.17). The vector calculated with cross product between the vectors representing the longitudinal and transverse axes was the third molecular axis necessary to calculate Q_{22}^2 (eq. 3.10) and η (eq. 3.15).

A third orientation criterion was based on the molecular steric and electric dipole. The steric dipole was represented by a vector bisecting the oxadiazole ring with the origin in the middle of the N-N bond and the extreme in the oxygen atom. The electric dipole was calculated using the usual formula

$$\mu = \sum_i q_i \mathbf{r}_i,$$ (3.16)

where q and $\mathbf{r}$ are the partial atomic charge and position vector of atom i for a given molecule. The direction of the electric dipole vector reads

$$\hat{\mu} = \frac{\mu}{|\mu|}.$$ (3.17)

V. S.	Origin	Extreme
1	Centre of oxadiazole	C in the 1st phenyl ring bonded to the oxadiazole
2	Centre of oxadiazole	C in the 1st phenyl ring bonded to the oxygen
3	Centre of oxadiazole	Oxygen bonded to the first phenyl ring
4	Centre of oxadiazole	Carbonyl
5	Centre of oxadiazole	C in the 2nd phenyl ring bonded to the carbonyl
6	Centre of oxadiazole	C in the 2nd phenyl ring bonded to the chain
7	Centre of oxadiazole	Last C of the chain

Table 3.1: Definition of the vector sets (V. S.) used to calculate the molecular axes used in the calculation of Q_{00}^2 and Q_{22}^2.

3.7 Uniaxial and Biaxial Order Parameters

Two different methods were used to calculate the biaxial order parameter for the molecule ODBP-Ph-C_7. One of them is given by equation 3.10, and consists of the

Figure 3.17: Some of the vectors used to define the orientation of the molecule ODBP-Ph-C$_7$.

method implemented by Allen [35]. The other one is based on ^{2}H NMR technique, and uses the formula 3.15, as described by Luckhurst [28]. Again, both equations above mentioned were used with both inertia axes and molecular vectors, as explained in the previous section.

Uniaxial order paremeters were calculated as explained in section 1.4.

Chapter 4

Simulation of the ODBP-Ph-C$_7$

4.1 Introduction

This chapter presents results from molecular dynamics simulations of the molecule ODBP-Ph-C$_7$. In order to cover the range of temperatures included in the nematic phase, five different simulations have been set up. These span the temperatures between the isotropic-nematic pre-transition region (488 K) and the nematic-smectic pre-transition one (448 K) (see figure 3.8). Three other temperatures (458 K, 468 K, 478 K) were adopted in between these extremes.

Results from an additional simulation will also be presented in which the partial atomic charges are neglected. This will allow conclusions to be drawn about the role played by charges in the onset of the nematic phase. The temperature chosen to run this simulation was 468 K, placed approximately in the middle of the nematic temperature range. Subsequently the charges were switched on again, and the simulation carried on until the system was equilibrated.

Finally, results will be presented for an isotropic phase which is rapidly quenched into the nematic regime and equilibrated until it was thermodynamically stable. The motivation for running this simulation is to show that the nematic phases previously simulated were not thermodynamically metastable phases, but genuine nematic phases. This "quench" run has been carried out both with and without the presence of electrostatic interactions.

4.2   Simulation of Different Temperatures

4.2.1   Simulation Details

The potential used to represent the intra and intermolecular interactions took a harmonic all-atom form, based on the AMBER [107] force field. Some of the force field parameters were directly obtained from *ab initio* calculations, whilst the rest were extracted from the OPLS-AA force field of Jorgensen [108], using the package Maestro 6.5.008 [109] to produce a force field file. A summary of the force field parameters is given in tables 4.1, 4.2 and 4.3.

Angle	k_θ/kJ mol^{-1}rad^{-2}	θ_0/ deg
CA-CA-CA	263.59	120.0
CA-CA-HA	146.66	120.0
CA-CA-CT	292.88	120.0
CA-CT-CT	263.59	114.0
CA-CT-HC	146.44	109.5
CT-CT-CT	244.35	112.7
CT-CT-HC	156.90	110.7
HC-CT-HC	138.07	107.8
CP-N-N	468.62	113.1
CP-OS-CP	627.61	111.0
OS-CP-N	585.77	115.0
N-CP-CP	527.20	120.0
OS-CP-CP	677.82	111.0
CP-OS-C	691.38	118.1
OS-C-O	694.56	123.4
CA-CP-OS	585.77	120.0

Table 4.1: Bond angle bending parameters.

Dihedral	V_1	V_2	V_3
HC-CT-CT-HC	0.000	0.000	1.331
CT-CT-CT-HC	0.000	0.000	1.531
CT-CT-CT-CT	7.280	-0.657	1.167
HC-CT-CA-CA	0.000	0.000	0.000
CT-CT-CA-CA	0.000	0.000	0.000
HC-CT-CT-CA	0.000	0.000	1.9333
CA-CA-CA-CA	0.000	39.784	0.000
CA-CA-CA-HA	0.000	39.784	0.000
HA-CA-CA-HA	0.000	39.784	0.000
CP-N-N-CP	0.000	39.784	0.000
CP-OS-CP-N	0.000	15.167	0.000
N-N-CP-OS	0.000	15.167	0.000
N-CP-CP-CA	0.000	4.540	0.000
OS-CP-CP-CA	0.000	9.000	0.000
CA-CA-CP-OS	0.000	39.784	0.000
CA-CP-OS-C	0.000	7.950	0.000
CP-OS-C-O	10.860	17.018	0.916
CP-OS-C-CP	10.860	17.018	0.916
OS-C-CP-CA	0.000	9.000	0.000
O-C-CP-CA	0.000	9.000	0.000
C-CP-CA-CA	0.000	39.784	0.000
C-CP-CA-H	0.000	39.784	0.000

Table 4.2: Torsional parameters expressed in kJ mol^{-1}.

Atom Type	$\epsilon/$ kJ mol^{-1}	$\sigma/$ Å	q / e
CA	0.293	3.550	-0.115
CA	0.293	3.550	0.135
CP	0.293	3.550	0.000
CT	0.276	3.550	-0.180
CT	0.276	3.550	-0.120
C	0.276	3.550	0.510
OS	0.586	2.900	-0.215
OS	0.586	2.900	-0.190
O	0.879	2.960	-0.430
N	0.711	3.250	-0.339
HA	0.126	2.420	0.155
HC	0.126	2.500	0.060

Table 4.3: Non-bonded parameters.

Molecular dynamic simulations were performed using the package DL_POLY 2.14 [110]. The SHAKE [111] procedure was applied to constrain bonds and allow a slightly larger timestep. A 2 fs timestep was used throughout. The leap-frog algorithm was used to solve the Newton's equations of motion. An Ewald sum [112] was employed to tackle the electrostatic interactions to maximize the accuracy of the results, despite the computational time involved for this procedure. The Ewald sum convergence parameter was chosen as 0.3208 Å and 6 wave-vectors were employed in each of the x, y and z directions. A cut-off of 9 Å was applied to the van der Waals interactions.

The simulation was initially started from an idealized cubic lattice in the gas phase, formed from 256 molecules, where all the molecules had exactly the same orientation. The system was then compressed at 1 K and 10 kPa using a Berendsen thermostat-barostat [65], with relaxation times of 1.0 ps and 4.0 ps respectively. Simulations were carried on until the density of a liquid crystal phase was approximately reached. During the period where the density of the system was increasing significantly, the orientational order was maintained reasonably well. The Q_{00}^2 corresponding to both the long and short axes and for the Q_{22}^2 had an approximate value of 0.9. After this the Berendsen thermostat-barostat was switched to a Nosé-Hoover one [113, 114] with the relaxation times of 1.0 ps and 4.0 ps respectively. Five different temperatures were used to run a series of simulations over periods of between 20 and 30 ns: 448 K, 458 K, 468 K, 478 K and 488 K. All the simulation were performed under the same pressure of 1 atmosphere. Coordinate data from the simulations was gathered periodically for subsequent analysis.

Due to the extraordinary high cost in terms of computing time all the simulation were run in parallel. Typically, 16 or 32 CPUs were used of a dual-processor dual care AMD opteron system, with myrinet interconnectors between four CPU compute nodes.

T/ K	V/ Å	ρ/ g cm^{-3}
448	262599 ± 1028	1.066 ± 0.004
458	264525 ± 1143	1.059 ± 0.004
468	263710 ± 1064	1.062 ± 0.004
478	265354 ± 1124	1.055 ± 0.004
488	267496 ± 1385	1.047 ± 0.004

Table 4.4: Box volumes and densities for a simulation of ODBP-Ph-C$_7$.

4.2.2   Structure and Order

Densities

From the values shown in table 4.4 it is possible to appreciate that the ODBP-Ph-C$_7$ has a reasonable high density. As expected, the results show that the density decreases as temperature increases. Equilibration of the densities for the different temperatures occurs over approximately a period of 20 ns, as can be appreciated in figure 6.1. Results in table 4.4 have been averaged from the last 4 ns of the runs, and their correspondent standard deviations are relatively small. Overall, they only represent the 0.4 % of the total magnitude of the densities.

Unfortunately, there are no experimental density results available for ODBP-Ph-C$_7$ for comparison. Nevertheless, the density is consistent with a fairly viscous nematic phase.

Radial Distribution Function $g_\parallel (r)$

The radial distribution function parallel to the long axis director (calculated using the long molecular axis defined with a vector going from the centre of the oxadiazole ring to the first carbon of the aliphatic chain, as explained in section 3.6) was calculated to study the structure of the system. The intermolecular distance was measured from the centres of the oxadiazole rings. The results for these calculations are shown in fig. 4.2. It can be seen that at the lowest temperature of 448 K the distribution is practically uniform throughout all the simulation box. However,
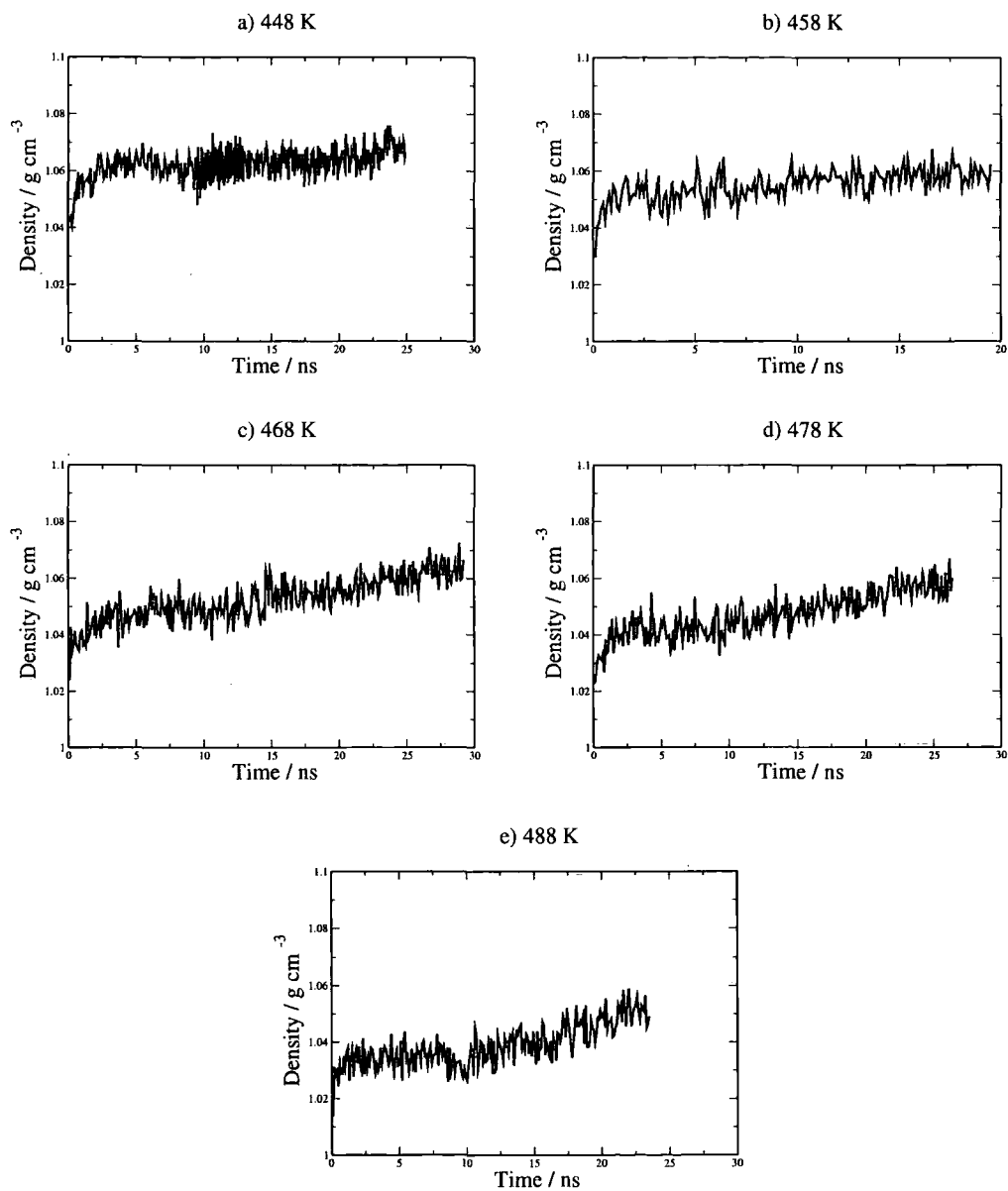
Figure 4.1: Evolution of the density of ODBP-Ph-C$_7$ with respect to simulation time for five different temperatures: a) 448 K, b) 458 K, c) 468 K, d) 478 K and e) 488 K.

as the temperature increases, $g_\parallel(r)$ adopts a wavy pattern. Nonetheless, this does not correspond to the typical sinusoidal curve characteristic of the smectic phases observed in other bent-core models simulations [100–102], since no period can be appreciated in the radial distribution function. For the middle temperatures (458 K, 468 K and 478 K, especially for the 468 K), a small step can be appreciated. The patterns produced by these simulations are rather similar, whereas the ones observed for 448 K and 488 K differ slightly. This was expected since the two latter are pre-transitional temperatures, whereas the three former are in the middle of the nematic phase temperature range. For the highest temperature (i.e. 488 K), the function adopts a curved shape, whereas for the lowest temperature a flatter curve is obtained.

In order to inspect visually the liquid crystalline phases produced in the different simulations, snapshots were produced for each temperature, as can be seen in figure 4.3. The color coding represents the orientation of the steric dipole (i.e., the transverse axis which bisects the oxadiazole in two identical parts, see section 3.6). Neglecting the color coding, it is possible to state that in 4.3 (a), (b) and (c) there is no molecular superstructure in the system. However, in (b) and (d) molecules start to cluster together and in (e) there are two domains formed, which explains the curved pattern detected in $g_\parallel(r)$ at this temperature (488 K). Therefore it is possible to conclude that the phases existing in the 448 K, 458 K, 468 K and 478 K simulations are nematic. In the 488 K simulations could be either two domains formed or a smectic phase.

Order Parameters

Uniaxial and biaxial order parameters Q_{00}^2 and Q_{22}^2 were calculated as described in section 3.7. To do so, the orientation of the molecules were defined in two different ways: one using the axes of inertia of the molecule and the other using three orthogonal vectors calculated with the vectors running from the centre of the oxadiazole ring to the first carbon of the aliphatic chain, as detailed in section 3.6.

After the initial compression from a gas phase lattice system, the Q_{00}^2 calculated for the long axis and Q_{22}^2 were approximately 0.9 at all temperatures. Both Q_{00}^2
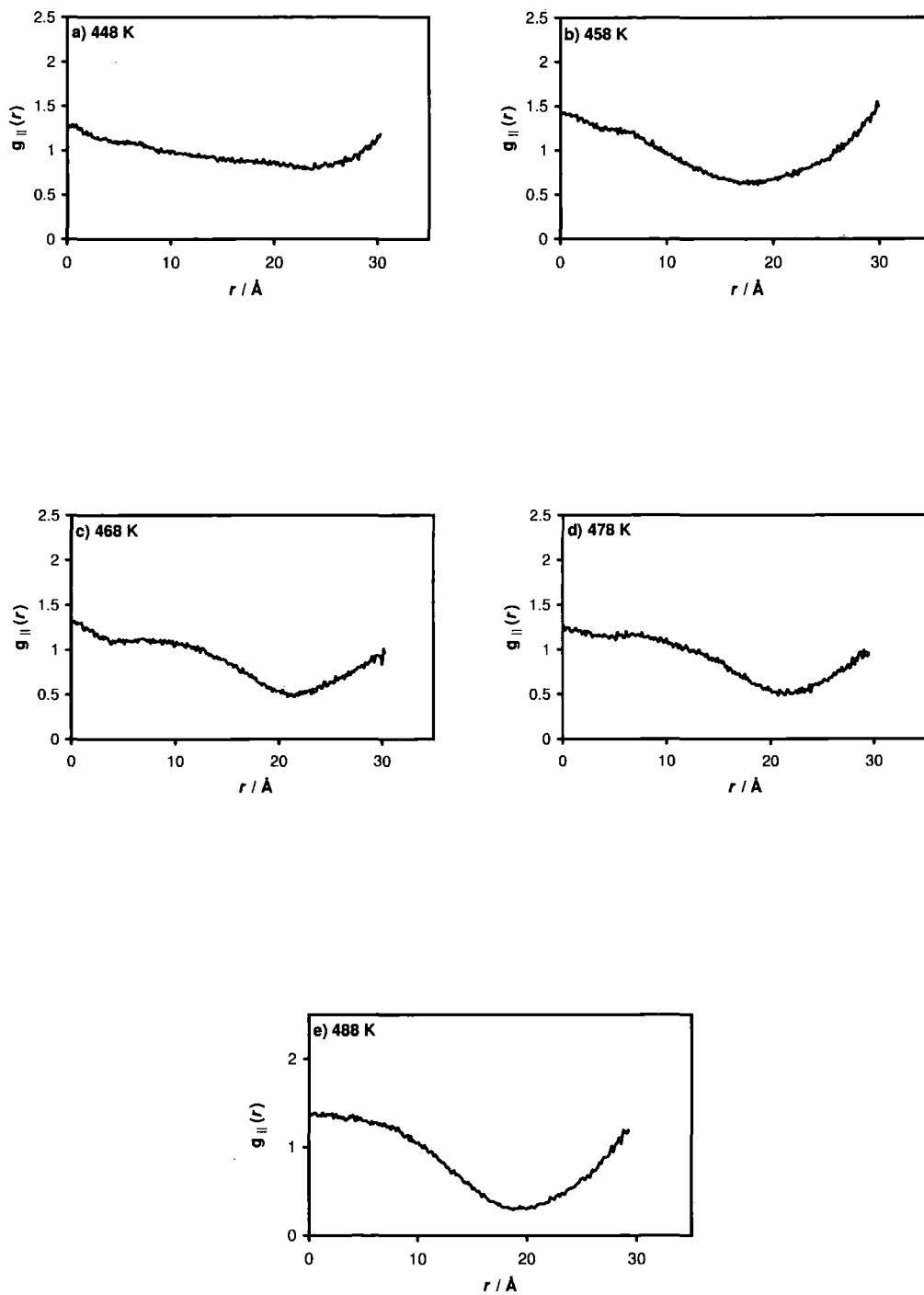
Figure 4.2: $g_{\parallel}(r)$ calculated for the simulations of ODBP-Ph-C$_7$ at five different temperatures: a) 448 K, b) 458 K, c) 468 K, d) 478 K and e) 488 K.
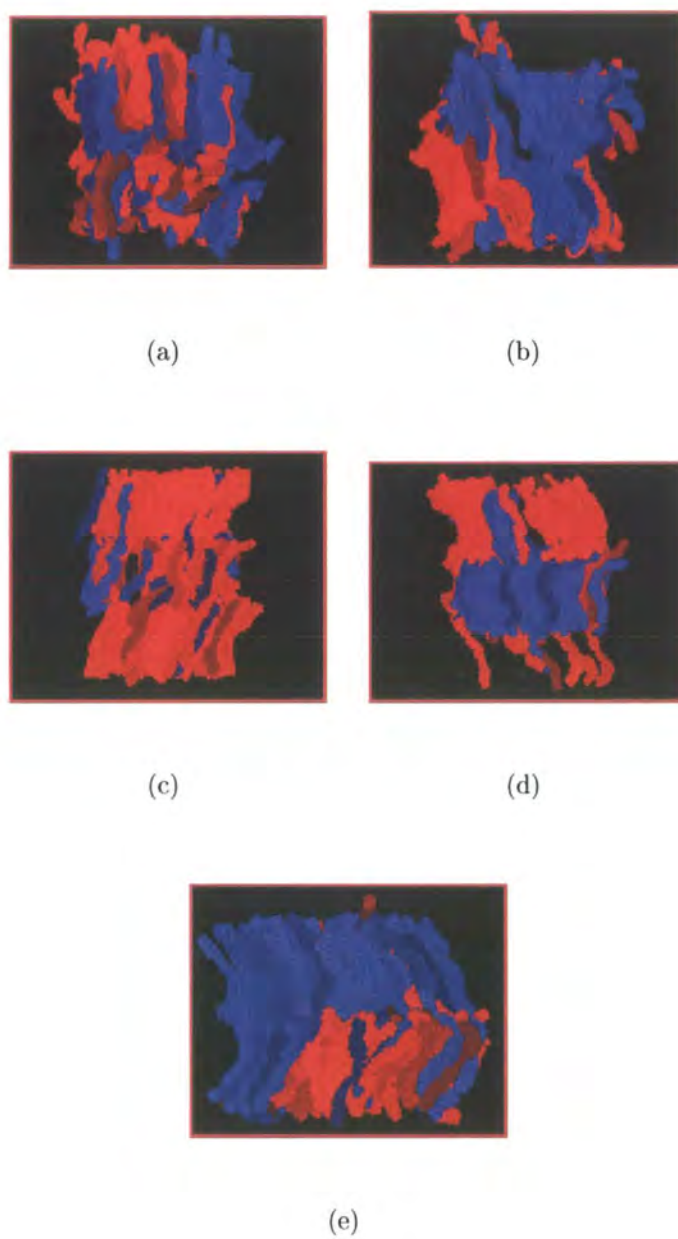
Figure 4.3: Snapshots from the simulation of ODBP-Ph-C$_7$ run at five different temperatures: 448 K (a), 458 K (b), 468 K (c), 478 K (d) and 488 K (e). The color coding represents the orientation of the molecular steric dipole moment.

Order Parameter	Temperature				
	448 K	458 K	468 K	478 K	488 K
Q_{00}^2 (I. A.)	0.80±0.02	0.72±0.02	0.85±0.01	0.86±0.03	0.73±0.03
Q_{22}^2(I. A.)	0.07±0.04	0.08±0.03	0.44±0.04	0.42±0.05	0.12±0.03
Q_{00}^2 (V.A.)	0.77±0.03	0.68±0.02	0.83±0.01	0.83±0.04	0.68±0.04
Q_{22}^2(V. A.)	0.07±0.03	0.08±0.04	0.43±0.04	0.43±0.05	0.14±0.04

Table 4.5: Order Parameters: Uniaxial order along the molecular long axis and biaxial order parameter calculated using the axes of inertia (Q_{00}^2 (I.A.) and Q_{22}^2 (I.A.)) and the axes calculated using the vectors with their origin in the centre of the oxadiazole ring and terminated with the first carbon of the aliphatic chain (Q_{00}^2 (V.A.) and Q_{22}^2 (V.A.)).

and Q_{22}^2 were monitored during the further progress of the simulations. Both order parameters decayed in approximately a hundred of picoseconds after the start of the simulation at room pressure for all the different temperatures considered. It can be appreciated in both figures 4.4 and 4.5 that the decay is equally dramatic for all the temperatures. It can be noticed comparing figures 4.4 and 4.5 that there is good agreement between the results obtained using vector representation of the molecular axes and the inertia tensor.

For most of the temperatures studied, Q_{00}^2 looked to be equilibrated after just few nanoseconds of simulation. However, fluctuations in Q_{22}^2 were encouraging enough to continue with the simulations. For all the temperatures, the average Q_{22}^2 within the first 10 ns of simulation is in a range of 0.08 - 0.1. Nonetheless, from the 12th ns onwards the biaxiality gradually starts to grow in the particular cases of the simulations run at 468 K and 478 K.

The value of Q_{22}^2 for the simulation at 448 K eventually decays despite being the highest one during the first half of the simulation (i.e. in the first 10 ns). This is opposite way around to what typically could be expected, since the higher order parameters should correspond to the lower temperatures. Nevertheless, it is not until 20 ns in the 468 K simulation and 15 ns in the 478 K simulation that Q_{22}^2 is sufficiently large to consider the system properly biaxial beyond any doubt. For the
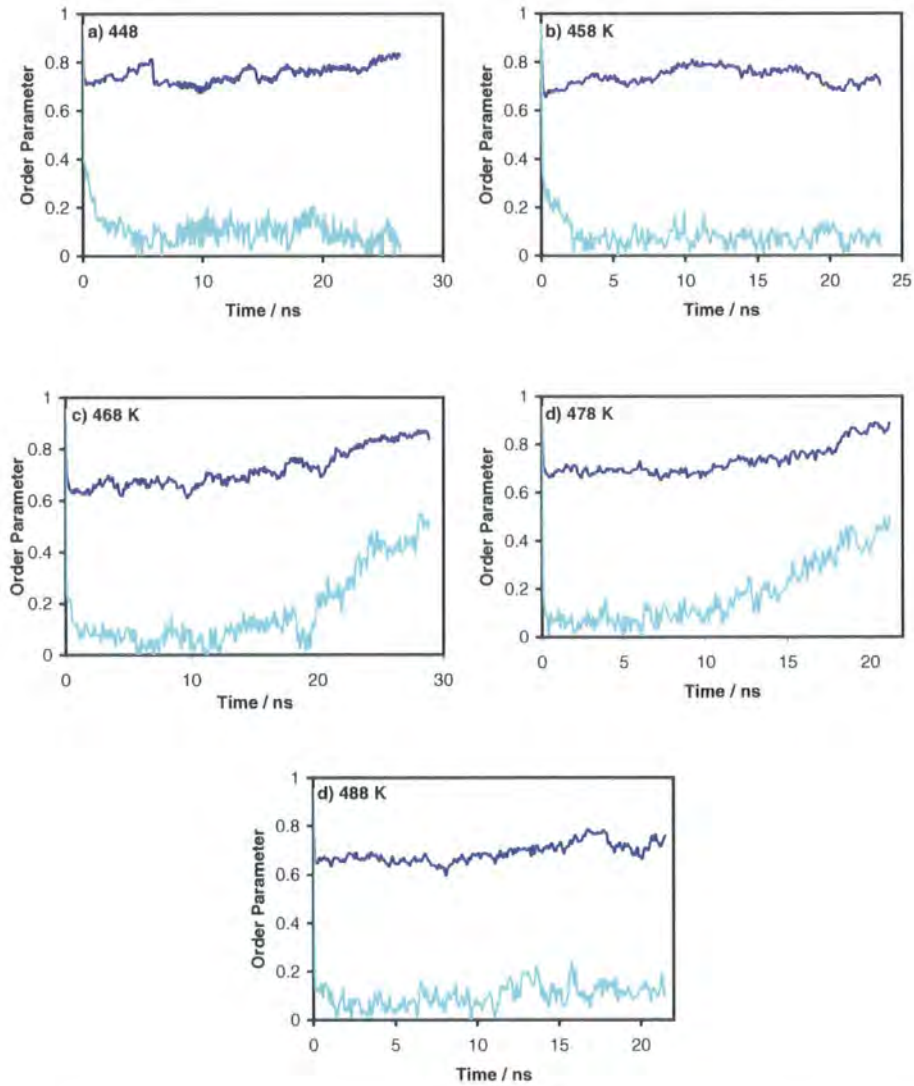
Figure 4.4: Q^2_{00} (navy blue) and Q^2_{22} (turquoise) calculated using the axes of inertia.
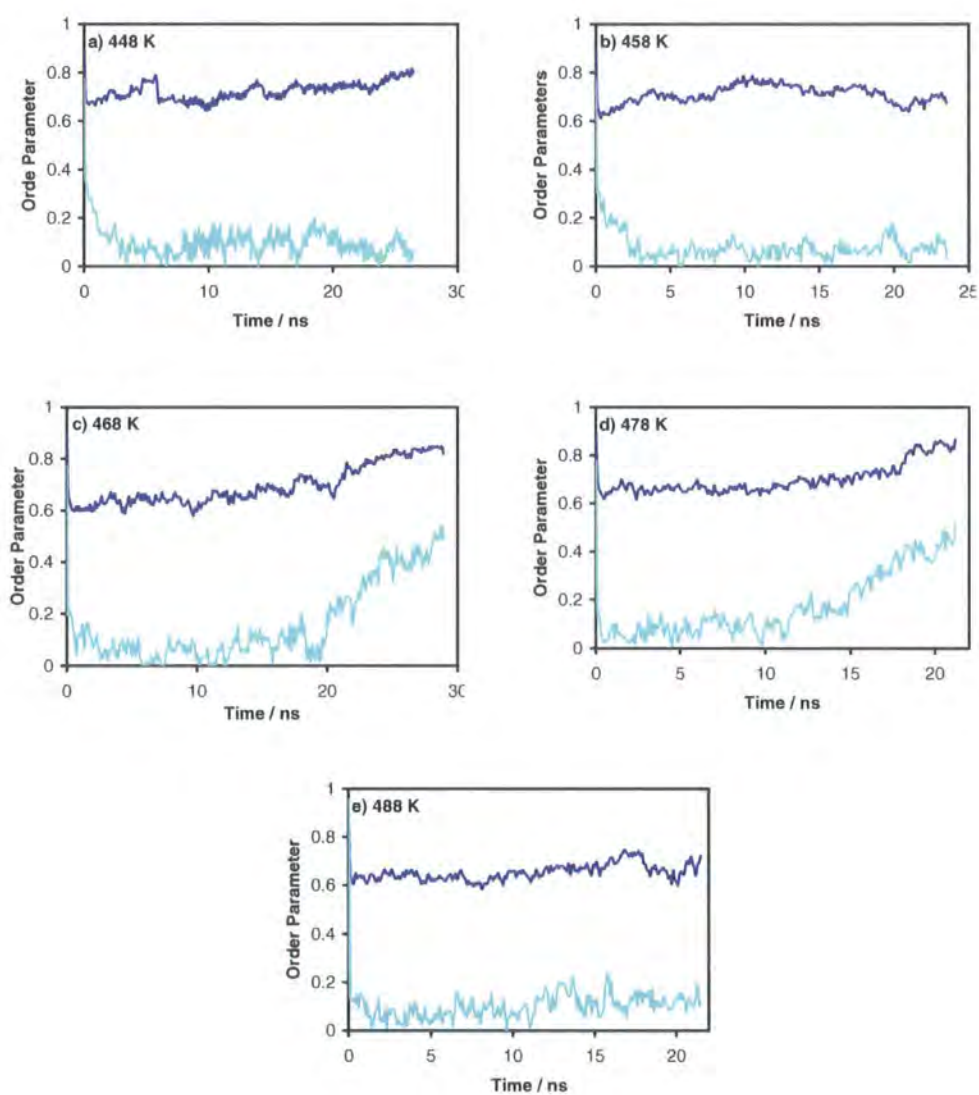
Figure 4.5: Q_{00}^2 (navy blue) and Q_{22}^2 (turquoise) calculated using the axes calculated with the vectors going from the centre of the oxadiazole to the first carbon of the aliphatic chain as explained in section 3.6.

other temperatures full growth of Q_{22}^2 never occurs, although in the 488 K simulation Q_{22}^2 is significant.

After the systems were equilibrated for a reasonable period simulations were carried on over a further period of 5 ns in order to gather sufficient amount of data to perform an accurate statistical analysis. The final order parameters for all the five different temperatures are summarized in table 4.5. The averaged results for Q_{00}^2 are large for a nematic phase. Nonetheless, they are not large enough to suspect the formation of a smectic phase. Different smectic phases formed by banana-shaped models have been reported [94, 100–102] and in all of them $Q_{00}^2 > 0.9$ for the long molecular axis. Aside from that, the patterns exhibited by $g_\parallel(r)$ in figure 4.2 do not show conclusive evidence that a smectic phase is formed in any of the systems.

It can be appreciated that the Q_{22}^2 is significantly smaller in the simulation run at the two lower temperatures. It is possible to conclude that a fully equilibrated biaxial phase does not exist for these two temperatures. By contrast, Q_{22}^2 values for the simulations performed at 468 K and 478 K illustrate perfectly the success in reproducing a biaxial nematic phase. Moreover, the value of Q_{22}^2 obtained in the simulation at 488 K is significant. Despite its small magnitude of 0.12, this still differs from zero and is very close to the experimental one [23]. However, as is discussed below (see sections 4.2.3 and 4.2.4), the raw order parameter data hides a much more complicated picture of molecular order in these systems.

Q_{00}^2	Temperatures				
	448 K	458 K	468 K	478 K	488 K
Steric Dip.	0.25±0.03	0.23±0.03	0.53±0.04	0.50±0.05	0.25±0.03
Electric Dip.	0.22±0.02	0.19±0.02	0.40±0.03	0.37±0.05	0.21±0.02
Quadrupole	0.21±0.03	0.18±0.02	0.42±0.04	0.40±0.05	0.21±0.02

Table 4.6: Uniaxial order parameters Q_{00}^2 calculated using the steric dipole (Steric Dip.), the electric dipole (Electric Dip.) and the molecular quadrupole, calculated over the final 4 ns of the simulation runs for ODBP-Ph-C$_7$.

Uniaxial order parameters for the steric dipole and the electric dipole were monitored throughout the simulations (see figures 4.6 and 4.7). The results of the av-

eraged order parameters calculated using steric and electric dipoles and quadrupole are shown in table 4.6. Q_{00}^2 exhibits larger values for the steric dipole than for the electric dipole and the quadrupole. It is noteworthy that the evolution of Q_{00}^2 calculated from the steric and electric dipoles is parallel to the evolution of Q_{22}^2.

Results shown in table 4.6 suggest that the orientational order perpendicular to the long axis direction is large enough to consider the phase biaxial. However, the same consideration is not possible for the rest of the temperatures. Memmer [94] found a value for Q_{00}^2 for the steric dipole similar to the results obtained for the 448 K, 458 K and 488 K simulations. In this case, the author considered the relative high value of Q_{00}^2 for the short axis was a consequence of the high molecular order along the main molecular axis, i.e. the longitudinal axis.

In order to check whether different segments from the molecule had a different contribution to the order parameters, a comprehensive test was carried out. Q_{00}^2 was calculated using each one of the different vectors representing the orientation of the molecular long axis (a summary of the vectors used in this calculation is given on table 3.1, see section 3.6). Subsequently, the average of all these order parameters $< Q_{00}^2 >$ was evaluated. Finally, the difference between each one of the order parameters and the average order parameter was plotted against time (fig. 4.8). The same process was also carried out to calculate Q_{00}^2 for the short molecular axis (fig. 4.9). It is possible to see in figure 4.8 that, albeit the deviation of Q_{00}^2 calculated with the axes calculated with whole molecule vectors (vector set 7, see table 3.1) is slightly larger than for the rest of the vector sets, there is no significant deviation of any Q_{00}^2 values calculated for the long axis with any of the vectors sets from $< Q_{00}^2 >$. The same result for Q_{00}^2 values calculated for the short axis is appreciated in figure 4.9.

The order parameters obtained using the method suggested by Bates and Luckhurst (see section 3.7) are equally interesting. One of the big advantages of this method dwells in the fact that they can be directly compared with the ^{2}H NMR experimental results, since both use the same expression to calculate the biaxial parameter η_{exp}. As with the Allen method, different criteria have been used to define the molecular axes used in the calculation of η: the principal axes of inertia and
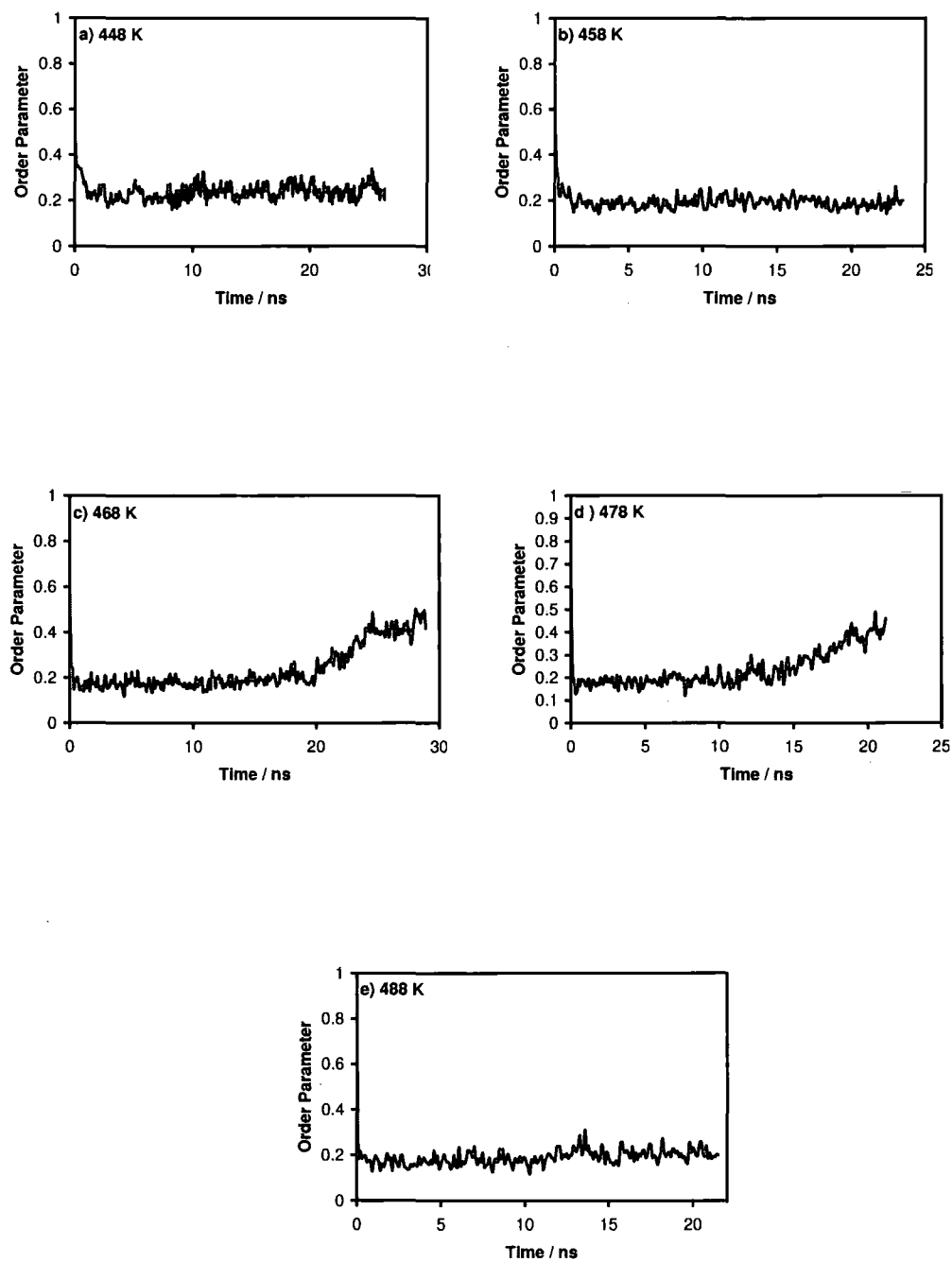
Figure 4.6: Q_{00}^2 calculated from the the molecular electric dipole moment of ODBP-Ph-C_7.
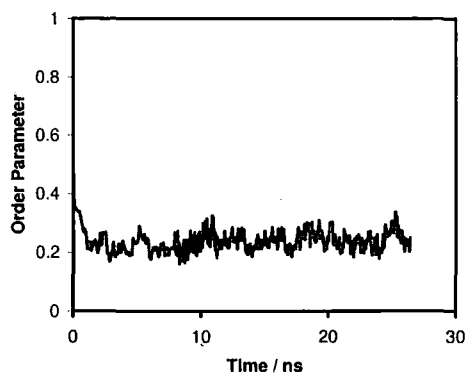
(a) 448 K
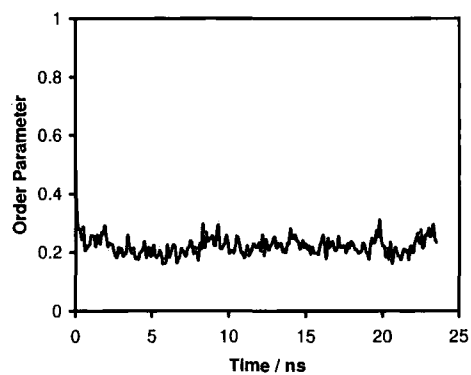
(b) 458 K
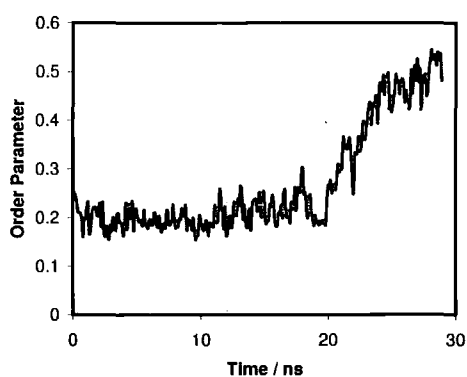
(c) 468 K
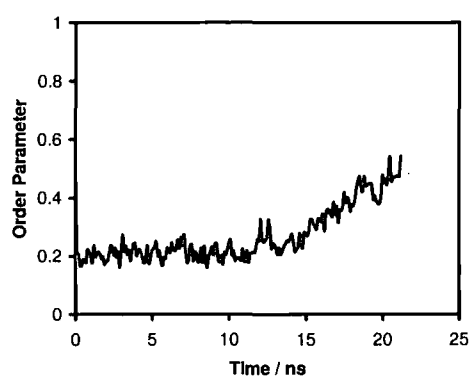
(d) 478 K
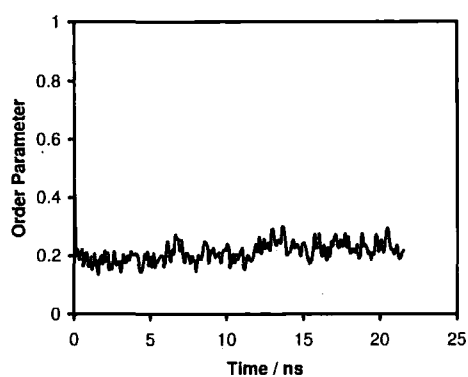
(e) 488 K

Figure 4.7: Q_{00}^2 calculated for the molecular short axis of ODBP-Ph-C$_7$ calculated geometrically.
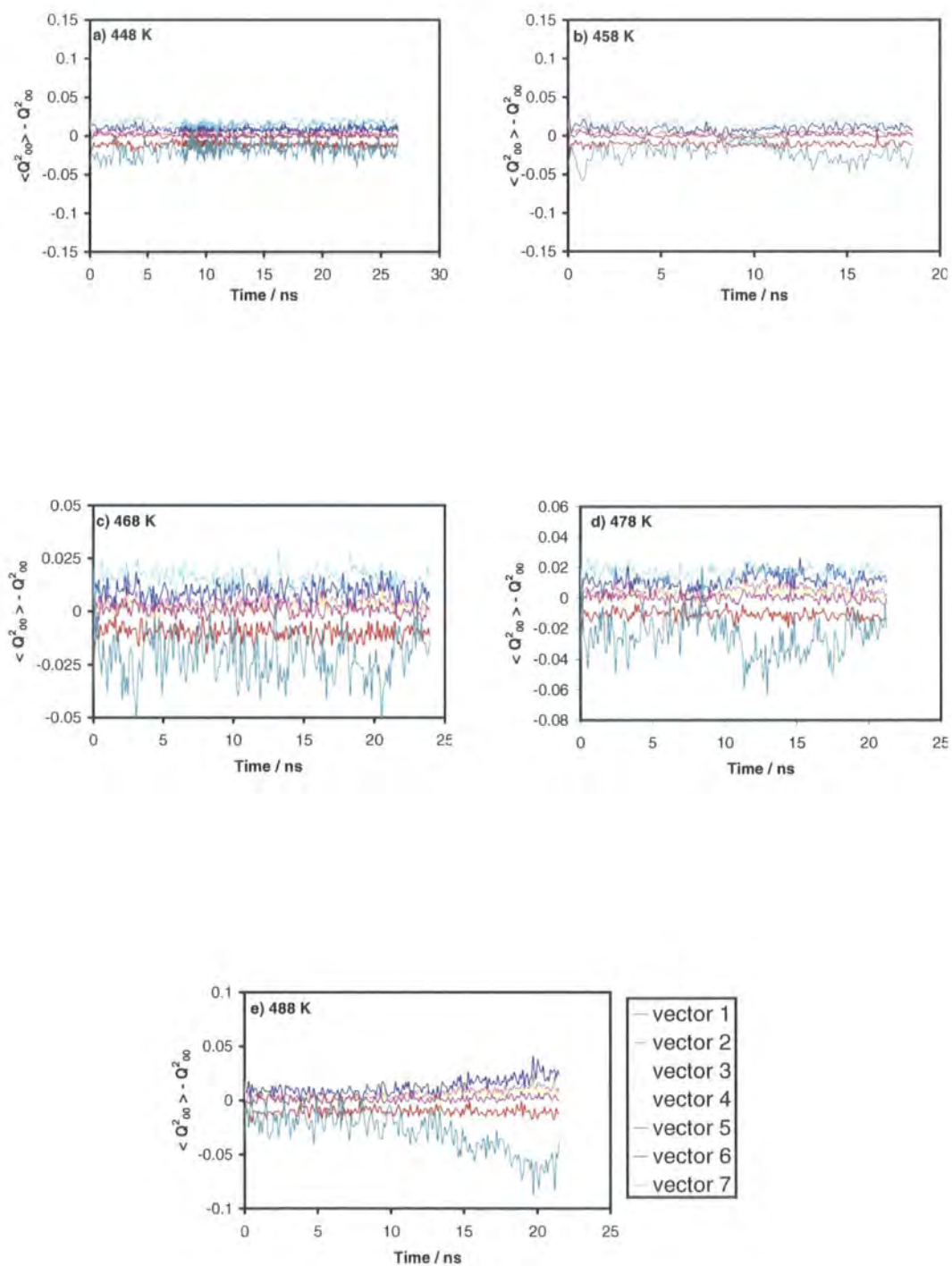
Figure 4.8: $<Q_{00}^2>$ - Q_{00}^2 for the long axis of ODBP-Ph-C$_7$.
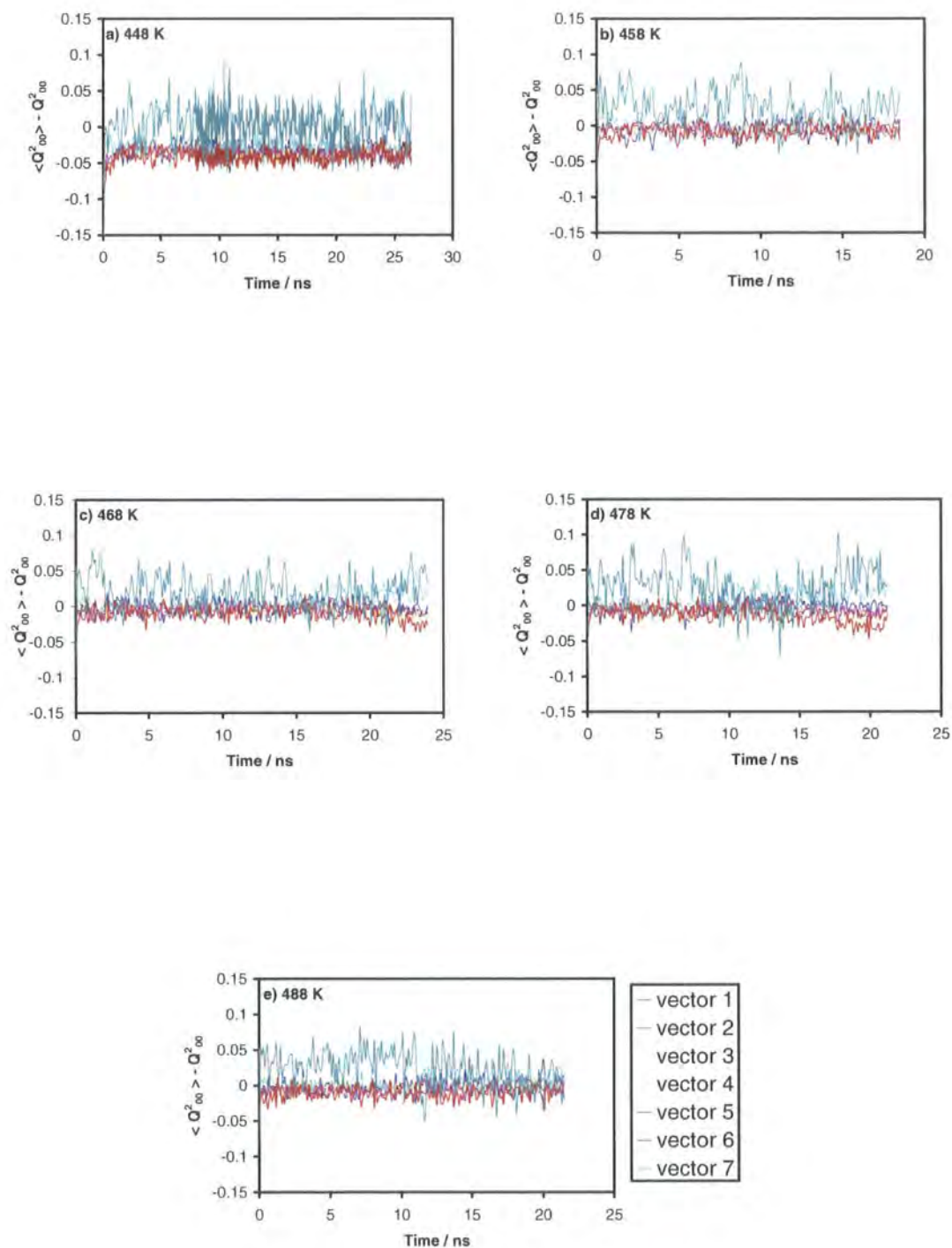
Figure 4.9: $\langle Q_{00}^2 \rangle$ - Q_{00}^2 for the short molecular axis of ODBP-Ph-C$_7$.

the different sets of vectors defined in section 3.6. As with other papers which use this formula [96], there is a variation in the results depending on which axis is used to calculate the order tensor. Hence results from the inertia long axis differ from those obtained when the order tensor is calculated with the molecular short axis parallel to the molecular dipole. Both differ from the results obtained from the axis parallel to the molecular arm. Nonetheless, the evolution of η across the different temperatures is always consistent with the results obtained from Allen's method, though no quantitative comparison between the results can be expected.

As can be appreciated in tables 4.7 and 4.8, all the biaxial parameters obtained by means of the secondary axes of inertia and the vectors running along the short axes are larger than zero. However, those corresponding to the temperatures 468 K and 478 K are considerable higher than the rest.

T / K	η_x	η_y	η_z
448	0.2±0.1	0.3±0.1	0.09±0.02
458	0.4±0.2	0.3±0.1	0.10±0.03
468	0.57±0.09	0.58±0.09	0.07±0.02
478	0.6±0.1	0.7±0.1	0.09±0.03
488	0.6±0.2	0.3±0.2	0.25±0.07

Table 4.7: Biaxial parameters η calculated with the inertia axes (x, y and z, where z is the long axis) for the simulation run at five different temperatures: 448 K, 458 K, 468 K, 478 K and 488 K.

As reviewed in chapter 3, there have been several different models designed to simulate liquid crystal phases formed from bent-core mesogens. However, just two of them have taken into consideration the molecular permanent dipole parallel to the molecular steric dipole. In the first case [100], one of the simulations assigned an inter-arm angle of 140^0 to the molecule, so the similarities with the present simulation are clear. As the system was cooled, a transition occured at a temperature of $T^* = 1.3$. The Q_{00}^2 registered for this particular case increased by 0.739, going from 0.194 to 0.933. Such a large value of Q_{00}^2 is more characteristic of smectic phases, as subsequently corroborated by the authors through the calculation of the radial distri-

T / K	η_x	η_y	η_z
448	0.3±0.1	0.2±0.1	0.09±0.02
458	0.3±0.1	0.4±0.2	0.11±0.04
468	0.60±0.09	0.58±0.09	0.08±0.02
478	0.6±0.1	0.59±0.08	0.11±0.03
488	0.3±0.1	0.3±0.2	0.7±0.1

Table 4.8: Biaxial parameters η calculated with three molecular axes (x, y and z) calculated with the vectors going from the centre of the oxadiazole ring to the C in the second phenyl ring bonded to the aliphatic chain (see section 3.6) for the simulation run at five different temperatures: 448 K, 458 K, 468 K, 478 K and 488 K.

T / K	η_{arm}	η_{dip}	η_{quad}
448	0.09±0.02	0.3±0.1	0.3±0.2
458	0.12±0.04	0.2±0.1	0.3±0.2
468	0.16±0.03	0.82±0.09	0.6±0.1
478	0.18±0.02	0.8±0.1	0.7±0.1
488	0.22±0.05	0.3±0.2	0.3±0.2

Table 4.9: Biaxial parameters η calculated with the molecular arm axis η_{arm}, the electric dipole η_{dip} and the quadrupole η_{quad}.

bution function parallel to the main director vector $g_{\parallel}(r)$. This suggested the liquid crystal phase to be a non-tilted smectic X, disposed in an antiferroelectric fashion and strongly biaxial ($Q_{22}^2 > 0.4$). No nematic phase was reported, contrasting with the results presented here. It therefore seems likely that molecular flexibility plays a crucial role in the stabilization of the nematic phase. Flexible chains have the effect of raising the free energy of smectic and crystalline phases, making it possible to obtained a nematic. The second previous literature model [102] had an inter-arm angle which was fixed at 120^0 and the molecule was provided with a transverse dipole moment. Once again, no nematic phase was detected. Instead, a phase transition from the isotropic phase directly into a smectic B phase was observed, with Q_{00}^2 changing from ≈ 0.1 to ≈ 0.9 . The smectic phase was also characterized in this case as polar antiferroelectric and strongly biaxial ($Q_{22}^2 = 0.38$). Nevertheless, it is noteworthy that the rigidity of this models combined with the presence of an electric dipole hinders the onset of a nematic (and by inference a biaxial nematic phase), stabilizing higher ordered phases, such as smectic B. Therefore it is possible to conclude that the molecular flexibility shown in the present model is extremely important for the recreation of a biaxial nematic phase.

Orientational Distribution Function

As explained in section 2.6, the orientation distribution function $f(\cos\theta)$ measures the distribution of molecules with respect to the cosine of the angles formed by the molecular axes and the correspondent director vector. In figure 4.10, it can be appreciated that most of the long axes of the molecules align parallel to the long axis director. It can be seen that the number of molecules perpendicular to this director vector is nil because the area below the curve $f(\cos\theta)$ is large for values of $\cos\theta$ close to 1 and -1 and zero for values of $\cos\theta$ close to 0. This is seen for all the temperatures. However, this is not the case for the short molecular axis. Although $f(\cos\theta)$ is peaked along the short axis director (see figure 4.11), a spread of orientations is seen. This is consistent with the uniaxial order parameter for the short axis. The simulation runs at 468 K and 478 K exhibit greater orientational order as expected, since the order parameters calculated already announced a high

order in this direction.

Two possible interpretations can be made for the results obtained. One is simply to assign lower orientational order to the 448 K, 458 K and 488 K results. A different interpretation involves the existence of different domains, each one with a slightly different director. In each one of these domains the molecular dipoles and short axis could be highly ordered parallel to their correspondent director. The order parameter and $f(\cos\theta)$ graphs are not able to distinguish between these two possibilities.

In figure 4.12 $f(\cos\theta)$ is plotted for the cosine of the angle formed by the electric dipole moment of each molecule in the system and the director vector associated with the molecular short axis. It is possible to appreciate that the area below the distribution function is larger for values of $\cos\theta$ closer to 1 and -1 than zero. This result shows that the molecular dipole and the transverse short axis are parallel.

Dihedral Angle Distribution Function

To study the molecular structure of the system at different temperatures, the key dihedral angles present in the molecule ODBP-Ph-C_7 (fig. 4.13) have been monitored for three different temperatures: 448 K, 468 K and 488 K. These are plotted in figure 4.14. φ_1 is typical of a highly conjugated structure. The absence of hydrogens in the oxadiazole ring bonded to the nitrogens, along with the high aromaticity of both rings, fosters the planar configuration of the rigid core of the molecule. By contrast, in the dihedral angle φ_2, the steric repulsion between the hydrogens bonded to the aromatic carbons and the carbonyl oxygen produces a preference for a non-planar configuration. Nevertheless, the conjugation of the ester oxygen electrons makes a small contribution to the planarity of the dihedral angle, as can be appreciated observing the small but non negligible populations for the angles of 0^0 and 180^0.

The situation is dramatically different regarding the dihedral angles φ_3 and φ_4. The conjugation of the oxygen lone pairs of electrons throughout the second phenyl ring produces a very strong planar configuration, typical of aromatic systems. This can be clearly observed in figure 4.14. These results are consistent with those found in the literature (see ref. [115–117] and the references in tables 8.4, 8.5 and 8.6).
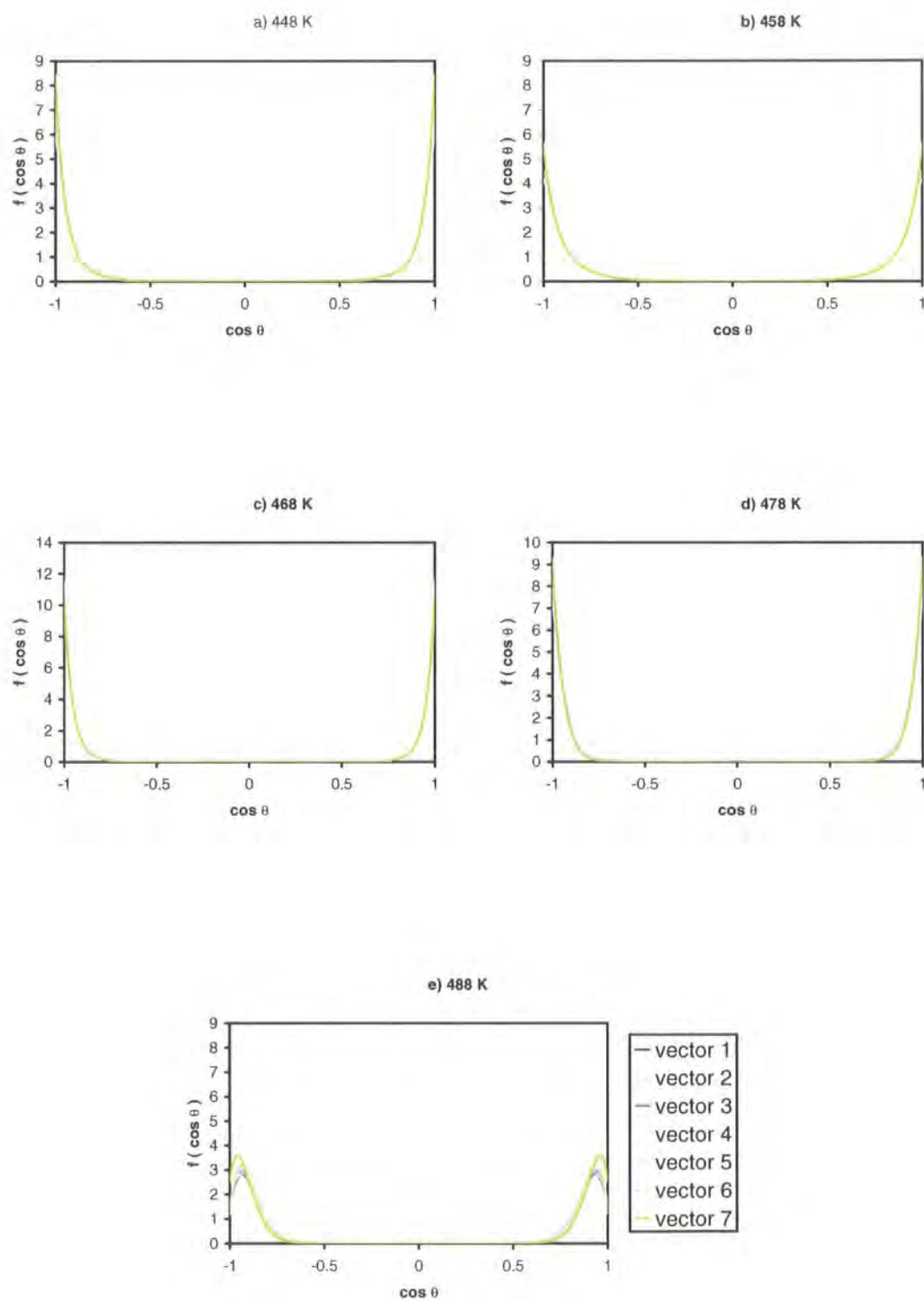
Figure 4.10: $f(\cos\theta)$ calculated for the long axis of ODBP-Ph-C_7 using series of different vector representations.
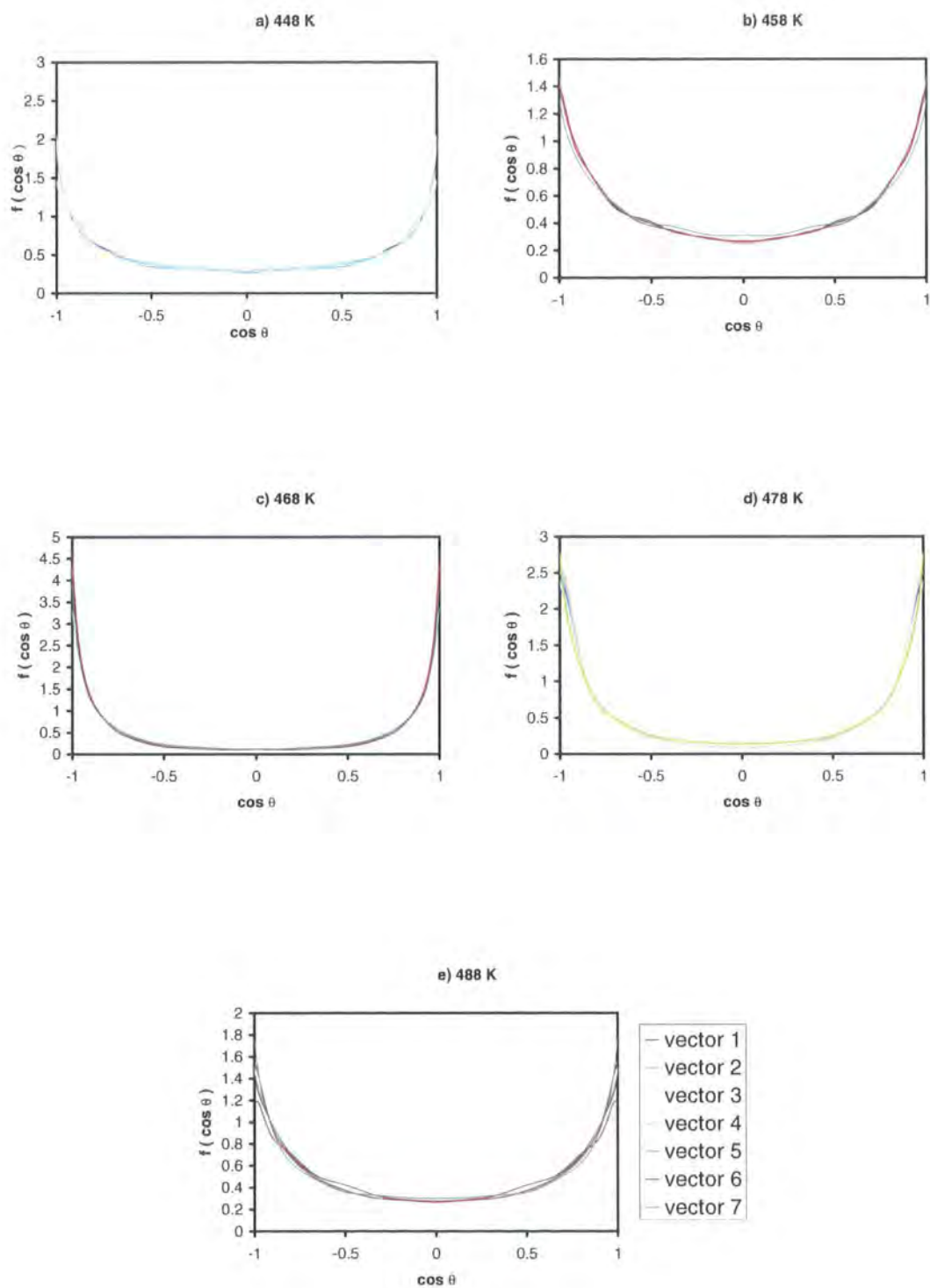
Figure 4.11: $f(\cos\theta)$ for the short axis of ODBP-Ph-C$_7$ using a series of different vector representations.
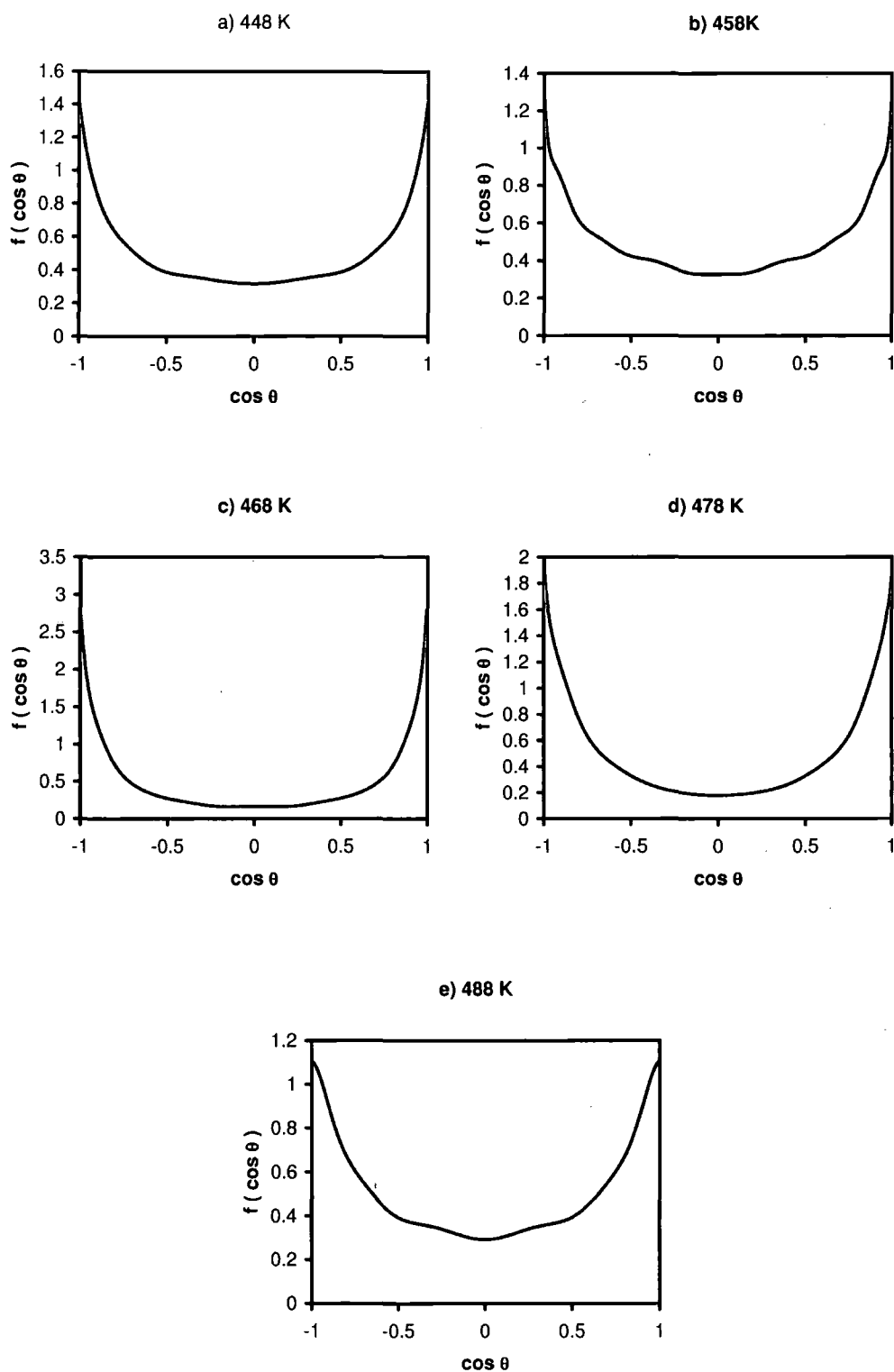
Figure 4.12: Orientational distribution function of the molecular dipole with respect to the short molecular axis director calculated at five different temperatures: a) 448 K, b) 458 K, c) 468 K, d) 478 K and e) 488 K.
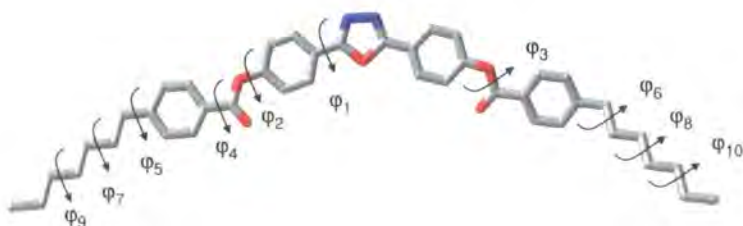
Figure 4.13: Representation of the dihedral angles studied in the molecule ODBP-Ph-C$_7$. Hydrogen atoms have been omitted for clarity. Carbon atoms are shown in grey, nitrogens in blue and oxygens in red.

These results are discussed more fully in relation to the *ab initio* potentials obtained for the dihedral angles in chapter 8.

The results for the dihedral φ_5, corresponding to the torsion about the bond between the first carbon in the aliphatic chain and the second phenyl ring can be seen in figure 4.14. A dihedral angle of 90^0 and 270^0 minimizes steric repulsions, explaining the the form of the graph. Finally, the distributions for the rest of the dihedral angles φ_6, φ_7, φ_8, φ_9 and φ_{10} along the aliphatic chain shown in figure 4.17 correspond to what has been observed in several different simulations for the same type of hydrocarbon chains. It is noteworthy that an odd-even effect can be appreciated in the dihedral angles φ_6, φ_7 and φ_8 of the aliphatic chain. In the even numbered dihedral angles the distribution of the *trans* conformation is more populated than in the odd-numbered ones. This effect is typical of nematic phases, and is caused by the tendency of the aliphatic chain to remain linear in a nematic environment. An alternative *trans-gauche-trans* conformation in the angles φ_6, φ_7 and φ_8, makes the chain linear, thus the *gauche* conformations are more favoured in the odd angles than in the even ones. This effect has been widely described in literature [118–122], and will be also studied in chapter 6.

To determine the influence of the local environment on the dihedral angle distributions and check for coupling between internal molecular structure and molecular order, the torsional energy for each one of the dihedral angles at three different
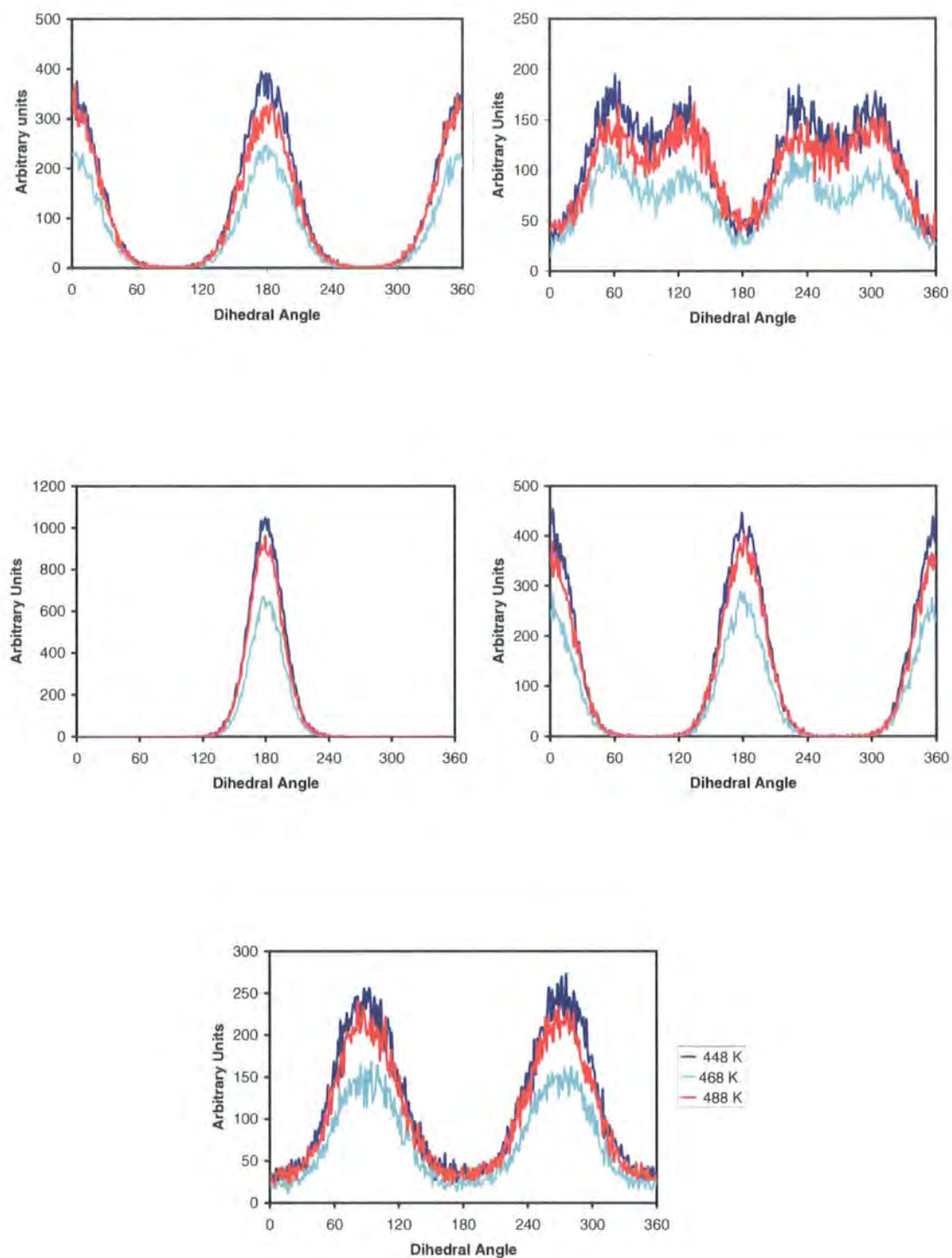
Figure 4.14: Distribution of the dihedral angles φ_1 (top left), φ_2 (top right), φ_3 (middle left), φ_4 (middle right) and φ_5 (bottom) at three different temperatures: 448 K (navy blue), 468 K (turquoise) and 488 K (red).
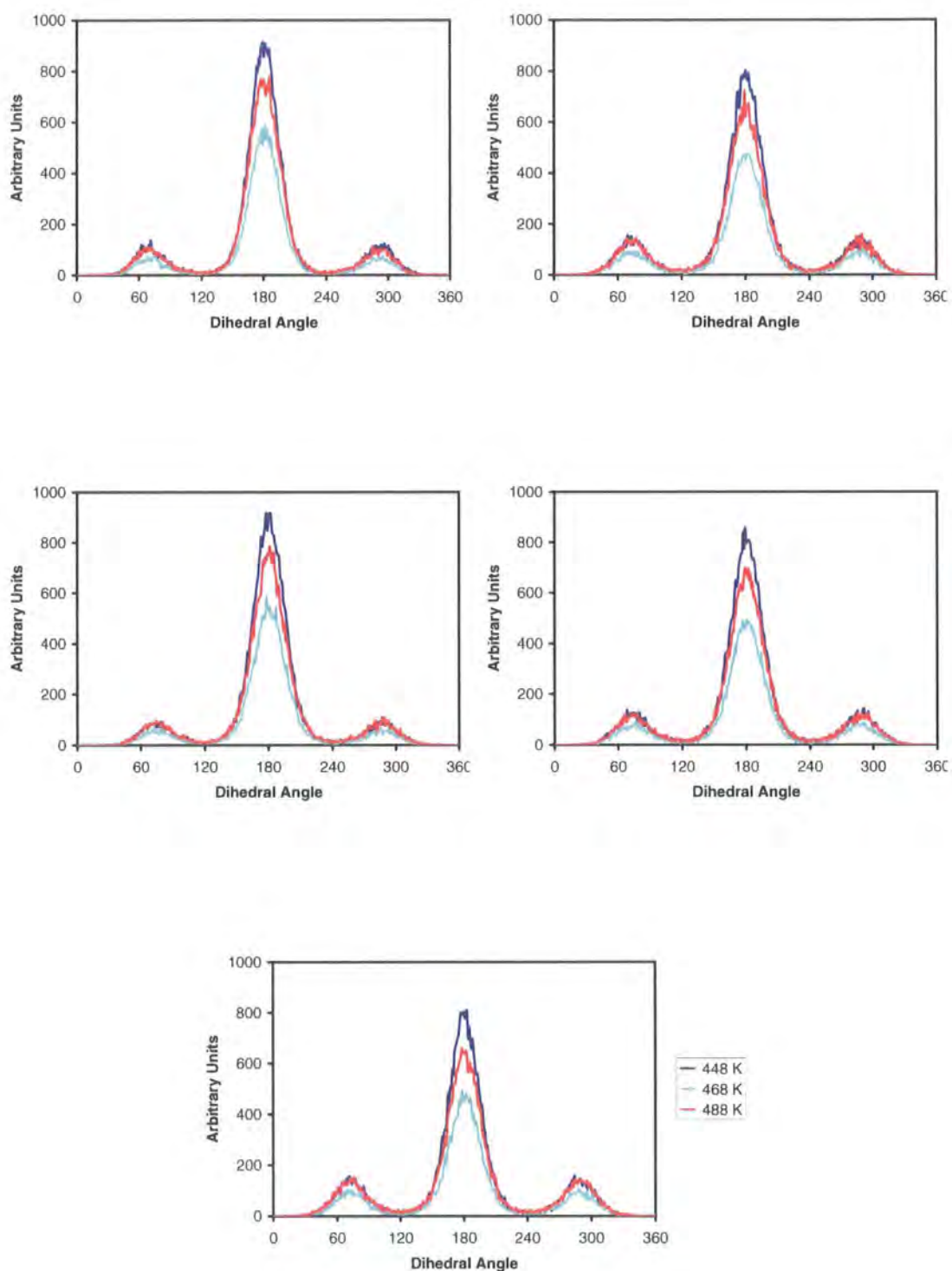
Figure 4.15: Distribution of the dihedral angles φ_6 (top left), φ_7 (top right), φ_8 (bottom left), φ_9 (bottom right) and φ_{10} (bottom) at three different temperatures: 448 K (navy blue), 468 K (turquoise) and 488 K (red).
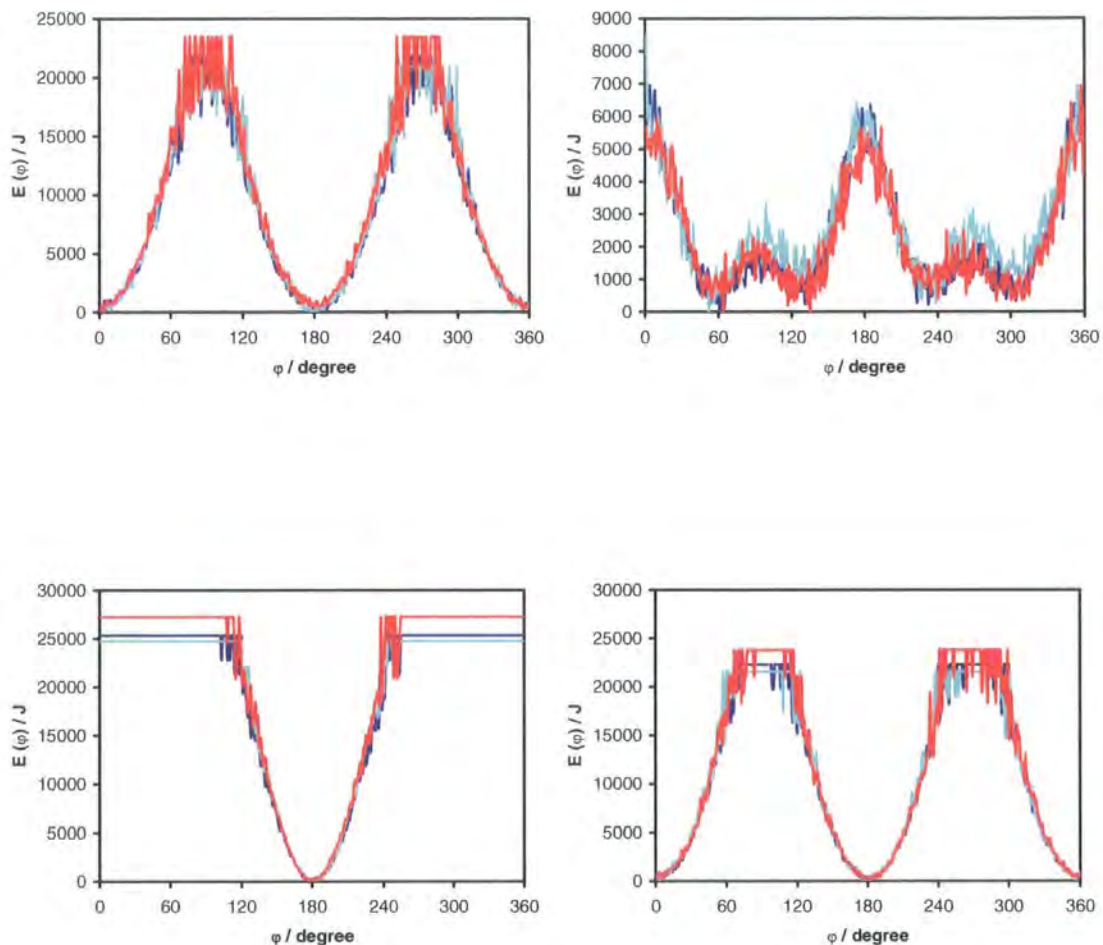
(a)
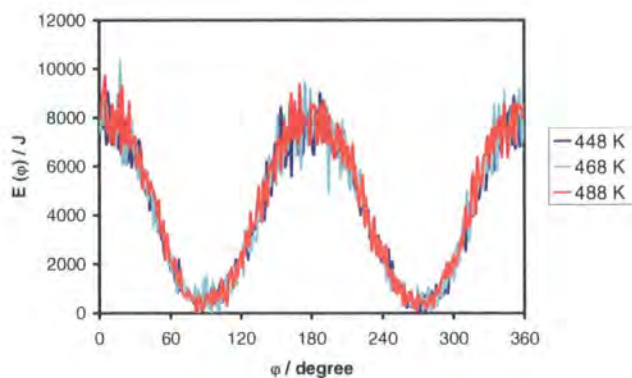
Figure 4.16: Distribution of the torsional free energy for the dihedral angles φ_1 (top left), φ_2 (top right), φ_3 (middle left), φ_4 (middle right) and φ_5 (bottom) at three different temperatures: 448 K (navy blue), 468 K (turquoise) and 488 K (red).
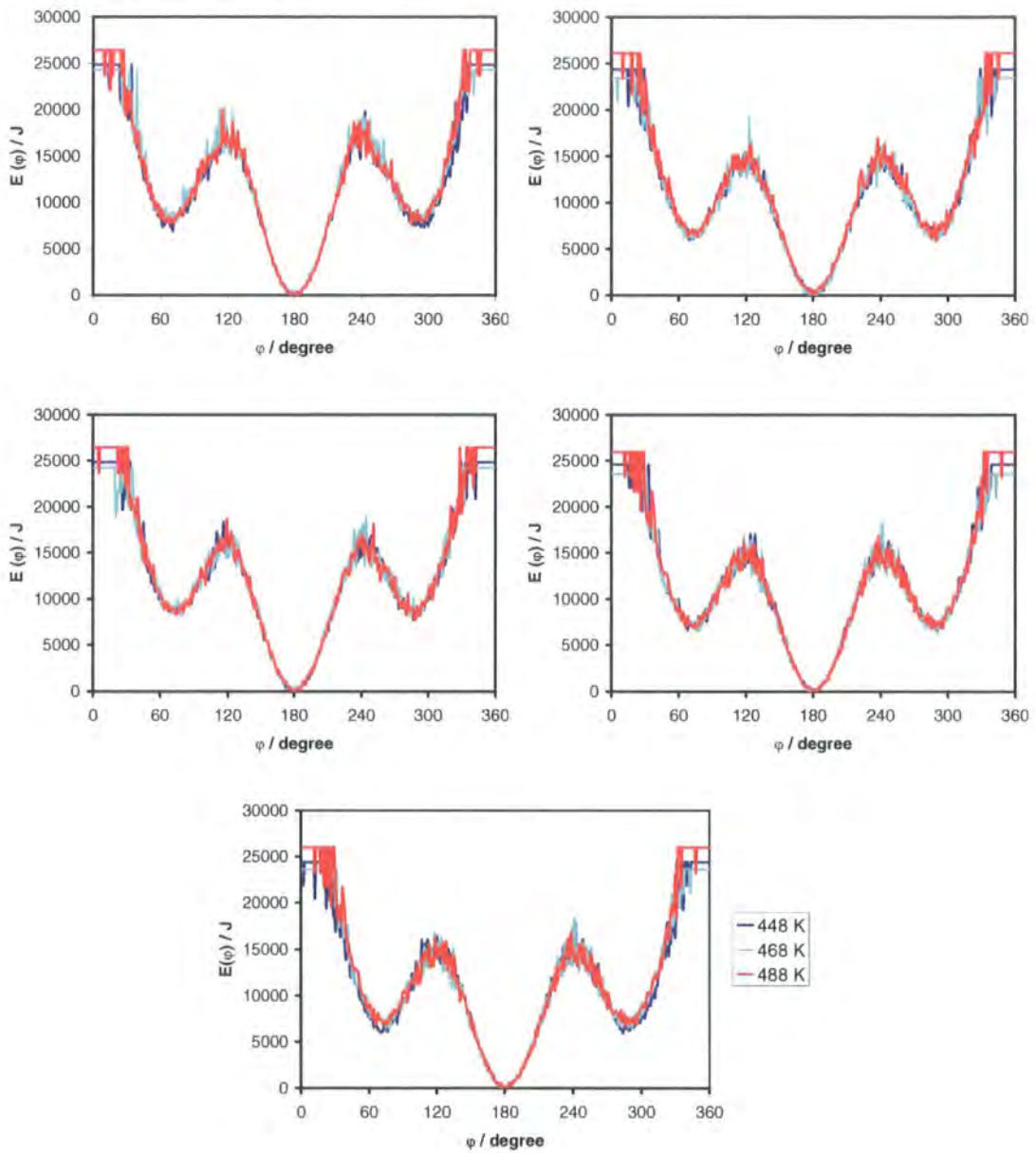
Figure 4.17: Distribution of the torsional free energy for the dihedral angles φ_6 (top left), φ_7 (top right), φ_8 (middle left), φ_9 (middle right) and φ_{10} (bottom) at three different temperatures: 448 K (navy blue), 468 K (turquoise) and 488 K (red).

temperatures was calculated using a Boltzmann inversion.

$$V(\varphi) = -RT \ln S(\varphi) + C, \tag{4.1}$$

where C is a constant and $V(\varphi)$ is the effective torsional free energy and $S(\varphi)$ is the dihedral angle distribution.

The results for the torsional angles located in the aromatic core are exhibited in figure 4.16, while those belonging to the aliphatic chain are shown in figure 4.17. It is possible to appreciate that the effective torsional free energy does not show any dependence with temperature over the range studied.

4.2.3   Orientational Correlation Factor $g_2(r)$

The orientational correlation functions provide information about the local and global order of the molecules within a system, as described in section 2.6.3. $g_2(r)$ has been calculated for distances corresponding to the separation between the geometrical centre of the oxadiazole rings in each molecule. In figures 4.18 and 4.19, $g_2(r)$ has been calculated using the electric and steric dipoles respectively for the different temperatures shown. It is possible to appreciate that despite the large local orientational order, this does not decay to zero in the nematic phase but to the square of the order parameter, as expected.

A common feature for each temperature is the existence of two principal peaks. The first one is produced at an intermolecular distance of approximately 3.5 Å and represents the strong orientational order existing between two neighbouring molecules. A second peak can be spotted, which is smaller than the first at a intermolecular distance of 6.8 - 7.0 Å, approximately equivalent to the space occupied by three molecules. Therefore, a high order is not only confined to neigbouring molecules but is extended to groups of around five molecules.

In the case of the $g_2(r)$ calculated using the electric dipole moment (fig. 4.18), the first peak is smaller and the second peak disappears, for all the temperatures considered. From this result can be inferred that even though the dipole moment contributes to the onset of molecular ordering along the steric dipole direction, the
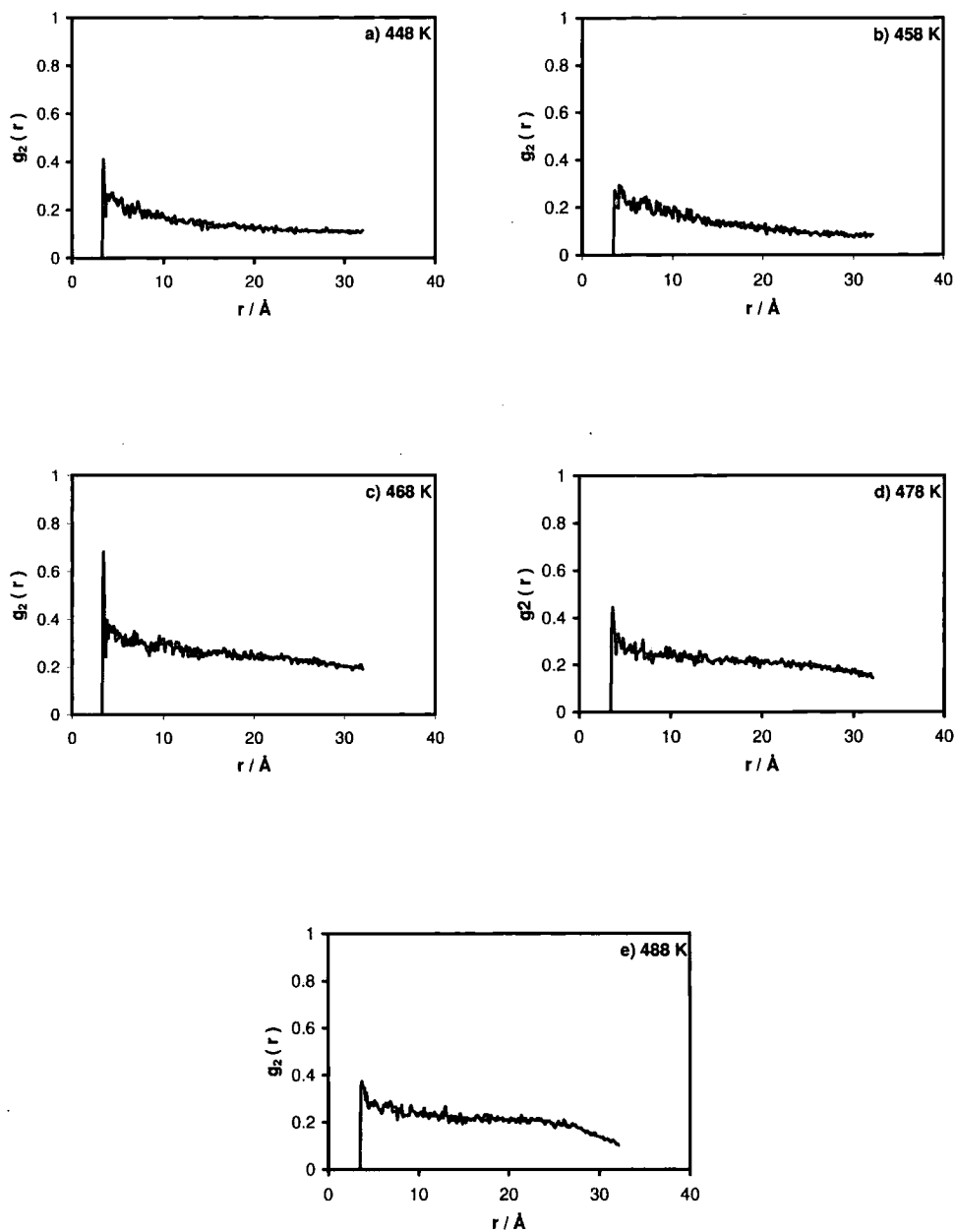
Figure 4.18: Orientational correlation function calculated using the molecular electric dipole moment for five different temperatures: a) 448 K, b) 458 K, c) 468 K, d) 478 K and e) 488 K.
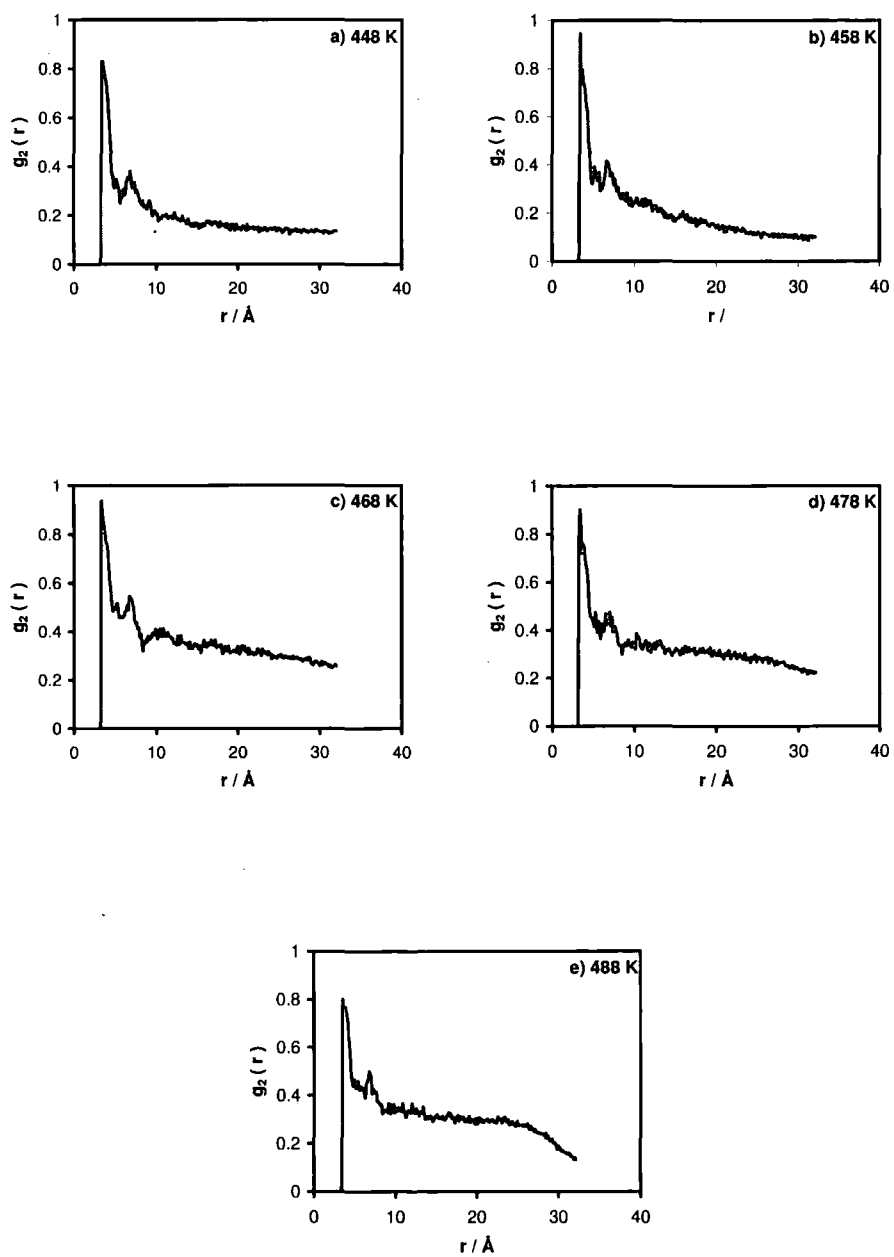
Figure 4.19: Orientational correlation function calculated using the molecular steric dipole for five different temperatures: a) 448 K, b) 458 K, c) 468 K, d) 478 K and e) 488 K.

molecular order at short range is due principally to the steric interaction between molecules, instead of electrostatic ones.

4.2.4   Dipole Correlation Function $g_1(r)$

Calculations of the dipole correlation function, $g_1(r)$, were performed to study the possible onset of ferroelectric or antiferroelectric domains within the system. In order to observe the analogies between the associations between the molecular electric dipoles and the associations between the steric dipoles, the pairwise dipole correlation function was also calculated for the latter. As above the pairwise intermolecular distances, r, are measured as the separation between the geometrical centre of the oxadiazole ring for two molecules. Overall, the values of $g_1(r)$ at short range are higher when calculated with the steric dipole for each temperature. The dipole correlation functions corresponding to the lower temperatures (448 K and 458 K), differ from those corresponding to the higher ones. It can be clearly appreciated in figures 4.20 and 4.21 that there is a sharp, albeit narrow, peak showing an antiparallel association at very short intermolecular distances (approximately 3.7 Å). This peak appears in the dipole correlation functions for both the dipole moment and the short molecular axis at all the temperatures with the exception of 488 K. However, it is likely to represent only a small number of molecular pairs corresponding to the simulations where two anti-parallel cores can approach closer than two parallel cores. It is obvious from figures 4.20 and 4.21 that the shape of the pairwise dipole correlation functions is not uniform throughout the temperature range. Two different groups could be established: one corresponding to the two lowest temperatures and one corresponding to the higher temperatures.

The $g_1(r)$ curves for the first group exhibit a preferred local parallel correlation which is stronger for the steric dipole. The intermolecular distances involved in range from 3.8 Å to 11.8 Å, covering a range of 8 Å. This result suggests the hypothesis of the existence of small ferroelectric domains scattered through the system as a whole. Beyond 11.8 Å a decay in the correlation function occurs for both the dipole moment and the short molecular axis. Eventually, for distances larger than 15 Å, the parallel correlation may be considered as zero.
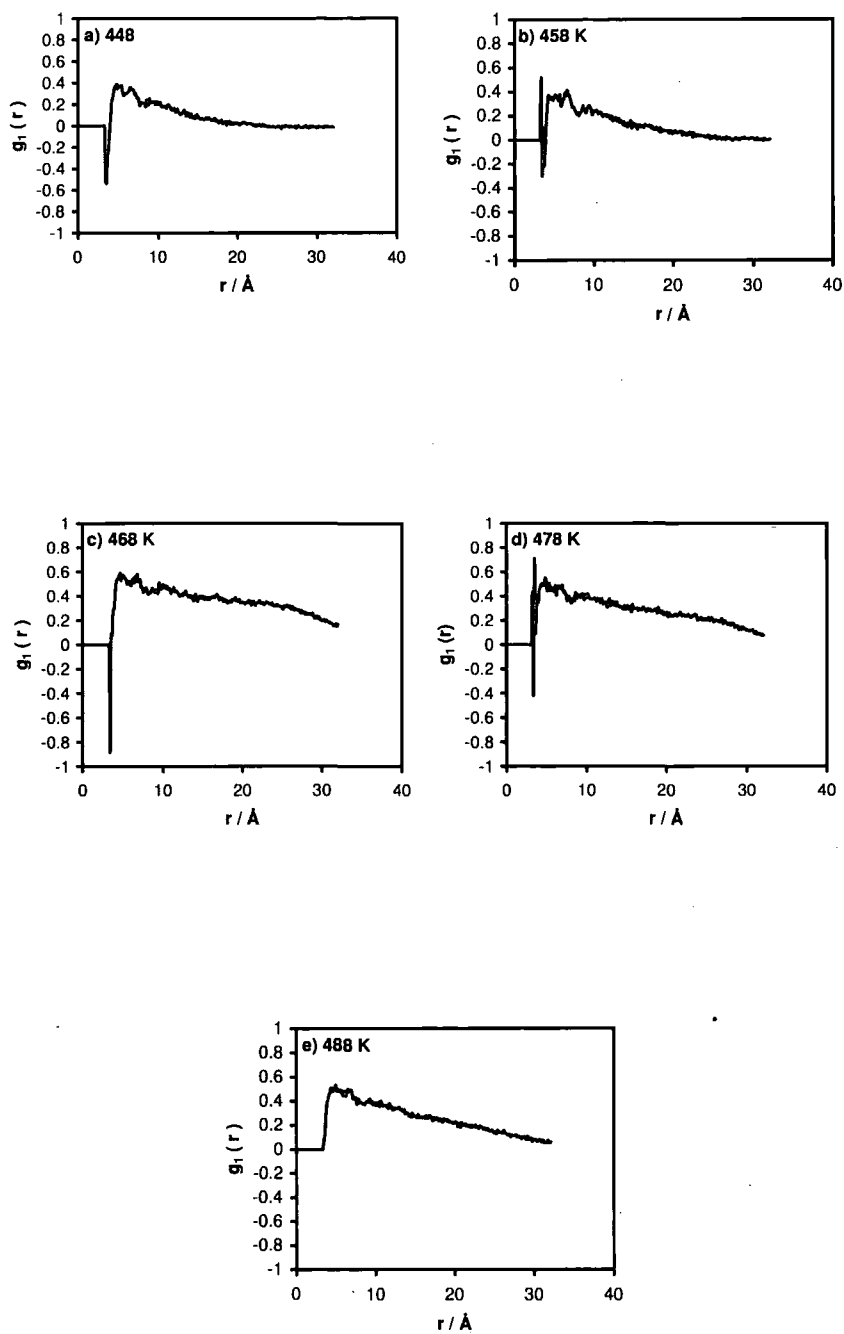
Figure 4.20: Pairwise dipole correlation factor calculated with the dipole axis for five different temperatures: 448 K, 458 K, 468 K, 478 K and 488 K.
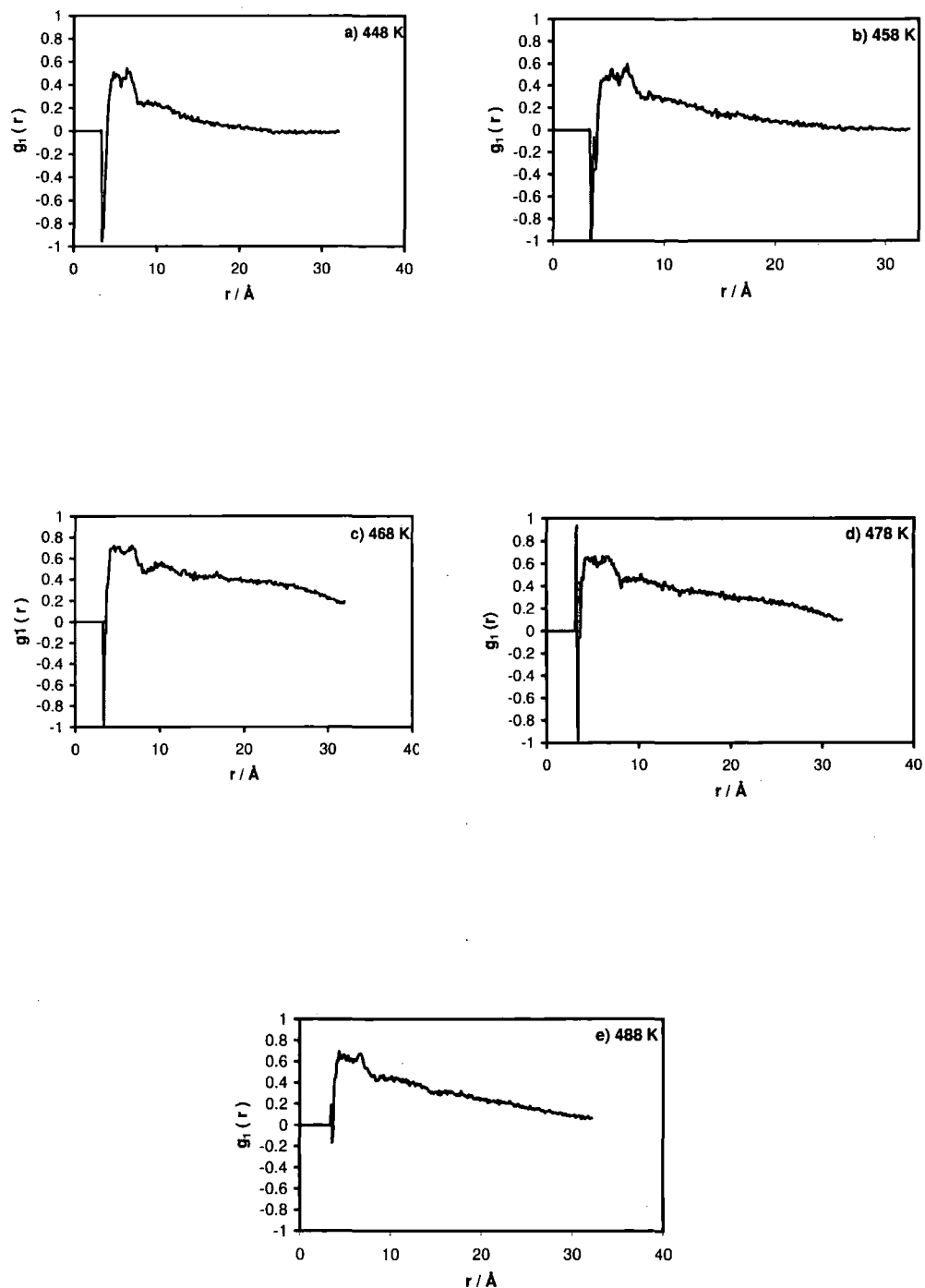
Figure 4.21: Pairwise dipole correlation $g_1(r)$ calculated with the steric dipole of the molecule for five different temperatures.

For the second group local parallel association is substantially stronger, especially in the case of the steric dipole and for the 468 K and 478 K simulations, $g_1(r)$ does not decay completely to zero, as it did for the the 448 K and 458 K simulations. $g_1(r)$ adopts a value of 0.17 Å for the largest intermolecular distance. This signifies the existence of a parallel correlation throughout the whole system, which implies that a single ferroelectric monodomain is either formed or in the process of forming.

The dipole correlation function obtained at 488 K is, to a considerable extent, similar to the ones obtained for 468 K and 478 K. Although the strength of parallel association is smaller initially, the decay of the correlation function is similar to the case run at 478 K. In the latter the correlation function adopts values below 0.1 for intermolecular distances larger than 31 Å, whereas in the former this occurs for slightly shorter distances of about 28 Å.

Aside from the parallel distribution functions, color coded snapshots of the simulation have been produced to illustrate the existence of ferroelectric domains in the systems (figure 4.3). It has been mentioned above that the color coding of the snapshots represent the orientation of the steric dipole moment. The calculation of the orientational distribution function showed that this was parallel to the electric dipole moment (see figure 4.12). These snapshots corroborate the results given by the $g_1(r)$ and the $g_{\parallel}(r)$. It is possible to notice that for the simulations run at 448 K no large ferroelectric domains can be appreciated, although small clusters involving three of four molecules are scattered throughout the simulation box. The ferroelectric domains begin to form at 458 K and merge into a single domain at 468 K. At 478 K and 488 K one of the domains still remains larger than the other. This could be indicative of a future mergence of the two existing domains into a single one. The appearance of single domains seems to be associated with the onset of the biaxial phase, since those systems in which larger monodomains can be observed have larger biaxial parameters. For the lower temperatures the relative sluggishness of molecular motion means that it will take much longer for ferroelectric domains to merge. The boundary region between domains is relatively disordered and the presence of many boundaries has a detrimental effect on both Q_{00}^2 and Q_{22}^2.

4.3 Simulation with the Charges off

4.3.1 Simulation Details

As mentioned in 4.1, further simulations with electrostatic interactions switched off were set up with the aim of studying the role electrostatic interactions play in the onset of the biaxial nematic phase. The force field used in this case was exactly the same as the one described in 4.2.1, with the single exception of not including electrostatic terms.

This simulation started with the compression of an idealized cubic lattice as described in section 4.2.1. The lattice was compressed until the density was approximately equal to that of a liquid crystal phase, using the same conditions as described in section 4.2.1. Once liquid phase densities were achieved, new simulations were started at 468 K and 1 atmosphere, continuing until the system was equilibrated.

4.3.2 Structure

Density

The density for the simulated system is shown in figure 4.22. The density converges fairly rapidly over the first 4 ns of the simulation. The average density of 1.048 ± 0.004 g cm^{-3} calculated over the final 5 ns of the run is slightly smaller than that for the charged system at the same temperature, but only by a factor of 1.3 %. We would expect removal of electrostatics to reduce the overall attractive energy of the system and the density to decrease slightly but the small change we see is accounted for by the fact that the electrostatic interactions only make a small contribution to the overall interaction energy of the system.

Orientation Correlation Function and the Absence of Domains

The radial distribution function parallel to the uniaxial director vector shows no structural order in the present simulation. Therefore, the superstructures seen in the previous section are absent here. In contrast, a practically flat line is seen in
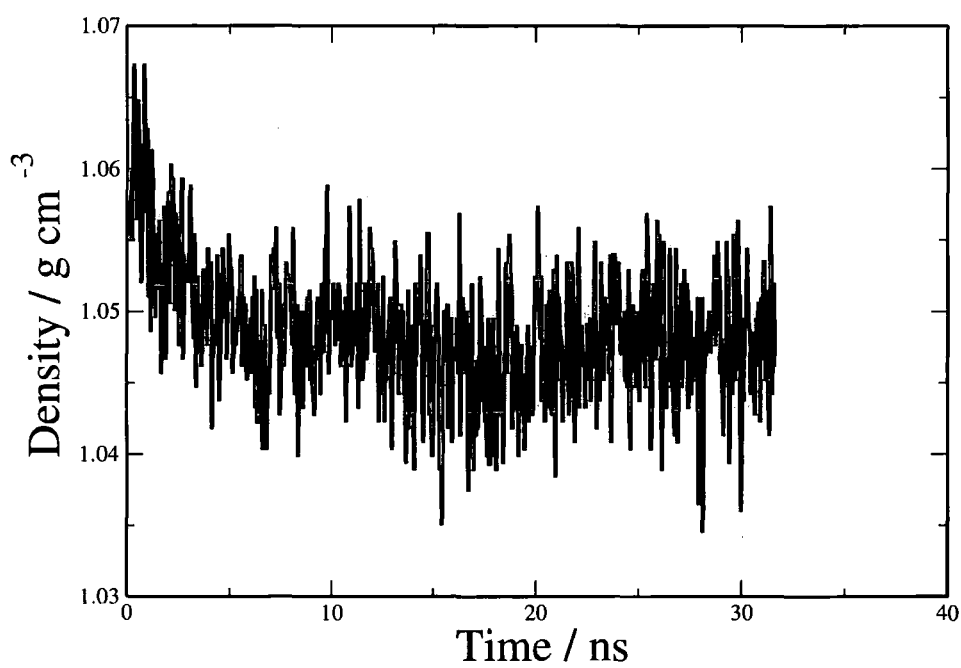
Figure 4.22: Evolution of the system density with respect to time for a system of ODBP-Ph-C_7 molecules without charges at 468 K.

figure 4.23. This is characteristic of nematic phases. Therefore, steric dipoles alone do not suffice to produce ferroelectric domains. The latter has a electric origin rather than a steric one. A visual examination of the snapshot shown in figure 4.23 provides further evidence for this. Ferroelectric order appears only to exist between nearest neighbours and next nearest neighbours.
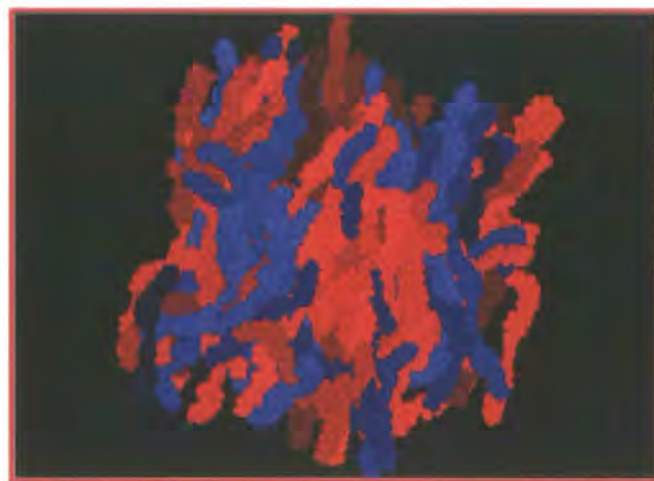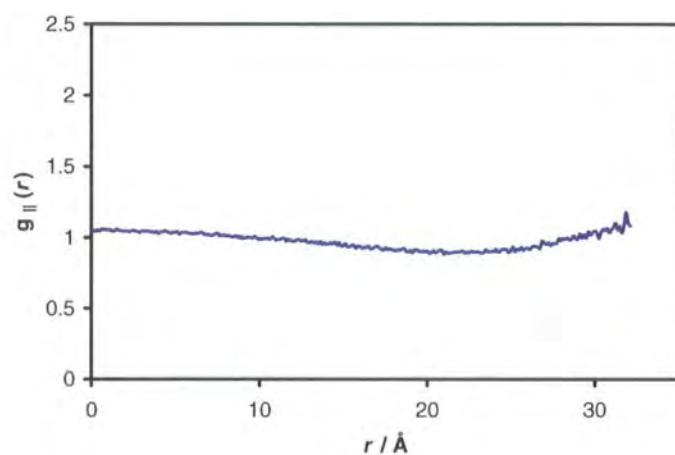
Figure 4.23: $g_{\parallel}(r)$ (top) and snapshot of the simulation run without partial charges. Snapshot of the simulation run without partial electric charges (bottom). The color coding responds to the molecular steric dipole.

Pairwise Dipole Correlation Function $g_1(r)$

For this system there is no electric dipole but $g_1(r)$ will still pick up local ordering of the anisotropic molecular cores. Therefore, it is possible to calculate $g_1(r)$ for the steric dipole of the molecule. In this manner is possible to determine which of the two types of interactions, electrostatic or the steric, play a crucial role in the formation of the domains described above (section 4.2.4). After the removal of the electrostatics, the short range parallel correlation starts at slightly closer distances than in the case of the simulation at the same temperature with the charges on (see figure 4.24). However, it decreases more dramatically, and eventually disappears at an intermolecular distance of approximately 12 Å.

This represents strong evidence for the responsibility of the molecular dipole moment in the formation of the ferroelectric domains. Furthermore, it also proves that the steric interactions between the hard cores of the molecules has a synergistic effect in promoting parallel order at very short range, but nevertheless has no effect in promoting parallel correlation at larger distances. At first sight this is a surprising result. We would normally expect long range ferroelectric interactions to be unfavorable. However, the key to understanding the behaviour explained above is the charge distribution in the core of the molecule. In ODBP-Ph-C$_7$ it seems likely that the strong quadrupole in the oxadiazole forwards strongly the formation of ferroelectric domains in which molecules are locally stacked with a slight offset. This type of "π-stacking" is common in aromatic systems and very well explains the results seen here.

4.3.3   Order Parameters

The uniaxial and biaxial order parameter results for the uncharged system are plotted in figure 4.25. Interestingly, Q_{00}^2 for the molecular long axis initially decays more slowly when the electrostatics are removed from the potential. This can be clearly appreciated by comparing figure 4.25, where Q_{00}^2 for the long axis are represented, with the equivalent figures for the same temperature shown in section 4.2.2 (figures 4.4 and 4.5). The final values for the Q_{00}^2 along the longitudinal axis are
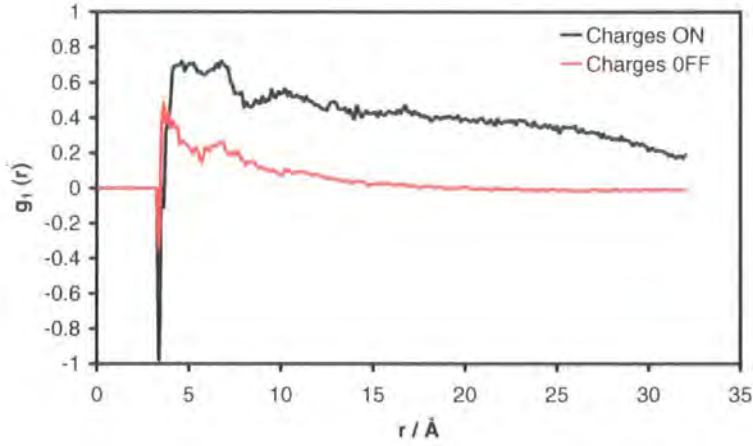
Figure 4.24: Pairwise dipole correlation function for the steric dipole for simulations at 468 K.

0.73 ± 0.02 and 0.70 ± 0.02, calculated with the inertia axes and the molecular vectors respectively.

η_x (I. A.)	η_y(I. A.)	η_z(I. A.)	η_{arm}(A.A.)	η_x(V.A.)	η_y(V.A.)	η_z(V.A.)
0.3 ± 0.1	0.3 ± 0.1	0.05 ± 0.02	0.07 ± 0.02	0.3 ± 0.1	0.3 ± 0.1	0.05 ± 0.02

Table 4.10: Biaxial parameters η calculated with the inertia axes (I.A.), arm axis (A.A.) and vectorial axes (V.A., as explained in table 4.8).

Aside from the uniaxial order parameters, the differences in the Q^2_{22} are more dramatic. With electrostatics Q^2_{22} grew from around the 15th ns of the simulation, but without electrostatics no such growth in Q^2_{22} occurs. Thus it is possible to conclude that the removal of the electrostatic interactions hinders the onset of the biaxial nematic phase.

The results for the biaxial phase parameters, η, obtained using the formula given by Bates and Luckhurst are summarized in table 4.10.
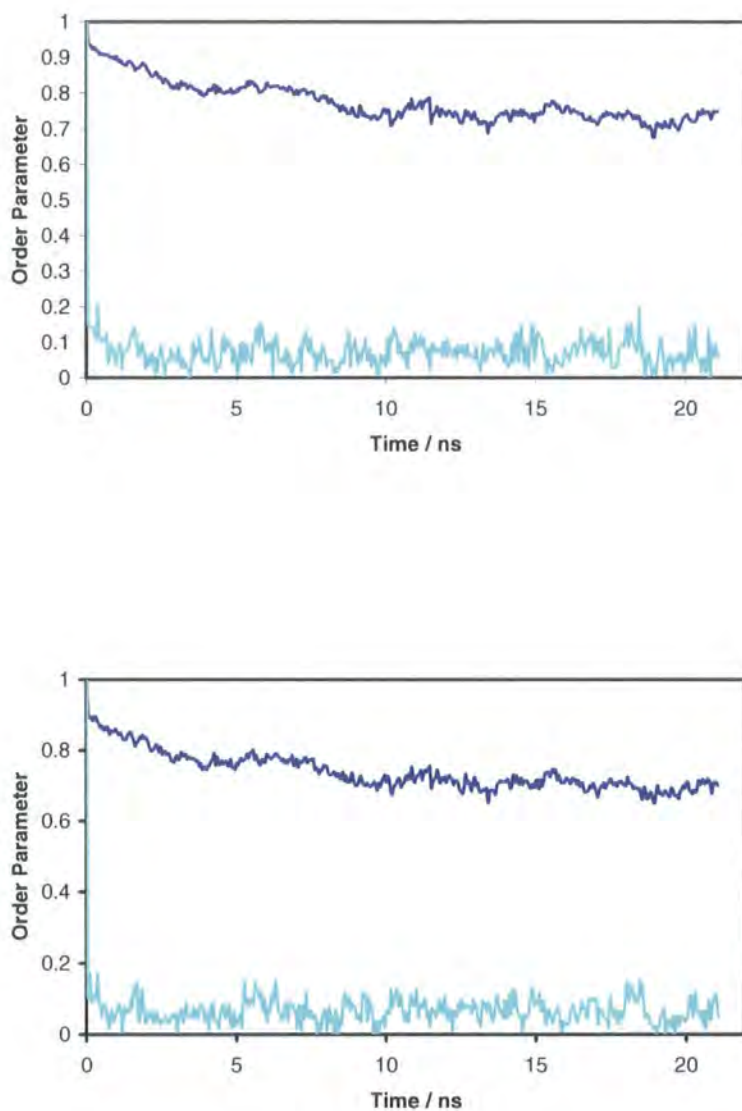
Figure 4.25: Q_{00}^2 along the longitudinal molecular axis (navy blue) and Q_{22}^2 (turquoise) calculated with the molecular axes of inertia (top) and the molecular axes calculated geometrically (bottom) for the simulation with the charges off at 468 K.
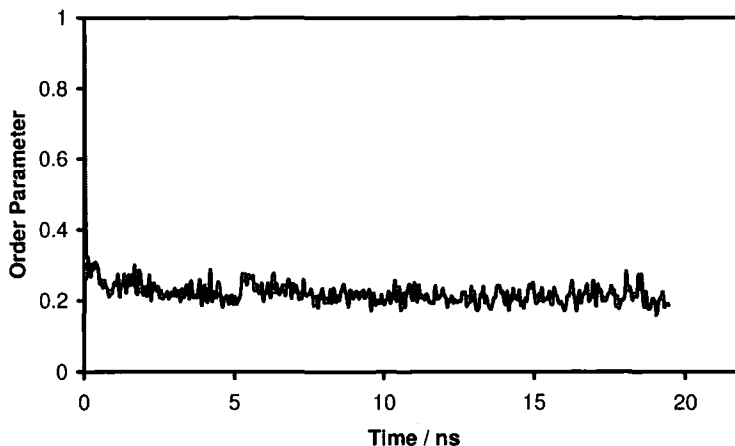
Figure 4.26: Uniaxial order for the steric dipole for the simulation run with the charges off at 468 K.

Uniaxial Order Parameters and $g_2(r)$ for the Steric Dipoles

The Q_{00}^2 along the steric dipole for the charges of the system has a value of 0.21 ± 0.02 at 468 K. It is interesting to notice that this value for the transverse molecular axis value is very similar to the ones for the systems simulated with the electrostatic interactions contributions at the temperatures of 448 K, 458 K and 488 K, although is just half of the ones found in the systems run with charges at 468 K and 478 K.

Despite the disappearance of the ferroelectric domains, a certain degree of long range order along the steric dipole direction remains in the system. This is shown also in the $g_2(r)$ of figure 4.27. This is expected for relatively small system sizes and occurs even in the simulation of systems were we expect no phase biaxiality. It is worth stressing that high local order is restricted to neighbouring molecules, and no second peak denoting high order between next nearest neighbours can be appreciated. It is possible to conclude that the second peak corresponding to the order correlation of nearest neighbouring molecules receives a rather important contribution from the quadrupole stacking (π-stacking).

Overall the results in this section are in agreement with previous attempts to simulate a bent-core system without electric dipole moments [91, 97, 101, 123] in so

far as no biaxial phase has been achieved with the electrostatic interactions off. Nevertheless the only liquid crystalline phase seen here has been a uniaxial nematic phase while for similar molecular shapes (i.e., inter-arm angles of 140^0 [91, 97, 101, 123]), different types of liquid crystalline phases have been reported, as mentioned above. Biaxial nematic phases have been predicted for chevron-like molecules using a hard rods models but this are with a very different inter-arm angle (i.e., 107^0) [91,92].
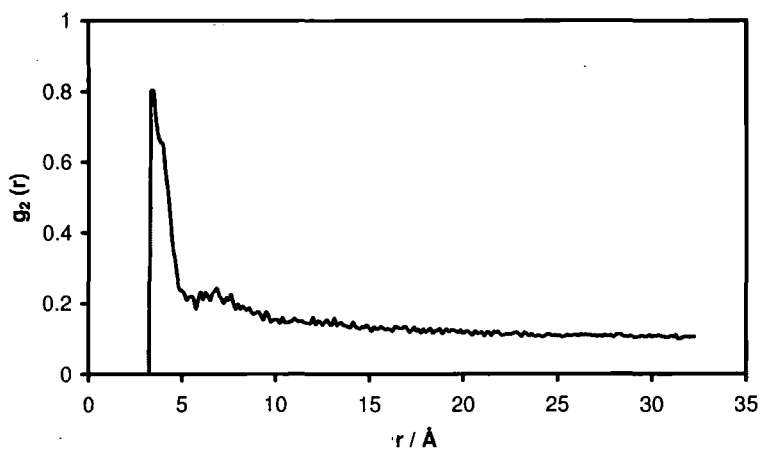
Figure 4.27: Orientational correlation factor $g_2(r)$ for the steric dipole for the simulation with the charges off at 468 K.

4.3.4 Switching on of Atomic Partial Charges

An additional simulation was started from end of the simulations of the previous section after first restoring the partial charges.

An immediate effect was to increase the density of the system, while destabilizing the nematic phase. Results showing these conclusions are plotted in figure 4.28 (a) and (b) respectively. After a period of 20 ns, the system seemed to equilibrate. The density averaged over the last 5 ns of simulation was 1.066 ± 0.004 g cm^{-3}, a value rather similar to 1.062 ± 0.004 obtained in the original 468 K simulation of section 4.2 with the charges on. The $g_\parallel(r)$ shown in figure 4.28 (b) was also averaged over the last 5 ns of simulation. The steps observed for the same temperature in

figure 4.2 show the destabilization of the nematic phase, and suggest the appearance of domains. This point is corroborated by visual analysis of snapshots from the simulation as shown in figure 4.29. The absence of ferroelectric domains after just 5 ns of simulation run can be appreciated in fig. 4.29 (a). After 12.5 ns of simulation the electric dipoles began to orientate parallel to each other forming ferroelectric domains (fig. 4.29 (b)). Eventually, one of the domains is gradually absorbed by the other (fig. 4.29 (c)).

Order Parameters

In figure 4.30 the evolution of Q_{00}^2 and Q_{22}^2 calculated using the same criteria as in figure 4.25 are shown. Despite the large values of Q_{00}^2 (0.93 ± 0.01 and 0.91 ± 0.01 for the inertia tensor and the vectors respectively, averaged over the final 5 ns of the run), the existence of a smectic phase in the system can be disregarded from the results obtained for $g_{\parallel}(r)$ and the snapshots from figure 4.29. Interestingly, the formation of domains approximately coincides in time with a step in Q_{22}^2 produced between the ns 8 and 11. Moreover, the second hump in Q_{22}^2 at around 17 ns coincides with the mergence of the ferroelectric domains. Therefore it seems rather clear that a connexion between ferroelectric domains and Q_{22}^2 exists. The final results for Q_{22}^2 calculated using the inertia tensor and the vectors (see above for Q_{00}^2) and averaged over 5 ns were 0.59 ± 0.03 in both cases. This results are very similar to those shown for the same temperature in table 4.5.

The calculation of $g_1(r)$ (see figure 4.31) was also carried out to corroborate the conclusions discussed above. By comparing these results with those obtained at the same temperature in section 4.2.3 it is possible to appreciate that the situation is rather similar in both cases, i.e., $g_1(r)$ shows long range orientational ferroelectric order.

The results for η calculated using different axes are shown in table 4.11. These results show biaxiality albeit their values are smaller than those shown in figures 4.7 and 4.8 for the same temperature. The calculation of η using the electric dipole and quadrupole yielded results of 0.68 ± 0.07 and 0.45 ± 0.07, which also show a high degree of phase biaxiality although these are smaller than those obtained for
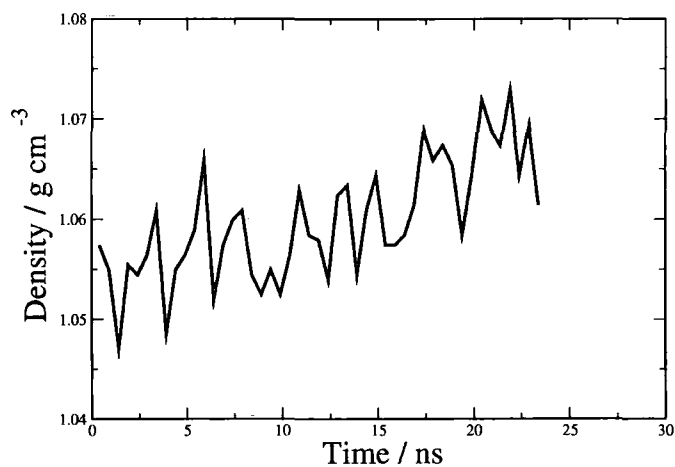
(a)
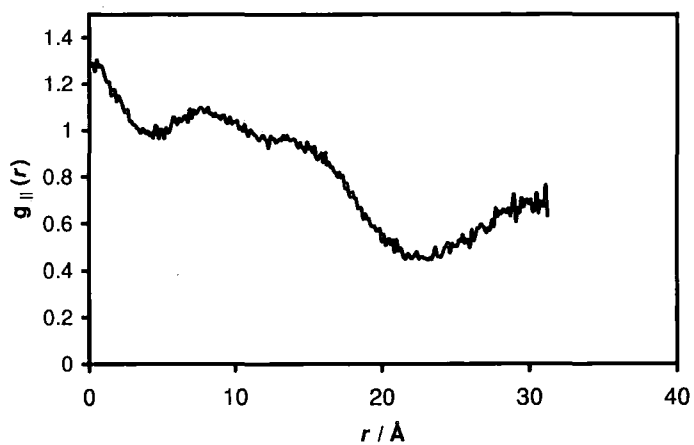
(b)

Figure 4.28: Evolution of the system density after switching on the electrostatic interactions again (a) and $g_{\parallel}(r)$ for this system (b). The steps shown in (b) are produced by the presence of ferroelectric domains in the nematic phase.
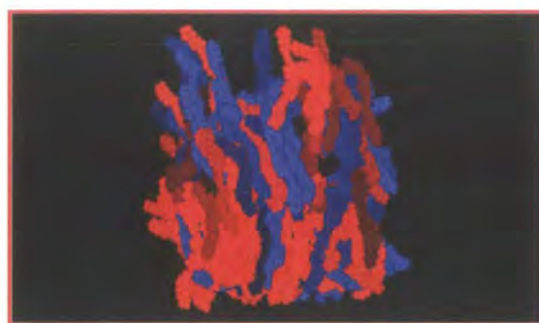
(a)
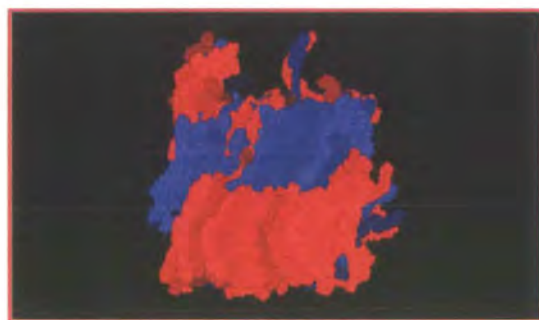
(b)

(c)

Figure 4.29: Snapshots of the simulation run after switching on the partial charges again. The snapshots have been produced after runs of 5 ns (a), 12.5 ns (b) and 25 ns (c).
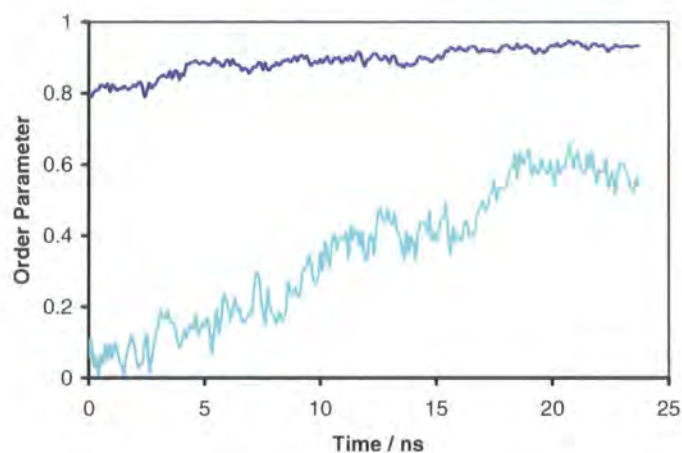
(a)
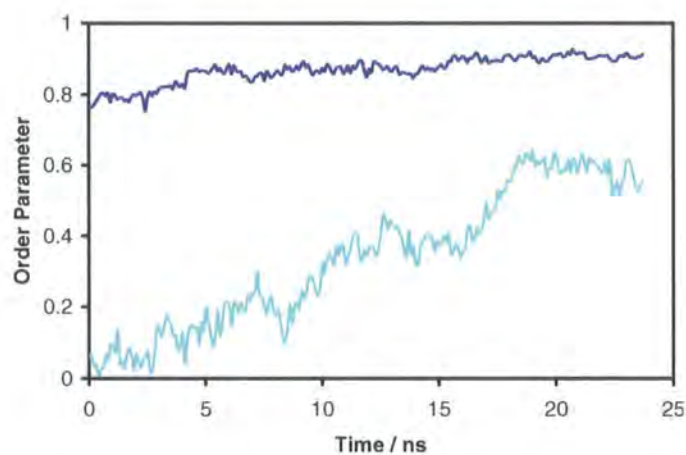
(b)

Figure 4.30: Q_{00}^2 along the longitudinal molecular axis (navy blue) and Q_{22}^2 (turquoise) calculated with the molecular axes of inertia (a) and the molecular axes calculated geometrically (b). It is possible to notice that results in (a) and (b) are rather similar, as found in previous occasions.
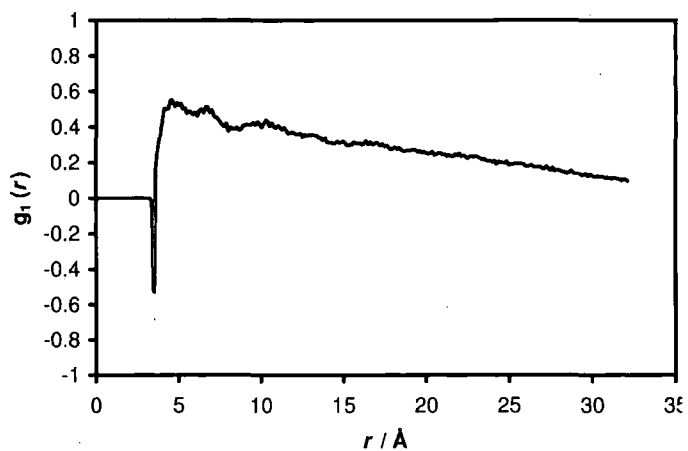
(a)
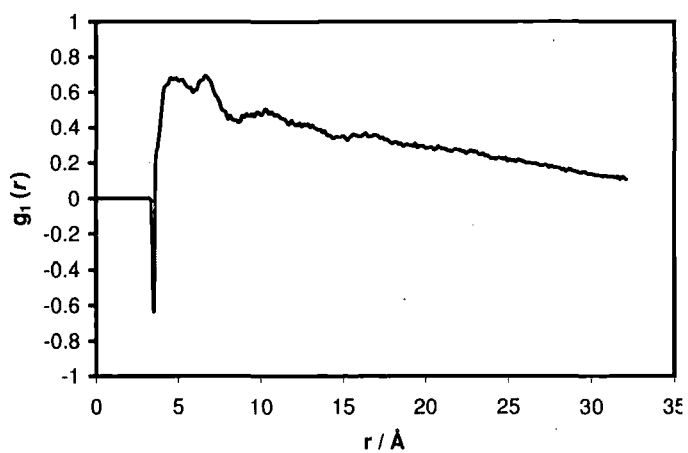
(b)

Figure 4.31: $g_1(r)$ calculated for the simulation with the charges switched on again using the electric dipole (a) and the steric dipole (b).

the same temperature previously (see table 4.9).

η_x (I. A.)	η_y(I. A.)	η_z(I. A.)	η_{arm}(A.A.)	η_x(V.A.)	η_y(V.A.)	η_z(V.A.)
0.39± 0.05	0.39±0.05	0.028±0.007	0.17±0.01	0.04±0.01	0.36±0.05	0.37±0.05

Table 4.11: Biaxial parameters η calculated with the inertia axes (I.A.), arm axis (A.A.) and vectorial axes (V.A., as explained in table 4.8).

4.4   Simulation of a "Grown" Nematic Phase with the Charges off

4.4.1   Simulation Details

The isotropic phase created in section 4.5.1 was used as the initial configuration for a new run, which aimed to explore the influence of the atomic charges in the onset of the biaxial nematic phase. Hence, a new simulation run was performed with the intention of producing a phase transition. The conditions chosen to run this simulations are the same as those used in section 4.3.1 to recreate the nematic phase (468 K, atomic charges off).

Growth of a liquid crystal phase from an isotropic liquid is an ambitious undertaking. Although it has been achieved previously for united atom models [38, 119] it has never been achieved before for an all-atom model.

4.4.2   Structure

Density

The time evolution of the density is shown in figure 4.32. The mean density is unchanging over the final 10 ns of the run. The averaged density of the bulk system for the final 8 ns is 1.049 ±0.004 g cm^{-3}. This is in full agreement with the density found when the ODBP-Ph-C$_7$ was simulated without electrostatic interactions starting from a biaxial phase. In that case the density obtained was 1.048 ± 0.004 g

cm^{-3}. The volume of the simulation box was 267079 ± 960 Å^3, which corresponds to a $64.4 \times 64.4 \times 64.4$ Å^3 cube.
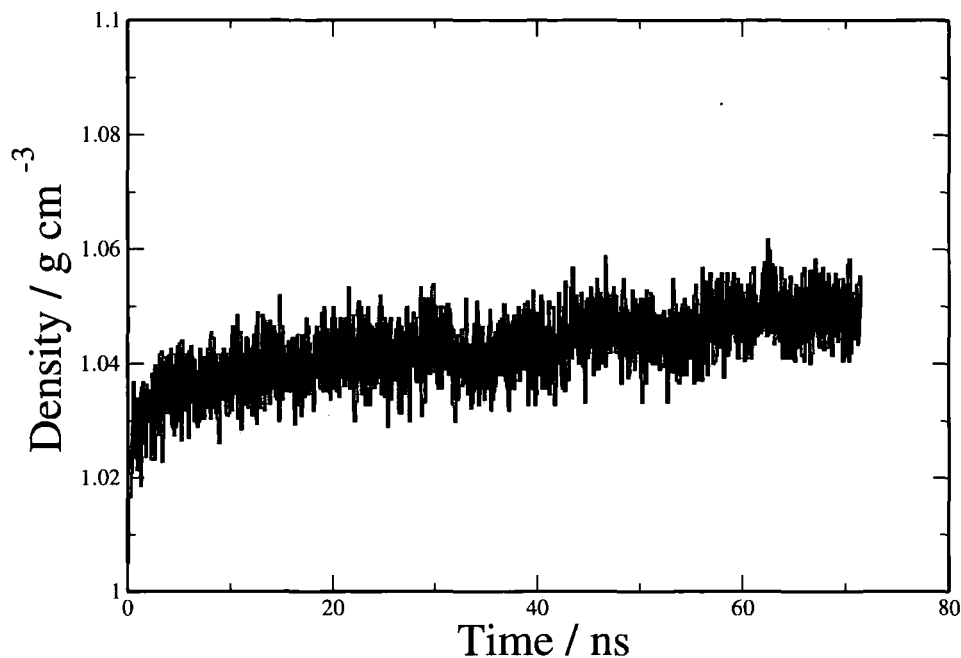
Figure 4.32: Evolution of the density during the isotropic-nematic phase transition with the electrostatic interactions off.

$g_\parallel(r)$ and Domains Formation

Calculations of the radial distribution function parallel to the uniaxial director vector calculated from the direction of the principal axis (calculated from the inertia tensor) have been carried out in the same manner as in previous sections. It is possible to notice a sinusoidal symmetry in $g_\parallel(r)$. This sort of pattern is indicative of the presence of a smectic phase. This is clearly in contrast with what has been observed in the simulation run directly from a biaxial nematic phase with partial charges at the same temperature (see figure 4.2). In that case, the oscillation presented by the $g_\parallel(r)$ was not symmetric. It is possible that while the $g_\parallel(r)$ curve in the 468 K simulation with charges on was indicative of domain formation, the curves seen here indicate genuine smectic layers.

The assumption of the formation of a smectic phase is encouraged by visual inspection of the system. In the snapshot shown in figure 4.33 four different layers can be noticed, albeit two outer ones are formed of few molecules and because of the periodic boundary conditions really belong to the same layer. This snapshot seems to represent a paraelectric non-tilted smectic phase. However, and as previously mentioned, due to the limited system size it is not possible to be sure that this is the case. Typically, from work on single-site potentials, at least a thousand molecules would be required to show convincing proof of smectic phase formation. Nonetheless it is possible to state that, unlike the systems simulated with charges, no ferroelectric domains exist in the present system, although it shows a larger superstructure in two different layers.

The results are not the same as those obtained for the simulation without charges at the same temperature, which was started from a biaxial nematic phase. In that case, the $g_{\parallel}(r)$ shows that the phase is purely nematic without any type of superstructure or domains in it. Therefore the uniaxial nematic phase formed by an hypothetical ODBP-Ph-C_7 with no partial charges in can be considered mechanically metastable at 468 K, although the onset of a possible smectic A phase is appreciated when the system is quenched from the isotropic phase in to the same temperature. Different simulations of isotropic phases quenches into lower temperatures would have provided further evidence on the metastability or the actual stability of the nematic phase and a subsequent transition into a smectic phase. Unfortunately the limitations in computational time have made this task impossible to fulfill, since 139.55 CPU days have been necessary to carry out the growth of the nematic phase without electrostatic charges using 16 processors, and many other simulations have been performed for this thesis, thus the computing time has been limited.

The absence of biaxiality is a common feature in the simulation of banana-shaped models in the absence of molecular electric dipoles and with a similar inter-arm angle. Johnston et al. [101] obtained a twist grain boundary blue phase using a two-sites Gay-Berne potential, with an inter-arm angle of 140^0. Nonetheless, there is an agreement in the absence of biaxial phase due to the steric dipole. By contrast, Memmer [94] predicted a transition between a uniaxial twisted nematic

and a antiferroelctric SmA phase using a model base on two Gay-Berne sites, as explained above. The antiferroelectric smectic A phase was claimed to be biaxial due to the ferroelectricity of the layers, although no Q_{22}^2 was calculated.
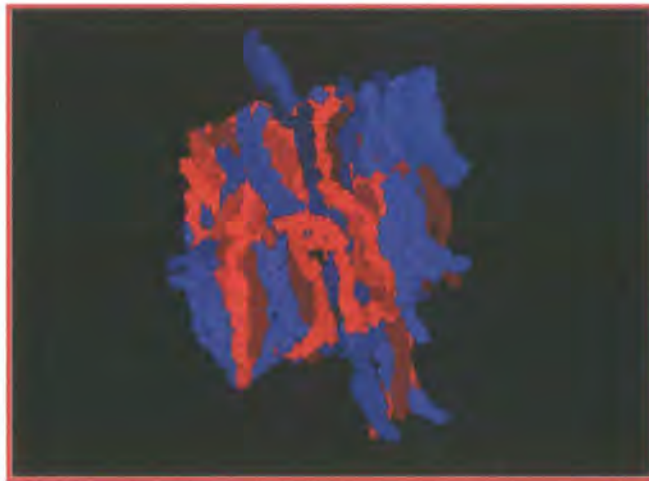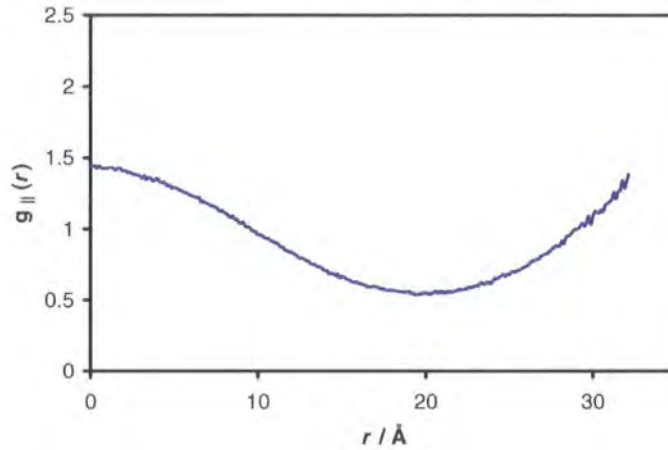
Figure 4.33: $g_\parallel(r)$ (top) and snapshot (bottom) of the quench of an isotropic phase at 468 K without the presence of electric dipoles in the simulation.

Pairwise Dipole Correlation Function $g_1(r)$

$g_1(r)$ was calculated to corroborate the absence of domains in the system. Figure 4.34 shows no evidence for such domains. The results are rather similar to the previous system simulated without charges, which was started directly from a biaxial

phase. A certain degree of parallel correlation at short range can be found (as in figure 4.3.2), but this decays rapidly.
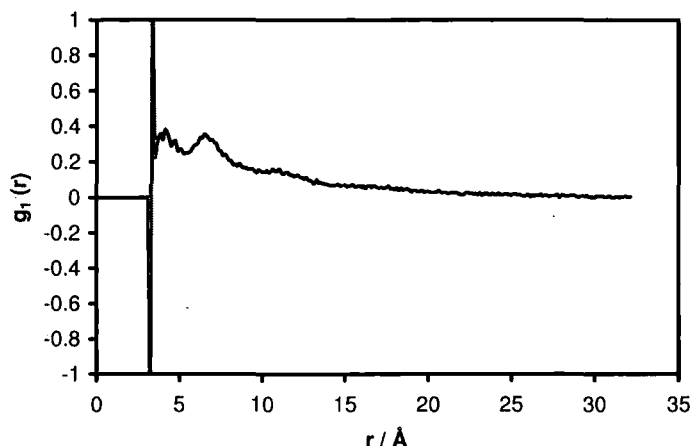
Figure 4.34: Pairwise dipole correlation factor $g_1(r)$ for the short molecular axis calculated geometrically for the quench of an isotropic phase at 468 K without the presence of electric dipoles in the simulation.

4.4.3   Order Parameters

Q_{00}^2 and Q_{22}^2 calculated in the same way as explained in section 4.2.2 were monitored throughout all the simulation. In figure 4.35 it can be seen that there are two major step changes in Q_{00}^2 as a function of time. These occur in the 20th and 55th ns. The rest of the time of simulation the order parameter remains practically constant. In contrast, the mean value of Q_{22}^2 remains constant throughout the simulation. The final results for the Q_{00}^2 and Q_{22}^2 are respectively 0.81± 0.02 and 0.09 ± 0.05 when calculated with the inertia axes and 0.78±0.02 and 0.08±0.04 when calculated with the vectorial axes.

The biaxial phase parameters η calculated using the method implemented by Bates and Luckhurst are consistent with those calculated in section 4.3. The biaxial parameters calculated using different criteria are summarized in table 4.12.
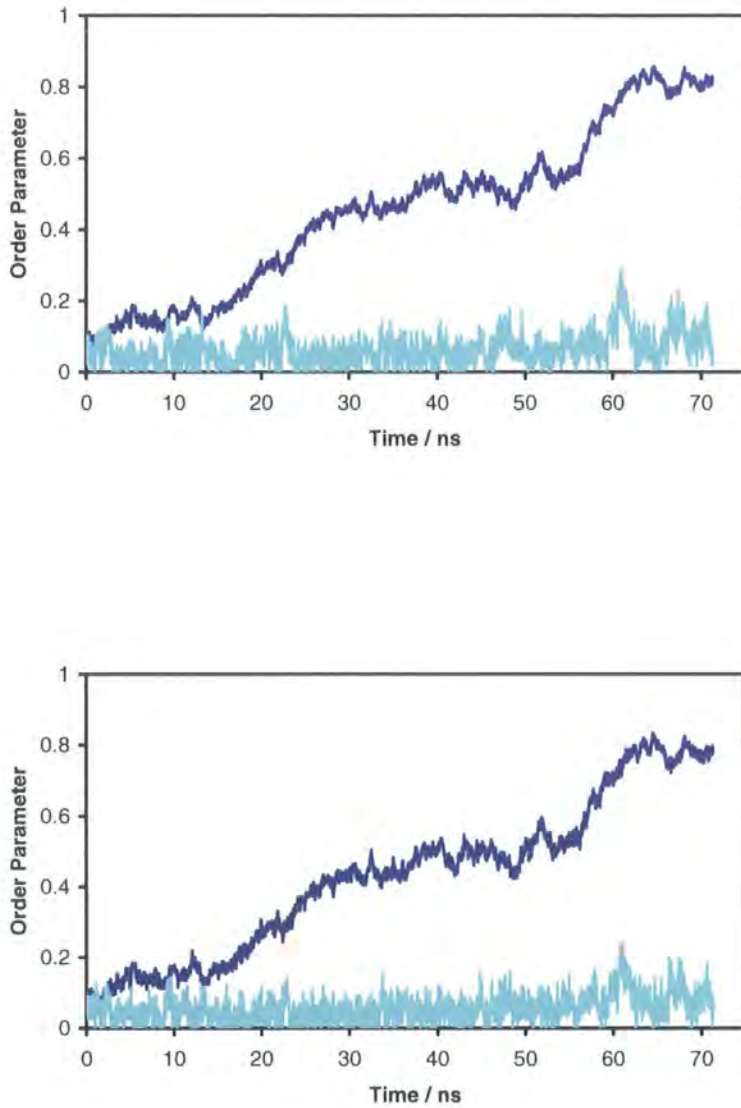
Figure 4.35: Q_{00}^2 along the transverse molecular axis and Q_{22}^2 calculated with the molecular axes of inertia (top) and the molecular axes calculated geometrically (bottom) for the quench of an isotropic phase at 468 K without the presence of electric dipoles in the simulation.

η_x (I. A.)	η_y(I. A.)	η_z(I. A.)	η_{arm}(A.A.)	η_x(V.A.)	η_y(V.A.)	η_z(V.A.)
0.4± 0.2	0.3±0.2	0.04±0.02	0.06±0.03	0.3±0.2	0.3±0.2	0.05±0.02

Table 4.12: Biaxial parameters η calculated with the inertia axes (I.A.), arm axis (A.A.) and vectorial axes (V.A., as explained in table 4.8).

Uniaxial Order Parameters of the Steric dipole and $g_2(r)$

Ordering of the steric dipole grown throughout the simulation (figure 4.36), in response to the slow growth of order for the long axis. The final Q_{00}^2 of 0.26 $\pm$ 0.03 is significantly smaller than the value of 0.53 $\pm$0.05 obtained previously for the simulation started from the biaxial phase at 468 K with the electrostatic charges on.
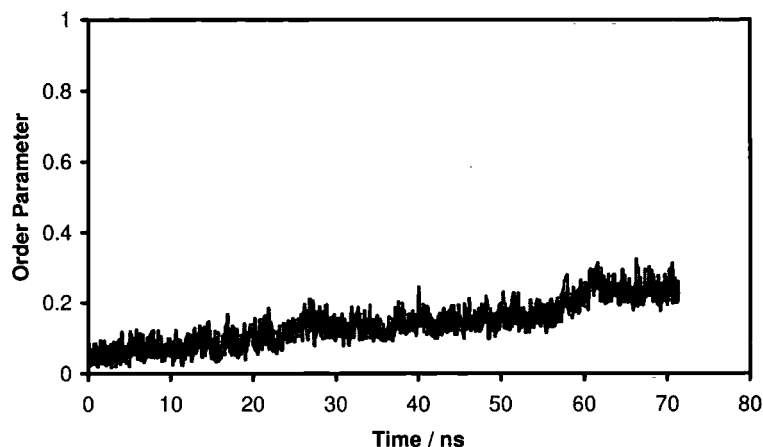
Figure 4.36: Q_{00}^2 for the molecular steric dipole calculated throughout the growth of the nematic phase without partial atomic charges.

$g_2(r)$ obtained in the present simulation is similar to the one obtained in section 4.3.3, for the short molecular axis. It is possible to appreciate that there is a high local orientational order at short range, promoted by the local steric interactions between the molecular cores (fig. 4.37), but that order decays to the square root of the Q_{00}^2 along the steric dipole.

4.5 Simulation of the Grown Nematic Phase

4.5.1 Simulation Details

A further compression run analogous to the one described in 4.2.1 was performed, but at an elevated temperature of 500 K. The product of this compression run was
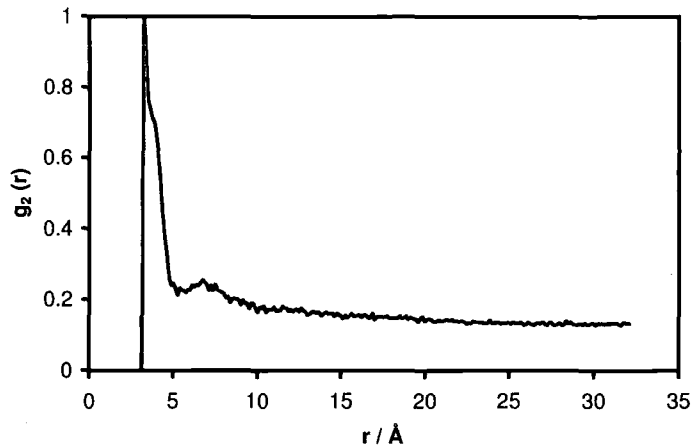
Figure 4.37: Orientational correlation factor $g_2(r)$ for the short molecular axis calculated geometrically.

an isotropic liquid phase, instead of a nematic one. The motivation for this run it to produce an isotropic phase which could be quenched into a biaxial nematic one. After liquid density was obtained the Berendsen thermostat-barostat was substituted by a Nosé-Hoover one with the same relaxation times of 1.0 ps and 4.0 ps respectively, and temperature and pressure were modified to 468 K and 1 atmosphere respectively. At the start of the equilibration run all the order parameters had a negligible initial value ($\langle 0.08 \rangle$).

4.5.2 Structure

Density

Simulations were carried out over approximately 100 ns. The evolution of the system density is shown in figure 6.8. The density calculated during the last 5 ns of simulation run was 1.064 ± 0.004 g cm^{-3} , and the system volume was 263189 ± 1065 Å^3. The final density compares well to that of the corresponding simulation, which was started directly from the biaxial phase (1.062 ± 0.004), within the range of errors.
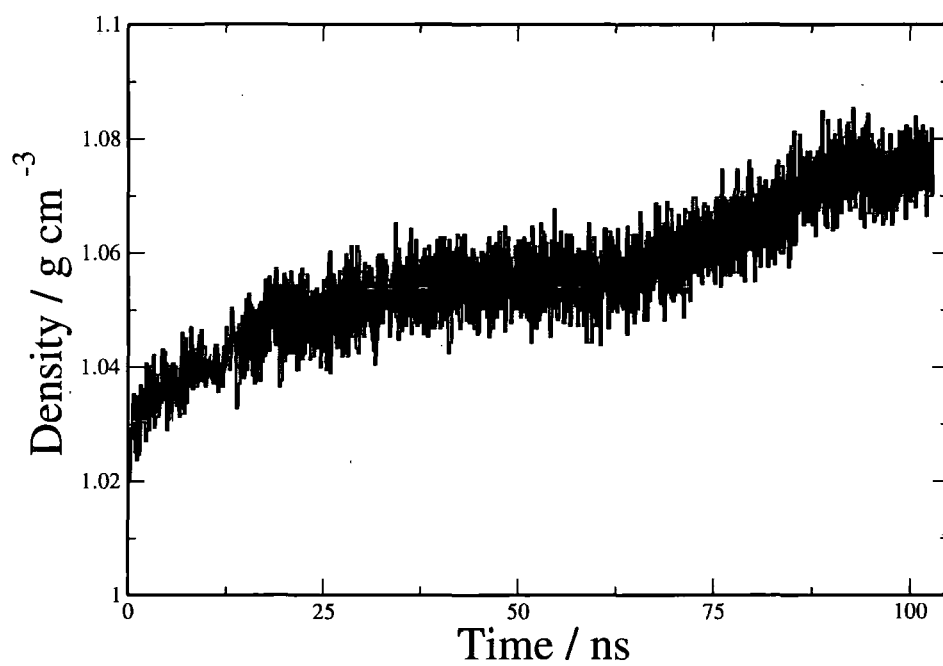
Figure 4.38: Evolution of the density with respect to time during the isotropic-nematic phase transition.

$g_{\parallel}(r)$ and Formation of Domains

A simple visual examination of the snapshot (such as the one shown in figure 4.39) leads to the conclusion that there are two antiferroelectric domains present in this simulation. Over a period of time it appears that the domains are gradually merging into a single one. Unfortunately, the high computing cost of cooling down an isotropic phase into the biaxial nematic limits the extension of this simulation. It should be agreed that the results presented for this run are already more than twice as long as any previous literature work, for system sizes that are 2.5 times larger that the longest previous literature simulations [1]. So these simulations are right on the limit of what is technically feasible.

The $g_{\parallel}(r)$ results shown in figure 4.39 are consistent either with the formation of two layers or with the formation of two main domains in the system. Visual inspection suggest that the latter may be more likely. In particular it should be noted that as a function of time, one domain appears to grow at the expense of the other one. Nevertheless, the limited system size makes it impossible to make definitive conclusions.

Pairwise Dipole Correlation Function $g_1(r)$

$g_1(r)$ results are shown in figure 4.40. These are rather similar to those obtained in section 4.2.4 for the same temperature and show the existence of pairwise dipole order at long range, confirming the presence of ferroelectric domains as seen in the snapshots.

4.5.3   Order Parameters

The results for Q_{00}^2 are plotted in figure 4.41. A gradual increase of Q_{00}^2 was observed throughout the simulation run. The biaxial order parameter, however, remained close to zero during the first part of the simulation. It was only after a long period of about 60 ns that a switch to biaxial ordering can be observed, and a significant

---

[1]The runs have expended approximately one order of magnitude more computer time than the previous largest runs in the scientific literature.
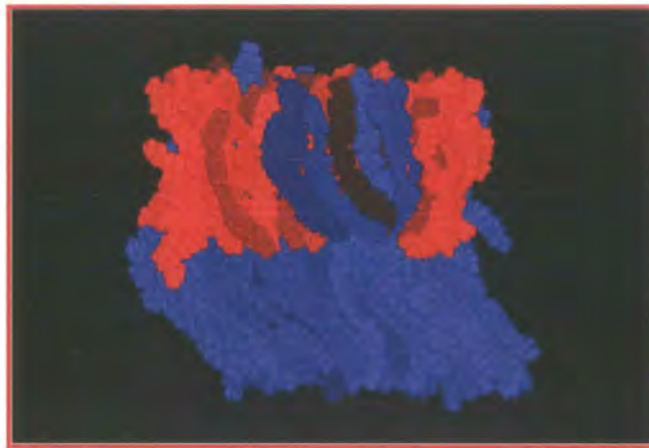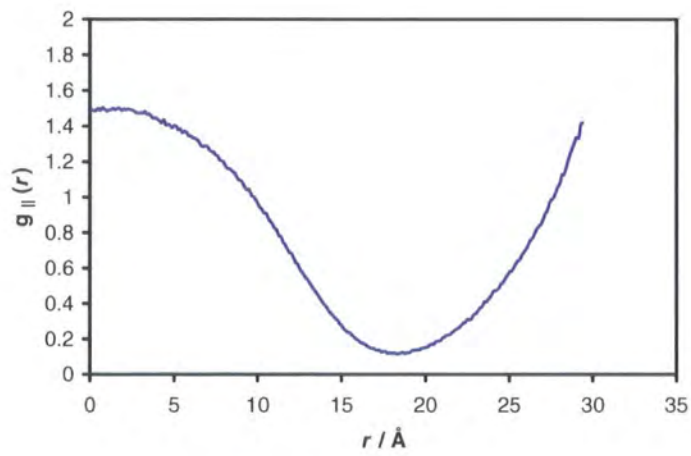
Figure 4.39: $g_{\parallel}(r)$ (top) and snapshot (bottom) for the growth of the liquid crystalline phase at 468 K.
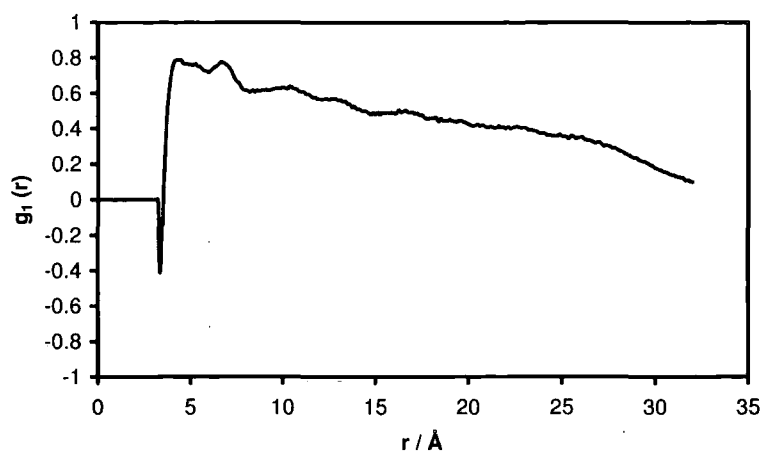
(a)
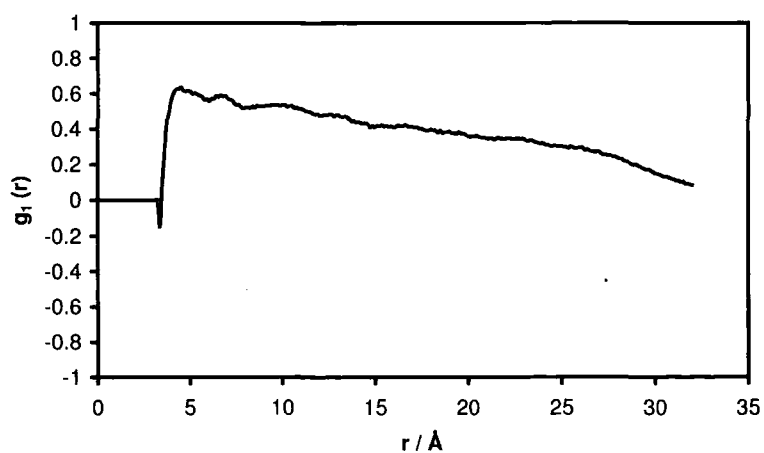
(b)

Figure 4.40: Pairwise dipole correlation factor $g_1(r)$ for the short molecular axis calculated with the steric dipole (a) and the electric dipole moment (b) for the growth of the nematic phase at 468 K.

biaxial order parameter of 0.2 can be detected. From this point on an extra 15 ns of simulation were carried out in order to equilibrate the new phase beyond doubt. The order parameters are summarized in table 4.13. After averaging the order parameters over the final 10 ns, Q_{00}^2 values for the long axis are found to be 0.66 ± 0.02 and 0.60 ± 0.02 when calculated with the inertia axes and the vectorial axes. Q_{22}^2 calculated with the inertia axes and the geometrical axes are 0.20 ± 0.03 and 0.22 ± 0.03 respectively. These values are smaller than the ones obtained directly from the biaxial phase at the same temperature (section 4.2), but considerably larger than zero and demonstrative of a biaxial, albeit small, order. It seems likely that despite growing the system over 100 ns the equilibration is still incomplete. The presence of a boundary between the two domains has the effect of reducing Q_{22}^2.

The results for the biaxial phase parameters η, calculated using the formula presented by Bates and Luckhurst, also show the existence of a biaxial phase. These results are summarized in table 4.13. It is noteworthy that the results obtained for the long axis and the arm axis are larger than any of the results obtained for the simulations run directly from the biaxial phase, including the one run at 468 K, which showed the higher order parameter using Allen's methodology Q_{22}^2.

η_x (I. A.)	0.4 ± 0.2	η_x(V.A.)	0.8 ± 0.04	η_{arm}	0.29 ± 0.04
η_y (I. A.)	0.8 ± 0.2	η_y(V.A.)	0.5 ± 0.2	η_{dip}	0.7 ± 0.2
η_z (I. A.)	0.41 ± 0.05	η_z(V.A.)	0.52 ± 0.07	η_{quad}	0.7 ± 0.2

Table 4.13: Biaxial parameters η calculated with the inertia axes (I.A.), arm axis (A.A.) and axes calculated using the vectors from the centre of the oxadiazole to the C in the second phenyl ring bonded to the aliphatic chain (V.A.).

Orientational Correlation Factor $g_2(r)$

The results obtained for the orientational correlation functions are similar to those obtained for the phase grown directly from a biaxial phase at the same temperature, as can be appreciated in figure 4.43.

The results for Q_{00}^2 for the steric dipole, the electric dipole moment and the quadrupolar moment are 0.37 ± 0.04, 0.30 ± 0.04 and 0.30 ± 0.04 respectively. These
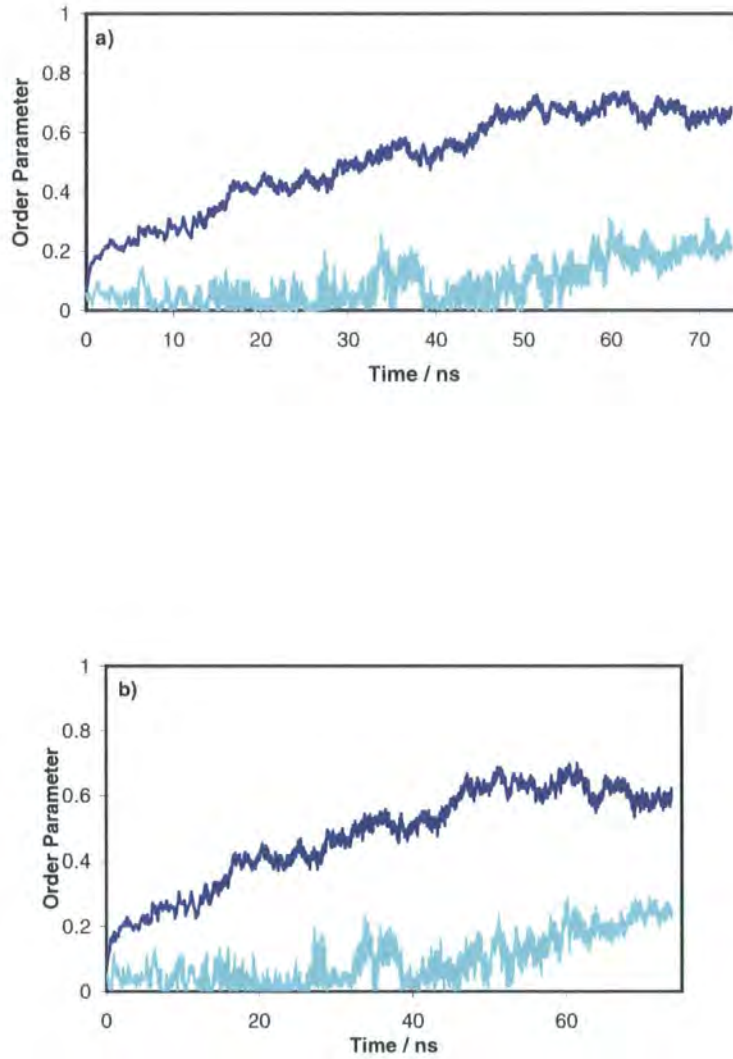
Figure 4.41: Q_{00}^2 along the longitudinal molecular axes and Q_{22}^2 calculated with the molecular axes of inertia (top) and the vectorial molecular axes (bottom) for the growth of the nematic phase at 468 K.

results are significantly bigger than those corresponding to lower temperatures, although smaller than those obtained for the simulation run directly from the biaxial phase at the same temperature (see section 4.6).

4.6 Discussion of the Results and Conclusions

It is the first time that a phase transition has been successfully simulated using a realistic potential in an all-atom system. Moreover, it is the first time that a nematic biaxial phase has been reproduced in an atomistic simulation. The simulation time required to equilibrate a nematic phase using an all-atom system turns out to be dramatically longer than that needed for systems of rigid particles (namely, spheres, spherocylinders or ellipsoids [35,91,100–102]) and an order of magnitude longer that the time necessary to equilibrate united-atom systems.

The experimentally claimed nematic range of temperatures for the molecule ODBP-Ph-C_7 has been reproduced in intervals of 10 K. From the results gathered in the previous sections it can be inferred that the simulation of the biaxial phase has been accomplished for the temperatures of 468 K and 478 K beyond doubt, since Q_{22}^2 and η calculated following the methodology suggested by Allen and by Bates and Luckhurst demonstrate strong biaxial ordering. In addition, a certain degree of biaxiality has been appreciated in the simulations at 458 K and 488 K. In both cases, although Q_{22}^2 values were significantly smaller than at 468 K and 478 K, the complete series of biaxial parameters η_α are superior than in those found in the simulations run at 468 K and 478 K. Nevertheless, no mergence of the different ferroelectric domains present in the simulation box has been observed, and it is possible that the systems run at 448 K and 458 K are not fully equilibrated or are in a pre-transitional state. It is also not entirely possible to fully rule out the formation of a stable or a metastable smectic phase in these two simulations. The impossibility of carry on with further simulations has prevented the clarification of this point.

In the progress of the simulation of the ODBP-Ph-C_7 at 448 K, there has been no sign of the onset of a biaxial phase. No formation of large ferroelectric domains has
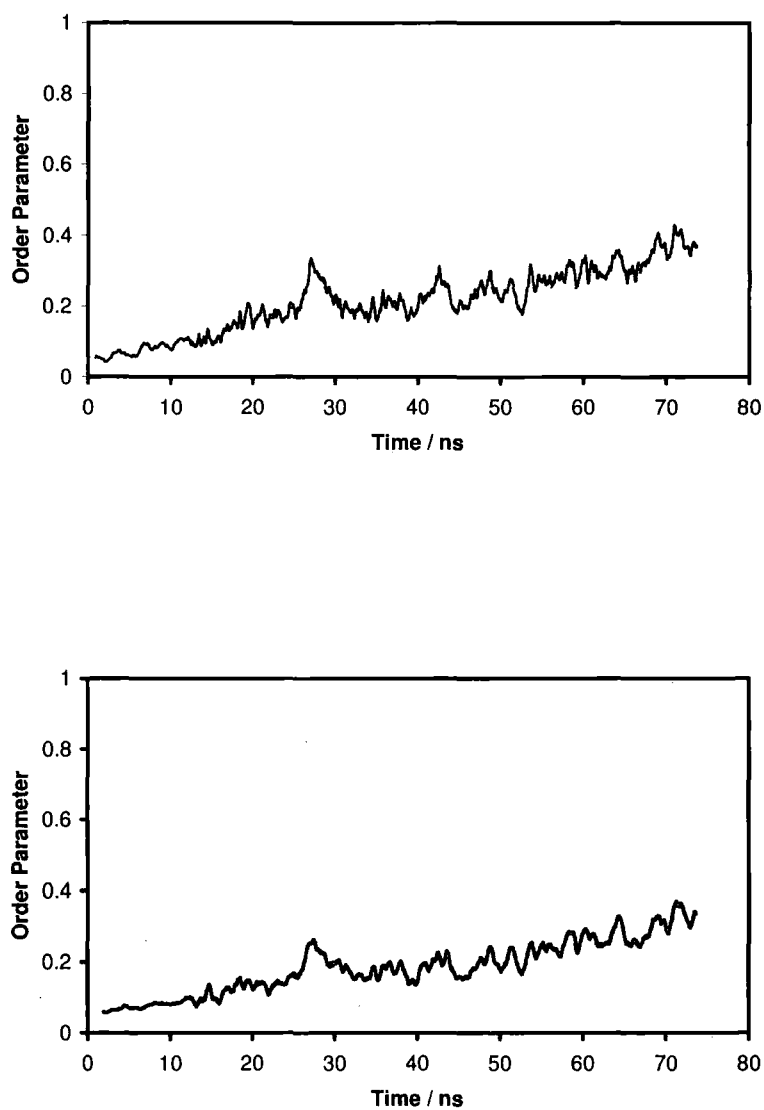
Figure 4.42: Q_{00}^2 for the steric dipole (top) and the electric dipole moment (bottom) for the growth of the nematic phase at 468 K.
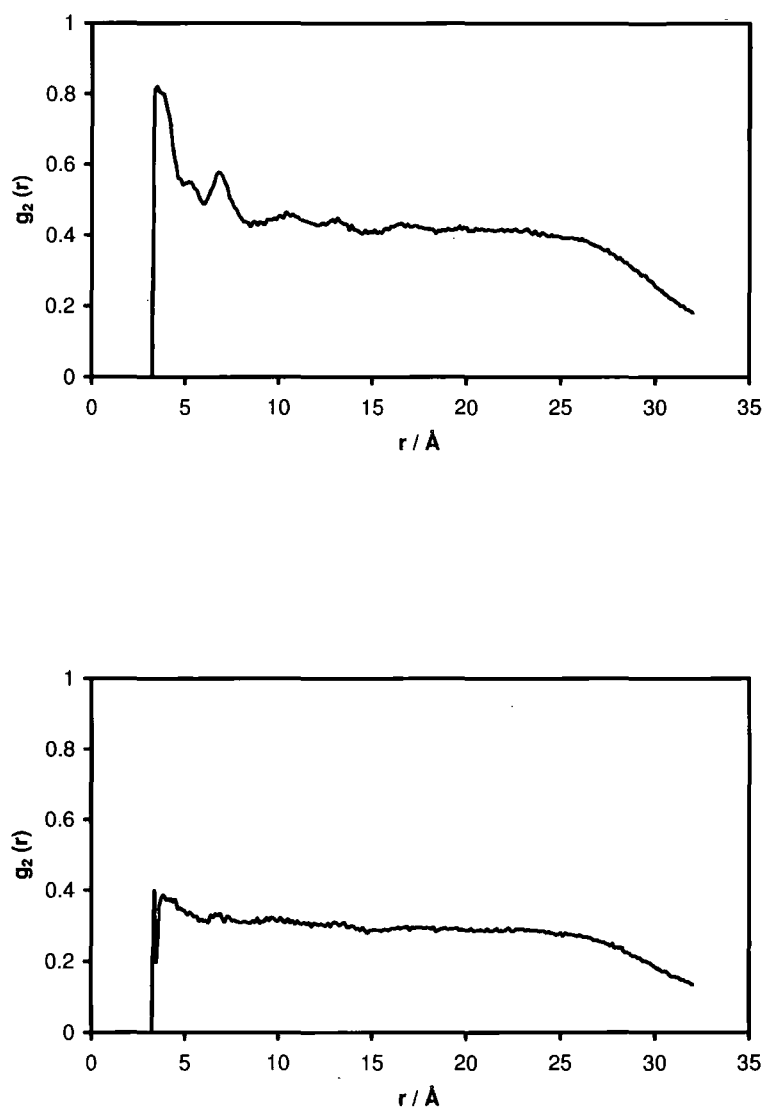
Figure 4.43: Orientational correlation factor $g_2(r)$ for the steric dipole (top) and the electric dipole moment (bottom) for the growth of the nematic phase at 468 K.

been appreciated either. It is possible that due to the lower temperature molecular motion is slower for this system and the timescale required to equilibrate a biaxial phase at this temperature is beyond the computational limits of this thesis.

A steric dipole is believed to stabilize the smectic phase, whereas the electric one is found to promote the biaxial ordering. There is a competition between the steric and the electrostatic interactions, since the ferroelectric order destabilizes the smectic phase because of steric repulsions between molecular arms with opposite orientations in neighbour layers [123]. This may have the repercussion of provoking the escape of the system to a biaxial nematic phase, since the high ferroelectric interactions would not make possible the existence of a uniaxial nematic phase. Hence in some sense the stability of the biaxial phase may be in response to the inability of the system to form a smectic phase. It is also worth commenting upon the nature of the electrostatic order in the system. Normally, the presence of layer range electrostatic interactions would be expected to destabilize ferroelectric order. One would not expect parallel pairing of the dipoles. Here however, it is clear that the nature of the core promotes favourable quadrupole interactions when the molecules are aligned so as to give ferroelectric ordering of the cores. Therefore, in the case of ODBP-Ph-C$_7$ it seems likely that quadrupolar stacking of the cores is the real driving force for biaxial ordering.

Regarding the two different methods used to calculate the biaxial order parameters, it seems possible to conclude that there is a qualitative agreement rather than a quantitative one, as could be expected from the different natures of the methods.

Chapter 5

Reproduction of the ^{2}H NMR Experiment

5.1 Introduction

Characterization of liquid crystalline phases using ^{2}H NMR has been described in the literature on several occasions (ref. [75, 124–126])

As previously explained in 3.3, the determination of the biaxial phase in ODBP-Ph-C$_7$ was not carried out directly by the method of labeling a particular position within the molecule with deuterium, due to the difficulties intrinsic to this procedure. Instead a deutered probe molecule, hexamethylbenzene (HMB) was introduced into the system with the hope that it would interact with the core of the ODBP-Ph-C$_7$ molecule and thus adopt the same orientation. The biaxial phase parameter η, measured by this method, albeit non negligible was quite small (just 0.11).

In chapter 4 simulations were carried out with the aim of clarifying the mechanisms responsible for the onset of the biaxial phase and of providing a direct measurement of the biaxial parameter for ODBP-Ph-C$_7$. However, it is also interesting to reproduce exactly (although with the inherent technical limitations, of course) the experiment carried out by Madsen and coworkers [23]. The motivation for this attempt is in the enormous controversy raised by this experiment, which arises not only over the capacity of ODBP-Ph-C$_7$ to generate a biaxial phase, but also to the ability of ^{2}H NMR to determine biaxial phases, especially in the temperature ranges

for which a biaxial phase is claimed·to exist for ODBP-Ph-C$_7$. With the aim of re-maining faithful to the original experiment, a number of probe molecules equivalent to that used in the experiment (1.5 ± 0.5 % wt) were introduced into the simulation. Therefore, 19 molecules of HMB (which approximately represents 1.5 % wt) were introduced in the simulation box in a random fashion. The simulation details are described in the next section.

Finally, it should be stated that although there has been previous work pre-senting results for the simulation with single-site potentials of systems formed by rod-like mesogens doped with bent-core molecules [127], no reproduction of a system composed of a banana-shaped molecule and a probe molecule has been reproduced to date.

5.2   Analysis of ODBP-Ph-C7

5.2.1   Simulation Details

Following the same procedure used in the simulations described in the previous chapter, an initial idealized lattice in the gas phase was set up, containing 256 ODBP-Ph-C$_7$ molecules with perfect orientational order and 19 HMB distributed randomly across the simulation box in the intermolecular gaps. The force field used to describe the intermolecular interactions was exactly the same as the one used previously. It was described in detail in tables 4.1, 4.2 and 4.3. The initial compression was similar to that carried out for the systems formed from pure ODBP-Ph-C$_7$, as described in the previous chapter. Once the system achieved the required density, corresponding to a liquid crystal phase, this was equilibrated over a period of 15 ns. The temperature and the pressure were identical to those of the experiment, i.e., 447 K and one atmosphere of pressure. Henceforth the simulation was run in thermodynamic equilibrium for another 5 ns, with the purpose of gathering a suitable amount of data to perform the corresponding statistical analysis.

5.2.2   Structure

Density

The density of the whole system was monitored throughout the entire simulation, as shown in figure 5.1. After an initial decay, the density increased until the 16 ns. Thereafter the calculated values for the density became stable.

The density and simulation box volume were averaged for a period of 4 ns. The values obtained for the density and the simulation box were 1.070 ± 0.004 g cm^{-3} and 266402 ± 920 Å^3 respectively. Apparently, the effect produced by the addition of the HMB molecule to the system formed of ODBP-Ph-C$_7$ was to increase the density with respect to the system without HMB at approximately the same temperature. However, this increment (0.004 g cm^{-3}) only represents 0.4 % and in addition is within the simulation errors. Hence it can be neglected as being an important factor.
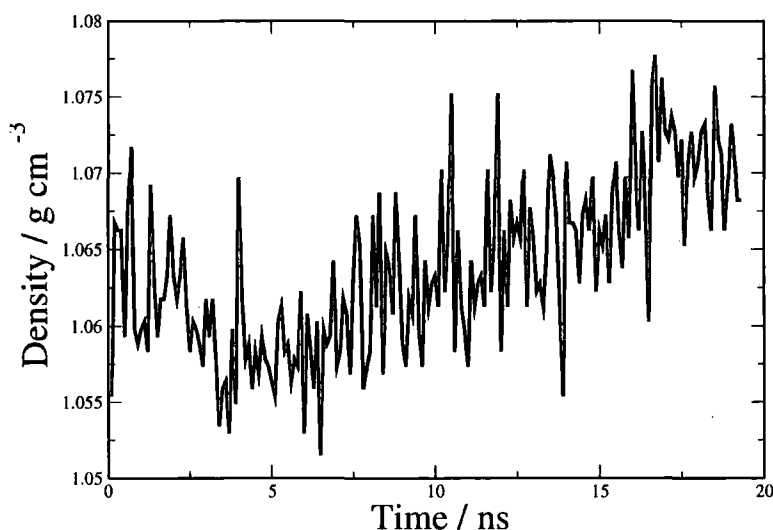
Figure 5.1: Evolution of the density with respect to the time.

Radial Distribution Function Parallel to the Long Axis $g_{\parallel}(r)$ and Domains

The results for $g_{\parallel}(r)$ do not show any sign of the presence of a highly structured phase. By contrast, the pattern exhibited by the function is rather similar to the

one shown in the simulation run at 448 K. Although the trend of the function in not absolutely monotonous, it can be clearly appreciated in figure 5.2 that it does not show a sinusoidal behavior, characteristic of smectic phases. A visual inspection of the snapshot shown in figure 5.2 (as in chapter 4, the color coding represents different orientations of the steric dipole) does not fully allow the presence of layers in the system to be ruled out. Therefore, a longer run of a larger system would be necessary to state whether different ferroelectric domains have formed or the system has become smectic.
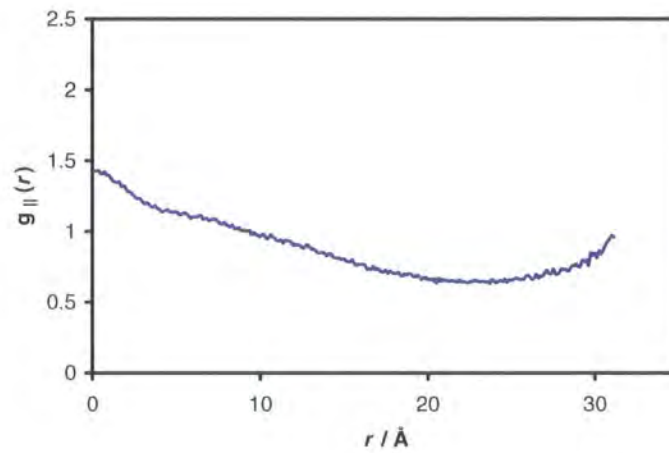
(a)

(b)

Figure 5.2: $g_{\parallel}(r)$ (a) and bulk system snapshot (b). The color coding has been established using the usual criteria.

Pairwise Dipole Correlation Function $g_1(r)$

The pairwise dipole correlation factor was calculated following the methodology explained in section 2.6.1. The results obtained are shown in figure 6.16 . These differ significantly from the results obtained for the 448 K simulation discussed in chapter 4. In the present case, the results of $g_1(r)$ obtained for both the steric and the electric dipoles exhibit a very strong parallel correlation at short range, in the same way as seen for the majority of systems with charges, which were studied in chapter 4. This correlation is significantly higher than in the case of the simulation run at the same temperature but in the absence of the probe molecule HMB. Therefore it seems that the presence of the probe molecule affects the temperature range of the biaxial phase. However, results are consistent with those obtained for the 468 K and 478 K simulations in chapter 4, where there was a strong parallel pairwise dipole correlation which produced ferroelectric domains (see figure 4.3), in the same way as in the present case (see figure 5.2). Parallel correlation does not occur at such a long range as in the case of the 468 K and 478 K simulations. $g_1(r)$ decays until it reaches values close to zero, at an intermolecular distance of approximately 25 Å. This suggests that there is more than one ferroelectric domain in the system as expected from figure 5.2. A longer simulation may be required to achieve the mergence of the domains into a single one.

5.2.3   Order Parameters

The evolution of the system was monitored using Q_{00}^2 for the long molecular axis and Q_{22}^2. These are shown in figure 5.4. After 15 ns of simulation stable values of both density and order parameters are obtained and thus system is considered equilibrated.

The value of Q_{00}^2 along the longitudinal axis is 0.90 ± 0.01 when calculated with the inertia axis and 0.88 ± 0.08 when calculated with the vectorial axes, which represents an increase of ~ 0.1 with respect to the simulation run at 448 K without the presence of the probe molecule HMB (see table 4.5). The values of Q_{00}^2 obtained for the long axis might be considered high for a nematic phase, suggesting the
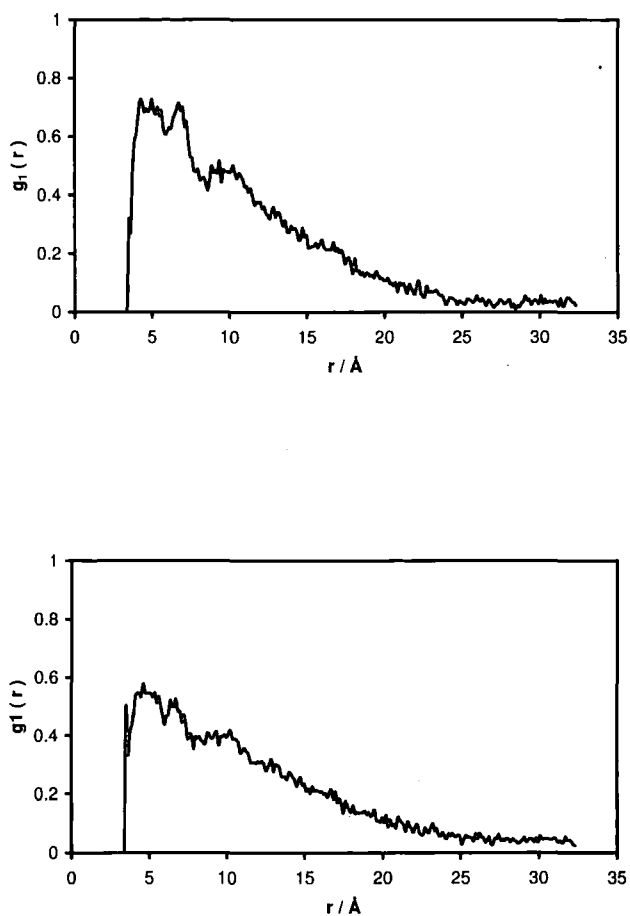
Figure 5.3: Pairwise dipole correlation factor $g_1(r)$ for the molecular short axis calculated geometrically (top) and the molecular dipole moment (bottom).
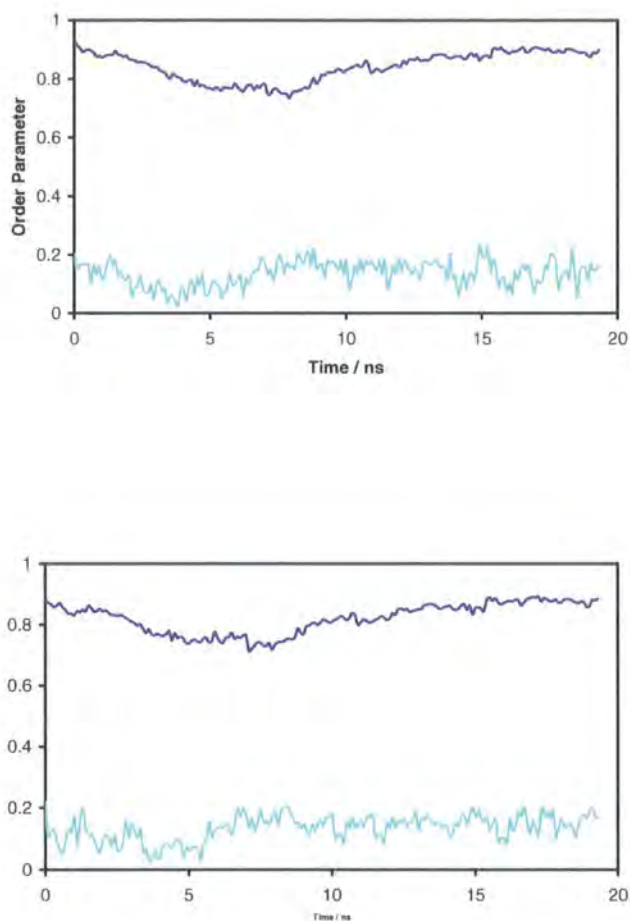
Figure 5.4: Uniaxial order parameter along the transverse axis and biaxial order parameter calculated using the inertia axes (top) and the axes calculated using the vectors from the centre of the oxadiazole ring to the C of the second phenyl ring bonded to the aliphatic chain (bottom).

existence of a smectic phase. However, the results yielded by $g_{\parallel}(r)$ and $g_1(r)$ suggest that the system is more likely to be in a nematic phase where different ferroelectric domains coexist. The values registered for Q_{22}^2 in this system are 0.13 ± 0.04 and 0.15 ± 0.03 when calculated with the inertia axis and the axes calculated using the vectors respectively, which are smaller than the same values for the 468 K simulations discussed in section 4.2 (0.44 ± 0.04 and 0.43 ± 0.04 respectively, see table 4.5). Therefore it seems likely that either the probe reduces biaxiality or that longer runs may be required to fully equilibrate the ordering of the short axis

η_x(I.A.)	η_y(I.A.)	η_z(I.A.)	η_{arm}(A.A.)	η_x(V.A.)	η_y(V.A.)	η_z(V.A.)
0.5 ± 0.1	0.4 ± 0.1	0.03 ± 0.01	0.05 ± 0.01	0.5 ± 0.1	0.5 ± 0.1	0.04 ± 0.01

Table 5.1: Biaxial parameter η calculated using the inertia axes (I.A.), the arm axes (A.A) and the axes calculated using the vectors with origin in the centre of the oxadiazole ring and extremes in the C of the second phenyl ring bonded to the chain (V.A.) (see section 3.6).

The values of the biaxial parameters η given in 5.1, are significantly smaller than those exhibited by pure ODBP-Ph-C$_7$. Indeed, no biaxiality at all can be claimed from η_{arm}, which is considered the most representative biaxial phase parameter [96]. These values are, considering their error, almost equal to zero, and approximately half of the value of the correspondent parameters for the 448 K simulation performed without the probe molecule (see tables 4.7, 4.8 and 4.9).

5.2.4 Uniaxial Order Parameter of the Steric and Electric Dipoles and $g_2(r)$

The Q_{00}^2 values for the steric and the electric dipoles, shown in figure 5.5, are 0.31 ± 0.03 and 0.27 ± 0.03 respectively. Both values are slightly larger than those obtained for the simulation run at 448 K (0.25 ± 0.03 and 0.22 ± 0.03 respectively) but still smaller than those obtained for the 468 K simulation (0.53 ± 0.04 and 0.40 ± 0.03 respectively). Therefore, it is possible that the equilibration of the biaxial phase has not been totally achieved.
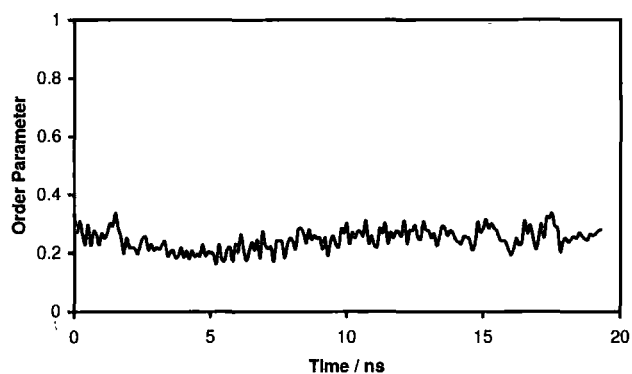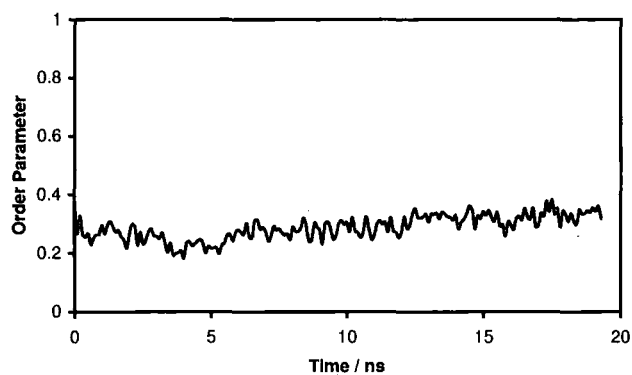
Figure 5.5: Uniaxial order parameter for the molecular short axis calculated geometrically (top) and the molecular dipole moment (bottom).

In good agreement with the order parameters, the orientational correlation function shows strong orientational correlation for the steric and the electric dipole moment (figure 5.6). The orientational order persists at a moderately high level throughout all the simulation box. More than one ferroelectric domain can be identified in the system, as can be seen in figure 5.2 (b). The orientational correlation between two molecules is higher for the steric molecular dipole than the electric one. This result is consistent with those observed in the previous chapter (figures 4.18 and 4.19).
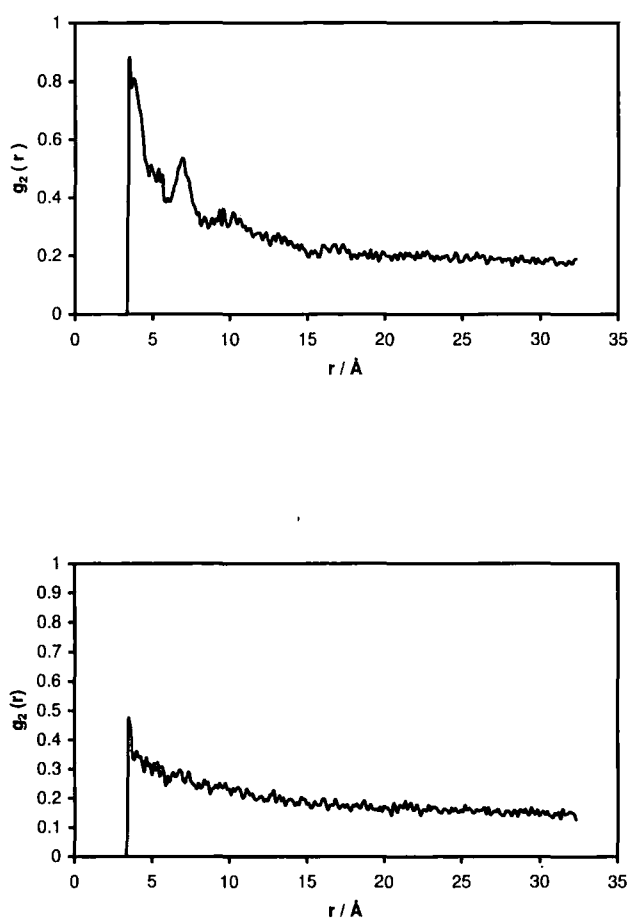
Figure 5.6: Orientational correlation factor $g_2(r)$ for the molecular short axis calculated geometrically (top) and the molecular dipole moment (bottom).

5.3 Analysis of HMB

5.3.1 Orientational Criteria in the Probe Molecule HMB

The biaxial parameters have been calculated using two different types of molecular axes: the molecular axes of inertia and the axes calculated with vectors. The way the latter have been evaluated is sketched in figure 5.7. Two perpendicular axes were calculated using vectors as shown in 5.7. The two axes within the molecular plane have been labeled $\vec{X}$ and $\vec{Y}$ in the sketch. A third axis coming out of the plane was defined as the cross product of the two previous ones, and labeled $\vec{Z}$.

The assignment of the axes of inertia has been accomplished using the same methodology as for the molecule ODBP-Ph-C_7. Hence, the $\vec{Z}$ axis is defined as the axis of inertia associated to the smallest eigenvalue obtained by diagonalizing the inertia tensor (see section 3.6), the $\vec{X}$ axis is assigned to the eigenvector associated to the largest eigenvalue and $\vec{Y}$ is given by the remaining eigenvector.
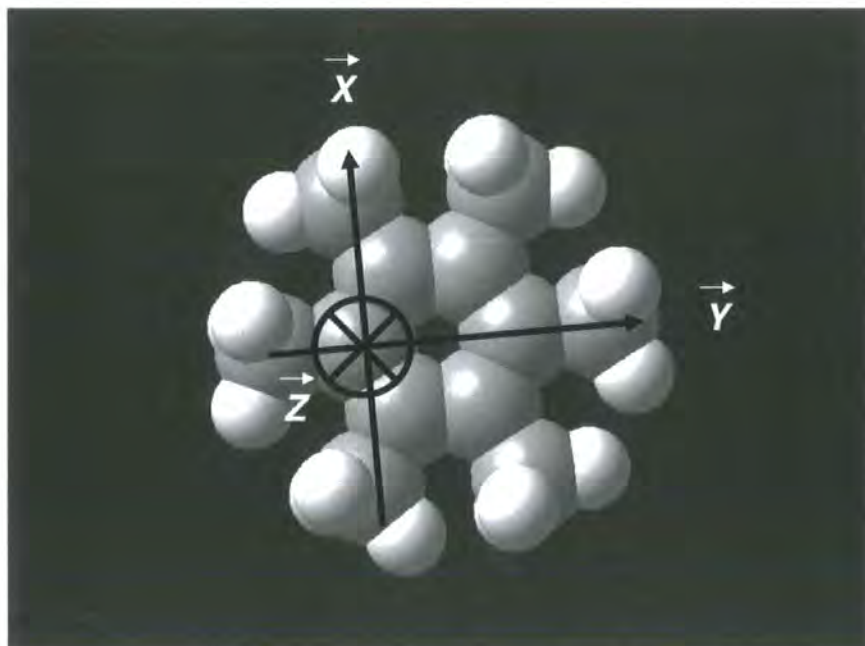
Figure 5.7: Orientational axes calculated geometrically for the probe molecule HMB.

5.3.2 Density Distribution of the Probe Molecule

In order to check that the adaptation of the probe molecule HMB to the system was correct and therefore its motion across the simulation box was fluent, seven different HMB molecules were chosen randomly and their movements throughout 4 ns were recorded (see figure 5.8). The positions of the molecules were given by their geometrical centre, calculated as the centre of the phenyl ring. Subsequently, the different positions of each one of the seven molecules were represented by spheres of different colors. The result is satisfactory and proves that the motion of the probe molecules along the system is undisturbed. Alongside the representation of the motion of the HMB molecules, a snapshot of the simulation of the ODBP-Ph-C$_7$ is shown in figure 5.8. This illustrates perfectly the interactions between the probe molecules and the mesogens, and how the former adopt the orientation of the rigid aromatic core of the latter.

5.3.3 Order Parameters

A comprehensive study of the orientational order of the molecule HMB has been accomplished with the object of describing, in the best possible way, the relation between the order parameters obtained in the laboratory from the probe molecule and those obtained in the simulation directly from the ODBP-Ph-C$_7$ mesogen.

	Q_{00}^2	Q_{22}^2
Axes of Inertia	0.19±0.07	0.22±0.08
Vectorial Axes	0.23±0.07	0.19±0.09

Table 5.2: Q_{00}^2 and Q_{22}^2 of the probe molecule calculated with the axes of inertia and the axes calculated using the vectors, as explained in section 5.3.1.

The results obtained for Q_{00}^2 and Q_{22}^2 of the probe molecule (tab. 5.2) are, in this case, very similar. The biaxial order represented by the probe is larger than the one calculated directly from the mesogen (see section 5.2.3), although the difference is within the error of the measure. This indicates that the determination of the degree of biaxiality through an indirect measure using a probe molecule yields satisfactory
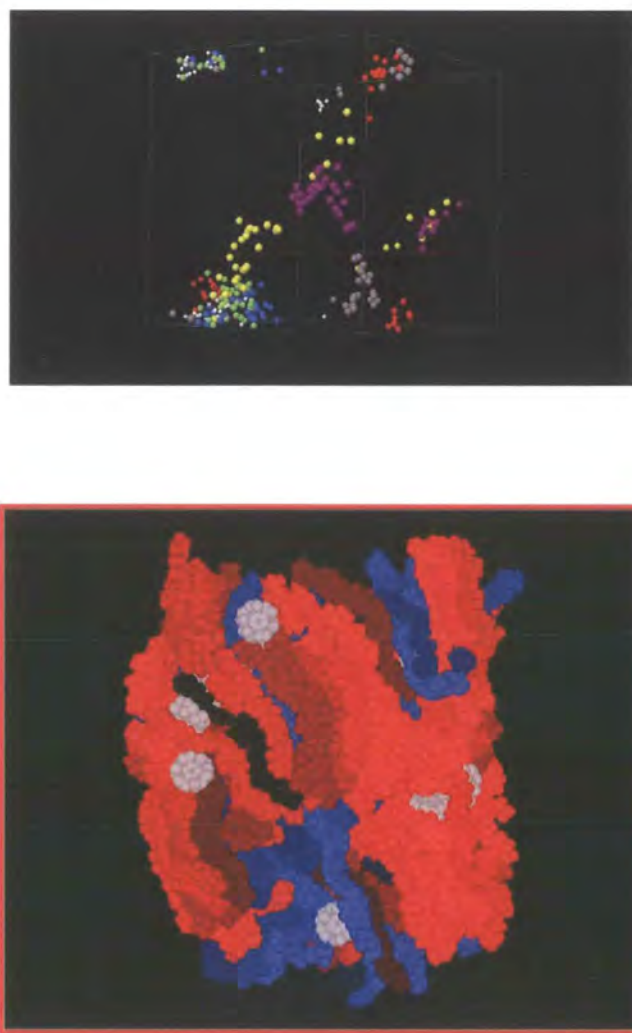
Figure 5.8: Distribution of the geometric centres of seven different HMB molecules chosen randomly and represented by spheres of different colors throughout a simulation of 4 ns (top). Snapshot of the simulation of the bulk system ODBP-Ph-C$_7$ (color coded) with the probe molecule (white) embedded in it (bottom).

results. This is an important result because the experimental claim for biaxiality in this molecule depends on the probe used in the ^{2}H NMR experiment being able to faithfully report on the ordering of the mesogen.

The values obtained for η are given in table 5.3. It is noteworthy that the the values of the biaxial parameters calculated with the three different axes of the probe molecule report exactly the same value ($\eta_\alpha = 0.6$, $\alpha = x, y, z$). This may also be mainly motivated by the symmetry of the molecule. This result is very close to that obtained in section 5.2.3 for η_x and η_y, but differs dramatically from those found for η_z and η_{arm}. Moreover, the values herein obtained for the biaxial parameters exceeds notably the experimental value of 0.11 [23]. η_α has been calculated for the final 4 ns every 0.1 ns and subsequently the average values have been calculated. In spite of the small values of the largest eigenvalue obtained by diagonalising the ordering tensor for each one of the probe molecule axis (see figure 5.7), η_α values are large. This is due to the fact that the values of the three eigenvalues obtained by diagonalizing the ordering tensor are, albeit small, very different from each other. The typical eigenvalues calculated with both the axes of inertia and the vectorial axes are ~ -0.2, ~ 0.0 and ~ 0.2. This has as a consequence that the numerator and denominator in equation 3.15 used to calculate η_α are quite similar, leading to η_α large values.

η_x(I.A.)	η_y(I.A.)	η_z(I.A.)	η_x(V.A.)	η_y(V.A.)	η_z(V.A.)
0.6 ± 0.2	0.6 ± 0.2	0.6 ± 0.3	0.6 ± 0.2	0.6 ± 0.2	0.6 ± 0.2

Table 5.3: Biaxial parameter η calculated using the inertia axes (I.A.) and the vectorial axes (V.A.).

5.4 Conclusions

The reproduction of the experimental determination of the biaxial phase of ODBP-Ph-C$_7$ using ^{2}H NMR has been successfully carried out using molecular dynamics simulations.

The simulation has been performed over a time period of approximately 20 ns.
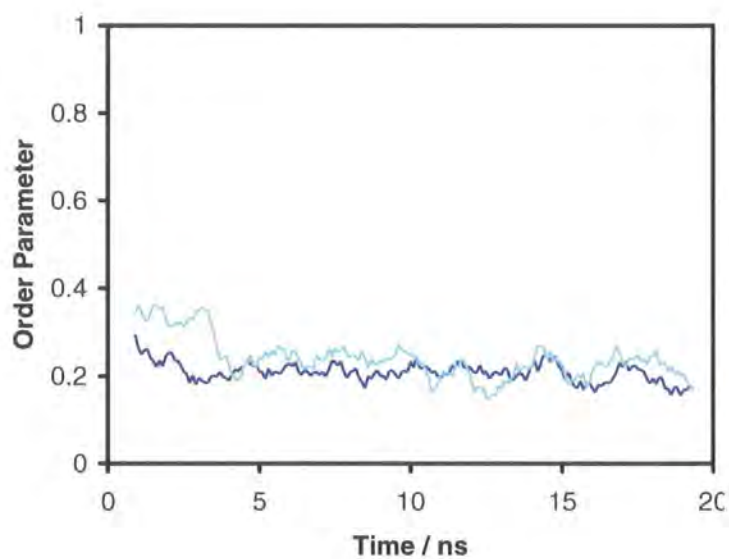
Figure 5.9: Q_{00}^2 calculated with the molecular $\overrightarrow{Z}$ axis of inertia (navy blue) and Q_{22}^2 calculated with the $\overrightarrow{X}$ and $\overrightarrow{Y}$ molecular axes of inertia (turquoise) for the probe molecule HMB.
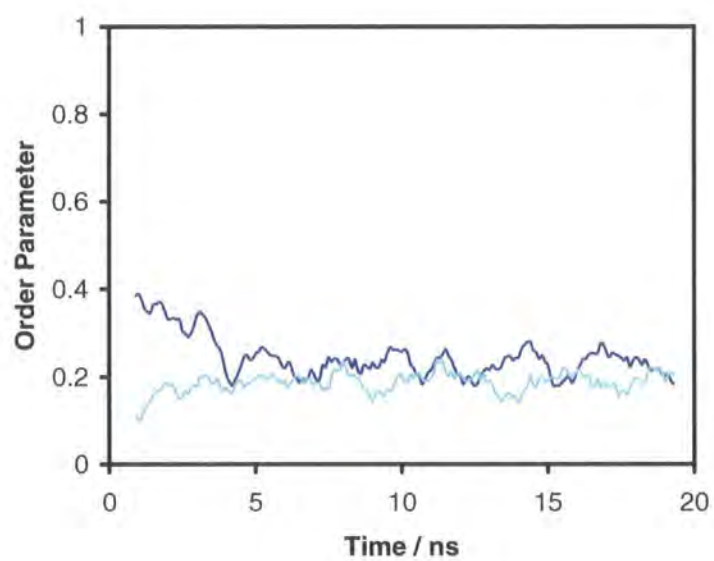
Figure 5.10: Q_{00}^2 calculated with the molecular $\overrightarrow{Z}$ vectorial axis (navy blue) and Q_{22}^2 calculated with the $\overrightarrow{X}$ and $\overrightarrow{Y}$ molecular vectorial axes (turquoise) for the probe molecule HMB.

The system formed from ODBP-Ph-C$_7$ and the probe molecule exhibited ferroelectric domains [1]. It therefore seems likely that the presence of the probe molecule does not alter the behaviour of the pure liquid crystalline phase, as studied in chapter 4.

The results presented here are in qualitative agreement with experiment. Nevertheless the magnitude of the biaxial parameters η obtained in the simulation are certainly larger than those obtained experimentally. This might be because of size effects, considering the limited dimensions of the simulation box available.

The order parameters calculated directly using the probe molecule show the existence of biaxiality in the system. This is more reduced than in previous simulations (see the previous chapter simulation runs at 468 K and 478 K) but moderately larger than the one exhibited by the pure ODBP-Ph-C$_7$ system simulated at approximately the same temperature (448 K).

---

[1]This is consistent with the majority of work presented in chapter 4, with the exception of the 448 K simulation, which had not formed domains during the time of the run.

Chapter 6

Simulation of Mixture E7

6.1 Introduction

The liquid crystalline phase or mesophase was discovered in the last part of the nineteenth century [1]. However, it was not until the decade of 1970 that industrial use was envisaged. A wide spectrum of employments have been developed ever since, such as the popular liquid crystal displays (LCDs), adaptive optics devices for telescopes, optical interconnectors, optical correlators and switchable windows [128]. With the intention of improving the performance of the different mesogens used for each one of these devices, mixtures of liquid crystals have been implemented in a way that the different components interact synergistically, so that the material properties of the mixture are improved over those of individual mesogens. Material properties, such as rotational viscosity, dielectric anisotropy, elastic constants or flexoelectricity (some of which will be introduced later), play a crucial role in the design of liquid crystal devices [129]. It goes without saying that both material properties and internal structure of a mixture of liquid crystals depend on the intermolecular interactions between the different components of it. The nature of these interactions is not always straightforward and, unfortunately, in many occasions remain elusive.

As computer power has increased through the past few years, atomistic simulations have emerged as a good alternative to the traditional methods of trial and error used in the past. The motivation of the work discussed in the present chapter is the elucidation of the intermolecular interactions responsible for internal struc-

ture of a liquid crystal, as well as the internal structure itself. Calculations in this chapter focus on the commercial mixture of liquid crystal molecules E7, synthesized and distributed by Merck.

6.2 Simulation Details
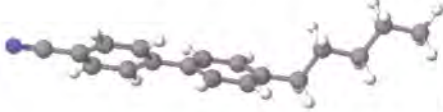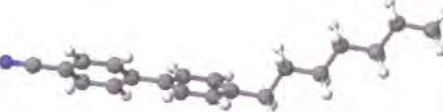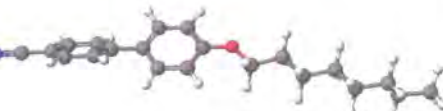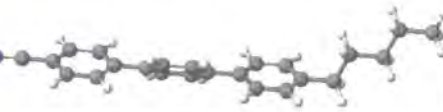
Strucutre of Molecule	Weight Percentage	No. of Mol.
5CB	51	141
7CB	25	62
8OCB	16	36
5CT	8	17

Table 6.1: Liquid crystal mixture E7. The composition is shown in terms of the weight percentage of each component in the mixture and the number of molecules corresponding to each type in the simulation.

The liquid crystal mixture E7 is composed of four different types of mesogens, all four of them are cyanobiphenyl derivatives. Different molecular structures and weight percentage in the mixture are detailed in table 6.1. The specific names of the mixture components, named from the most to the least abundant are 4-cyano-4'-n-pentyl-biphenyl (5CB), 4-cyano-4'-n-heptyl-biphenyl (7CB), 4-cyano-4'-n-octyloxy-biphenyl (8OCB) and 4-cyano-4'-n-pentyl-terphenyl (5CT).

Molecular dynamics simulations have been undertaken using the commercial package DL-POLY 2.14 [110]. The potential employed was the atomistic potential described in equation 2.13, in section 2.3.3. As previously each atom in the system was included. The intramolecular part of the potential involved stretching, bending and torsional parameters whereas the intermolecular part was represented by electrostatic and van der Waals parameters. Most of these parameters, specially those

concerning the aliphatic chains and the internal structure of the phenyl rings were the same as those used in the simulations of the bent-core molecule ODBP-Ph-C$_7$ (see chapters 4 and 5). Additional parameters used for the cyano groups (see tables 6.2, 6.3 and 6.4) were extracted from the OPLS-AA force field by Jorgensen and co-workers [108], using the same procedure as the one related in section 4.2.1, and the parameters representing the inter-phenyl dihedral angle were calculated using *density functional theory ab initio* methods using a plane wave basis set and the functional PW91 [130]. Bond lengths were constrained using the SHAKE algorithm [111] to allow the use of longer time steps.

Angle	k_θ/ kJ mol^{-1}rad^{-2}	θ_0/deg
CA-CA-CZ	292.88	120.0
CA-CA-NZ	711.28	180.0

Table 6.2: Bond angle bending parameters.

Dihedral Angle	V_1	V_2	V_3
CA-CA-CA-CZ	0.000	39.748	0.000
CA-CA-CA-NZ	0.000	0.000	0.000

Table 6.3: Torsional angle parameters in kJ mol^{-1}.

Dihedral Angle	V_2	V_4	V_6	V_8	V_{10}	V_{12}
CA-CA-CA-CA	3.208	0.972	0.379	0.149	0.056	0.025

Table 6.4: Torsional angle parameters for the inter ring dihedral angle in kJ mol^{-1}. In this case the Fourier series have been expanded to the 12th term. The odd terms are zero due to the symmetry of the torsional energy.

The electrostatic interactions were tackled using an Ewald sum [112], with a convergence parameter of 0.29 Å^{-1} and six k vectors in the x, y and z directions.

Seven different simulations have been performed and all of them were initially compressed from the same idealised cubic lattice of 256 molecules, with an almost

perfect orientational order along the z axis. Each position of the lattice was occupied by a molecule. The type of the molecule (5CB, 7CB, 8OCB, 5CT) was chosen at random and the direction of the molecule along $z+$ or $z-$ was also chosen at random. In this manner it was possible to avoid ferroelectric order and to achieve a homogeneous molecular distribution within the bulk system.

The simulation was started from an idealized cubic lattice with a density typical of a gas phase. Subsequently it was compressed until a condensed phase was achieved. The short range van der Waals interactions were truncated using different cut-offs during the compression[1]. Once the compression was concluded the cut-off was fixed to 9 Å. Thereafter, the system was equilibrated at the temperature of 300 K. This temperature was chosen for being approximately in the middle of the interval of temperatures within the nematic phase. After a period of equilibration of 19.2 ns five more simulations were started at 280 K, 290 K, 310 K, 320 K and 330 K, while the simulation originally run at 300 K was continued. All these temperatures are included in the nematic range.

An extra simulation forced the loss of nematic order by increasing the temperature over the nematic-isotropic transition. Thereafter, a new simulation starting from the isotropic liquid was performed in order to reproduce the transition between the isotropic and the nematic phases. The temperature chosen to carry out the quench of the isotropic phase into the nematic was 300 K, due to the fact that this is approximately in the middle of the experimental temperature range for the nematic phase.

6.3 System Structure and Order Parameters

Throughout the different simulations, densities and order parameters have been monitored to check the evolution of the systems and characterize the phase represented by each system. In figure 6.1, it is possible to observe the densities of the systems run at six different temperatures. The densities decrease as the temperature

---

[1]To avoid problems with the Verlet neighbour list in DLPOLY the cut off parameter was set to be large initially.

increases, as expected. The values of the densities averaged throughout the simulations run are shown in table 6.5. Experimental measures provide a density of 1.03 g cm^{-3} at 300 K [131]. The density obtained in the present work at the same temperature is 1.061 g cm^{-3}, a result approximately 3 % larger than the experimental one.

Temperature / K	Density / gcm^{-3}	Volume / Å^3
280	1.073 ± 0.003	106731 ± 303
290	1.065 ± 0.003	107506 ± 365
300	1.061 ± 0.004	107940 ± 410
310	1.054 ± 0.004	108576 ± 438
320	1.047 ± 0.004	109324 ± 475
330	1.040 ± 0.004	110118 ± 437

Table 6.5: Density and volume averages of the simulations of the mixture of liquid crystals E7 performed at six different temperatures from the nematic phase.

In figure 6.2 it is possible to observe that two different order parameters have been calculated for each temperature. The one represented by the black line has been calculated using the principal molecular axis of inertia to represent the molecular orientation, whereas the one represented by the red line has been calculated using the vector running along the spine of the molecule from the aromatic carbon bonded to the aliphatic chain to the cyano group as illustrated in figure 6.3. The methodology used to calculate the order parameter is the same as the one used in chapters 4 and 5, and it has been explained in chapter 2. The order parameter calculated using the principal axis of inertia is always larger than the one obtained with the vectors representing the orientation of the aromatic core, suggesting not only does the aromatic rigid core contribute to the orientational order but also the aliphatic chain does. The mean order parameters calculated from the final 2 ns of the runs in figure 6.2 are given in table 6.6. The values calculated are very similar to each other with the exception of the 290 K result, which is slightly smaller. Here it would seem that, particularly at 290 K, 20 ns might not be large enough for accomplishing the
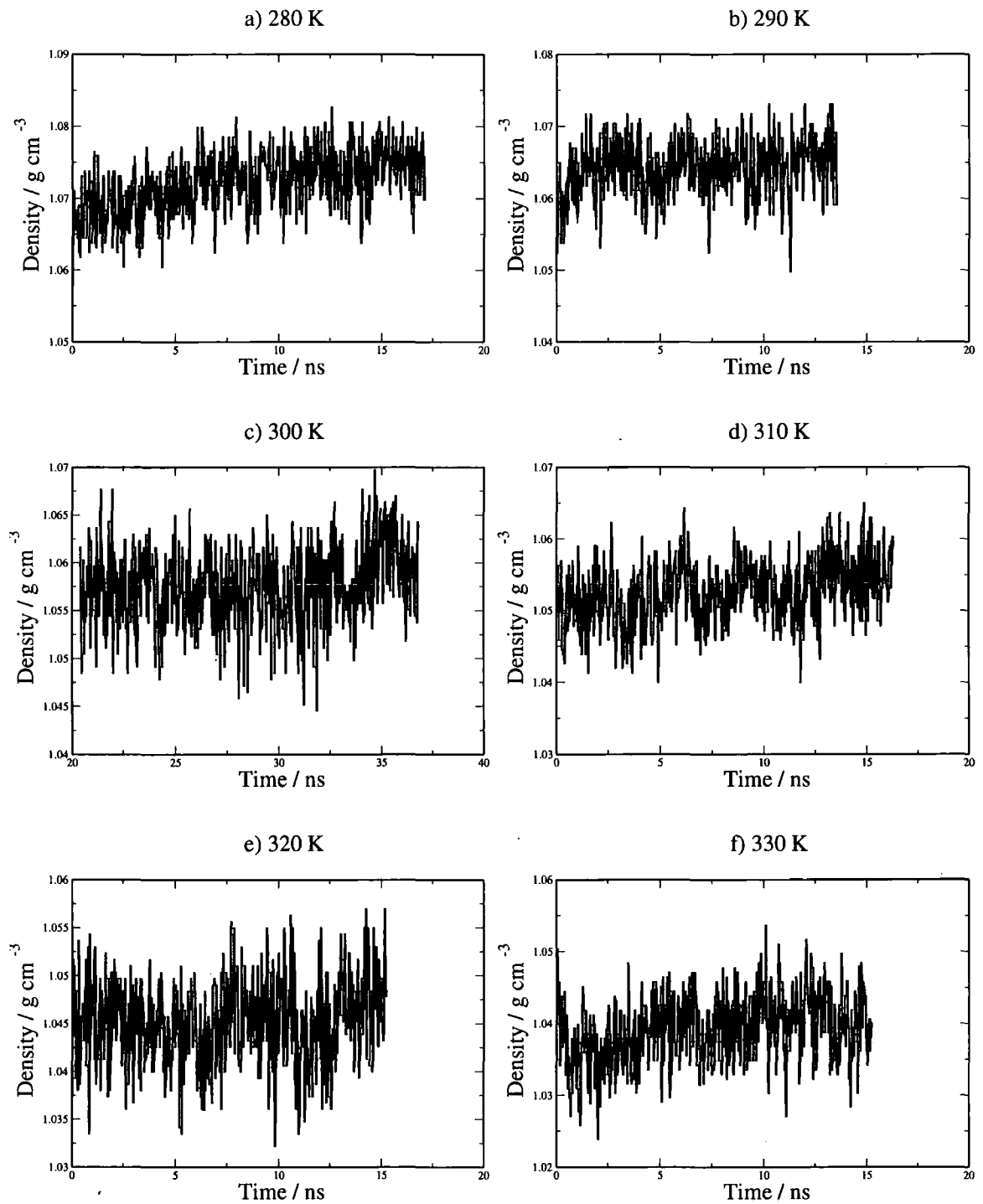
Figure 6.1: Densities for the simulations run at different temperatures: a) 280 K, b) 290 K, c) 300 K, d) 310 K, e) 320 K and f) 330 K.

equilibration of the mixture.

Order parameters have been experimentally determined for the mixture E7 [132]. The experimental results were smaller than the calculated values. Experimental order parameters at 300 K and 330 K fitted from refractive index data using the Haller method [133] are ~ 0.72 and ~ 0.50 respectively, whereas the values shown in table 6.6 are 0.83 $\pm$ 0.01 and 0.82 $\pm$ 0.02 respectively. It seems likely that the slightly higher density obtained in the simulation pushes up the order parameter and most likely pushes the phase transition to higher temperatures. So the results in table 6.6 reflect a higher overall order parameter and fail to show the strong temperature dependence that we would expect close to the nematic-isotropic phase transition. The fact that both densities and order parameters calculated from runs at different temperatures are larger than the experimental ones, suggest that the force parameters used to simulate the mixture E7 are slightly too attractive, constituting a source of inaccuracy.

Temp.	E7	5CB	7CB	8OCB	5CT
280 K	0.824 $\pm$ 0.004	0.820 $\pm$ 0.009	0.780 $\pm$ 0.008	0.88 $\pm$ 0.01	0.91 $\pm$ 0.01
290 K	0.78 $\pm$ 0.01	0.77 $\pm$ 0.01	0.78 $\pm$ 0.02	0.80 $\pm$ 0.01	0.90 $\pm$ 0.01
300 K	0.83 $\pm$ 0.01	0.82 $\pm$ 0.01	0.84 $\pm$ 0.02	0.84 $\pm$ 0.02	0.88 $\pm$ 0.03
310 K	0.84 $\pm$ 0.02	0.83 $\pm$ 0.02	0.84 $\pm$ 0.03	0.84 $\pm$ 0.03	0.89 $\pm$ 0.02
320 K	0.84 $\pm$ 0.02	0.82 $\pm$ 0.02	0.85 $\pm$ 0.03	0.86 $\pm$ 0.03	0.89 $\pm$ 0.03
330 K	0.82 $\pm$ 0.02	0.81 $\pm$ 0.02	0.83 $\pm$ 0.02	0.85 $\pm$ 0.03	0.86 $\pm$ 0.05

Table 6.6: Order parameters for different temperatures, calculated from the final 2 ns with the axes of inertia for the mixture overall (E7) and for each one of the different types of molecules within the mixture (5CB, 7CB, 8OCB and 5CT).

It might be considered that the order parameters obtained are rather high for a nematic phase. Two different tests were carried out to confirm that liquid crystalline phases simulated were indeed nematic rather than smectic. The first one consisted of a visual inspection of the snapshot of different simulations. This inspections are useful since they normally indicate reasonably clearly whether layers form in a sys-
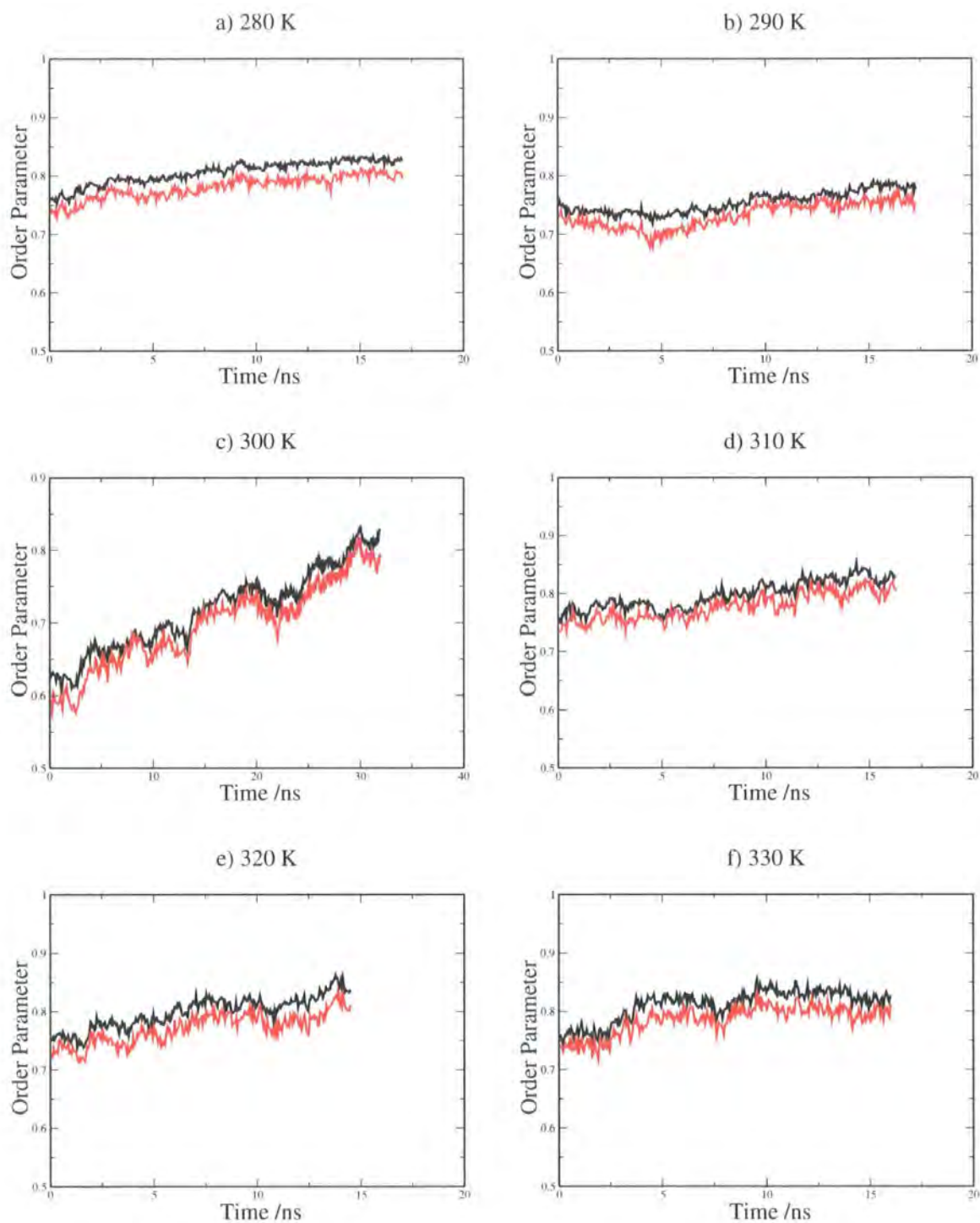
Figure 6.2: Uniaxial order parameters Q_{00}^2 for simulations of the liquid crystals mixture E7 calculated using the molecular axis of inertia and the vectors running along the spine of the molecule at the temperatures : a) 280 K, b) 290 K, c) 300 K, d) 310 K, e) 320 K and f) 330 K.
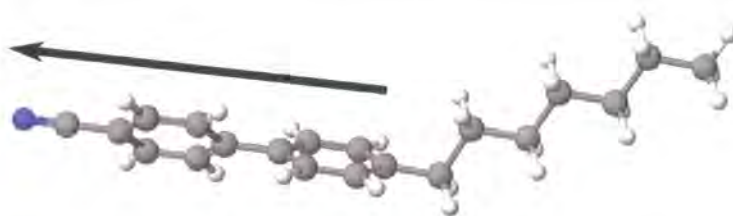
Figure 6.3: Vector used to define the orientation of the aromatic core. The figure shows 7CB but a similar vector is used for 5CB, 8OCB and 5CT.

tem. No layers can be appreciated in figure 6.4 for any of the temperatures exposed. Aside from that, it is also possible to notice that the different types of molecules are homogeneously distributed across the bulk system. This assertion is corroborated in figure 6.5, where the different types of molecules are presented separately. Figure 6.5 shows that each type of molecules is homogeneously distributed throughout the system, with the possible exception of 5CT, which exhibits a slight clustering.

In addition, the radial distribution function parallel to the director vector was also calculated. The results are shown in figure 6.6. The pattern exhibited by the function for all the temperatures is characteristic of the isotropic and nematic phases.

It is possible to notice in table 6.6 that the order parameters for 5CB, 7CB and 8OCB are similar at the same temperature. However, the ordering of the 5CT is higher. This is not surprising since this type of molecule has an extra aromatic ring, which increases its tendency to be ordered.

Mixtures of liquid crystals have been previously studied for different models. Bemrose *et al.* [134,135] studied the order parameter of a mixture with two components using a Gay-Berne single site model. The axial ratio of the two components of the mixture were 3.5:1 and 3:1. This work showed that the order of a type of molecule is higher as its molecular length increases, which agrees with the results presented here. There have been a series of theoretical studies by Lekkerkerker [136–139] and Sluckin [140] which presented the same conclusion.

To check whether the phases obtained are simply mechanically stable or are thermodynamically stable, an extra simulation has been performed to quench a bulk system of the E7 mixture from the isotropic liquid phase into a nematic one at a temperature of 300 K. The evolution of the density during this simulation is shown
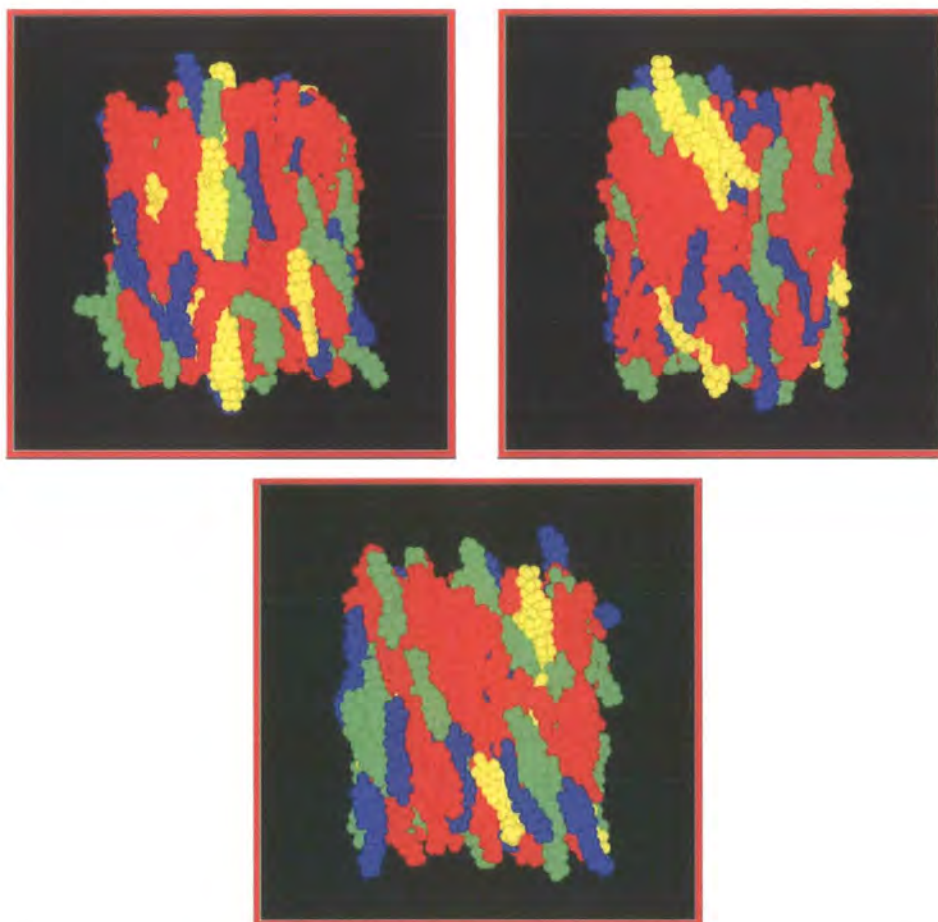
Figure 6.4: Snapshots of the simulations at three different temperatures: 280 K (top left), 300 K (top right) and 320 K (bottom). The color coding corresponds to different types of molecule: 5CB (red), 7CB (green), 8OCT (blue) and 5CT (yellow).
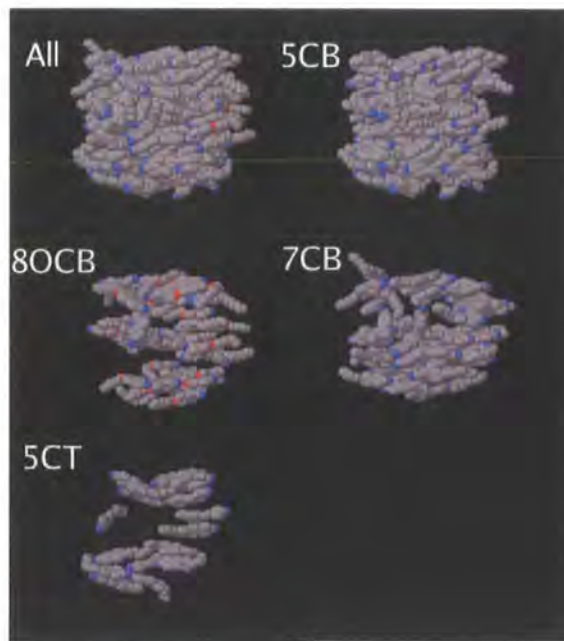
Figure 6.5: Snapshot showing the distribution of molecules in the bulk system regarding the type of molecule at a temperature of 300 K.

in figure 6.8. Density increases gradually over the first 80 ns of the run. During the same period the order parameter gradually grows from a value close to zero to a similar one obtained in the simulation at 300 K (see fig. 6.9). The main changes in both the density and the order parameter occur over the period from 50 ns to 80 ns. As with single site potentials this rise in order parameter corresponds to the alignment of the local director for clusters of molecules which have already formed in the simulation. The overall increment in density throughout the simulation is 0.03 g cm^{-3} approximately and the change in the order parameter is approximately 0.7. Two snapshots corresponding to the beginning and the ending can be seen in figure 6.7. These two snapshots perfectly illustrate the difference in orientation between the initial and final configurations. Therefore it is possible to state that the isotropic-nematic phase transition has been successfully accomplished. It is also possible to assert that the system simulated directly from the nematic phase at 300 K is thermodynamically stable, rather than just mechanically stable.

After 100 ns of simulation, the transition period is over, as can be seen in figure 6.9, and the system can be considered equilibrated, since there is no significant change in the order parameter during the final 15 ns of simulation. The order param-

a) 280 K   b) 300 K
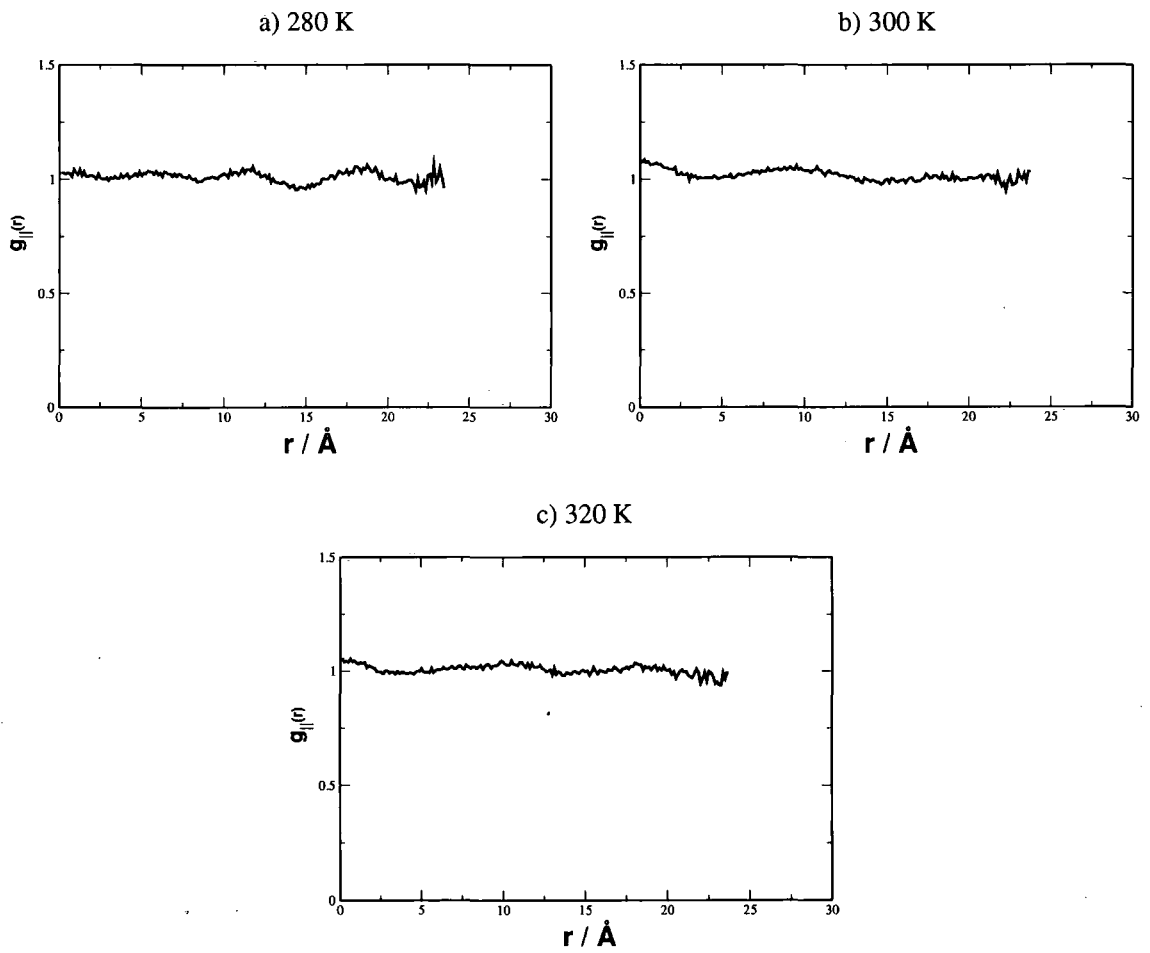
c) 320 K

Figure 6.6: $g_\parallel(r)$ calculated for three different temperatures: a) 280 K, b) 300 K and c) 320 K.

(a)   (b)

(c)
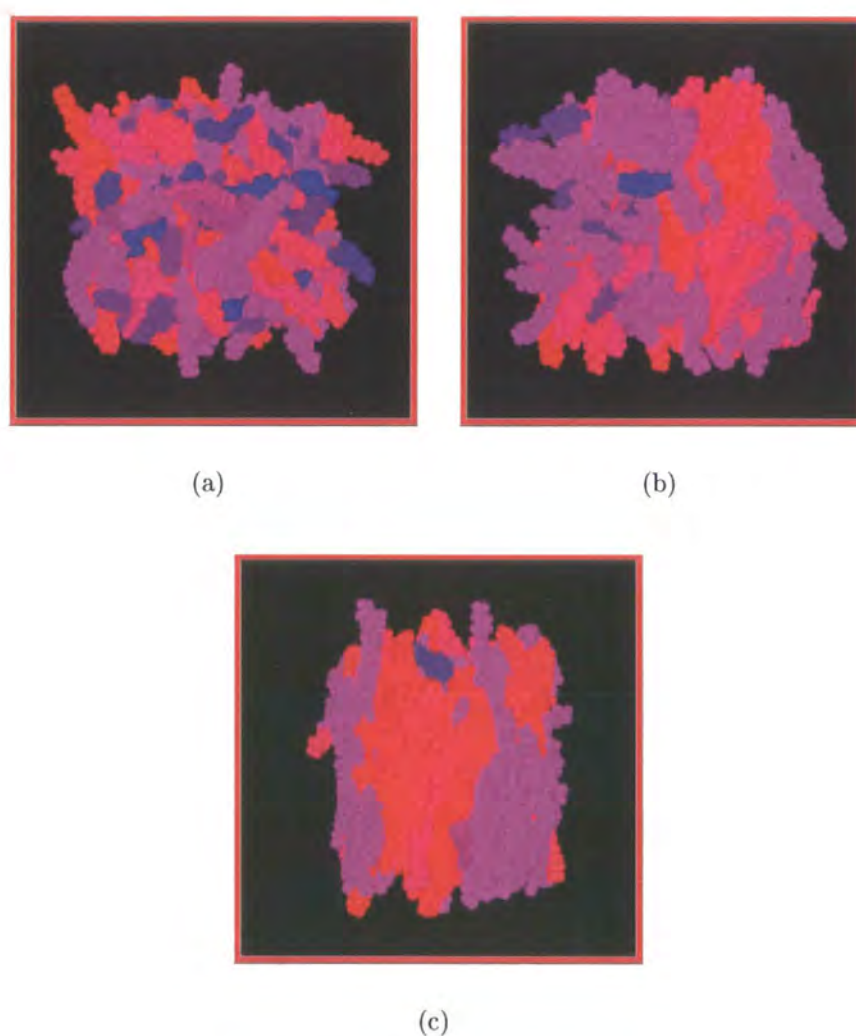
Figure 6.7: Snapshots corresponding to the beginning (a), middle (b) and ending (c) of the simulation of the isotropic-nematic phase transition. The molecules have been color coded according to their orientation with respect to the director vector. It is possible to see in (b) that ordered clusters form in the simulation box before the system becomes nematic in (c).

eter averaged over the final 5 ns is shown in table 6.7, alongside the order parameters for each one of the molecular types. The overall order parameter obtained is similar to the one obtained in the simulation run at the same temperature (300 K) but started directly from the nematic phase (table 6.6). However, the order parameters for the different types of molecules are not as similar. Specifically for 5CT, which differs in 0.1 from one system to the other. This occurs because in the system we see less clustering of the longer 5CT molecules. Consequently, the local environment of 5CT does not lead to as high orientational order.

Type of Molecule	Order Parameter
E7	0.81 ± 0.01
5CB	0.81 ± 0.01
7CB	0.82 ± 0.01
8OCB	0.81 ± 0.02
5CT	0.79 ± 0.01

Table 6.7: Order parameters for the simulation started from the isotropic phase and quenched into a nematic phase. All the order parameters have been calculated using the molecular axis of inertia.

6.4 Dihedral Angle Distribution

The distribution of the different dihedral angle configurations is a key factor in the orientational order of the molecules, as well as in their orientational correlation. For instance, the distribution of the dihedral angles in an aliphatic chain in a mesogen can confer to it a rod-like aspect. Moreover, in the case of cyanobiphenyl derivatives the inter-ring dihedral angle can transform a flat rigid core into an angular one, with each of the aromatic rings in a different plane.

The particular dihedral angles considered are shown in figure 6.10. For clarity the dihedral angles in each molecule have been named using different letters from the Greek alphabet, hence φ corresponds to the 7CB, α to the 8OCB and γ to the 5CT. To discriminate between different dihedral angles within the same type of
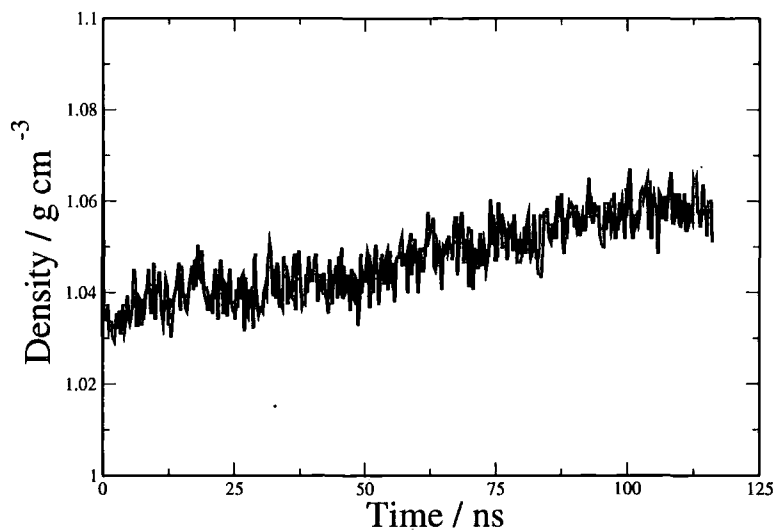
Figure 6.8: Evolution of the density with respect to time for the mixture of liquid crystals, E7, simulated as it changes from the isotropic phase into the nematic phase.
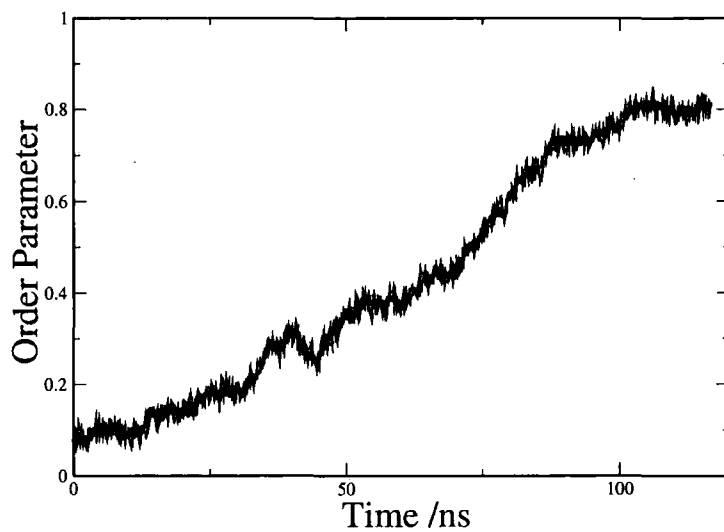
Figure 6.9: Evolution of the order parameter calculated using the molecular axis of inertia during the transition between the isotropic and the nematic phases.

molecule, these have been numbered (i.e. φ_1, φ_2, etc).
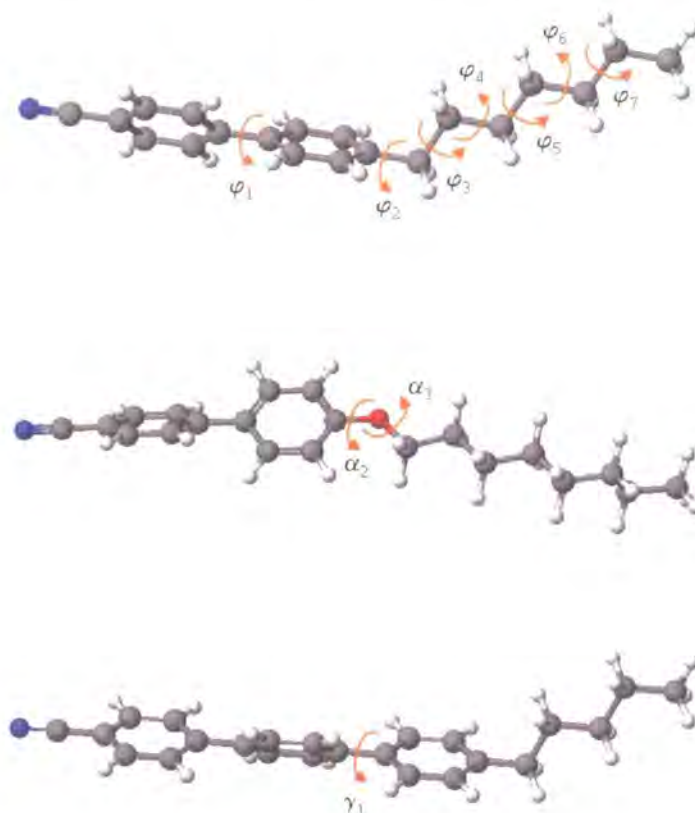
Figure 6.10: Dihedral angles studied in the 7CB (top), 8OCB (middle) and 5CT (bottom).

In figure 6.12 it is possible to observe that the rotation about the inter-ring bonds (φ_1 and γ_1) is in good agreement with the results obtained for the inter-ring dihedral angle in the cyanobiphenyl using the same potentials, obtained from *ab initio* calculations using DFT methods in ref. [141]. Figure 6.12 also shows the distribution of two dihedral angles of the molecule 8OCB. In contrast with the other types of molecules, in 8OCB the aliphatic chain is linked to the aromatic core through an oxygen atom. Although there is practically free rotation about the phenyl-oxygen bond, the dihedral angle rotating about the bond between the oxygen and the first carbon of the aliphatic chain has a clear preference for angles close to 180^0. It is possible to notice a difference between the dihedral angles α_2 and α_3 and their homologous φ_2 and φ_3 in 7CB (fig. 6.13). In 7CB there is no free

rotation in φ_2, but the aliphatic chain prefers to line perpendicular to the plane of the second phenyl ring. This can be concluded from the symmetry of the dihedral angle distribution of φ_2 in figure 6.13, where it is possible to see two maxima at 90^0 and 270^0. This does not apply to α_2 in 8OCB, where the aliphatic chain prefers to line in the same plane as the second phenyl ring.
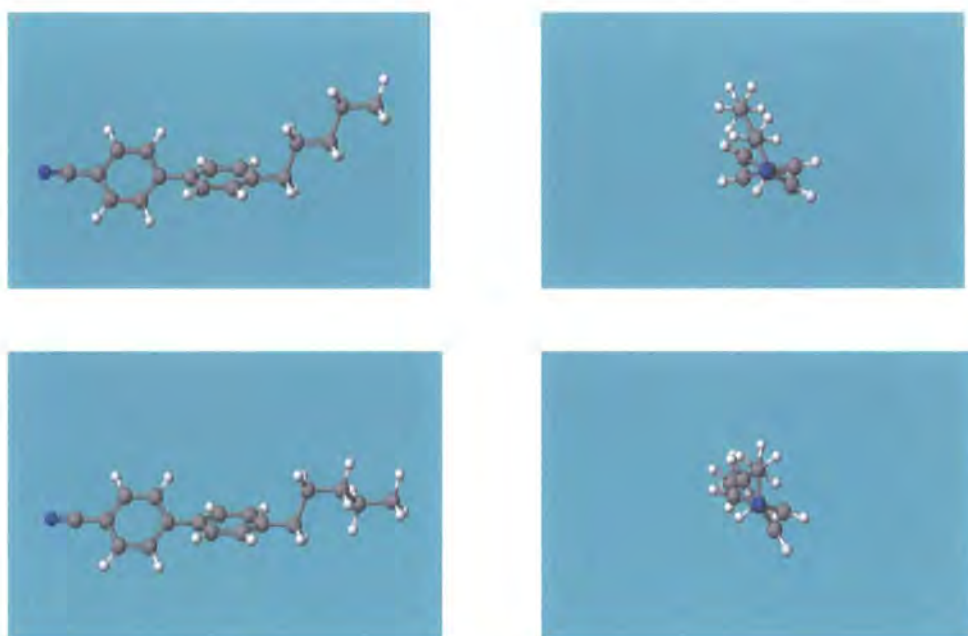
Figure 6.11: Different conformations adopted by the aliphatic chain of a typical mesogen (5CB) from a side view (left) and an end view (right). An odd-even effect can be appreciated in the dihedral angles of the aliphatic chain (see text).

In figure 6.13 the distribution of the dihedral angles along the 7CB aliphatic chain are shown. By observing the distributions of $\varphi_3, \varphi_4, \varphi_5$ and φ_6 it is possible to notice that the population of the *trans* conformation is higher for φ_3 and φ_5 than for φ_4 and φ_6, creating an odd-even effect (see figure 6.11). This is corroborated in table 6.8, where it is possible to see the percentage of each configuration, calculated by integrating over all the dihedral angle distributions. This effect, consistent with previous simulations for different types of mesogens such as *trans*-4-(*trans*-4-n-pentylcyclohexyl)-cyclohexylcarbonitrile (CCH5) [118], 5CB [120] and 4,4'-di-

n-pentyl-bibicyclo[2.2.2]octane [119], can be found in nematic phases, but not in isotropic or gas phases [122,142], and it is due to the fact that in the nematic phase, the aliphatic chain tends to be as elongated as possible, adopting in some cases *gauche* conformations (as can be seen in figure 6.11) to confer a calamitic shape to the mesogen and is favoured by the nematic field. It is possible to appreciate that this effect only lasts for the first carbons in the chain, since the populating of φ_7 is more similar to the one of φ_6 than to the one of φ_5.
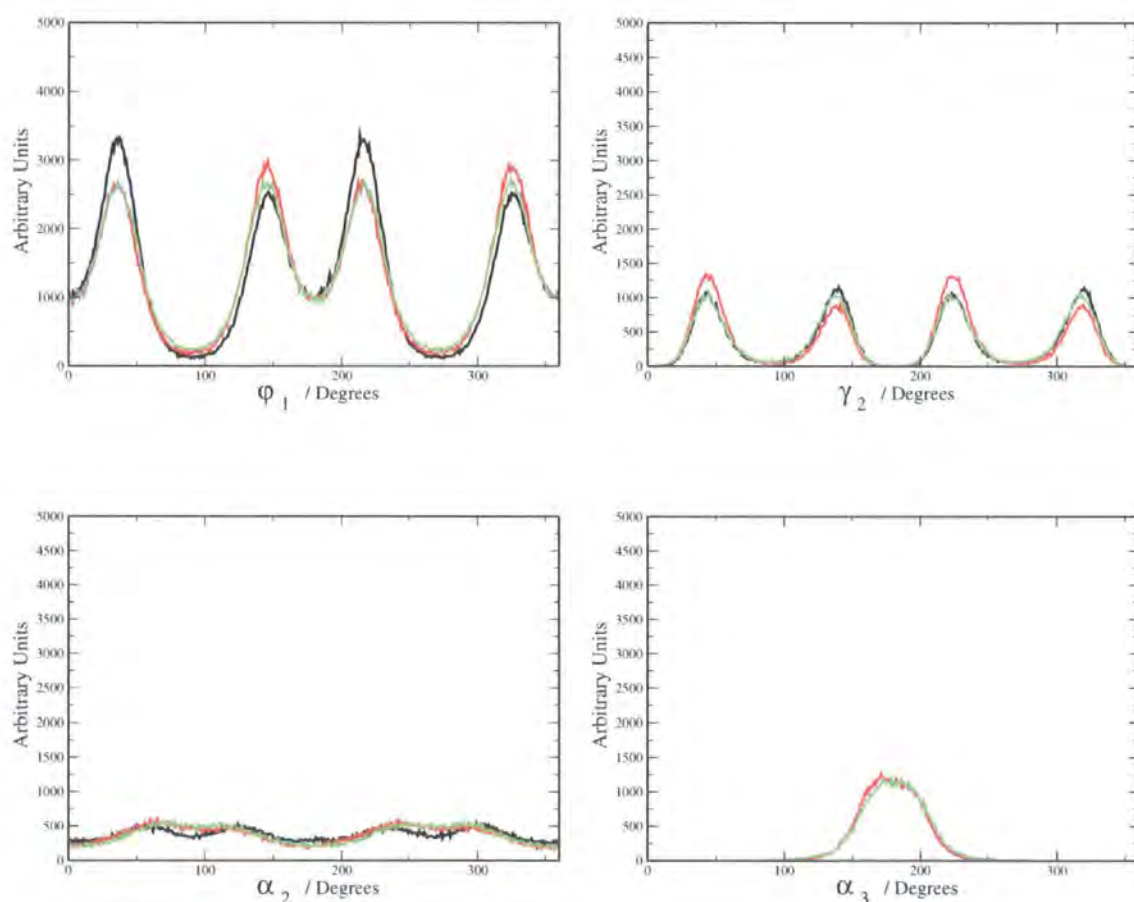
Figure 6.12: Dihedral distribution function calculated for different dihedral angles belonging to the three types of molecules 7CB (φ_1), 8OCB (α_2, α_3) and 5CT (γ_1) (see fig. 6.10) at three different temperatures: 280 K (black line), 300 K (red line) and 330 K (green line).

To check whether the environment at different temperatures influences dihedral angles the Boltzmann inversion has been calculated for $\varphi_1, \varphi_2, \varphi_3$ and φ_4. It can be seen in figure 6.14 that there is no major change in the torsional potentials for the
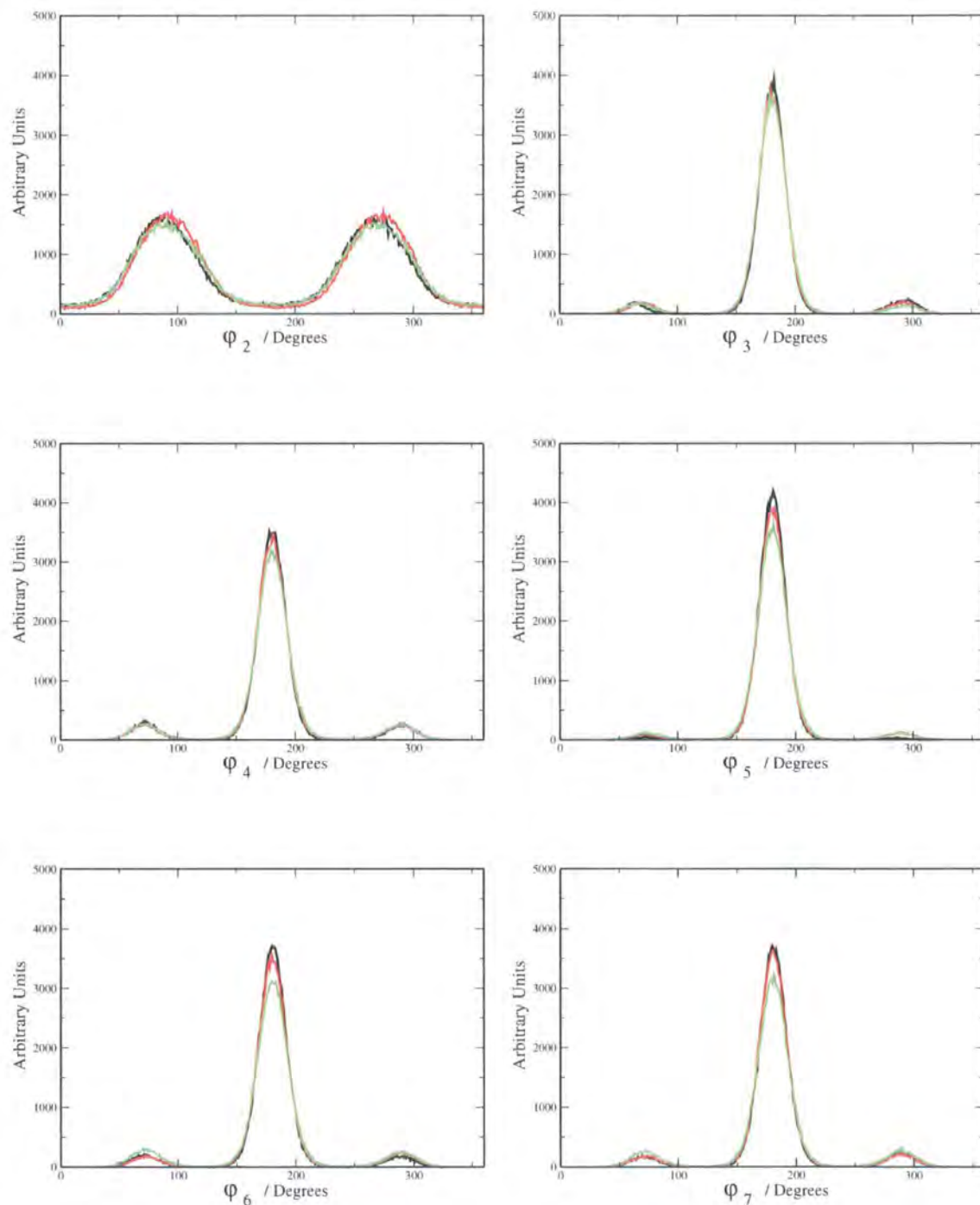
Figure 6.13: Dihedral angle distribution for dihedral angles in the aliphatic chain of the molecule 7CB (see fig. 6.10). The distribution has been calculated for three different temperatures: a) 280 K (black), b) 300 K (red) and c) 330 (green).

Dihedral Angle	trans	gauche +	gauche -
φ_3	94.8 %	2.9 %	2.3 %
φ_4	87.6 %	6.2 %	6.3 %
φ_5	96.4 %	1.9 %	1.7 %
φ_6	88.8 %	5.5 %	5.7 %
φ_7	89.1 %	5.6 %	5.3 %

Table 6.8: Percentage of trans conformation in the aliphatic chain dihedral for the molecule 7CB at 300 K.

three different temperatures for the dihedral angle studied. This was to be expected since there is little change in orientational order in going from one temperature to the next.

6.5 Orientational Correlation Function $g_2(r)$ and Dipole Correlation Function $g_1(r)$

The orientational correlation function $g_2(r)$, detailed in section 2.6.3, has been calculated for each type of molecule within the mixture at a temperature of 300 K, for the simulation started directly from the nematic phase. This monitors the correlation between the orientation of a certain type of molecule and the rest of the molecules present in the system. Intermolecular distances have been measured from the centre of the first aromatic ring in each molecule and the angle between two different molecules defining their orientational correlation has been calculated using the inertia axis. The results can be appreciated in figure 6.15. A common feature between all the types of molecule is the higher value of $g_2(r)$ at short distances, in an approximate range of $3.5 - 5$Å. It is noteworthy that at larger distances, the orientational correlation gradually decays to approximately the square of the order parameter, for each species[2]. It is possible to notice a higher orientational corre-

---

[2]Strictly, we only expect the long range value of $g_2(r)$ for a species to tend to $\langle S_2 \rangle$ if the correlation measured is restricted to an average over molecules of that species. However, in practice
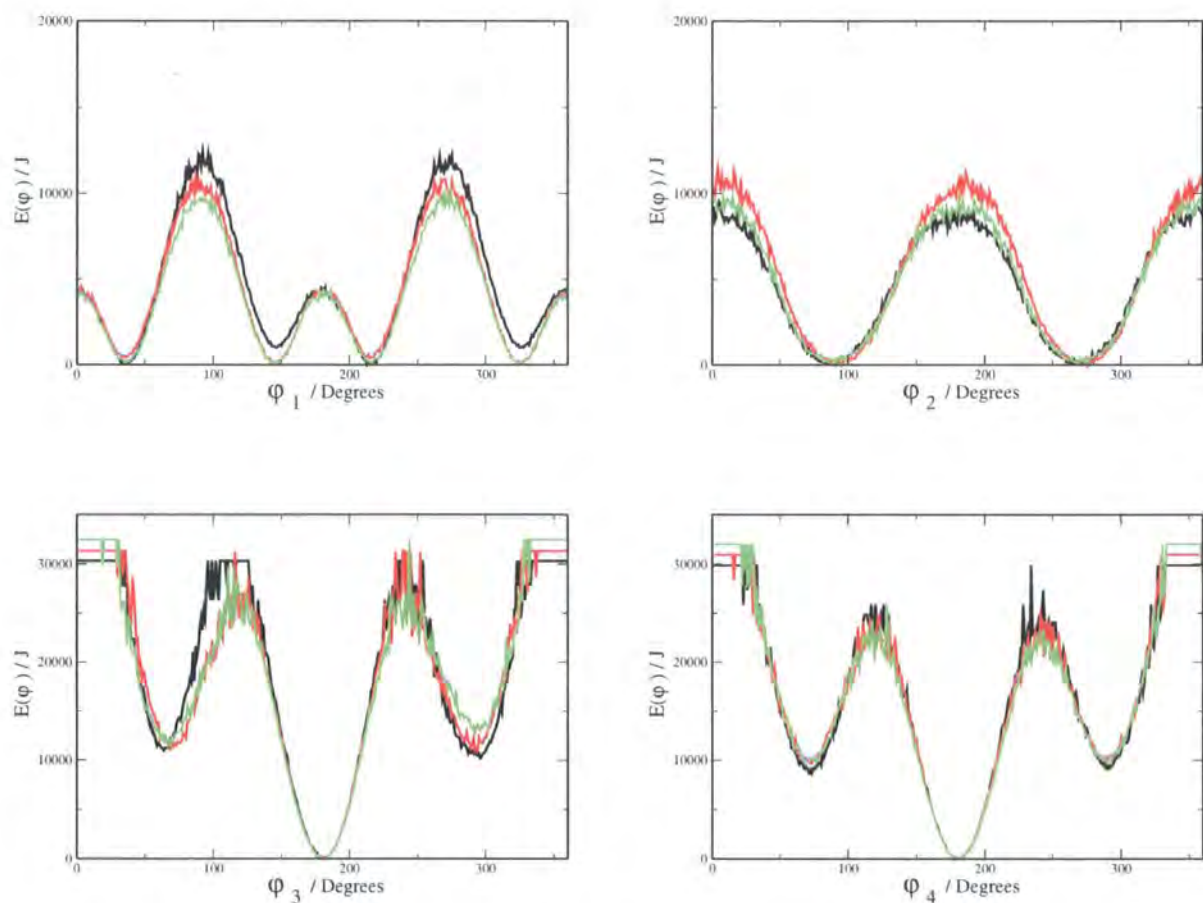
Figure 6.14: Torsional potentials calculated with a Boltzmann inversion for four different dihedral angles ($\varphi_1, \varphi_2, \varphi_3$ and φ_4) of the molecule 7CB (see fig. 6.10) at three different temperatures: 280 K (black line), 300 K (red line) and 330 K (green line).

lation for the 5CT. The extra aromatic ring present in this molecule confers on it the ability to orientate more strongly with neighbouring molecules. This result is in agreement with the order parameter results in table 6.6, where it is possible to notice that the order parameter of 5CT is larger than for the other molecular types. While the relative order parameters can be sensitive to the number of molecules present for each species (system size effects) we expect the relative $g_2(r)$ calculated here not to be.

$g_2(r)$ has also been calculated considering only the correlation between molecules of the same type. The results obtained in this way are rather similar to those shown in figure 6.15, although $g_2(r)$ for 5CT was slightly higher. This is consistent with the minor clustering of this molecule observed in figure 6.5.
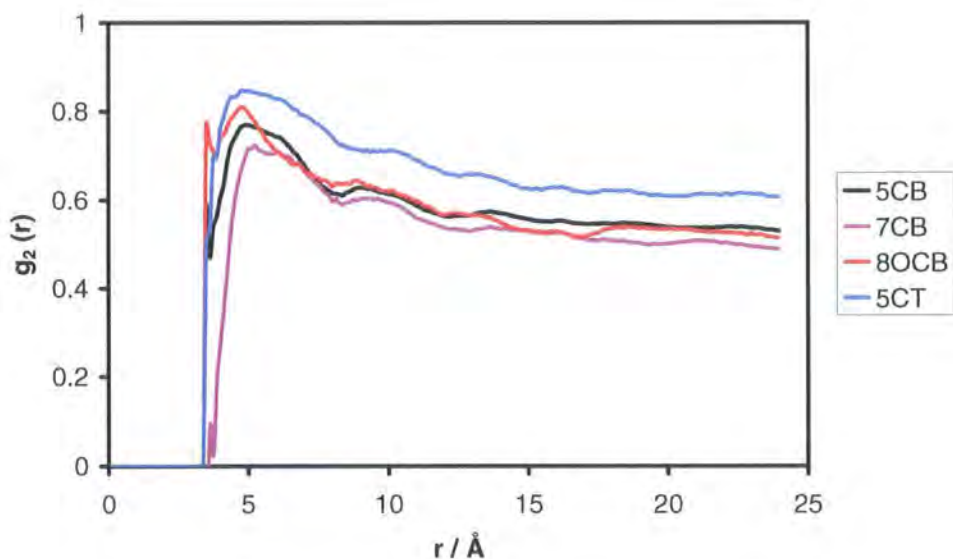
Figure 6.15: $g_2(r)$ calculated for each type of molecule within the liquid crystals mixture E7.

It is well known that the dipole in cyano-aromatic derivative liquid crystals is rather large (for instance, the experimental measurement of the dipole moment in 5CB produces a result of 4.85 D). Thus a strong anti-parallel orientation is to be

---

the results are the same as the $g_2(r)$ measured here, albeit more noisy.

expected in a mixture formed from cyano-biphenyl / cyano-terphenyl derivatives. Calculations of the pairwise dipole correlation function, $g_1(r)$, have been performed measuring the distance between molecule from the cyano group and the centre of the first phenyl ring. $g_1(r)$ has been calculated at two different temperatures to check whether it is temperature dependent. The results are shown in figure 6.16. anti-parallel pairwise correlation represented by negative peaks can be appreciated in both plots (a) and (b) at an approximate intermolecular distance of $r \approx 3.5\,\text{Å}$. Moreover, it is possible to appreciate a wide positive peak centred at an intermolecular distance of $r \approx 6.5\,\text{Å}$ for the cyano group and it is also possible to observe a second wide negative peak at long distance ($r \approx 8\,\text{Å}$) for the first ring.

Previous studies on the dipole correlation function of the PCH5 (4-(4-pentyl-cyclohexyl)-benzonitrile) [143], in the pretransitional region (i.e., just above the isotropic-nematic transition) have shown that there is anti-parallel dipole correlation in the isotropic phase within the pretransitional region. Hence, the calculated value of the Kirkwood factor g_1 is negative and consistent with both experimental and simulation results [143]. Therefore, considering that the structure of 5CB and the PCH5 are rather similar, it definitely makes sense to assume that the anti-parallel dipole correlation exists at lower temperatures in the nematic phase.

It must be stressed that not only do anti-parallel dipole correlations exist at short range, but parallel dipole correlations exist as well. However, the former are significantly more frequent and therefore their contribution to the overall dipole correlation function is larger, masking the contribution from parallel dipole correlation. This has been inferred from experimental dielectric studies of liquid crystals in both isotropic and none polar liquid crystal solvents [144–149]. In these works, the behaviour of different molecules was determined by a balance between the parallel and anti-parallel dipole correlation. In order to assess the relative importance of antiparallel and parallel correlation, $g_1(r)$ was decomposed into two separated functions. In one of them, just the parallel correlations were registered, whereas in the other just the negative one was considered. The histograms produced by the two functions were normalized separately. The results obtained in this way are shown in figure 6.17. It is noted that even though a parallel dipole correlation exists throughout the
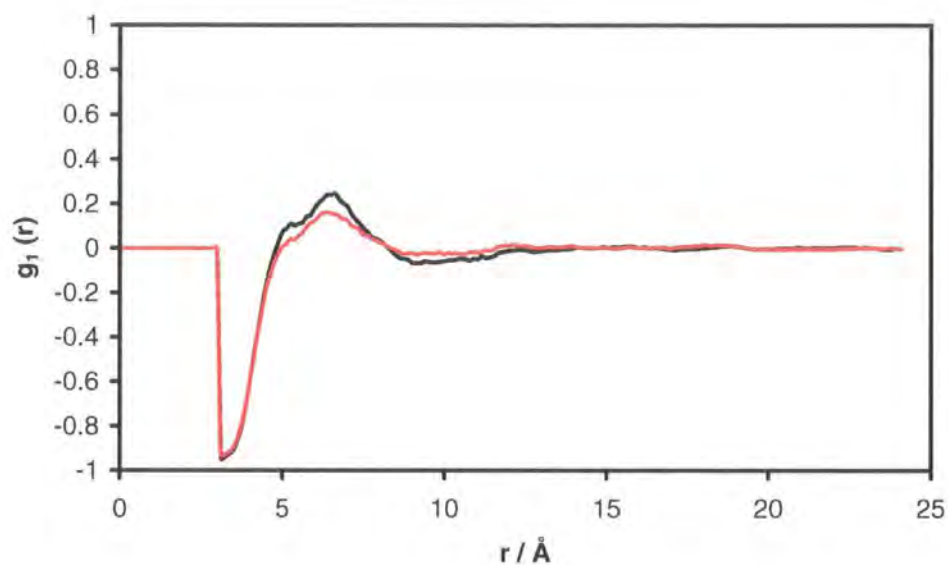
(a)
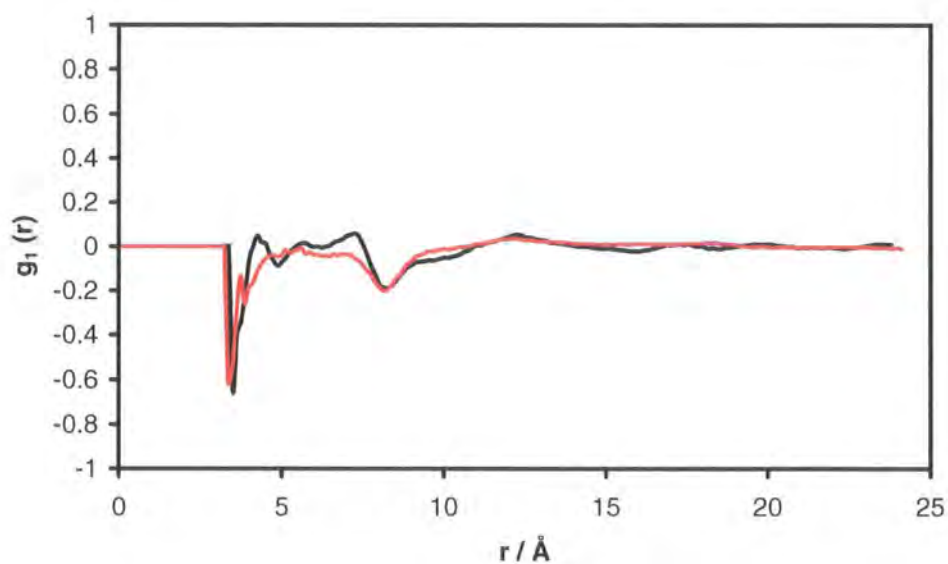
(b)

Figure 6.16: Pairwise dipole correlation function $g_1(r)$ measured over all types of molecule in the mixture E7. Distances between molecules have been measured from the cyano groups (a) and the centres of the first phenyl ring, which is bonded to the cyano groups (b). In both cases the black line represents $g_1(r)$ at 280 K and the red one represents $g_1(r)$ at 330 K.
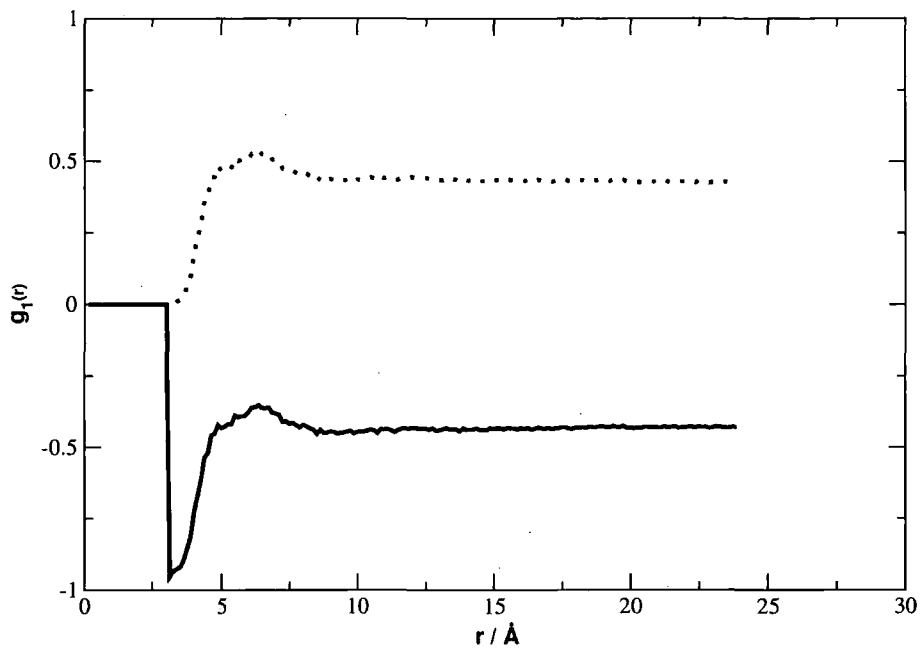
(a)
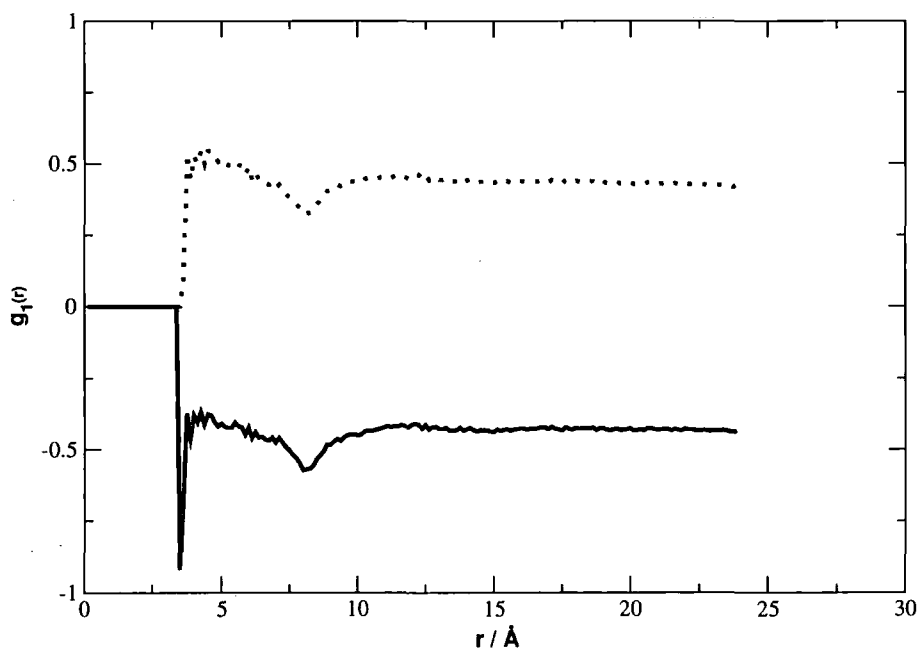
(b)

Figure 6.17: Pairwise dipole correlation function, $g_1(r)$, resolved into parallel (dotted line) and anti-parallel (bold line) components, at the temperature of 300 K. The distances between molecules have been measured from the cyano group (a) and the centre of the first phenyl ring (b).

entire simulation box, this is weaker and its peaks are not so localized as in the case of the anti-parallel dipole correlation. Although this can be appreciated for $g_1(r)$ calculated using both the cyano and the first phenyl ring intermolecular distances, this contrast is more noticeable in the case of the former.

From the results shown in figures 6.16 and 6.17, two possible configurations can be suggested, as shown in figure 6.18. The configuration labeled as (a) is based on the two anti-parallel peaks found at ≈ 3.5 Å in figure 6.17 (a) and at ≈ 8 Å in figure 6.17 (b). Both distances correspond to the cyano-cyano group and first phenyl-first phenyl distances in figure 6.18 (a), respectively. Another possible configuration, although less probable than the other, is the one labeled as (b) in figure 6.18. This is based on the anti-parallel peak observed at ≈ 3.5Å in figure 6.17 (b), corresponding to the distance between the first phenyl rings.
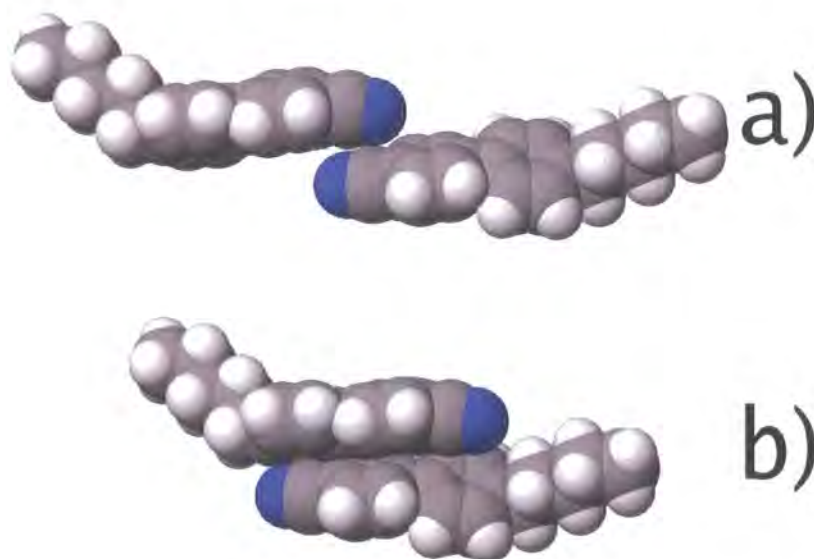
Figure 6.18: Suggested preferred configurations for the pairwise molecular orientations, based on $g_1(r)$ (see figures 6.16 and 6.17).

6.6   Conclusions

The liquid crystal mixture E7 has been simulated in the nematic phase at a fully atomistic (all-atom) simulation level. This is the first time that a multi-component liquid crystal mixture has been simulated in detail for this type of model. This paper reports the growth of a nematic phase from an isotropic liquid, noting that it occurs over a 100 ns timescale. This timescale is much longer than expected and almost an order of magnitude longer than the timescale required for united atom models.

We find that the cyanoterphenyl component 5CT is more highly ordered than the cyanobiphenyl components in the mixture. We have also been able to look in detail at dipole correlation in E7. Individual molecules show both parallel and anti-parallel dipole correlation. However, the anti-parallel dipole correlation is more localised and two distinct molecular pair configurations can be recognised which account for the form of the dipole correlation factor, $g_1(r)$.

The expected temperature dependence of the order parameter was not observed in this study. This is almost certainly because the simulated density is slightly too high ($\sim 3\%$). This increases the stability of the nematic phase, leads to a higher than expected ordering of the molecules and removes the expected strong variation of $\langle S_2 \rangle$ with temperature.

Finally, we note that the work presented here opens up the possibility of using atomistic simulation as a means of studying material properties in liquid crystals. Work in this area will be presented in chapter 7.

Chapter 7

Material Properties of the Mixture of Liquid Crystal Molecules E7

7.1 Rotational Viscosity

7.1.1 Introduction

In the design of new liquid crystal displays (LCDs), the material properties of the compounds forming such devices are crucial to optimize the final performance of the devices. One of this key material properties is the rotational viscosity, henceforth named as γ_1. The importance of γ_1 can be appreciated by the fact that both switching times of a twisted nematic liquid crystal display, when an electric field is turned on / off depend on this material property.

$$\tau_{on} = \frac{\gamma_1 d^2}{\epsilon_0 \Delta\epsilon} \left(\frac{1}{U^2 - U_0} \right),$$
(7.1)

$$\tau_{off} = \frac{\gamma_1 d^2}{k\pi^2},$$
(7.2)

where d is the cell thickness, k is a constant depending on the elastic constants of the material, U is the voltage across the cell, U_0 is the threshold voltage, ϵ_0 is the permittivity of the free space and $\Delta\epsilon$ is the dielectric anisotropy.

The rotational viscosity can be calculated using different experimental tech-

niques. An electro-optical method based on the phase-decay-time measurement of a parallel-aligned liquid crystal cell under small excitation voltage [150] was used by Wu and Wu to calculate the rotational viscosity of the liquid crystal mixture E7 amongst others. These experimental results were fitted using the Osipov-Terntjev [151] and the Diogo-Martis [152] theories. Wu and co-workers [153] used values of the temperature-dependent Leslie viscosity coefficients obtained experimentally for 4-methoxybenzylidene-4'n-butylaniline (MBBA) to fit the analytical functions of Leslie, which subsequently were used to calculate the rotational viscosity of different compounds, such as the mixture of liquid crystals, E7. Zakharov and Dong [154] used NMR data to obtained experimentally the order parameters of the mesogens 4-n-octyloxy-4'-cyanobiphenyl (8OCB) and used it to calculate the orientational time correlation functions which allowed them to compute the rotational viscosity.

Several methods have been described to calculate the rotational viscosity from molecular simulations. These are divided into non-equilibrium and equilibrium methods. Non-equilibrium methods have been used by Kuwajima and Manabe [155] to calculate the rotational viscosity from atomistic simulations by applying an aligning field. Sarman used different non-equilibrium methods to calculate the rotational viscosity from a single-site simulation by constraining the director [156, 157]. Equilibrium methods use equilibrium molecular dynamics simulations to calculate the rotational viscosity using the appropriate Green-Kubo formulae, derived by Foster [158] and rederived by Sarman and Evans [159] and used to calculate the rotational viscosities of a single-site system formed from mesogenic rods [160, 161]. These methods are described in section 7.1.2.

7.1.2 Computational Method

As above exposed, two different techniques have been applied in the evaluation of the rotational viscosity, the DAVFC and the DMSD methods. The first one was derived by Evans and Sarman form the SLLOD equations of motion [159]. They showed that the rotational viscosity is given by the following expression:

$$\gamma_1 = \frac{1}{\beta V \int \langle \Omega_2(t)\Omega_2(0) \rangle}, \tag{7.3}$$

where β is the product between the Boltzmann constant and the temperature, V is the volume and Ω_2 is defined below.

Five different steps were applied in the calculation of γ_1 using this method. In first place the director vector was calculated for every timestep diagonalizing the ordering tensor, as explained in section 1.4. The orientation of the different molecules were represented by the molecular axes of inertia. Secondly the orientation of the director vector was contrasted with the orientation of the previous time step director vector, in order to check that this had not changed. In third place the director angular velocity was calculated using the formula:

$$\Omega = \mathbf{n} \times \bar{\mathbf{n}}, \tag{7.4}$$

where $\mathbf{n}$ is the director vector and $\dot{\mathbf{n}}$ its derivative with respect to time. Fourthly, the angular velocity was transformed into the director frame in such a manner that $\Omega \rightarrow (\Omega_1, \Omega_2, 0)$, using the formula:

$$\begin{pmatrix} \Omega'_1 \\ \Omega'_2 \\ \Omega'_3 \end{pmatrix} = \begin{pmatrix} u_{1x} & u_{1y} & u_{1z} \\ u_{2x} & u_{2y} & u_{2z} \\ u_{3x} & u_{3y} & u_{3z} \end{pmatrix} \begin{pmatrix} \Omega_1 \\ \Omega_2 \\ \Omega_3 \end{pmatrix}, \tag{7.5}$$

where $\Omega'_3 = 0$ and the first term in the right hand side of the equation corresponds to the rotation matrix and is created from the eigenvectors associated with the three eigenvalues obtained from diagonalizing the ordering tensor (eq. 1.3), as explained in section 1.4:

$$\begin{aligned} \mathbf{u}_1 &= \left(u_{1x}, u_{1y}, u_{1z} \right), \\ \mathbf{u}_2 &= \left(u_{2x}, u_{2y}, u_{2z} \right), \\ \mathbf{u}_3 &= \left(u_{3x}, u_{3y}, u_{3z} \right). \end{aligned} \tag{7.6}$$

This transformation is very important because equation 7.3 was derived on the assumption that the director orientation is constant.

Finally, the director angular correlation function is averaged over many different time origins in order to produce good statistics, and thus accurate results.

A second method has been implemented using the director mean square displacement (DMSD). In this method the rotational viscosity may be evaluated by means of the formula:

$$\gamma_1 = \lim_{t \to \infty} \lim_{V \to \infty} \frac{2t}{\beta V \left\langle \left| \mathbf{n}\left(t\right) - \mathbf{n}\left(0\right) \right|^2 \right\rangle}, \tag{7.7}$$

where $\mathbf{n}$ is the director vector. The process to obtain γ_1 from the DMSD is described below:

- firstly the director vector was calculated for every timestep diagonalising the ordering tensor,

- secondly, its orientation was checked with respect to the previous timestep to prevent the director flipping through approximately 180^0;

- thirdly, the director mean square displacement, given by

$$\left\langle \left| \mathbf{n}\left(t\right) - \mathbf{n}\left(0\right) \right|^2 \right\rangle, \tag{7.8}$$

was calculated, (here it was is necessary to average over many time steps in order to achieve good statistics);

- finally, the director mean square displacement was plotted against time.

At long times it is possible to fit DMSD using a linear expression:

$$\left\langle \left| \mathbf{n}\left(t\right) - \mathbf{n}\left(0\right) \right|^2 \right\rangle = mt + c. \tag{7.9}$$

Subsequently the rotational viscosity γ_1 can be calculated using the expression:

$$\gamma_1 = \frac{2}{m\beta V}. \tag{7.10}$$

7.1.3   Results

DAVCF have been calculated at six different temperatures using the method detailed in the previous section. Plots showing the director angular velocity correlation function against time can be seen in figure 7.1. The pattern exhibited by the DAVCF is similar to that observed in previous computer simulations of both single site [159] and atomistic models [160]. It is noteworthy that atomistic simulations present significantly noisier DAVCF functions than more simplistic models.

The integration of the DAVCF has been accomplished in order to evaluate the rotational viscosity of the mixture E7, using equation 7.3. The results of these calculations are shown in table 7.1. As was expected, the value of γ_1 decreases as the temperature increases. γ_1 calculated for the 280 K simulation was 484 ± 1 mPa s. This value is one order of magnitude larger than the values of γ_1 calculated for the rest of the temperatures. Differences between γ_1 calculated for consecutive temperatures decrease as the temperature increase. There is, however, an anomalous behaviour in the simulation run at 290 K which exhibited a lower order parameter. For this temperature the rotational viscosity is considerably smaller than the correspondent to the immediately higher temperature of 300 K.

T / K	$\int_0^\infty \langle \Omega_2(t) \cdot \Omega_2(0) \rangle \, dt \, / \, ps^{-1}$	$\gamma_1 / mPa\,s$
280	7.500×10^{-8}	484 ± 1
290	1.620×10^{-6}	23.00 ± 0.07
300	5.000×10^{-7}	76.6 ± 0.3
310	1.110×10^{-6}	35.5 ± 0.1
320	1.448×10^{-6}	27.9 ± 0.1
330	1.938×10^{-6}	21.34 ± 0.08

Table 7.1: Rotational viscosity calculated using the DAVCF.

Calculation of director mean square displacements have also been undertaken. The results of these are exhibited in figure 7.2. Again, the pattern obtained from the DMSD is very similar to the ones obtained in previous simulations [160]. By using equation 7.10, it is possible to calculate γ_1 from the slope of the DMSD shown
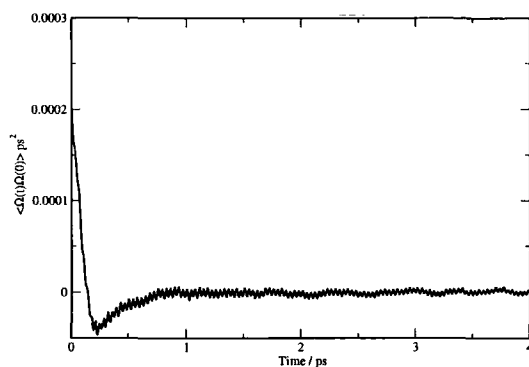
(a) 280 K   (b) 290 K
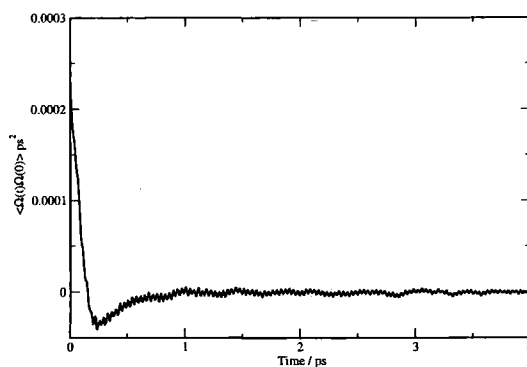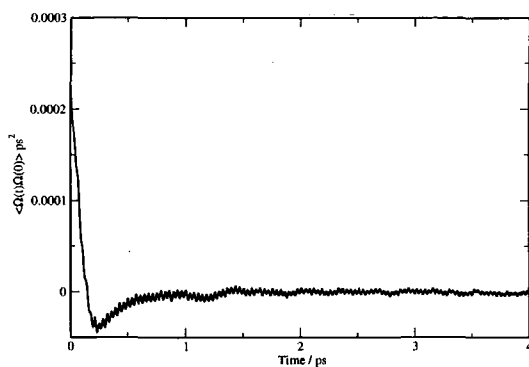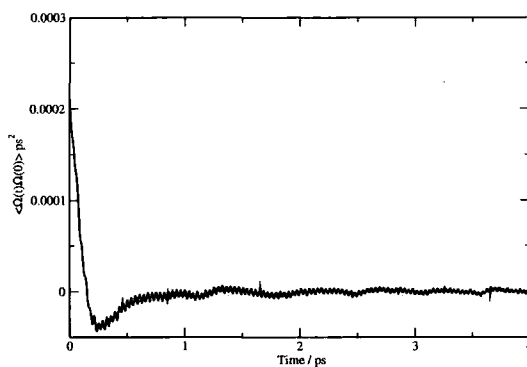
(c) 300 K   (d) 310 K
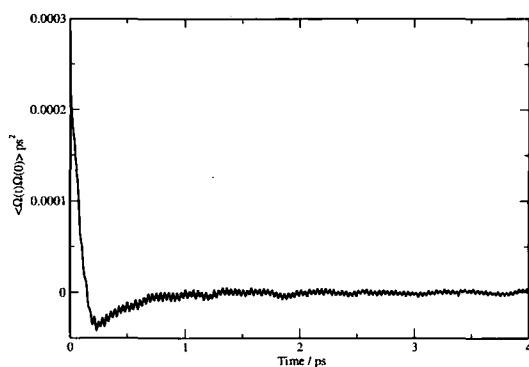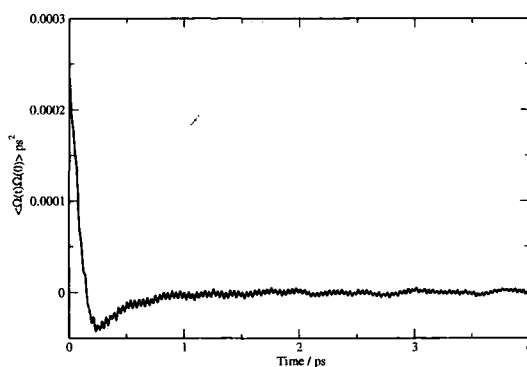
(e) 320 K   (f) 330 K

Figure 7.1: Angular velocity correlation function calculated at six different temperatures for the mixture of liquid crystals E7.

in figure 7.2. The results of these calculations are shown in table 7.2. As with the rotational viscosities calculated using the DAVCF, these decrease as the temperature is increased. However, this time there is no unexpected behaviour at 290 K. The values of γ_1 provided by calculations using DMSD are almost twice as large as those found using the DAVCF. However, the standard deviation of the former is slightly larger than the the latter. Experimental results presented by Wu and Wu [150] and theoretical results obtained from analytical functions of Leslie coefficients [153] provided similar results for γ_1 for the mixture E7. At approximately 320 K, γ_1 was in a range of $\sim 35 - 50$ mPa s. This result is certainly smaller that the 112.4 ± 0.4 mPa s obtained in the present work using DMSD, albeit it would be possible to say that they are in a reasonable agreement with the 27.9 ± 0.1 mPa s obtained using the DAVCF. At approximately 310 K, the results obtained by fitting γ_1 using the Leslie coefficients shown in [150, 153] are ~ 80 mPa s. This is larger than the 35.5 ± 0.1 mPa s yielded by the DAVCF but smaller than the 120.4 ± 0.4 mPa s produced by the DMSD. At an approximated temperature of 300 K, the experimental value of γ_1 was ~ 150 mPa s, while the results obtained here were 76.6 ± 0.3 mPa s and 205.8 ± 0.8 mPa s using the DAVCF and the DMSD respectively. Overall the experimental results are smaller than the ones produced by the simulations but it is encouraging that both simulation methods lead to results that are of the correct magnitude. It is predictable that the simulations results should be slightly larger than experimental ones because both the averaged density and the order parameters are larger in the simulated systems than experiment. In section 6.3 this result was attributed to the molecular potential being slightly too attractive. Experimentally, we expect a weaker attraction between molecules to increase the movement of the director and decrease the order parameter. Both factors would head to a decrease in γ_1 values. The results therefore are consistent and reasonable but point to the necessity of obtaining extremely accurate intermolecular potentials as the next stage to obtaining accurate material properties.
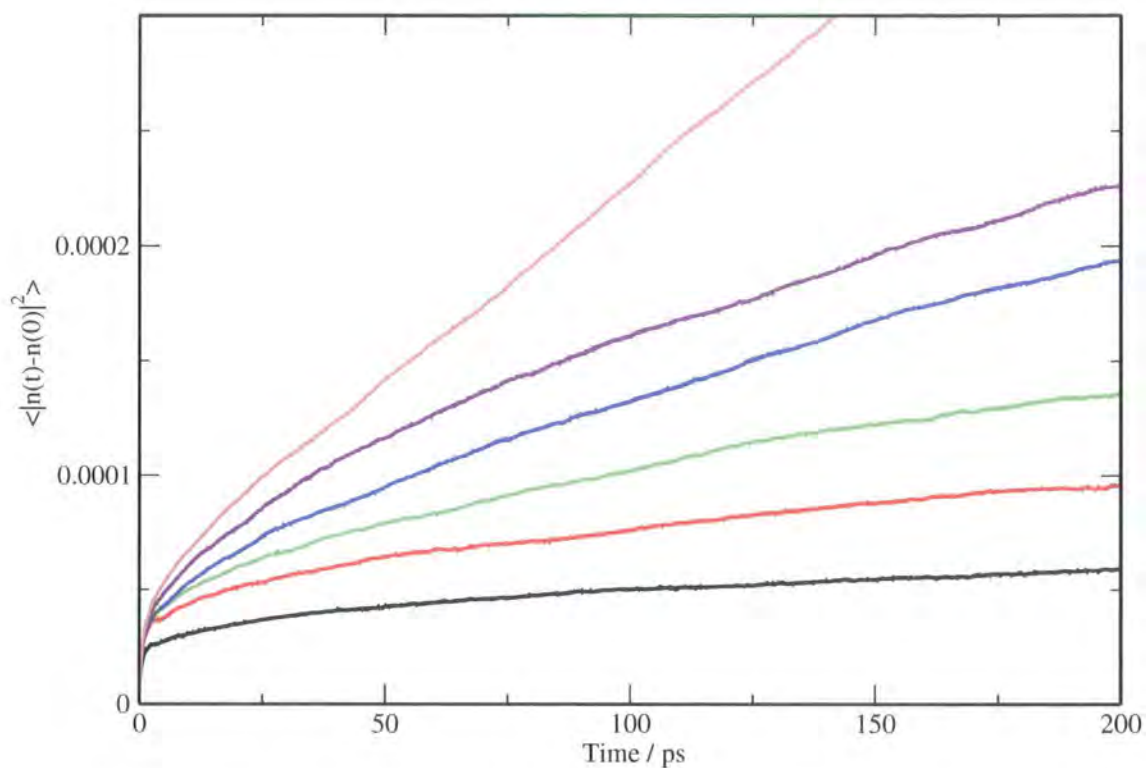
Figure 7.2: Director mean square displacement calculated for six different temperatures: 280 K (black), 290 K (red), 300 K (green), 310 K (blue), 320 K (purple) and 330 K (mauve).

T / K	$\lim\limits_{t\to\infty}\langle |\mathbf{n}(t) - \mathbf{n}(0)|^2 \rangle$ / ps^{-1}	γ_1/mPa s
280	$1.007\times10^{-7}\pm0.001$	720 ± 2
290	$2.167\times10^{-7}\pm0.001\times10^{-7}$	344 ± 1
300	$3.722\times10^{-7}\pm0.002\times10^{-7}$	205.8 ± 0.8
310	$6.547\times10^{-7}\pm0.001\times10^{-7}$	120.4 ± 0.4
320	$7.193\times10^{-7}\pm0.002\times10^{-7}$	112.4 ± 0.4
330	$1.72828\times10^{-6}\pm0.00001\times10^{-6}$	47.9 ± 0.2

Table 7.2: Rotational viscosity calculated using DMSD.

7.2   Flexoelectric Coefficients

7.2.1   Introduction

Flexoelectricity is giving by a deformation of the director vector characterizing a nematic phase as a consequence of the application of an external mechanical distortion or an electromagnetic field. In these cases a net polarization is induced across the nematic. An inverse effect is also possible. In a nematic which shows a flexoelectric response a contribution is made to the director deformation by the application of an electric field which is coupled to the flexoelectricity. This phenomenon was firstly defined by Meyer in 1969 [162], although on that occasion it was presented as a piezoelectric effect in liquid crystals. It was not until 1974 when de Gennes [163] renamed it as the flexoelectric effect.

The flexoelectric effect is mostly exhibited by molecules with anisotropic shape (such as those which are wedge shaped or chevron shaped) and microscopic polarizability. If wedge shaped molecules, which have a permanent dipole moment along the molecular axis are subject to a splay deformation in terms of the surrounding director field, then a net polarization is induced across the sample as illustrated in figure 7.3. Likewise chevron shaped molecules with transverse permanent dipoles exhibit spontaneous polarization under bend deformation, as shown in 7.3. For symmetry reasons twist deformations have no contributions to the flexoelectricity [164].

Flexoelectricity may also arise when the molecules belong to neither of the types above mentioned, do not have a permanent dipole moment but do have a quadrupolar moment instead. This was firstly noticed by Marceau and Prost [165] in quadrupolar mesogens when the application of a splay deformation produces the invasion of the intermolecular space between two molecules by another one situated above. The return of the latter molecule to the primitive position above is hindered by the charges of opposite sign in the molecular quadrupoles of the molecules which have suffered the splay, as indicated in figure 7.4. This phenomenon has been noted for different systems [166, 167].

The flexoelectric effect is not only present in nematic phases, but also in smectic ones [167, 168]. Moreover, it has also been seen in twisted nematic phases [169].
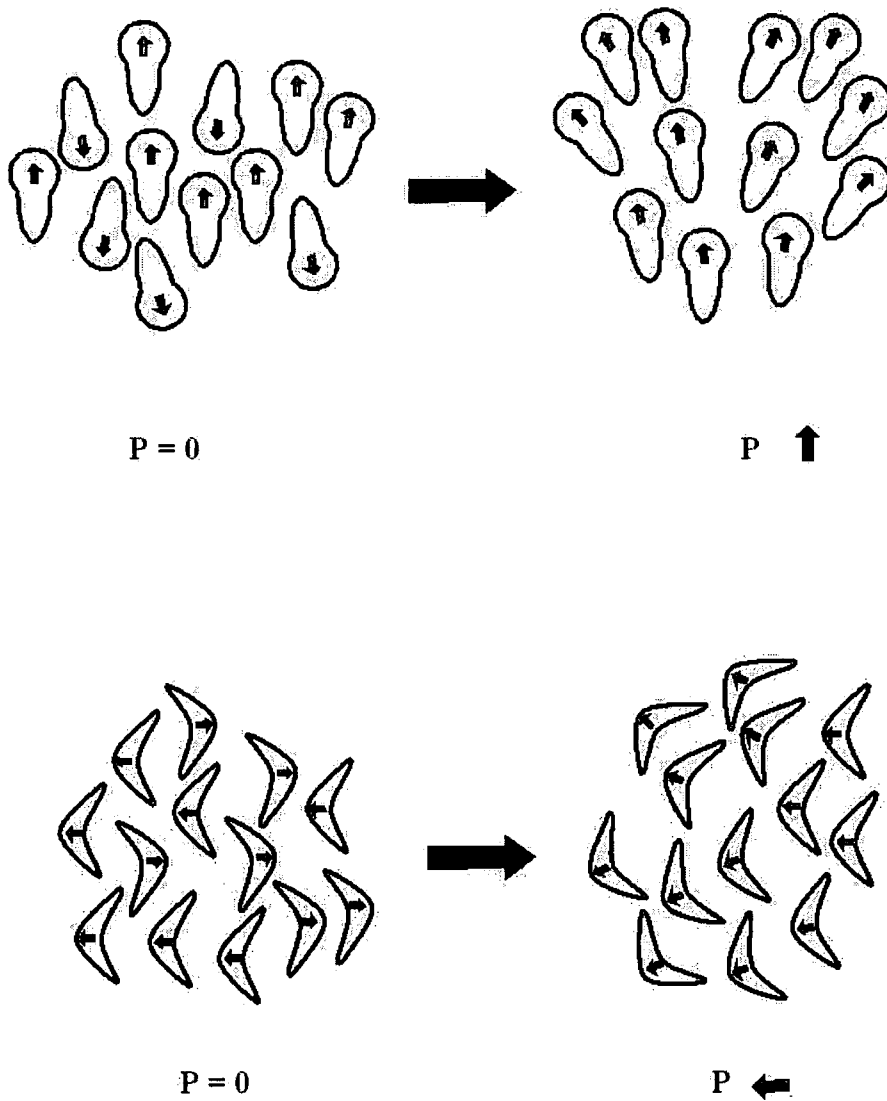
Figure 7.3: Representation of pear-shaped molecules with a permanent longitudinal dipole (top) where a splay deformation gives rise to a net polarization across the sample and bent-core molecules with a transverse dipole moment (bottom) where a bend deformation gives rise to a net polarization across the sample.
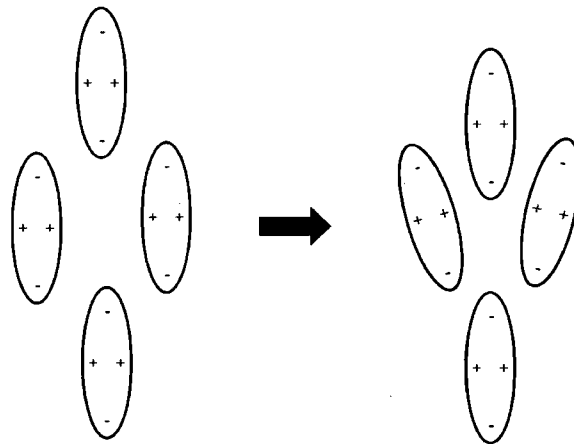
Figure 7.4: Flexoelectric effect produced by quadrupolar molecules.

It must be added that not only do molecules with a non-symmetric shape cause flexoelectricity. By contrast, molecules with a symmetric shape, such as 5CB and PCH5 (which have a rod-like symmetric shape), can also produce a flexoelectric effect. It is well known that these two types of molecules, as well as many other cyanophenyl derivatives (see chapter 7), develop an antiparallel pairwise dipole correlation between nearest neighbours . In the presence of a splay or bend deformation, this antiparallel correlation is partially broken, which eventually produces a net polarization [170] .
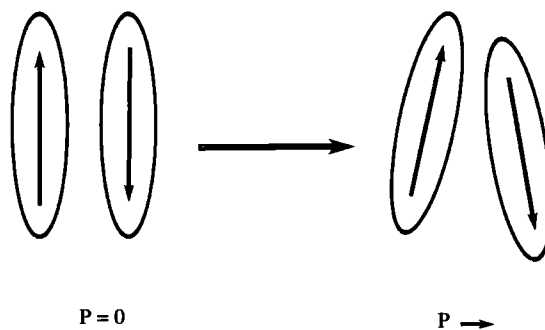
Figure 7.5: Induced flexoelectric behaviour of a mesogen with a symmetric shape. The vectors inside the ellipsoids represent the molecular dipole.

The flexoelectric polarization vector can be defined as:

$$P^f = e_s \mathbf{n} \cdot (\nabla \cdot \mathbf{n}) + e_b \mathbf{n} \times \nabla \times \mathbf{n}, \qquad (7.11)$$

where e_s and e_b are the splaying and bending flexoelectric coefficients, respectively, and $\mathbf{n} \cdot (\nabla \cdot \mathbf{n})$ and $\mathbf{n} \times \nabla \times \mathbf{n}$ are splay and bend director deformations.

Experimental Techniques for the Determination of the Flexoelectric Coefficients

Despite difficulties involving the experimental measurements of the flexoelectric coefficients, several different techniques have been developed. Basically these can be gathered into two groups: direct and indirect methods. In the former, the director is modified using either mechanical or thermal methods so the induced polarization can be measured. In the latter, an electric field is applied producing a deformation in the director vector, which can be used to calculate the flexoelectric coefficients.

Using indirect methods it is possible to calculate either the addition $e_s + e_b$ or the difference $e_s - e_b$ of the flexoelectric coefficients. Regarding the addition, Prost and Pershan [171] presented the first results using this method in 1980. Although they were able to measure $e_s + e_b$ for the mesogen N-(p-methoxibenzylidene)-p'-butylaniline (MBBA), they failed in determining its sign. Latterly, Dozov et al. [172] were able to evaluate $e_s + e_b$ and its sign again for the same molecule. In the experiment they performed the mesogen sample was disposed in a hybrid aligned nematic cell (HAN).

Henceforth, HAN cells have been widely used in the determination of flexoelectric coefficients. Madhusudana and Durand used such a cell to calculate $e_s + e_b$ for MBBA considering the fact that positive and negative voltages have different effects in the director distortion [173]. This technique was lately improved by Warrier and Madhusudana [174]. Additional methods have been subsequently developed for the evaluation of the sum of the flexoelectric coefficients [175–178].

In addition to the determination of $e_s + e_b$, it is also possible to determine experimentally $e_s - e_b$. Although this does not require the use of a non-uniform electric field or a weak surface anchoring, as in the cases previously exposed, it presents the difficulty of requiring a non-coplanarity between the director and the applied field.

Dozov has proposed a technique to carry out the evaluation of $e_s - e_b$ using an in plane electric field perpendicular to the initial molecular field [179]. This can also be used to evaluate the chiral flexoelectric effect [180–182].

The perturbation of the directors required in direct methods may be achieved by several methods. One includes applying a pressure pulse using a loud speaker [183]. Another involves applying heat pulses by means of a laser [184, 185].

Theories Involving the Evaluation of the Flexoelectric Coefficients

Due to the difficulties involved in the experimental calculation of the flexoelectric coefficients, different theories have been elaborated in an attempt to predict and describe the flexoelectric effect. These cover a wide range going from an Osanger-like theory [186] to mean field theory [187] and density functional theories [188, 189].

Simulations of the Flexoelectric Effect

Despite the interest aroused by the flexoelectric phenomenon, to the best of the author's knowledge it is possible to find just three simulations in the literature and just one of them used an atomistic model [170]. In the latter only a single molecular type was simulated. The method used to calculate the flexoelectric coefficient on that occasion was the same as the one used in the present work, and it will be subsequently explained in detail.

Previously to the the work mentioned above, two different simulations were performed with the intention of calculating the flexoelectric coefficients. In the first one [190], the flexoelectric coefficients were evaluated from expressions derived on the basis of density functional theory. The molecular model chosen to represent the wedge-shaped mesogens was based in a pear-shape body accomplished combining a sphere represented by a Lennard-Jones potential and an ellipsoid represented by a Gay-Berne potential with an inter-site distance of d. The molecular potential reads

$$U_{i,j} = U_i^{GB} U_j^{GB} + U_i^{LJ} U_j^{LJ} + U_i^{GB} U_j^{LJ} + U_i^{LJ} U_j^{GB}, \qquad (7.12)$$

where i and j represent two different molecules. In this model, the molecular steric

dipole was calculated as

$$p^* = \left(\frac{4\pi}{3}\right) \epsilon_{LJ}^* \sigma_{LJ}^* d^*, \qquad (7.13)$$

where ϵ_{LJ}^* and σ_{LJ}^* are the Lennard-Jones well depth and radius respectively.

In the second case [191], the molecular model proposed to represent the pear-like mesogens was rather similar to that detailed above. However, the flexoelectric coefficients were evaluated using the linear response theory of Nemstov and Osipov [192]. This method, which was also used to calculate the flexoelectric coefficients in reference [170], will be also used here with the same purpose. A brief review of the two methods will be presented below.

Density Functional Approach

In the first one [190], the flexoelectric polarizability P^f was defined as

$$P^f = \rho p \int d\mathbf{u}_i f_0(\mathbf{u}_i) \delta f(\mathbf{u}_i) \mathbf{u}_i, \qquad (7.14)$$

where ρ is the number density, p is the steric dipole, u_i represents the orientation of the molecule i, f_0 is the orientation distribution function (ODF) in the uniaxial equilibrium and δf is the perturbation affecting the equilibrium, given by [186]

$$\delta f(u_i) = \rho \int d\mathbf{r}_{ij} d\mathbf{u}_j c(\mathbf{r}_{ij}, \mathbf{u}_i, \mathbf{u}_j)(\mathbf{r}_{ij}\nabla) \times f_0(\mathbf{u}_j), \qquad (7.15)$$

where $\mathbf{r}_{ij}$ is the intermolecular distance and $c(\mathbf{r}_{ij}, \mathbf{u}_i, \mathbf{u}_j)$ is the direct pair correlation function (DPCF). (For more details of the calculation of the DPCF see [190].)

After comparing 7.11 and 7.14 it is possible to derive an expression for the flexoelectric coefficients e_s and e_b,

$$e_s = \rho^2 p \int d\mathbf{r}_{ij} d\mathbf{u}_i d\mathbf{u}_j f_0(\cos\beta_i) u_{i,z} \times f_0'(\cos\beta_j) u_{j,x} r_{ij,x} c(\mathbf{r}_{ij}, \mathbf{u}_i, \mathbf{u}_j), \qquad (7.16)$$

$$e_b = \rho^2 p \int d\mathbf{r}_{ij} d\mathbf{u}_i d\mathbf{u}_j f_0(\cos\beta_i) u_{i,x} \times f_0'(\cos\beta_j) u_{j,x} r_{ij,z} c(\mathbf{r}_{ij}, \mathbf{u}_i, \mathbf{u}_j). \qquad (7.17)$$

Linear Response Theory Approach

The flexoelectric polarization vector can be described as

$$P_\alpha^f = E_{\alpha\beta\gamma}\gamma_{\beta\gamma}, \tag{7.18}$$

where $\gamma_{\beta\gamma}$ is the deformation tensor given by

$$\gamma_{\alpha\beta} = \frac{\partial\theta_\alpha}{\partial r_\beta}, \tag{7.19}$$

where θ represents the rotational angle of the director about the coordinate axis α. At the same time, eq. 7.19 can be rewritten as

$$\frac{\partial\theta_\alpha}{\partial r_\beta} = \epsilon_{\alpha\mu\nu}n_\mu\partial_\beta n_\nu. \tag{7.20}$$

Here $\epsilon_{\alpha\mu\nu}$ is the Levi-Civita tensor, n is the director vector and $\partial_\beta n_\nu = \frac{\partial n_\nu}{\partial r_\beta}$.

The response function reads:

$$E_{\alpha\beta\gamma} = \frac{\beta}{V}\langle P_\alpha\Pi_{\beta\gamma}\rangle, \tag{7.21}$$

where P_α is the polarization given by the expression

$$P = \sum_{i=1}^{n} q_i \cdot \mathbf{r}_i, \tag{7.22}$$

where q is the atomic charge and r the atom position. The summation runs over the n atoms in the system, and

$$\Pi_{\beta\gamma} = -\frac{1}{2}\sum_{i\neq j} r_{ij\alpha}\tau_{ij\beta}, \tag{7.23}$$

where $r_{ij\alpha}$ represents the intermolecular vector between i and j, and $\tau_{ij\beta}$ is the torque exerted by molecule i on j and reads

$$\tau_{ij\beta} = \sum_k \mathbf{r}_k^c \times \mathbf{F}_{kj}. \tag{7.24}$$

Here, r_k^c is the position vector of the atom k in molecule i relative to the centre of

mass of i. F_{kj} is the force on k exerted by molecule j and can be calculated as the summation of the forces from each one of the l atoms in molecule j on the atom k in molecule j

$$\mathbf{F}_{kj} = \sum_l \mathbf{F}_{lk}. \tag{7.25}$$

Moreover, F_{lk} is the result of the addition of two forces, the electrostatic force (F_{lk}^{elec}) and the van der Waals force (F_{lk}^{vdw}):

$$\mathbf{F}^{elec} = \frac{1}{4\pi\epsilon_0} \frac{q_k q_k}{r_{kl}^2} \widehat{\mathbf{r}}_{kl}, \tag{7.26}$$

$$\mathbf{F}^{vdw} = 24\epsilon_{kl} \left[\frac{2\sigma_{kl}^{12}}{r_{kl}^{13}} - \frac{\sigma_{kl}^6}{r_{kl}^7} \right] \widehat{\mathbf{r}}_{kl}, \tag{7.27}$$

where $\overrightarrow{r_{kl}}$ is the unit vector along the direction of the intermolecular vector between atoms k and l. The other symbols have their usual meanings.

In order to find a suitable expression to calculate the flexoelectric coefficients e_s and e_b, it is necessary to rewrite the response tensor as

$$E_{\alpha\beta\gamma} = E_1\epsilon_{\alpha\beta\gamma} + E_2\epsilon_{\lambda\alpha\beta}n_\lambda n_\gamma + E_3\epsilon_{\lambda\gamma\beta}n_\lambda n_\alpha + E_4\epsilon_{\lambda\alpha\gamma}n_\lambda n_\beta, \tag{7.28}$$

which represents a third rank pseudo tensor in its most general form, and consist of the director components and the Levi-Civita tensor.

When the expression showed above is multiplied by the deformation tensor $\gamma_{\beta\gamma}$, the result is:

$$E_{\alpha\beta\gamma}\gamma_{\beta\gamma} = (E_3 - E_1)n_\alpha\partial_\gamma n_\gamma = (E_1 - E_2)n_\gamma\partial_\gamma n_\alpha. \tag{7.29}$$

Given that the first term in equation 7.29 equals the flexoelectric polarization, as can be seen in equation 7.11, it is possible to establish the following correlation between both expressions:

$$[\mathbf{n} \cdot (\nabla \cdot \mathbf{n})]_\alpha = n_\alpha\partial_\gamma n_\gamma \tag{7.30}$$

$$[\mathbf{n} \times \bigtriangledown \times \mathbf{n}]_\alpha = -n_\gamma \partial_\gamma n_\alpha. \tag{7.31}$$

Thus

$$e_s = E_3 - E_1, \tag{7.32}$$

$$e_b = -\left(E_1 + E_3\right). \tag{7.33}$$

It is possible to find a suitable expression for e_s multiplying eq. 7.28 by $\epsilon_{\mu\beta\gamma}n_\mu n_\alpha$, which allows for the calculation of the flexoelectric splay coefficient directly from the response tensor

$$E_{\alpha\beta\gamma}\epsilon_{\mu\beta\gamma}n_\mu n_\alpha = 2\left(E_1 - E_3\right), \tag{7.34}$$

and therefore

$$e_s = -\frac{1}{2}E_{\alpha\beta\gamma}\epsilon_{\mu\beta\gamma}n_\mu n_\alpha = -\frac{1}{2}\left[E_{zxy} - E_{zyx}\right], \tag{7.35}$$

which is the final expression used to calculate e_s. Analogously, if the equation 7.28 is multiplied by $\epsilon_{\mu\alpha\beta}n_\mu n_\gamma$, the resultant expression is

$$E_{\alpha\beta\gamma}\epsilon_{\mu\alpha\beta}n_\mu n_\gamma = 2\left(E_1 - E_2\right), \tag{7.36}$$

which leads to the expression

$$e_b = -\frac{1}{2}E_{\alpha\beta\gamma}\epsilon_{\mu\alpha\beta}n_\mu n_\gamma = -\frac{1}{2}\left[E_{xyz} - E_{yxz}\right]. \tag{7.37}$$

Therefore and summarizing, the two flexoelectric coefficients can be calculated from the response tensor using

$$e_s = -\frac{1}{2}\left[E_{zxy} - E_{zyx}\right] \tag{7.38}$$

$$e_b = -\frac{1}{2}\left[E_{xyz} - E_{yxz}\right]. \tag{7.39}$$

7.2.2 Results

Polarization

The polarization of the system overall has been calculated using equation 7.22. It is possible to notice that there is a small net polarization in the system. This is mainly caused by size effects, since the number of molecules in the system is limited. The simulation time also contributes to the existence of such polarization. It is necessary consider that the simulation times achieved in the present work are somewhat smaller that the actual times required for molecular reorientation (~ 100 ns). The system polarization evolution with respect to time is shown in figure 7.6 for three different temperatures.

T / K	p_x ($\times 10^{-30}$ C m)	p_y ($\times 10^{-30}$ C m)	p_z ($\times 10^{-30}$ C m)	$|\mathbf{p}|$ ($\times 10^{-30}$ C m)
280	-17.3 ± 23.8	28.8 ± 23.8	-41.6 ± 11.2	62.1 ± 16.2
290	-21.6 ± 32.1	5.8 ± 24.8	-29.6 ± 13.9	53.1 ± 19.7
300	-21.2 ± 44.9	-9.8 ± 42.9	-37.6 ± 17.0	75.4 ± 20.4
310	8.2 ± 36.1	5.4 ± 33.4	-27.8 ± 13.1	55.6 ± 19.0
320	-3.6 ± 33.8	-1.4 ± 32.4	-5.1 ± 18.8	47.0 ± 19.4
330	4.7 ± 30.3	-3.9 ± 45.3	-34.2 ± 15.5	62.5 ± 22.7

Table 7.3: Averaged system polarizations calculated at six different temperatures for the mixture of liquid crystals E7.

Flexoelectric Coefficients

The splay and bend flexoelectric coefficients have been calculated using the formulae 7.38 and 7.39 respectively. The results obtained in these calculations can be seen in table 7.5. Experimental results of $e_s + e_b$ have been previously reported [193]. These reported a value of $15 \pm 2 \, \mathrm{pC \, m^{-1}}$ at 20^0 C. The most similar temperature simulated in the present work is 290 K, and the value of $e_s + e_b$ calculated at such temperature was $78.7 \, \mathrm{pC \, m^{-1}}$. Albeit the results from the experiment and the simulation differ significantly from each other, it is remarkable that both are within the same order
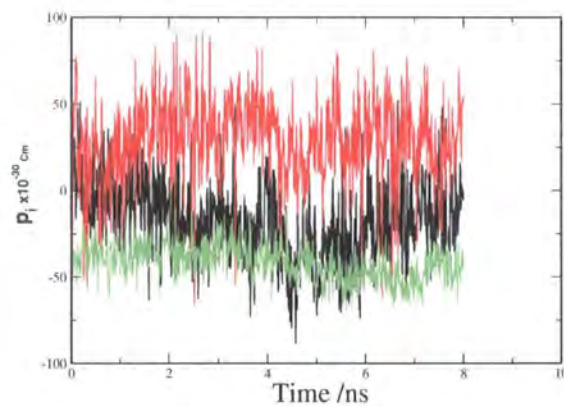
(a)
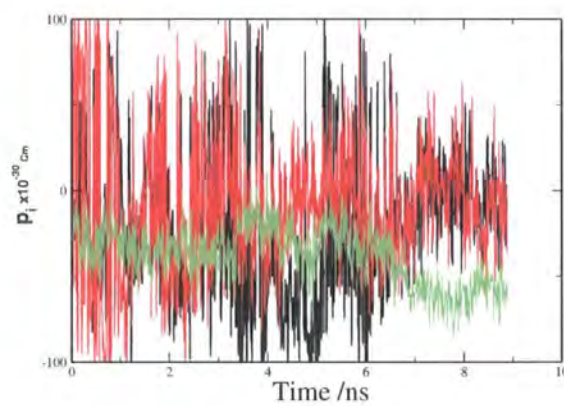
(b)
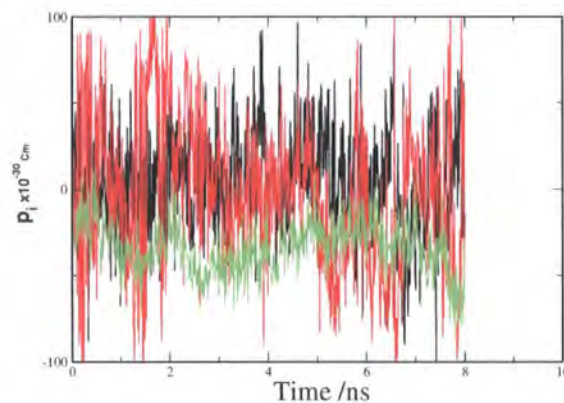
(c)

Figure 7.6: Evolution of the three components of the system polarization p_i ($\times 10^{-30}$C m) with respect to simulation time at three different temperatures: 280 K (a), 300 K (b) and 330 K (c). The component of the polarization parallel to the director is represented by a black line, whereas the red and green lines represent the components perpendicular to the director.

of magnitude. Previous work [194], calculated the value of $(e_s - e_b)/K$, where K represents the average of the elastic constants. The result obtained in this work was $e_s - e_b/K = 1.7\,\mathrm{C\,m^{-1}N^{-1}}$. Raynes et $al.$ reported experimental values of the three elastic constants K_{11}, K_{22} and K_{33} [195] which can bee seen in table 7.4. Hence calculating the average of the three constants it is possible to determine $e_s - e_b$, which corresponds to $22.67\,\mathrm{pC\,m^{-1}}$. The difference between the splay and bend coefficients in the present work at 290 K is $39.7\,\mathrm{pC\,m^{-1}}$, which is significantly close to the experimental result obtained by Hermann et $al.$.

K_{11}/pN	K_{22}/pN	K_{33}/pN
11.7	8.8	19.5

Table 7.4: Elastic constants for the liquid crystal mixture E7 obtained from experiment at room temperature (20^0) taken from reference [195].

Although the value of the standard deviation is rather large in all the cases, a trend can be appreciated from the coefficients. There is a marked temperature dependence for both the splay and bend coefficients, especially in the case of the splay. The splay flexoelectric coefficient decreases its value as the temperature increases, but always keeps a positive sign. In the case of the bend flexoelectric coefficient, there is also a decreasing trend as the temperature increases, with the single exception of e_b calculated at 280 K. In this case, there is an actually change in the sign of the coefficient. However, the large errors quoted in these results make it difficult to come to definitive conclusions.

An explanation of the temperature dependence of the coefficients can be elucidated from the preferred molecular configuration. E7 is a mixture of cyanobiphenyl and cyanoterphenyl derivatives, which have an aliphatic chain appended to the rigid aromatic core. The conformation of such a chain is temperature dependent as shown in table 7.20 (in this particular case the dihedral angles present in the aliphatic chain of the 7CB are chosen, although an identical behaviour has been observed in the other types of molecule). $Gauche$ conformations have a larger population in the even number of torsional angles (φ_4 and φ_6). This is due to the fact that the in this conformation the aliphatic chain can still remain linear (see section 6.4). However,

Temperature / K	e_s/pCm^{-1}	e_b/pCm^{-1}
280	91.2 ± 244.1	-41.7 ± 102.3
290	59.2 ± 161.0	19.5 ± 110.6
300	10.6 ± 201.1	15.4 ± 154.1
310	24.7 ± 167.6	-2.1 ± 109.2
320	7.7 ± 99.3	-2.3 ± 87.8
330	0.4 ± 187.7	-4.9 ± 100.9

Table 7.5: Flexoelectric coefficients for the liquid crystal mixture E7 calculated in the present work.

the population of *gauche* conformations increase for all the dihedral angles as temperature increases. This confers a bow-shaped aspect to the molecules, instead of its characteristic rod-like shape.

Although the variation of the molecular shape does not affect the molecular dipole overall, it does affect its components. It is possible to appreciate in table 7.7 that the transverse component of the molecular dipole increases at the expense of its longitudinal one as the temperature increases and thus molecules become slightly more curved. This change in the components of the dipoles affects the transcient dimers formed as a consequence of dipole-dipole interactions. Such interactions, which were based on the longitudinal molecular dipole, become weaker, dipole correlation is reduced and this reduces the flexoelectric coefficients as temperature increases.

The temperature dependence observed in this work was not detected by previous works using approximate models. Zakharov and Dong [196] used a dipolar Gay-Berne model representing 5CB (which is the most common type of molecule in the mixture E7) to calculate the flexoelectric coefficients. Here, the flexoelectric coefficients remained constant with respect to the temperature. It is important to recognise that the model used in the Zakharov *et al.* study did not take into account important factors such as the internal structure of the molecules or molecular flexibility.

Dihedral Angle	Conformation (%)	Temperature / K					
		280	290	300	310	320	330
	gauche -	2.1	1.7	2.4	2.6	3.0	3.9
φ_3	trans	93.4	95.3	94.8	92.9	94.6	92.7
	gauche +	4.5	3.0	2.8	4.5	2.4	3.4
	gauche -	4.6	5.8	6.3	7.7	7.6	8.4
φ_4	trans	90.5	88.4	87.6	84.7	85.4	83.4
	gauche +	4.9	5.8	6.1	7.6	7.0	8.2
	gauche -	2.0	1.4	1.7	2.1	2.5	3.0
φ_5	trans	95.5	96.7	96.4	94.7	94.8	94.3
	gauche +	2.5	1.8	1.9	3.2	2.7	2.8
	gauche -	4.3	5.2	5.6	6.9	6.3	7.3
φ_6	trans	91.4	89.2	88.7	86.6	86.6	85.1
	gauche +	4.2	5.6	5.6	6.4	7.0	7.6
	gauche -	5.37	4.7	5.3	5.5	6.1	6.9
φ_7	trans	89.3	91.0	89.1	87.2	87.7	86.2
	gauche +	5.3	4.3	5.6	7.3	6.2	6.8

Table 7.6: Population of the different dihedral angles at six different temperatures for several different dihedral angles in the molecule 7CB. (The dihedral angles are defined in section 6.4).

Temperature / K	$\langle|\mathbf{m}|\rangle$ $(\times10^{-30}\,C\,m)$	$\langle|\mathbf{m}_l|\rangle$ $(\times10^{-30}\,C\,m)$	$\langle|\mathbf{m}_t|\rangle$ $(\times10^{-30}\,C\,m)$
280	8.85 ± 0.03	8.41 ± 0.02	2.08 ± 0.03
290	8.88 ± 0.03	8.41 ± 0.03	2.07 ± 0.06
300	8.86 ± 0.04	8.41 ± 0.03	2.09 ± 0.06
310	8.87 ± 0.03	8.40 ± 0.03	2.11 ± 0.07
320	8.88 ± 0.03	8.40 ± 0.03	2.12 ± 0.06
330	8.88 ± 0.03	8.40 ± 0.03	2.15 ± 0.07

Table 7.7: Molecular dipole moments ($|\mathbf{m}|$) and their longitudinal ($\mathbf{m}_l$) and transversal ($\mathbf{m}_t$) components averaged over all the molecules in the system.

$Temperature/K$	e_s vdW	e_b vdW	e_s elec	e_b elec
280	-55 ± 239	-35 ± 100	146 ± 71	-6 ± 21
290	67 ± 166	4 ± 101	-3 ± 41	4 ± 24
300	26 ± 210	8.8 ± 144	-2 ± 57	-7 ± 35
310	-7 ± 160	-2 ± 101	31 ± 44	0 ± 26
320	11 ± 98	-1 ± 88	-3 ± 32	-1 ± 21
330	13 ± 185	-1 ± 98	13 ± 55	-4 ± 25

Table 7.8: Contributions from the van der Waals and electrostatic interactions to the flexoelectric coefficients. All the coefficients are expressed in $pC\,m^{-1}$.

Some simulations performed using less realistic models than the one described above have also predicted a temperature dependence for the flexoelectric coefficients. The results obtained in the simulation of the mesogen PCH5 [170] are particularly relevant as far as the present work is concerned. Firstly, although the PCH5 is not a component of the mixture E7, it is a cyanophenyl derivative, hence it is thought to exhibit dipole correlation from the longitudinal dipole moment. Secondly the same method used for the calculation of the flexoelectric coefficients here was used in that work. As seen here, the PCH5 flexoelectric coefficients seen in that study are temperature dependent. The 4'-methoxybenzylidene-4-n-butylaniline (MBBA) has been simulated using a mean field approach [166], showing that the flexoelectric coefficients decreased with the temperature.

7.3 Conclusions

Atomistic simulation of the liquid crystal mixture E7 has been used to calculate two key material properties: the rotational viscosity and the flexoelectric coefficients.

Both methods used to calculate the rotational viscosity are in approximately agreement with the experimental data. Given limited system sizes, the slightly high density in the simulated system and the limited simulation times possible, the fact that values are obtained which are quite close to experiment is an excellent result. For rotational viscosities, the errors calculated for the mean square displacement are slightly larger than those calculated for the director angular velocity correlation function. This is the opposite to what has been described in previous work for PCH5, where the errors of the DAVCF were found to be larger than those of the DMSD [170].

The calculated values of e_s and e_b are consistent with those found experimentally, belonging to the same order of magnitude. However, the standard deviations calculated for the above mentioned results are large. This is due to limitations in both system size and simulation time. Nevertheless, it must be stressed that the simulations carried out in the present work are currently at the limit of what is feasible. Therefore it is possible to assert that the present work opens a possible path

to the future characterization of material properties based exclusively on computer simulation.

Chapter 8

Calculation of Torsional Potentials Using *ab initio* Methods

8.1 Introduction

The current generation of fast computer processors has extended the range of systems that can be modeled by high level *ab initio* calculations. In particular it is now possible to develop force fields to describe complex mesogenic molecules, or at least an important part of them, starting purely from quantum mechanical calculations.

In the present chapter results for torsional energies obtained using density functional theory are provided for different molecules that normally constitute the core of a large number of mesogens. Subsequently the torsional parameters are calculated by fitting the obtained energies. These parameters are extremely useful when performing atomistic simulations of liquid crystals, as has been proved in previous chapters (4, 5, 6). Indeed, the ability mesogens have to form superstructures or to locally self-assemble depends crucially upon the dihedral angles between their rigid cores. This makes the calculation of torsional parameters for atomistic potentials a task worth being undertaken, despite being a painstaking one.

In this chapter, torsional potentials are found for biphenyl, 2-fluoro-6-phenylpyridine, 2-phenylpyrimidine and 5-phenylpyrimidine. In addition torsional barriers involved in the central rigid core of the thermotropic biaxial mesogen ODBP-Ph-C_7 have also been calculated indirectly by finding torsional energies of methyl benzoate, phenyl

204
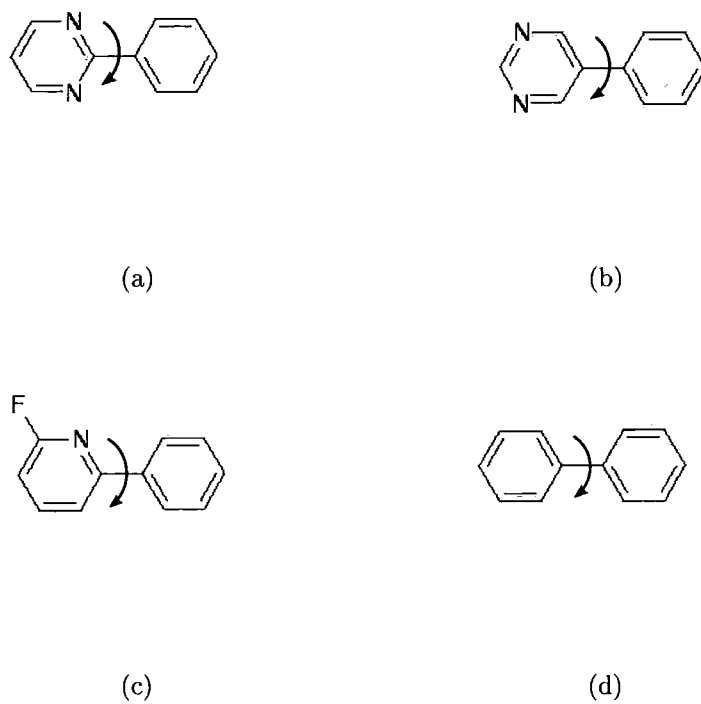
Figure 8.1: Structures of (a) 2-phenylpyrimidine, (b) 5-phenylpyrimidine, (c) 2-fluoro-6-phenylpydine and (d) biphenyl.

acetate, phenylbenzoate and 2,5-diphenyl-1,3,4-oxadiazole. The four latter structures can be considered components of ODBP-Ph-C$_7$. These will be used to develop a liquid crystal force field.

(a)   (b)

(c)   (d)
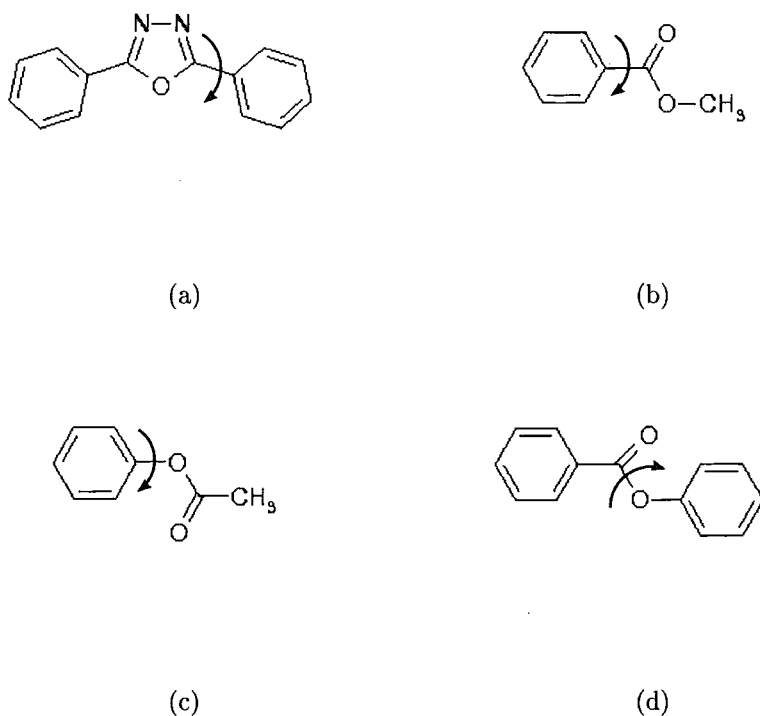
Figure 8.2: Structures of (a) 2,5-biphenyl-1,3,4-oxadiazole, (b) methyl benzoate, (c) phenyl acetate and (d) phenylbenzoate.

8.2   *Ab Initio* Calculations of Dihedral Angle Potentials

Traditional *ab initio* methods involve solving the time independent Schrödinger equation.

$$[-\frac{\hbar^2}{2m} \nabla^2 +V]\psi = E\psi \tag{8.1}$$

However, this only has an exact solution for one electron systems. To solve the

electronic structure of a molecule means dealing with a many-electron problem. This means that it is necessary to tackle the interaction between each electron of the molecule and the rest of the electrons. Hartree handled this problem by neglecting part of the electron-electron interactions and allowing the electron to move in an effective potential due to the other electrons. Later, the addition of Fermi statistics to the Hartree approach produced the Hartree-Fock method, where the effect of the electron exchange is taken into account. Nevertheless, the Schrödinger Equation is not the only way to cope with multiple-electron systems. As will be introduced below, using the Density Functional Theory, elaborated firstly by Hohenberg and Kohn [197] and secondly by Kohn and Sham [198], it is possible to face this problem starting from a charge density functional.

8.2.1 Born-Oppenheimer Approximation

The Born-Oppenheimer approximation asserts that due to the different time scales for the motions of electrons and nuclei, the former can be considered as though they were static, whereas the electrons are in continuous motion.

8.2.2 Density Functional Theory

There are two principles asserted by density functional theory:

1. The total energy of a system composed of electrons and nuclei is a unique functional of the electronic density.

2. The variational minimum of the system total energy is equivalent to the ground state energy for that system.

The charge density is given by monoelectron wave functions:

$$\rho(r) = \int \psi(r)\psi^*(r)dr. \tag{8.2}$$

Making use of this theory the total energy equation can be written in the following way

$$E = \int \mathbf{v}(r)\rho(r)dr + \frac{1}{2}\int\int\frac{\rho(r)\rho(r')}{|r-r'|}drdr' + G[\rho],\tag{8.3}$$

where the first term in eq. 8.3 is the potential between electrons and nuclei, the second one is the Hartree coulombic potential between electrons and the last one is a functional of the electron density, in which are included the kinetic energy of the electrons and the exchange-correlation energy

$$G[\rho] = T_s[\rho] + E_{xc}[\rho].\tag{8.4}$$

Obviously this theory alone does not solve the whole problem and a problem still arises with writing down the exchange-correlation energy. Even though the theory guarantees that the total energy is a functional of the density, unfortunately it does not explain which form the latter should take. The first functional was introduced by Kohn and Sham along with the Kohn-Sham equations [198]. Later, different models have been suggested [199, 200].

Charge Density Functionals

The *Local Density Approximation* (LDA) introduced the first widely used density functional. This theory considers each electron as being in a homogeneous electron gas. This approximation is not very accurate since the electron cloud around the molecule is highly inhomogeneous. However, the results obtained by means of this functional have proved to be sensible. The form adopted by this functional is

$$E_{ex} = \int dr\rho(r)\epsilon_{ex}(\rho(r))\tag{8.5}$$

To deal with the inaccuracy introduced by the *Local Density Approximation*, a

new theory was developed. In it, apart from one term representing the density of charge in an ideal electron gas, a new term representing the charge density gradient within the electronic cloud is incorporated. Hence this new scheme was entitled the *General Gradient Approximation* (GGA). However, in contrast to the LDA, there is not a unique form for this functional but several. One of the most widely used was developed for Perdew, Burke and Ernzerhof (PBE) [199]. This one has been used in this project.

8.2.3 Geometry Optimization

The conformation of a nematic mesogen plays a fundamental role in the nematic-isotropic transition. The most significant factor in determining conformation is the torsional angle of the molecule. Therefore, special care has been taken in order to calculate the torsional potential of the central cores for the mesogenic groups studied in the present project. For this a special subroutine was inserted in the Density Functional Theory package CASTEP [201], in order to constrain the different dihedral angles in study while the rest of the structure was relaxed. In this way their torsional energy was obtained.

In order to relax the structure a geometry optimization was carried out. This means that the nuclei positions can be recalculated using the force on them. Nevertheless, the calculation of the ion forces must be carried out very carefully, since Density Functional Theory is based in the Born-Oppenheimer approximation. The force is calculated as the derivative of the energy in the following way

$$F_I = - \left\langle \frac{\partial E}{\partial R_I} \right\rangle, \qquad (8.6)$$

where F_I is the force on nucleus I and R_I is its position. Equation 8.6 constitutes the Hellmann-Feynman theorem [202]. The forces are affected by the positions of the nuclei, so that an error known as Pulay force is introduced with this theorem. Fortunately, for plane wave basis sets the wavefunctions are independent of the nu-

clear position, therefore they are not affected by this error. The latter is modified each time the ionic position is modified, according to the Born-Oppenheimer approximation. Therefore the charge distribution for the new conformation might not be the one belonging to the ground state. Thus the electronic density, and therefore the energy, must be recalculated each time the structure is modified.

8.2.4 The CASTEP Package

To represent the liquid crystal molecule in the gas phase, that is, without interacting with another molecule, the molecule is isolated in a supercell sufficiently large to avoid possible intermolecular interactions. To represent the electronic structure of the molecules a plane wave basis set is used. This is possible by using the Bloch's Theorem, which asserts that a wave function can be expressed as the product of a cell periodic part and a wavelike part [203]

$$\psi_{n,k}(r) = \underbrace{u_{n,k}(r)}_{\substack{periodic \\ part}} \underbrace{\exp(ikr)}_{\substack{wavelike \\ part}} \tag{8.7}$$

This makes possible the use of plane waves in the construction of electronic waves functions. These are expanded as the following functions :

$$\psi_{n,k}(r) = \sum_G u_{n,k}(G) \exp(i(k+G)r), \tag{8.8}$$

where $u_{n,k}$ are the expansion coefficients, and G are the wavevectors. The latter are chosen in order to be commensurate to the supercell. These electronic wave functions will be used in the CASTEP program to represent the charge density (equation 8.2).

Thus, plane waves are used to describe the valence electrons. To avoid the requirement for an excessive number of plane waves, the core electrons are described by a set of pseudo-potentials. These represent the potential between the nucleus and the valence electrons screened by the core electrons.

8.3   Force Field Parametrization

8.3.1   Calculation of the Conformational Energies
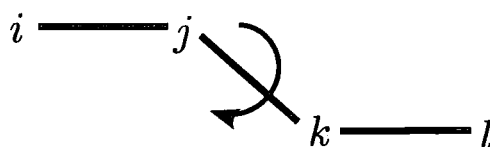
Figure 8.3: Scheme of a dihedral angle formed of the atoms i, j, k and l.

In order to calculate the torsional energy of a particular conformation it is necessary to constrain the dihedral angle involved in the calculation and allow the rest of the molecule to relax. For a dihedral angle formed from four atoms i, j, k and l (see figure 8.3), a restriction must be applied to each one of its atoms in order to constrain the rotation of the dihedral angle about the j-k bond. Firstly, the motion of atom i is confined to the plane formed by i-j-k, by applying the constrain force F_i^c:

$$F_i^c = F_i - (F_i \cdot \hat{n}_{ijk}) \, \hat{n}_{ijk}, \qquad (8.9)$$

where $\hat{n}_{ijk}$ is the unit vector normal to the i-j-k plane. Analogously, the motion of the other atom located in the extreme of the chain of four atoms defining the dihedral angle, l, is confined into the j-k-l plane. The constraint force over the atom l, F_l^c, is given by:

$$F_l^c = F_l - (F_l \cdot \hat{n}_{jkl}) \, \hat{n}_{jkl}, \qquad (8.10)$$

where $\hat{n}_{jkl}$ is the unit vector normal to the j-k-l plane.

The central atoms j and k are only allowed to move along the j-k bond, the one which the dihedral angle rotates about or, in other words, the one which constitutes the intersection of the i-j-k and j-k-l planes. Therefore, the constrain forces F_j^c and F_k^c are applied in order to constrain the movement of atoms j and k respectively.

$$F_j^c = (F_j \cdot \hat{n}_{jk}) \, \hat{n}_{jk}, \tag{8.11}$$

$$F_k^c = (F_k \cdot \hat{n}_{kj}) \, \hat{n}_{kj}, \tag{8.12}$$

where $\hat{n}_{jk}$ is the unit vector along the bond formed from the atoms j and k.

8.3.2 Torsional Potentials

The function used to represent the torsional energy of a certain molecule is based on a Fourier series:

$$E_{ijkl}^{tors} = \sum_n \frac{1}{2} V_{ijkln}^{tors} \left(1 + \cos\left(n\phi_{ijkl} + \delta_n\right)\right) \tag{8.13}$$

where ϕ_{ijkl} is the dihedral angle formed of the i, j, k and l. The Fourier series is expanded up to the nth term. Normally, $n = 3$ is enough to represent most torsional angles, although extension to $n = 12$ may be needed in the representation of some dihedral angles [141]. δ_n represents the phase angle, and depends on the expansion term:

$$\begin{cases} n \, odd \Rightarrow \delta_n = 0^0 \\ n \, even \Rightarrow \delta_n = 180^0 \end{cases} \tag{8.14}$$

V_{ijkl}^{tors} is the nth order force constant. Subsequently, it will be explained how to obtain a complete series of these constants by fitting the torsional energy calculated with the *ab initio* methods.

8.3.3 Fitting Process

With the aim of calculating torsional constants which can subsequently be used to represent a certain dihedral angle within a particular type of molecule, the fitting of the torsional energy calculated via *ab initio* methods is carried out. The proper fitting of the torsional constants is a non-trivial task, due to the fact that the non-bonded interactions must be considered at the same time, making the process more difficult. Hence, it is necessary to consider the whole molecule during the fitting of the torsional energy. This has often been neglected in the fitting of torsional potentials for liquid crystal molecules [204].

The procedure to carry out the fitting and the subsequent calculation of the torsional parameters can be described in four steps:

1. An initial guess of the torsional constants V_{ijkl} is made. This is introduced in a force field alongside the rest of the force constants describing the different interactions of the atoms forming the molecule (stretching, bending and non-bonded interactions normally).

2. The molecular energy is minimized for several different dihedral angles. During this step the dihedral angles chosen remain fixed while the torsional energy is minimized, while the rest of the molecule is allowed to relax.

3. The sum of the square of the difference between the torsional energy obtained using the *ab initio* methods and the energy obtained in the minimization described above is calculated using the formula:

$$\chi^2\left(\{V_{ijkl}\}\right) = \sum_a \left|E^{ab}\left(\phi_a\right) - E^{ff}\left(\phi_a\right)\right|^2 \qquad (8.15)$$

4. The process is repeated until the constants which minimize χ^2 are found.

In the present work the parametrization of the torsional energy has been accomplished truncating the Fourier expansion at the third term.

8.4 Calculations

8.4.1 Calculations Details

The graphic interface MSModelling was used to draw a model of each molecule. The software itself created the input files with coordinates and control parameters which would be used by CASTEP. A plane wave basis set was used for the valence electrons and ultra-soft pseudopotentials of the Vanderbilt form were used for the electron-ion interaction [205]. The PBE [199] generalized gradient approximation was used to tackle the exchange-correlation interactions. In all the molecules the plane wave basis set was expanded to a kinetic energy cutoff of around 400 eV. The convergence criteria for the energy was of at least $5 \cdot 10^{-7}$ eV/atom. The geometry optimization was carried out until the residual force on the atoms converged to 0.001 eV Å^{-1}. A geometry optimization was performed, during which the torsional angle in the study was constrained at a specified value, while the rest where allowed to relax.

The calculation was performed for the molecules 2-phenylpyrimidine, 5-phenylpyrimidine, 2-fluoro-6-phenylpyridine, biphenyl, methyl benzoate, phenyl acetate, phenylbenzoate and 2,5-diphenyl-1,3,4-oxadiazole, in the dihedral angles given in figures 8.1 and 8.2. These molecules are often part of the rigid core in many mesogens. The final four have a special importance in this work since they constitute the rigid core of the banana-shaped molecule ODBP-Ph-C_7.

8.4.2 Calculation Results

The torsional energy profile calculated for all the structures formed from two aromatic rings, alongside the correspondent fitted energy, is shown in figure 8.4. In the planar conformation the inter-ring dihedral angle is equivalent to either 0^0 or 180^0, whereas in the non-planar conformation it is either 90^0 or 270^0.

Method	Ref.	$\triangle E_0$	$\triangle E_{90}$	O. T. A.
PBE (GGA)		9.309	11.299	$\sim 35^0 - 40^0$
Fitted Energy		9.526	11.661	$\sim 35^0 - 40^0$
PW-DFT(GGA)	[206]	8.394	10.421	
Fitted potential	[206]	8.587	10.420	
MM4	[207]	10.324	7.719	
HF/6-31G*//MP2/6-31G*	[208]	13.605	6.079	45.7^0
MP2/cc-pVQZ//MP2/6-31G*	[208]	9.456	8.877	45.7^0
MP2/6-31G(d)	[209]	16.306	8.780	46^0
B3LYP/6-31G(d)	[209]	8.394	10.035	46^0
B3LYP/cc-pVTZ	[210]	8.008	8.877	39.1^0
B3LYP/6-311G*	[211]	9.070	7.526	42.5^0
Electron diffraction	[212, 213]	5.886	6.658	44.4^0
Raman scattering	[214]	5.886	5.886	
NMR	[215]	7.622	20.455	$34^0_a, 37.2^0_b$

Table 8.1: Comparison of the torsional barrier (in $kJ \, mol^{-1}$) and the optimized torsional angle (O. T. A.) for biphenyl between this work and previous studies. $_a$ ME method, $_b$ AP method.

The biphenyl torsional energy profile is shown in figure 8.4. For this molecule, torsional barriers at 0^0 of 9.309 kJ mol^{-1} and at 90^0 of 11.299 kJ mol^{-1} have been found in this work (see table 8.1). The fitting of these results produces torsional barriers of 9.526 kJ mol^{-1} at 0^0 and 11.661 kJ mol^{-1} at 90^0, in good agreement with the *ab initio* results. In both molecules, the coplanarity between the two rings generates steric repulsion forces between opposite hydrogens belonging to each of the rings. Aside from that, the perpendicular disposition between both rings constitutes an important hinderance for the π conjugation between the two rings, destabilizing significantly the molecule. Therefore the global torsional energy minimum is produced by a compromise between steric and electronic effects, at a dihedral angle of approximately 35^0. These results for biphenyl are in good agreement with previous NMR studies, although the optimized conformation characterized using electron diffraction provides a larger torsion angle, as shown in table 8.1. These results also show that the torsional barrier created by the electronic effects is larger than the one created by the steric ones. Again, the calculations accomplished in the present work are in good agreement with this. Previous calculations showed similar results to those herein presented [209] (see table 8.1), although in ref. [210] $\triangle E_{90}$ is significantly smaller. However, in other works carried out using wavefunction based methods [208, 211], the torsional barrier obtained for the planar conformation (0^0) was higher than the one obtained for the non-planar conformation (90^0).

The same lecture could be made from the results obtained from the 5-phenylpyrimidine, which has a similar structure to biphenyl. Two torsional barriers have been found for this molecule, $\triangle E_0$ and $\triangle E_{90}$, as can be appreciated in table 8.2, and an optimized inter-ring dihedral angle is found of approximately $35^0 - 40^0$. In this case the agreement between the plane-wave based DFT methods and the fitted energy data (with difference of 0.961 kJ mol^{-1} for $\triangle E_0$ and 1.571 kJ mol^{-1} in the case of $\triangle E_{90}$) is not as good as in the case of biphenyl. The existence of these two torsional barriers has the same causes as explained above for the biphenyl. The results obtained fitting the torsional energy are not as accurate as the ones obtained in the case of the biphenyl, although they are still in reasonably good agreement with those produced by the DFT calculations, as can be appreciated in figure in figure 8.4.

A previous study of the conformation of the 5-phenylpyrimidine [216] agreed with the fact that the optimized conformation of the molecule is in between the planar and non-planar conformations, in agreement with the present work. Studies of the crystal structure of 2,5-diphenylpyrimidine [217] determined an optimized torsional angle for the 5-phenylpyrimidine moiety of 34.6^0. This is in very good agreement with the results herein presented. Moreover, studies of the same type of torsional angle in 2-(4-n-propoxyphenyl)- and 2-(4-n-butoxyphenyl)-5-phenylpyrimidine [218] and 1,4-bis(5-phenyl-2-pyridinyl)-phenylene [219] provided results in a range between $35^0 - 39^0$, again in excellent agreement with the present work. Aside from that, the differences between $\triangle E_0$ and $\triangle E_{90}$ in [216] has been found to be 8.2 kJ mol^{-1}, while in this work it is just 1.558 kJ mol^{-1}.

Molecule	Method	$\triangle E_0$	$\triangle E_{90}$
2-phenylpyrimidine	PBE (GGA)	0.250	29.947
2-phenylpyrimidine	Fitted Energy	0.511	27.625
5-phenylpyrimidine	PBE (GGA)	9.360	10.918
5-phenylpyrimidine	Fitted Energy	8.399	9.347
2,4-biphenyl-1,3,5-oxadiazole	PBE (GGA)	0.403	28.861
2,4-biphenyl-1,3,5-oxadiazole	Fitted Energy	0.000	25.569

Table 8.2: Planar and perpendicular rotational barriers for the 2-phenylpyrimidine, 5-phenylpyrimidine and 2,4-biphenyl-1,3,5-oxadiazole. The results are shown in kJ mol^{-1}.

DFT calculations have been also performed for the 6-fluoro-2-phenylpyridine. Two torsional barriers have been found in this calculation, one at 0^0, with a value of 2.439 kJ mol^{-1} obtained from the *ab initio* data and 2.886 kJ mol^{-1} obtained from the fitted energy. The other torsional barrier, at 90^0, was found to be 20.225 and 19.040 kJ mol^{-1} for the *ab initio* and fitted energy respectively.

Results for both the torsional energy and the optimized conformation of 6-fluoro-2-phenylpyridine and 2-phenylpyridine are shown in table 8.3. These go from 0.63 to 6.234 kJ mol^{-1} in the case of the 0^0 torsional barrier and from 12.39 to 15.10 kJ mol^{-1} in the case of the 90^0 one. It is noteworthy to remark that in the case of the

6-fluoro-2-phenylpyridine the presence of the fluorine atom in the molecule increases the size of the torsional barriers significantly, specially in the case of $\triangle E_{90}$. This is a clear evidence of the contribution the fluorine atom makes to both the electronic effects responsible of the stabilization of the molecule and the steric effects of rotation past the 90^0 barrier. A similar effect occurs when a fluorine atom is introduced in a biphenyl molecule [141], albeit in that case the difference is not so dramatic.

Type of Mol.	Method	Reference	$\triangle E_0$	$\triangle E_{90}$	O. T. A.
2-F-6-phpyr	PBE (GGA)	Present work	2.439	20.225	$\sim 20^0$
2-F-6-phpyr	Fitted Energy	Present work	2.886	19.040	$\sim 20^0$
2-phpyr	HF/6-31 G(d)	[220]	2.09	12.39	27.9^0
2-phpyr	B3LYP/6-31 + G(d)	[220]	0.68	14.97	21.89^0
2-phpyr	BPW91/6-31 + G(d)	[220]	0.63	15.10	21.69^0
2-phpyr	MP2/6-31 G(d)	[220]	4.22	13.28	31.49^0
2-phpyr	BP86/6-31 G(d)	[221]	6.246	6.293	15.0^0
2-phpyr	BP86/6-311 G(d)	[221]	6.243	6.280	18.1^0
2-phpyr	BP86/6-311 G(2d,2p)	[221]	6.238	6.276	18.2^0
2-phpyr	B3LYP/6-31 G(d)	[221]	6.238	6.268	18.2^0
2-phpyr	B3LYP/6-311 G(d)	[221]	6.234	6.264	20.4^0
2-phpyr	B3LYP/6-311 G(2d,2p)	[221]	6.230	6.259	20.8^0
2-phpyr	HF/6-31 G(d)	[222]	2.09	12.39	27.90^0
2-phpyr	B3LYP/6-31+G(d)	[222]	0.68	14.97	21.89^0
2-phpyr	BPW91/6-31+G(d)	[222]	0.63	15.10	21.69^0
2-phpyr	MP2(fc)/6-31G(d)	[222]	4.22	13.28	31.49^0

Table 8.3: Torsional barriers (in kJ mol^{-1}) and optimized torsional angles (O. T. A.) for the dihedral angle of the 6-fluoro-2-phenylpyridine shown in fig. 8.1 (c) and its equivalent dihedral angle in the 2-phenylpyridine.

A certain similarity can be found between the structures of the 2-phenylpyrimidine and the 6-fluoro-2-phenylpyridine. This gives them a similar rotational energy pro-

file for the inter-ring dihedral angle. In both cases, the situation of the nitrogen atoms in the molecule eliminates the repulsive steric interactions between hydrogens on both sides of the inter-ring angle. However, this effect is less dramatic in the case of the 6-fluoro-2-phenylpyridine, since it has just one atom of nitrogen and therefore steric repulsion between hydrogens. Therefore, the minimum torsional energy is associated with conformation which is close to the planar conformation (i.e., inter-ring dihedral angles of approximately 10^0) in the case of the 2-phenylpyrimidine. This result is in reasonable agreement with the X-ray structural data of the same torsional angle of 18.3^0 in the 5-bromo-2-phenylpyrimidine [217]. More structural data is available for the same type of dihedral angle in the molecules 2-(4-n-propoxyphenyl)- and 2-(4-n-butoxyphenyl)-5-phenylpyrimidine [218] and 1,4-bis(5-phenyl-2-pyridinyl)-phenylene [219]. In those particular cases the range of torsional angles was found in a range between 3^0 and 9^0.

The torsional barrier found for the 2-phenylpyrimidine at 0^0 was 0.250 kJ mol^{-1} calculated with the plane-wave based DFT methods and 0.511 kJ mol^{-1} for the fitted energy. These results show a $\triangle E_0$ very close to zero, in agreement with the above discussion. By contrast, the torsional barrier found at 90^0 was 29.947 kJ mol^{-1}, calculated from plane-wave based DFT calculations (27.625 kJ mol^{-1} from the fitted energy). Hence it is clear that in this case electronic effects are mainly responsible for the torsional barrier rather than steric ones. Previous studies [216] concluded the same thing, albeit the difference between the torsional energies at 0^0 and 90^0 was just of 8.7 kJ mol^{-1}, significantly smaller than in the present work.

Calculations of torsional barriers in the components of the ODBP-Ph-C$_7$ rigid core have been also performed. The rotational energy profiles are shown in figure 8.5, as well as the profiles of the correspondent fitted energies.

The optimized structure of the 2,5-diphenyl-1,3,4-oxadiazole is associated with a planar conformation for the molecule. This can be gathered from the results obtained for the torsional barriers of 0.403 and 0.000 kJ mol^{-1} for the *ab initio* and the fitted energy data respectively at 0^0 and 28.861 and 25.569 kJ mol^{-1} for the *ab initio* and the fitted energy data respectively at 90^0. Similarly to 2-phenylpyrimidine and the 6-fluoro-2-phenylpyridine, the absence of steric repulsions in the molecules

(a)

(b)

(c)

(d)
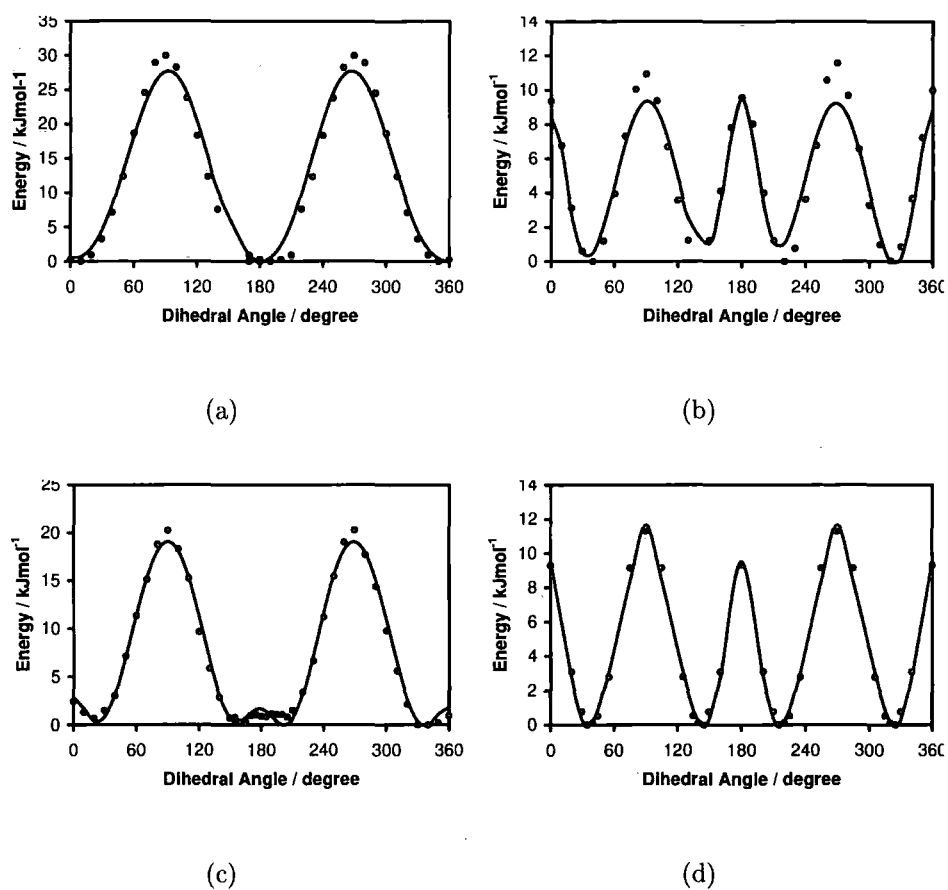
Figure 8.4: Torsional potentials for (a) 2-phenylpyrimidine, (b) 5-phenylpyrimidine, (c) 6-fluoro-2-phenylpyridine and (d) biphenyl. In all the cases the calculated *ab initio* data is represented by filled circles and the fitted energy is represented by a bold line.

makes the contribution of electronic factors to the torsional barrier more important. Therefore, the conjugation between the $N = C$ double bond and the phenyl ring plays an important role in the conformation of the 2,5-diphenyl-1,3,4-oxadiazole. Hence the rotational energy minimum is associated with a planar conformation. Structural determinations of the torsional angle existing between the phenyl and 1,3,4-oxadiazole rings were carried out by Doroshenko *et al.* [115] . In his work a non-planar conformation is found, with torsional angles in an interval between 59.4^0 and 39.0^0 found in the crystalline phase. Moreover, quantum-mechanical calculations at the semi-empirical level (AM1) were undertaken to optimize the geometry of the molecule. This calculation yielded a result similar to the experiment, with optimized torsional angle between 23.2^0 and 69.6^0. Nevertheless, it is worth mentioning that the accuracy of the DFT methods used in the present work is noticeable larger that that of the semi-empirical methods used in ref. [115]. Moreover, more recent studies of the 2,5-diphenyl-1,3,4-oxadiazole embedded in larger molecules have produced a quasi-planar conformer, with torsional angles going from 3.46^0 to 4.86^0 in ref. [116] and 6.1^0 to 6.3^0 in [117] .

A slightly smaller torsional barrier was found for the dihedral angle studied in the methyl benzoate (fig. 8.2 (b)). This molecule presented a single torsional barrier of 23.201 kJ mol^{-1} from *ab initio* methods (23.854 kJ mol^{-1} from the fitted energy). The existence of a torsional barrier in the non-planar configuration can be explained by considering that a perpendicular orientation of the carbonyl group with respect to the phenyl ring inhibits the conjugation of the oxygen lone electron pair through the molecular π−orbitals, and hence resonance stabilization is eliminated. It is noteworthy that there is good agreement existing between the DFT results and their corresponding fitted values. Moreover, a very good agreement has been achieved between the results in the present work and the available experimental data for the same type of molecule. For instance, the torsional barrier detected using ^{13}C NMR [223] was 20.58 kJ mol^{-1}. The results obtained through indirect infrared methods [224] provide a result of 22.18 kJ mol^{-1}, and even closer to the one obtained in the present work. In general, previous *ab initio* calculations performed on the same molecule yielded significantly larger torsional barriers [223,225]. Nevertheless,

SCF/STO-3G calculations produced a torsional barrier of 21.13 kJ mol^{-1} in methyl benzoate [226] and 22.849 kJ mol^{-1} in ethyl benzoate [227]. However, the basis set used in the present work is notably more complete. Other studies of the torsional barrier of the ethylbenzoate using different methods produced results between 20.347 and 40.694 kJ mol^{-1} (see table 8.4). Results obtained for the same type of dihedral angle in phenylbenzoate molecules normally produced higher torsional barriers (see table 8.4). This is in contrast with the results obtained by gas phase electron diffraction [228], which assigned a torsional barrier of just 14.6 kJ mol^{-1} to this dihedral angle.

(a)

(b)

(c)

(d)
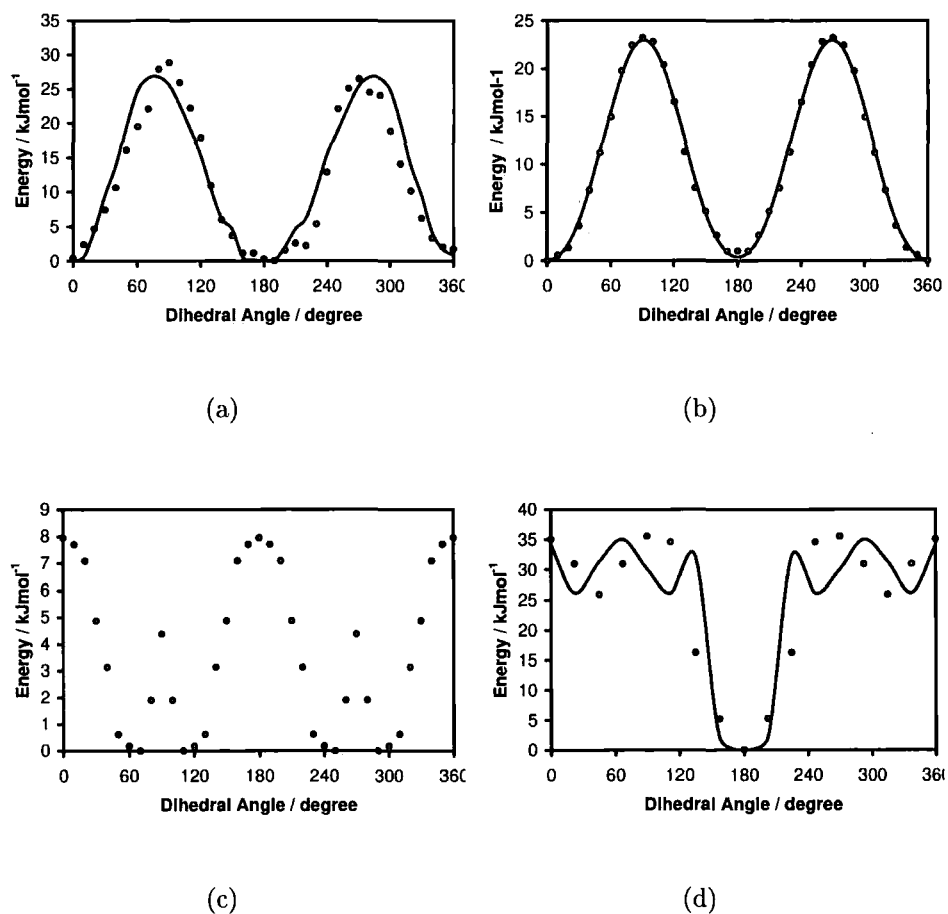
Figure 8.5: Torsional potentials for (a) 2,5-diphenyl-1,3,4-oxadiazole, (b) methyl benzoate, (c) phenyl acetate and (d) phenylbenzoate. In all the cases the calculated *ab initio* data is represented by filled circles and the fitted energy is represented by a bold line. No good fit was obtained for phenyl acetate.

The rotational profiles of phenyl acetate and phenylbenzoate differ significantly

Type of Mol.	Method	Reference	ΔE_{90}	O. T. A.
Me benzoate	PBE (GGA)	Present work	23.2009	0^0
Me benzoate	Fitted Energy	Present work	23.8537	0^0
Me benzoate	RHF/6-31 G*	[225]	33.0	0^0
Me benzoate	MP2/6-31 G*	[225]	27.2	0^0
Me benzoate	^{13}C NMR	[223]	20.58^a	0^0
Me benzoate	HF/6-311 G*	[223]	34.48^b 32.43^c	0^0
Me benzoate	MP2/6-31 G*	[223]	29.04^b 26.28^c	0^0
Ph benzoate	RHF/6-31 G**	[228]	33.9	0^0
Ph benzoate	GED	[228]	14.6	0^0
Ph benzoate	B3LYP/6-31 G*	[229]	31.4	1.2^0
Ph benzoate	B3LYP/6-31+G*	[229]	28.4	1.9^0
Et benzoate	SCF/STO-3G	[227]	22.849	0^0
Et benzoate	SCF/6-31 G	[227]	40.694	0^0
Et benzoate	SCF/6-31 G**	[227]	35.050	0^0
Et benzoate	MP2/STO-3G	[227]	20.347	0^0
Et benzoate	MP2/6-31 G	[227]	26.807	0^0
Ph benzoate	B3LYP/6-31 G*	[230]	31.63	1.5^0
Ph benzoate	HF/6-31 G*	[230]	33.89	0^0
Me benzoate	Indirect IR methods	[224]	22.18	0^0
Me benzoate	SCF/STO-3G	[226]	21.13	0^0
Me benzoate	SCF/AM1	[231]	10.9	0^0
Ph benzoate	SCF/AM1	[231]	9.8	0^0

Table 8.4: Torsional barriers (in kJ mol^{-1}) and Optimized torsional angles (O. T. A.) for the dihedral angle of the methyl benzoate (Me benzoate) shown in fig. 8.2 (b) and its equivalent dihedral angle in the phenylbenzoate (Ph benzoate) and ethyl benzoate (Et benzoate). ^{a} at -170^0C, ^{b} at 25^0C, ^{c} at -182^0C.

from the ones described above. Phenyl acetate shows two torsional barriers at 0^0 and 90^0, as can be seen in figure 8.5, similarly to biphenyl and 5-phenylpyrimidine. However, the torsional barrier produced by electronic effects at 90^0 is significantly smaller that the one caused by the steric factors at 0^0. This is expected since the conjugation is significantly smaller than, for instance, in the case of methyl benzoate. By contrast, the steric repulsion between the the hydrogens in the phenyl ring and both the oxygen in the carbonyl group or the methyl group bonded to the carbonyl group is significant. The predominance of the steric effects over the electronic effects is reinforced by the fact that the dihedral angle associated with the minimum torsional energy is approximately 60^0 and is thus closer to a non-planar conformation than to a planar one. This is in contrast with what has been above described for biphenyl and 2-phenylpyrimidine, where electronic effects were more important than steric ones and the torsional barrier at the non-planar conformation was higher than the one at the planar conformation. There is an excellent agreement between the minimum torsional energy region calculated in the present work ($\sim 60^0$) and the optimized structure found by gas electron diffraction, which provided a dihedral angle of 65^0 [232]. A similar result of $64^{+24}_{-12}{}^0$ was obtained also with gas electron diffraction for the equivalent dihedral angle in the phenylbenzoate [228]. Previous calculations of torsional energy at different levels for phenyl acetate [233] and the equivalent torsional angle in the phenylbenzoate [228, 229, 231] provided lower barriers (see table 8.5).

Both steric and electronic factors are crucial in the torsional energy profile of the phenylbenzoate. In the torsional energy profile shown in figure 8.5, the *trans* conformation is considered to occur at a torsional angle of 180^0, as shown in figure 8.2. In this case, the bond between $C - O$ has a certain double bond character, due to the conjugation of the oxygen lone pair of electrons and the $\pi*$ orbital of $C = O$. This stabilizes considerably the planar conformation of the dihedral angle. However, the destabilization caused by the very strong steric repulsion between the two phenyl rings in the *cis* conformation, when the torsional angle is equal to 0^0, makes the population in this conformation negligible. Also, due to the electronic factors mentioned above, the non-planar conformation is also highly unstable. All

Type of Mol.	Method	Ref.	$\triangle E_0$	$\triangle E_{90}$	O. T. A.
Ph acetate	PBE (GGA)	Pres. work	7.9496	4.3815	$\sim 60^0 - 70^0$
Ph benzoate	B3LYP/6-31+G*	[229]	3.01	0.29	64.2^0
Ph benzoate	B3LYP/6-31 G*	[229]	1.59	1.59	49.5^0
Ph benzoate	RHF/6-31G**	[228]	-	5.4	91.7^0
Ph benzoate	GED	[228]	5.02	0.12	$64^{+24}_{-12}{}^0$
Ph acetate	MM "inference method"	[233]	5.02	0.25	$\sim 60^0$
Ph benzoate	AM1 SCF	[231]	5.52	1.76	50.3^0
Ph benzoate	B3LYP/6-31 G*	[230]	1.55	1.51	$\sim 50^0 - 60^0$
Ph benzoate	HF/6-31 G*	[230]	5.86	-	$\sim 50^0 - 60^0$
Ph acetate	PCMODEL (MMFF94)	[234]	-	-	58^0
Ph acetate	B3LYP/6-311 G**	[234]	-	-	$0^0{}_L \quad 64^0{}_G$
Ph acetate	GED	[234]	-	-	$\sim 65^0$

Table 8.5: Torsional barriers (in kJ mol^{-1}) and optimized torsional angles (O. T. A.) for the dihedral angle of the phenyl acetate shown in fig. 8.5 (c) and its equivalent dihedral angle in the phenylbenzoate. $_L$ Local minimum, $_G$ Global minimum.

previous studies of the phenylbenzoate central dihedral angle agree in assigning the minimum torsional energy to the planar conformation associated with a torsional angle of 180^0 (see table 8.6). Two torsional energies are presented in table 8.6. $\triangle E_{cis-trans}$ represents the local minimum of the torsional energy between the *cis* and *trans* conformations (see figure 8.5). Its value is 25.94 kJ mol^{-1} calculated with DFT (26.21 kJ mol^{-1} with the fitted energy). It is noteworthy that both results are rather similar. Previous results [230, 231] are in a reasonably good agreement with this work. The calculated torsional barrier between the local and minimum energy, $\triangle E_{tors.}$, is 35.04 kJ mol^{-1} using the DFT method and 34.05 kJ mol^{-1} is the result obtained for the fitted energy. Again these results are consistent with each other. Similar torsional barriers have been fond using DFT methods [230], although the basis set used in this work is more complete.

Method	Reference	$\triangle E_{cis-trans}$	$\triangle E_{tors.}$	O. T. A.
PBE (GGA)	Present work	25.94	35.04	180^0
Fitted Energy	Present work	26.21	34.05	180^0
AM1-SCF	[231]	21.3	24.3	180^0
B3LYP/6-31 G*	[230]	32.18	33.05	180^0
MP2/6-31 G*(d_0)	[235]	42.2	-	-
RHF/4-31 G**	[228]	-	-	179^0
RHF/6-31 G**	[228]	-	-	180^0
BP86/6-31 G**	[228]	-	-	181.4^0

Table 8.6: Torsional energy differences (in kJ mol^{-1}) between *cis* and *trans* conformations ($\triangle E_{cis-trans}$), torsional barrier ($\triangle E_{tors.}$) and optimized torsional angles (O. T. A.) for phenylbenzoate.

8.4.3 Torsional Constants

The results obtained from the fitting of the torsional energies to equation 8.13 given in 8.4.1 are shown in table 8.7.

Structure	V_1	V_2	V_3
2-phenylpyrimidine	-0.3498	7.2230	0.3518
5-phenylpyrimidine	-0.2457	6.6156	0.0796
6-fluoro-2-phenylpyridine	-0.0158	9.5026	0.0866
2,4-biphenyl-1,3,5-oxadiazole	1.3666	4.8076	-1.5534
biphenyl	-8.3593	2.5251	-0.9755
methyl benzoate	-0.1755	1.0862	0.0861
phenylbenzoate	8.0951	6.0154	-3.8004

Table 8.7: Torsional parameters for all the structures calculated in kJ mol^{-1}. The bonds about which the torsional barrier have been calculated are specified in figures 8.1 and 8.2.

8.5 Conclusions

DFT methods have been used to calculate torsional energies of the molecules biphenyl, 2-phenylpyrimidine, 5-phenylpyrimidine, 6-fluoro-2-phenylpyridine, 2,5-diphenyl-1,3,4-oxadiazole, methyl benzoate, phenyl acetate and phenylbenzoate.

Both the torsional profiles and the estimated optimum conformations presented in this work are generally in good agreement with those obtained experimentally, albeit the torsional barriers are in some cases overestimated.

The torsional energies have been subsequently employed in the fitting of torsional constants. These can be used in the development of liquid crystal force fields, entailing a significant improvement in the quality of the simulations of liquid crystals.

Chapter 9

Summary and Forthcoming Work

9.1 Summary

Atomistic simulations of low-weight thermotropic biaxial liquid crystal ODBP-Ph-C_7 and the mixture of liquid crystals E7 have been undertaking in this thesis. The former have been used to explain the mechanisms responsible for the onset of the biaxial phase. The simulations have been run at five different temperatures covering the nematic range [23] (448 K, 458 K, 468 K, 478 K and 488 K). Ferroelectric domains have been observed in all the systems. For the 468 K simulation a single monodomain forms, and for the 478 K one it seems that a single monodomain is forming. However, limitations in simulation time have made impossible to detemine if the different domains formed in each one of the simulations will eventually merge into a single one, as in the case of the 468 K simulations. The formation of layers within the systems simulated seems unlikely, but due to system size limitation it is not possible to rule it out. Biaxial phase order parameters have been calculated using two different methods [35, 96]. Both methods agreed in the existence of a biaxial phase in the 468 K and 478 K simulations. Even though it is not possible to state that there is a biaxial phase in the 448 K, 458 K and 488 K simulations, it is possible that further simulations will produce the onset of the biaxial phase.

Simulations with the electrostatic charges off have been performed to study the role played by the electrostatic charges in the phase biaxiality. Removal of charges led to the disappearance of the ferroelectric domains and the formation of a uniaxial

nematic phase. When switching on the partial charges again, a biaxial phase formed from the uniaxial one, accompanied by the reformation of the ferroelectric domains.

The growth of a liquid crystalline phase from the isotropic phase was accomplished with the electrostatic charges on and off. This is the first time an isotropic-liquid crystal phase transition has been achieved using molecular simulations at a fully atomistic level (all-atom). The simulations show that the time required to reproduce a phase transition at this level (~ 100 ns) is two orders of magnitude longer than the one required for an united-atom model (~ 1 ns) and several orders of magnitude longer than typical for single-site models [1]. The growth of a liquid crystal phase with the charges off did not produce a biaxial phase. By contrast, it seemed that a smectic phase formed. It is thus likely that ferroelectric domains stabilize the biaxial phase and destabilize the smectic phase. The growth of a liquid crystalline phase from an isotropic phase with the charges on produced a biaxial phase.

Simulations have been also useful to examine the experimental ^{2}H NMR results obtained previously for ODBP-Ph-C$_7$ and which still remain questioned due to the extreme experimental conditions in which they have been obtained. Simulations of the system formed from ODBP-Ph-C$_7$ and the probe molecule hexamethylbenzene have been undertaken in order to reproduce the experiment and to measure indirectly the biaxial phase parameter η [23]. Even though η calculated from the simulations and experimental η did not agree quantitatively, both agreed on the formation of a biaxial phase by the ODBP-Ph-C$_7$.

Atomistic simulations of the mixture of liquid crystals E7 have been undertaken to study the structure of the liquid crystalline phase formed by the mixture. Simulations at six different temperatures (280 K, 290 K, 300 K, 310 K, 320 K and 330 K) have been performed covering the nematic range. An anti-parallel pairwise dipole correlation between neighbouring molecules has been observed. However, parallel pairwise dipole correlation has been also appreciated, although this is weaker. The

---

[1]For single-site models, growth of a liquid crystal phase can occur in $\sim 10^5$ time steps. An equivalent timestep for such a simulation would be $\sim 10^{-14}$ s, corresponding to a total time of $\sim 10^{-9}$ s $\equiv 1$ ns.

correlation between the different types of molecule are very similar but for the 5CT, which has a stronger orientational correlation due to the extra phenyl ring in the molecule core, which increases the attractive quadrupolar forces between molecules. The density achieved in the different simulations have turned out to be slightly high in comparison to experiment. This is likely caused by the use of slightly too attractive potential parameters.

The simulations have been also used to calculate key material properties for a liquid crystal, such as the rotational viscosity and the flexoelectric coefficients. Two different techniques were used to calculate the former with consistent results. The results obtained for the flexoelectric coefficients are consistent with simulations of other mesogens and in the same order of magnitude that the experimental results.

Finally *ab initio* calculations using DFT methods have been carried out for eight different molecules which represent typical components of common mesogens. The motivation for these calculations was in the parametrization for torsional potential of dihedral angles, which are crucial in determining the conformations of many liquid crystal molecules.

9.2 Forthcoming Work

The different results obtained in the simulations of the ODBP-Ph-C_7 performed at different temperatures suggest that maybe not all the systems are perfectly equilibrated. Therefore, further simulations would be necessary to state whether the different ferroelectric domains appreciated in all the simulations with the charges on eventually merge into a single one. The use of a larger number of processors than available for this thesis would facilitate run simulation of larger systems, thus checking whether system size effects influence the biaxial phase and distinguishing between domains and layers. An effective way of overcoming the system size and simulation time limitations is given by coarse-grained models. The design of a coarse-grain model which faithfully reproduced the molecular symmetry and, in particular, the quadrupoles and dipole present in the ODBP-Ph-C_7 would certainly produce very interesting results.

Limitations in system size and simulation time also apply to the simulations of the mixture of liquid crystals E7. Here it would be interesting to experiment with united-atom models to see if the latter was able to reproduce E7 with fewer simulation sites. Further simulations would provide higher quality results.

Finally, it would be interesting to undertake *ab initio* calculations in order to find torsional parameters involved in the siloxane tetrapode molecule claimed to be a biaxial thermotropic mesogen by Merk *et al.* [24]. This would allow brief atomistic simulation of the molecule in a liquid phase in order to create a coarse-grain model which could successfully reproduce the biaxial phase formed by this type of molecule. Simulations of this system would allow for the study of phase biaxiality which almost certainly possesses a different origin to the biaxial ordering than that seen in ODBP-Ph-C$_7$.

Bibliography

[1] F. Reinitzer, *Monatshefte fur Chemie*, 1888, **9**, 421.

[2] Z. O. Lehnmann, *Phys. Chem.*, 1889, **4**, 462.

[3] M. J. Freiser, *Phys. Rev. Lett.*, 1970, **24**(19), 1041.

[4] S. Chandrasekhar, V. N. Raja, and B. K. Sadashiva, *Mol. Cryst. Liq. Cryst. Lett. Sect.*, 1990, **7**, 65.

[5] J. Malthele, L. Liebert, A.-M. Levelut, and Y. Galerne, *C. R. Acad. Sci. Paris*, 1986, **303**, 1073.

[6] B. R. Acharya, A. Primak, and S. Kumar, *Phys. Rev. Lett.*, 2004, **92**(14), 145506.

[7] B. R. Acharya, A. Primak, and S. Kumar, *Liq. Cryst. Today*, 2004, **13**, 1 – 4.

[8] ed. J. W. Goodby, *Handbook of Liquid Crystals*, Vol. 3, Wiley-VCH, 1998.

[9] V. Percec, P. W. Chu, G. Ungar, and J. P. Zhou, *J. Am. Chem. Soc.*, 1995, **117**, 11441.

[10] S. A. Ponomarenko, N. I. Boiko, V. P. Shibaev, R. M. Richardson, I. J. White-house, E. A. Rebrov, and A. M. Muzafarov, *Macromolecules*, 2000, **33**, 5549.

[11] R. M. Richardson, S. A. Ponomarenko, N. I. Boiko, and V. P. Shibaev, *Liq. Cryst.*, 1999, **26**, 101.

[12] H. F. Leube and H. Finkelmann, *Makromol. Chem-Macro. Chem. Phys.*, 1991, **192**(6), 1317 – 1328.

[13] K. Severing and K. Saalwächter, *Phys. Rev. Lett.*, 2004, **92**(12), 125501.

[14] K. Severing, E. Stibal-Fischer, A. Hasenhindl, H. Finkelmann, and K. Saalwächter, *J. Phys. Chem. B*, 2006, **110**, 15680 – 15688.

[15] I. Saez and J. Goodby, *Liq. Cryst.*, 1999, **26**(7), 1101–1105.

[16] I. Saez, J. W. Goodby, and R. M. Richardson, *Chem. Eur. J.*, 2001, **7**, 2758 – 2764.

[17] I. Saez and J. W. Goodby, *J. Mat. Chem.*, 2001, **11**, 2845.

[18] H. Frey and C. Schlenk, *Topics in Current Chemistry*, 2000, **210**, 69–128.

[19] G. R. Newkome, C. N. Moorefield, and F. Vögtle, *Dendrimers and Dendrons*, Wiley-VCH, 2001.

[20] Tschierske, *J. Mater. Chem.*, 2001, **11**, 2647–2671.

[21] G. Friedel, *Ann. Physique*, 1922, p. 18.

[22] L. J. Yu and A. Saupe, *Phys. Rev. Lett.*, 1980, **45**(12), 1000 – 1003.

[23] L. A. Madsen, T. J. Dingemans, M. Nakata, and E. T. Samulski, *Phys. Rev. Lett.*, 2004, **92**(14), 145505.

[24] K. Merkel, A. Kocot, J. K. Vij, R. Korlacki, G. H. Mehl, and T. Meyer, *Phys. Rev. Lett.*, 2004, **93**(23), 237801.

[25] J. L. Figueirinhas, C. Cruz, D. Filip, G. Feio, A. C. Ribeiro, Y. Frere, T. Meyer, and G. H. Mehl, *Phys. Rev. Lett.*, 2005, **94**(10), 107802.

[26] R. Amaranatha Reddy and C. Tschierske., *J. Mat. Chem.*, 2006, **16**, 907 – 961.

[27] M. R. Wilson, *J. Mol. Liq.*, 1996, **68**, 23–31.

[28] G. R. Luckhurst, *Thin Solid Films*, 2001, **393**, 40 – 52.

[29] N. Metropolis, A. W. Rosenbluth, M. N. Rosnbluth, A. H. Teller, and E. Teller, *J. Chem. Phys.*, 1953, **21**, 1087.

[30] B. J. Alder and T. E. Wainwright, *J. Chem. Phys.*, 1957, **27**(5), 1208–1209.

[31] B. J. Alder and T. E. Wainwright, *J. Chem. Phys.*, 1959, **31**(2), 459–466.

[32] M. R. Wilson, *Int. Rev. Phys. Chem.*, 2005, **24**(3-4), 421 – 455.

[33] C. M. Care and D. J. Cleaver, *Rep. Prog. Phys.*, 2005, **68**, 2665–2700.

[34] ed. J. P. Hansen and I. R. McDonald, *Theory of Simple Liquids*, Academic Press, 1986.

[35] M. P. Allen, *Liq. Cryst.*, 1990, **8**(4), 499 – 511.

[36] S. Esteban-Martin and J. Salgado, *Biophys. J.*, 2007, **92**(3), 903 – 912.

[37] J. Aittoniemi, T. Rog, P. Niemela, M. Pasenkiewicz-Gierula, M. Karttunen, and I. Vattulainen, *J. Phys. Chem. B*, 2006, **110**(51), 24462 – 24464.

[38] A. J. McDonald and S. Hanna, *J. Chem. Phys.*, 2006, **124**(16), 164906.

[39] D. L. Cheung, S. J. Clark, and M. R. Wilson, *J. Chem. Phys.*, 2004, **121**(18), 9131 – 9139.

[40] M. R. Wilson, *Molec. Phys.*, 1994, **81**(3), 675 – 690.

[41] J. C. Shelley, M. Y. Shelley, R. C. Reeder, S. Bandyopadhyay, and M. L. Klein, *J. Phys. Chem. B*, 2001, **105**(19), 4464 – 4470.

[42] H. Meyer, O. Biermann, R. Faller, D. Reith, and F. Muller-Plathe, *J. Chem. Phys.*, 2000, **113**(15), 6264 – 6275.

[43] D. Reith, H. Meyer, and F. Müller-Plathe, *Macromol.*, 2001, **34**, 2335 – 2345.

[44] F. Müller-Plathe, *Chem. Phys. Chem.*, 2002, **3**, 754 – 769.

[45] Z. E. Hughes, M. R. Wilson, and L. M. Stimson, *Soft Matter*, 2005, **1**(6), 436 – 443.

[46] D. Frenkel, B. M. Mulder, and J. P. McTague, *Phys. Rev. Lett.*, 1984, **52**, 287.

[47] P. Bolhuts and D. Frenkel, *J. Chem. Phys.*, 1997, **106**, 666.

[48] A. Stoobants, H. N. W. Lekkerkerker, and D. Frenkel, *Phys. Rev. Lett.*, 1986, **57**, 1452.

[49] J. E. Lennard-Jones, *Proc. R. Soc. Lond. Ser. A*, 1924, **106**, 463.

[50] J. G. Gay and B. J. Berne, *J. Chem. Phys.*, 1981, **74**, 3316.

[51] L. F. Rull, *Physica A*, 1995, **220**, 113.

[52] E. de Miguel, E. M. del Rio, J. T. Brown, and M. P. Allen, *J. Chem. Phys.*, 1996, **105**, 4234.

[53] G. R. Luckhurst, R. A. Stephens, and R. W. Phippen, *Liq. Cryst.*, 1990, **8**(4), 451–464.

[54] R. Berardi, A. Emerson, and C. Zannoni, *J. Chem. Soc. Faraday Trans.*, 1993, **89**, 4069–4078.

[55] C. Zannoni, *J. Mater. Chem.*, 2001, **11**(11), 2637 – 2646.

[56] ed. M. R. Wilson, J. M. Ilnytskyi, L. M. Stimson, and Z. E. Hughes, *Computer Simulations of liquid crystals and polymers*, Pasini, P. and Zannoni, C. and Zümer, S., 2004.

[57] N. L. Allinger, *Rev. Phys. Org. Chem.*, 1976, **13**, 1.

[58] O. Burkert and N. L. Allinger, *Molecular Mechanics, ACS Monograph 177*, American Chemical Society, Washington, DC., 1982.

[59] R. H. Boyd, *J. Chem. Phys.*, 1968, **49**, 2574.

[60] ed. M. P. Allen and D. J. Tildesley, *Computer Simulations of Liquids*, Clarendon Press, Oxford, 1987.

[61] L. Verlet, *Phys. Rev.*, 1967, **159**(1), 98 –103.

[62] R. W. Hockney, *Methods comput. Phys.*, 1970, **9**, 136 – 211.

[63] ed. D. Potter, *Computational Physics*, Wiley, New York, 1972.

[64] ed. D. Frenkel and B. Smit, *Understanding Molecular simulation*, Academic Press, Oxford, 2002.

[65] H. J. C. Berendsen, J. P. M. Postma, W. F. van Gunsteren, A. DiNola, and J. R. Haak, *J. Chem. Phys.*, 1984, **81**, 3684.

[66] B. Rosi, F. M. P., I. Dozov, and N. Kirov, *Phys. Rev. A*, 1987, **36**(6), 2879 – 2884.

[67] F. Biscarini, C. Chiccoli, P. Pasini, F. Semeria, and C. Zannoni, *Phys. Rev. Lett.*, 1995, **75**(9), 1803 – 1806.

[68] A. Ferrarini, G. R. Luckhurst, P. L. Nordio, and S. J. Roskilly, *J. Chem. Phys.*, 1994, **100**, 1460.

[69] J. P. Straley, *Phys. Rev. A*, 1974, **10**(5), 1881 – 1887.

[70] R. Alben, *Phys. Rev. Lett.*, 1973, **30**(17), 778 – 781.

[71] D. W. Allender and J. W. Doane, *Phys. Rev. A*, 1978, **17**(3), 1177 – 1180.

[72] J. Malthete, L. Liebert, A. M. Levelut, and Y. Galerne, *Acad. Sci. Ser. Gen., Ser. 2*, 1986, **303**(12), 1073 – 1076.

[73] S. Chandrasekhar, B. K. Sadashiva, B. R. Ratna, and V. N. Raja, *Pramana*, 1988, **30**(5), L491 – L494.

[74] K. Praefcke, B. Kohne, B. Gundogan, D. Demus, S. Diele, and G. Pelzl, *Mol. Cryst. Liq. Cryst. Lett.*, 1990, **7**, 27.

[75] J. R. Hughes, G. Kothe, G. R. Luckhurst, J. Malthete, M. E. Neubert, I. Shenouda, B. A. Timimi, and M. Tittelbach, *J. Chem. Phys.*, 1997, **107**(21), 9252–9263.

[76] F. P. Nicolettat, G. Chidichimo, A. Golemme, and N. Picci, *Liq. Cryst.*, 1991, **10**(5), 665 – 674.

[77] E. A. Oliveira, L. Liebert, and A. M. Figueiredo Neto, *Liq. Cryst.*, 1989, **5**(6), 1669 – 1675.

[78] S. Chandrasekhar, G. G. Nair, D. S. Shankar Rao, S. Krishna Prasad, K. Praefcke, and D. Singer, *Mol. Cryst. Liq. Cryst.*, 1996, **288**, 7.

[79] K. Praefcke, B. Kohne, B. Gundogan, D. Singer, D. Demus, S. Diele, G. Pelzl, and U. Bakowsky, *Mol. Cryst. Liq. Cryst.*, 1991, **198**, 393 – 405.

[80] I. D. Fletcher and G. R. Luckhurst, *Liq. Cryst.*, 1995, **18**(2), 175 – 183.

[81] L. Omnes, B. A. Timimi, T. Gelbrich, M. B. Hursthouse, G. R. Luckhurst, and D. W. Bruce, *Chem. Commun.*, 2001, p. 2248.

[82] G. Pelzl, S. Diele, and W. Weissflog, *Adv. Mat.*, 1999, **11**(9), 707 – 724.

[83] R. Hashim, G. R. Luckhurst, and S. Romano, *Molec. Phys.*, 1985, **56**(6), 1217 – 1234.

[84] *Elementary Theory of Angular Momentum*, Wiley, New York, 1957.

[85] P. J. Camp and M. P. Allen, *J. Chem. Phys.*, 1997, **106**, 6681.

[86] S. Sarman, *Journal of Chemical Physics*, 1996, **105**(10), 4211 – 4222.

[87] S. Sarman, *Phys. Chem. Chem. Phys.*, 2000, **2**, 3831 – 3839.

[88] R. Berardi and C. Zannoni, *J. Chem. Phys.*, 2000, **113**, 5971–5979.

[89] M. A. Bates and G. R. Luckhurst, *Phys. Chem. Chem. Phys.*, 2005, **7**, 2821 – 2829.

[90] P. A. Lebwohl and G. Lasher, *Phys. Rev. A*, 1972, **6**, 426.

[91] P. J. Camp, M. P. Allen, and A. J. Masters, *J. Chem. Phys.*, 1999, **111**(21), 9871 – 9881.

[92] P. I. C. Teixeira, A. J. Masters, and B. M. Mulder, *Molec. Cryst. Liq. Cryst.*, 1998, **323**, 167 – 189.

[93] Y. Lansac, P. Maiti, N. Clark, and M. Glaser, *Physical Review E*, 2003, **67**(1), art. no. – 011703.

[94] R. Memmer, *Liq. Cryst.*, 2002, **29**(4), 483.

[95] S. J. Johnston, R. J. Low, and M. P. Neal, *Phys. Rev. E*, 2002, **65**(5), art. no. 051706.

[96] M. A. Bates and G. R. Luckhurst, *Phys. Rev. E.*, 2005, **72**(5), 051702.

[97] J. Xu, R. L. B. Selinger, J. V. Selinger, and R. Shashidhar, *J. Chem. Phys.*, 2001, **115**(9), 4333.

[98] J. D. Weeks, D. Chandler, and H. C. Andersen, *J. Chem. Phys.*, 1971, **54**, 5237.

[99] A. Deward and P. J. Camp, *Phys. Rev. E*, 2004, **70**(011704).

[100] S. J. Johnston, R. J. Low, and M. P. Neal, *Phys. Rev. E*, 2002, **66**(6), 061702.

[101] S. J. Johnston, R. J. Low, and M. P. Neal, *Phys. Rev. E*, 2002, **65**(5), 051706.

[102] S. Orlandi, R. Berardi, J. Steltzer, and C. Zannoni, *J. Chem. Phys.*, 2006, **124**(12), 124907.

[103] Y. Galerne, *Mol. Cryst. Liq. Cryst.*, 1998, **323**, 211.

[104] A. J. Blake, D. W. Bruce, I. A. Fallis, S. Parsons, and M. Schröder, *J. Chem. Soc. Chem. Commun.*, 1994, **1994**, 2471 – 2473.

[105] S. Krishna Prasad, D. S. Shankar Rao, S. Chandrasekhar, and S. Kumar, *Mol. Cryst. Liq. Cryst.*, 2003, **396**, 121 – 139.

[106] J. Stamatoff, P. E. Cladis, D. Guillon, M. C. Cross, T. Bilash, and P. Finn, *Phys. Rev. Lett.*, 1980, **44**(23), 1509–1512.

[107] W. D. Cornell, P. Cieplak, C. I. Bayly, I. R. Gould, K. M. M. Jr., D. M. Ferguson, D. C. Spellmeyer, T. Fox, J. W. Caldwell, and P. A. Kollman, *J. Am. Chem. Soc.*, 1995, **117**, 5179.

[108] W. Jorgensen, D. Maxwell, and J. TiradoRives, *J. Am. Chem. Soc.*, 1996, **118**(45), 11225–11236.

[109] Maestro molecular modelling interface. copyright 1999-2003 schrödinger,inc. 1999.

[110] T. R. Forester and W. Smith, *DL_POLY is a package of molecular simulation routines written by W. Smith and T. R. Forester, copyright The Council for the Central Laboratory of the Research Councils, Daresbury Laboratory at Daresbury, Nr. Warrington (1996)*.

[111] J. P. Ryckaert, G. Ciccotti, and H. J. C. Berendsen, *J. Comput. Phys.*, 1977, **23**(3), 327 – 341.

[112] M. P. Allen and D. J. Tildesley, Oxford University Press, Oxford, 1987; chapter 1.

[113] S. Nosé, *Mol. Phys.*, 1984, **52**, 255.

[114] W. G. Hoover, *Phys. Rev. A*, 1985, **31**, 1695.

[115] H. Zhao, Y. Wei, and W. Hua, *J. Mol. Struct.*, **553**.

[116] C.-H. Mao, Q.-M. Wang, R.-Q. Huang, L. Chen, J. Shang, and H.-B. Song, *Act. Cryst. E*, **60**(10).

[117] A. Carella, A. Castaldo, R. Centore, A. Fort, A. Sirigu, and A. Tuzi, *J. Chem. Soc. Perkin Trans. 2*, **2002**.

[118] M. Wilson and M. Allen, *Liq. Cryst.*, 1992, **12**(1), 157–176.

[119] C. McBride, M. R. Wilson, and J. A. K. Howard, *Mol. Phys.*, 1998, **93**(6), 955–964.

[120] C. W. Cross and B. Fung, *J. Chem. Phys.*, 1994, **101**, 6839.

[121] M. R. Wilson, *Liq. Cryst.*, 1996, **21**, 437.

[122] M. J. Cook and M. R. Wilson, *Molec. Cryst. Liq. Cryst.*, 2001, **363**, 181.

[123] Y. Lansac, M. P. K., N. A. Clark, and M. A. Glaser, *Phys. Rev. E.*, 2003, **67**(1), 011703.

[124] D. Goldfarb, R. Poupko, and Z. Luz, *J. Chem. Phys.*, 1983, **79**(8), 4035 – 4041.

[125] P. J. Collings, *Phys. Rev. Lett.*, 1979, **42**(15), 996 – 999.

[126] D. J. Photinos, P. J. Bos, J. W. Doane, and M. E. Neubert, *Phys. Rev. A*, 1979, **20**(5), 2203 – 2212.

[127] K. P. Maiti, Y. Lansac, M. A. Glaser, and N. A. Clark, *Phys. Rev. Lett.*, 2002, **88**(6), 065504.

[128] I. C. Sage, W. A. Crossland, and T. D. Wilkinson in *Handbook of Liquid Crystals*, ed. D. Demus, J. Goodby, G. W. Gray, H.-W. Spiess, and V. Vill, Vol. 1; Wiley-VCH, Weinheim, 1998; chapter IX.1-IX.2.

[129] P. Collings and M. Hird, *Introduction to liquid crystals*, Taylor & Francis, 1997.

[130] D. L. Cheung, S. J. Clark, and M. R. Wilson, *Phys. Rev. E*, 2002, **65**, art. no. 051709.

[131] A. Y. G. Fuh, K. L. Huang, C. H. Lin, I.-I. C. Lin, and I. M. Jiang, *Chinese J. Phys.*, 1990, **28**, 551.

[132] H. Allison and H. F. Gleeson, *Liq. Cryst.*, 1993, **14**(5), 1469 – 1478.

[133] I. Haller, *Prog. Solid St. Chem.*, 1975, **10**, 103.

[134] R. A. Bemrose, C. M. Care, D. J. Cleaver, and M. P. Neal, *Mol. Cryst. Liq. Cryst. Sci. Tec. A*, 1997, **299**, 27 – 32.

[135] R. A. Bemrose, C. M. Care, D. J. Cleaver, and M. P. Neal, *Mol. Phys.*, 1997, **90**(4), 625 – 635.

[136] H. N. W. Lekkerkerker, P. Coulon, R. Vanderhaegen, and R. Deblieck, *J. Chem. Phys.*, 1984, **80**(7), 3427 – 3433.

[137] T. Odijk and H. N. W. Lekkerkerker, *J. Phys. Chem.*, 1985, **89**(10), 2090 – 2096.

[138] G. J. Vroege and H. N. W. Lekkerkerker, *Rep. Prog. Phys.*, 1992, **55**(8), 1241 – 1309.

[139] G. J. Vroege and H. N. W. Lekkerkerker, *J. Phys. Chem.*, 1993, **97**(14), 3601 – 3605.

[140] T. J. Sluckin, *Liq. Cryst.*, 1989, **6**(1), 111 – 131.

[141] D. L. Cheung, S. J. Clark, and M. R. Wilson, *Phys. Rev. E*, 2002, **65**, 051709.

[142] M. Wilson, *Liq. Cryst.*, 1996, **21**(3), 437–447.

[143] M. J. Cook and M. R. Wilson, *Liq. Cryst.*, 2000, **27**, 1573.

[144] D. A. Dunmur and K. Toriyama, *Mol. Cryst. Liq. Cryst.*, 1991, **198**, 201 – 213.

[145] D. A. Dunmur and K. Toriyama, *Mol. Cryst. Liq. Cryst. Sci. Tec. A.*, 1995, **264**, 131 – 144.

[146] K. Toriyama and D. A. Dunmur, *Mol. Phys.*, 1985, **56**(2), 479 – 484.

[147] K. Toriyama, S. Sugimori, K. Moriya, D. A. Dunmur, and R. Hanson, *J. Phys. Chem.*, 1996, **100**(1), 307 – 315.

[148] D. A. Dunmur, *Liq. Cryst.*, 2005, **32**(11-12), 1379 – 1387.

[149] D. A. Dunmur and P. Palffy-Muhoray, *Mol. Phys.*, 1992, **76**(4), 1015 – 1024.

[150] S. T. Wu and C. S. W, *Phys. Rev. A*, 1990, **42**(4), 2219.

[151] M. A. Osipov and E. M. Terentjev, *Z. Naturforsch. Teil. A.*, 1989, **44**, 785.

[152] A. C. Diogo and A. F. Martins, *Mol. Cryst. Liq. Cryst.*, 1981, **66**, 133 – 146.

[153] H. Wang, T. X. Wu, S. Gauza, J. R. Wu, and S.-T. Wu, *Liq. Cryst.*, 2006, **33**(1), 91 – 98.

[154] A. V. Zakharov and R. Y. Dong, *Phys. Rev. E*, 2000, **63**, 011704.

[155] S. Kuwajima and A. Manabe, *Chem. Phys. Lett.*, 2000, **332**(1-2), 105 – 109.

[156] S. Sarman, *J. Chem. Phys.*, 1995, **103**(23), 10378 – 10386.

[157] S. Sarman, *J. Chem. Phys.*, 1995, **103**(1), 393 – 416.

[158] D. Forster, *Annals of Physics*, 1974, **84**, 505.

[159] S. Sarman and D. J. Evans, *J. Chem. Phys.*, 1993, **99**(11), 9021 – 9036.

[160] D. Cheung, S. J. Clark, and M. R. Wilson, *Chem. Phys. Lett.*, 2002, **356**, 140–146.

[161] A. Cuetos, J. M. Ilnytskyi, and M. R. Wilson, *Molec. Phys.*, 2002, **100**(24), 3839 – 3845.

[162] R. Meyer, *Phys. Rev. Lett.*, 1969, **22**(18), 918 – 921.

[163] ed. T. P. of Liquid Crystals, *Handbook of Liquid Crystals*, Claredon press, Oxford, 1974.

[164] P. Rudquist and S. T. Lagerwall, *Liq. Cryst.*, 1997, **23**, 503.

[165] J. Prost and J. P. Marceau, *J. Phys. (Paris)*, 1977, **38**, 315.

[166] A. Ferrarini, *Phys. Rev. E*, 2001, **64**, 021710.

[167] J. P. Marceau and J. Prost, *Mol. Cryst. Liq. Cryst.*, 1980, **58**, 259.

[168] P. Martinot-Lagarde and G. Druand, *J. Phys. Lett.*, 1980, **41**(2), L43.

[169] M. Čepič and B. Žekš, *Phys. Rev. Lett.*, 2001, **87**, 085501.

[170] D. L. Cheung, S. J. Clark, and M. R. Wilson, *J. Chem. Phys.*, 2004, **121**(18), 9131 – 9139.

[171] J. Prost and P. S. Pershan, *J. Appl. Phys*, 1976, **47**, 2298.

[172] I. Dozov, I. Penchev, P. Martinot-Lagarde, and G. Durand, *Ferr. Lett.*, 1984, **2**, 135.

[173] N. V. Madhusudana and G. Durand, *J. Phys. Lett.*, 1985, **46**(5), L195.

[174] S. R. Warrier and N. V. Madhusudana, *J. Phys. II*, 1997, **7**(12), 1789.

[175] T. Takahasi, H. Nishijou, M. Usui, M. Kimura, and T. Akahane, *Jap. Jour. Appl. Phys.*, 1998, **37**, 1865.

[176] N. T. Kirkman, T. Stirner, and W. E. Hagston, *Liq. Cryst.*, 2003, **30**(9), 1115.

[177] L. M. Blinov, M. I. Barnik, M. Ozaki, N. M. Shtykov, and K. Yoshino, *Phys. Rev. E*, 2001, **62**(6), 8091.

[178] L. M. Blinov, M. I. Barnik, M. Ozaki, and K. Yoshino, *Phys. Rev. E*, 2001, **64**, 031707.

[179] I. Dozov, M.-L. P., and G. Durand, *J. Phys. Lett.*, 1982, **43**, 365.

[180] R. B. Meyer, *Phys. Rev. Lett.*, 1969, **22**, 918.

[181] S. D. Lee and J. S. Patel, *Phys. Rev. A*, 1990, **42**(2), 997.

[182] S. D. Lee, J. S. Patel, and R. B. Meyer, *J. Appl. Phys.*, 1990, **67**(3), 1293.

[183] G. Z. Zhu, Y. Jin, and J. B. Song, *Phys. Lett. A*, 1985, **109**, 279.

[184] L. Blinov, D. Z. Radzhabov, S. V. Yablonski, and S. S. Yakovenko, *Nuovo Cimento D*, 1990, **12**, 1353.

[185] L. M. Blinov, M. I. Barnik, H. Okaha, M. Ozaki, N. M. Shtykov, and K. Yoshino, *Eur. Phys. J. E*, 2001, **4**, 183.

[186] J. P. Straley, *Phys. Rev. A*, 1976, **14**, 1835.

[187] M. A. Osipov, *Sov. Phys. JETP*, 1983, **85**, 1167.

[188] Y. Singh and U. P. Singh, *Phys. Rev. A*, 1989, **39**, 4254.

[189] A. M. Somoza and P. Tarazona, *Molec. Phys.*, 1991, **72**, 911.

[190] J. Seltzer, R. Berardi, and C. Zannoni, *Chem. Phys. Lett.*, 1999, **299**, 9 – 16.

[191] J. L. Billeter and R. A. Pelcovits, *Liq. Cryst.*, 2000, **27**(9), 1151 – 1160.

[192] M. A. Osipov and V. B. Nemtsov, *Sov. Phys. Crstallogr.*, 1986, **31**, 125.

[193] S. A. Jewell and J. R. Sambels, *J. Appl. Phys.*, 2002, **92**(1), 19 – 24.

[194] D. S. Hermann, P. Rduquist, K. Ichimura, K. Kudo, L. Komitov, and S. T. Lagerwall, *Phys. Rev. E*, 1997, **55**(3), 2857 –2860.

[195] E. P. Raynes, C. V. Brown, and J. F. Strömer, *Appl. Phys. Lett.*, 2003, **82**(1), 13.

[196] A. V. Zahkarov and R. Y. Dong, *Eur. Phys. J. E*, 2001, **6**, 3.

[197] P. Hohenberg and W. Kohn, *Phys. Rev. B*, 1964, **136**, 846.

[198] W. Kohn and L. J. Sham, *Phys. Rev. A.*, 1965, **140**(27), 1133.

[199] K. Perdew, J. P.and Burke and M. Ernzerhof, *Phys. Rev. Lett.*, 1996, **77**, 3865.

[200] J. P. Perdew, J. A. Chevary, S. H. Vosko, K. A. Jackson, D. J. Singh, and C. Fiolhais, *Phys. Rev. B*, 1992, **46**, 6671.

[201] Castep version 3.9, academic version, licensed under the ukcp-msi agreement. 1999.

[202] R. P. Feynman, *Phys. Rev.*, 1939, **56**(4), 340 – 343.

[203] M. D. Segall, P. J. D. Lindan, M. J. Probert, C. J. Pickard, P. J. Hasnip, S. J. Clark, and M. C. Payne, *J. Phys. Condens. Matter*, 2002, **14**, 2717 – 2744.

[204] R. Berardi, L. Muccioli, and C. Zannoni, *ChemPhysChem*, 2004, **5**, 104–111.

[205] D. Vanderbilt, *Phys. Rev. B*, 1990, **41**, 7892.

[206] D. L. Cheung, S. J. Clark, and M. R. Wilson, *Phys. Rev. E*, 2002, **65**(5), art. no. 051709.

[207] N. Nevins, J.-H. Lee, and N. L. Allinger, *J. Comput. Chem.*, 1996, **14**, 695.

[208] S. Tsuzuki, T. Uchimaru, K. Matsumura, M. Mikami, and K. Tanabe, *J. Chem. Phys.*, 1999, **110**, 2858.

[209] A. Karpfen, C. H. Choi, and M. Kertesz, *J. Chem. Phys. A*, 1997, **101**, 7426.

[210] S. Arulmozhiraja and T. Fujii, *J. Chem. Phys.*, 2001, **115**, 10589.

[211] F. Grein, *J. Phys. Chem. A*, 2002, **106**, 3823–.

[212] A. Almenningen, O. Bastiansen, L. Fernholt, B. N. Cyvin, S. J. Cyvin, and S. Samdal, *J. Mol. Struct.*, 1985, **128**, 59.

[213] O. Bastiansen and S. Samdal, *J. Mol. Struct.*, 1985, **128**, 115.

[214] L. A. Carreira and T. G. Towns, *J. Mol. Struct.*, 1977, **41**, 1.

[215] G. Celebre, G. de Luca, M. Longeri, C. Veracini, and J. W. Emsley, *J. Chem. Soc. Faraday Trans.*, 1991, **87**, 2623.

[216] V. Barone, L. Commiso, F. Lelj, and N. Russo, *Tetrahedron*, 1985, **41**(10), 1915 – 1918.

[217] G. Huges, C. Wang, A. S. Batsanov, M. Fern, S. Frank, M. R. Bryce, I. F. Perepichka, A. P. Monkman, and B. P. Lyons, *Org. Biomol. Chem.*, 2003, **1**, 3069 – 3077.

[218] G. Winter, H. Hartung, and M. Jaskolki, *Molec. Cryst. Liq. Cryst.*, 1987, **149**, 17.

[219] R. Gomper, H. Mair, and K. Polborn, *Synthesis*, 1997, **1997**(6), 696.

[220] H. Alyar, M. Bahat, E. Kasap, and Z. Kantarci, *Czec. J. Phys.*, 2006, **56**(4), 349–358.

[221] K. D. Dobbs and K. Sohlberg, *J. Chem. Theory Comp.*, 2006, **2**, 1530–1537.

[222] A. Göller and U.-W. Grummt, *Chem. Phys. Lett.*, 2000, **321**, 399–405.

[223] D. M. Pawar, K. K. Wilson, and E. A. Noe, *J. Org. Chem.*, 2000, **65**, 1552–1553.

[224] T. B. Grindley and A. R. Katritzky, *J. Chem. Soc. Perkin II*, 1974, (3), 289 – 293.

[225] R. J. Abraham, S. Angiolini, M. Edgar, and F. Sancassan, *J. Chem. Soc. Perkin II*, 1995, (11), 1973–1979.

[226] T. Schaefer, T. A. Wildman, and R. Sebastian, *Theochem.*, 1982, **89**, 23 – 101.

[227] M. R. Nelson and R. F. Borkman, *Theochem.*, 1998, **432**, 247 – 255.

[228] T. Tsuji, H. Takeuchi, T. Egawa, and S. Konaka, *J. Am. Chem. Soc.*, 2001, **123**, 6381 – 6387.

[229] R. Wrzalik, K. Merkel, and A. Kocot, *J. Mol. Model*, 2003, **9**, 248 – 258.

[230] T. Imase, S. Kawauchi, and J. Watanabe, *Macromol. Theory Simul.*, 2001, **10**, 434 – 440.

[231] P. Coulter and A. H. Windle, *Macromol.*, 1989, **22**, 1129 – 1136.

[232] T. Egawa, T. Yamada, and S. Konaka, *Chem. Phys. Lett.*, 2000, **324**, 260–264.

[233] J. P. Hummel and P. J. Flory, *Macromol.*, 1980, **13**, 479.

[234] R. J. Abraham, M. Mobli, J. Ratti, F. Sancassan, and T. A. D. Smith, *J. Phys. Org. Chem.*, 2006, **19**, 384–392.

[235] ed. R. L. Jaffe, D. Y. Yoon, and A. D. McLean, *Computer simulations of polymers*, R.J. Roe, Prentice Hall, N.J., 1991.

Appendix A

Conferences, Courses and Seminars Attended

A.1 Conferences

British Liquid Crystal Society Conference

University of Manchester, U.K., 5th-7th, 2004

Work presented in poster format.

British Liquid Crystal Society Winter Workshop

University of Hull, U.K., 15th-17th December. 2004

Work presented in poster format.

British Liquid Crystal Society Conference

University of Exeter, UK, 22nd-24th March, 2005

Work presented in poster format.

Thermodynamics 2005

Sesimbra, Portugal, 6th-8th April, 2005

Work presented in poster format.

DL_POLY Training Day

Daresbury Laboratory, U.K., 27 April, 2005

6th Liquid Matter Conference

Utrecht, the Netherlands, 2nd-6th July, 2005

Work presented in poster format.

Royal Society Discussion Meeting on New Directions in Liquid Crystal Science

London, U.K., 5th-6th December, 2005

British Liquid Crystal Society Conference

University of York, U.K., 11th-13th April, 2006

Work presented in poster format.

21st International Liquid Crystal Conference

Keystone, Colorado, U.S.A., 2nd-7th July, 2006

Work presented in poster format.

Flexoelectricity in Liquid Crystals

University of Oxford, U.K., 19th September, 2006

A.2   Courses

Introduction to FORTRAN Programming

Information Technology Service, Durham University

Numerical Methods and Data Analysis

Department of Chemistry, Durham University

Diffraction and Scattering Methods

Department of Chemistry, Durham University

Practical and Electronic Structure Calculations

Department of Chemistry, Durham University

Teaching and Demonstrating

Centre for Learning, Teaching and Research in Higher Education, Durham University

A.3 Seminars

Protein folding and misfolding from and NMR perspective

Prof. J. Waltho, 18th February, 2004

Expression of quantum cellular automata, surface bound mixed-valence complexes as field switchable charge containers

Prof. Thomas P. Fehlner, 10th March, 2004

Bottom-up assembly of peptide-based supermolecular and nanoscale structures

Dr. D. N. Woolfson, 24th March, 2004

Gas sorption by organic crystals

Prof. Leonard J. Barbour, 15th November, 2004

New methodology for organic synthesis

Prof. Varinder Aggarwal, 17th November, 2004

Computer simulations of chemical reactions in complex systems: from proton transfer to ligand binding

Prof. Markus Meuwly, 23rd February, 2005

Molecular tailoring of solid surfaces

Prof. J. P. S. Badyal, 4th May, 2005

Understanding phase transitions in chiral systems of biological interest

Prof. George Jackson, 18th May, 2005

First-principles predictions for water: clusters and condensed phases

Prof. Pavel Kocovsky, 25th May, 2005

Protein folding - nature's origami

Dr. Lorna Smith, 22nd June, 2005

Chemical Nanoengineering

Prof. Jon A. Preece, 26th October, 2005

How do calculated kinetic isotope effects relate to transition state structure

Prof. Ian Williams, 16th November, 2005

Mass spectrometry: the analytical challenge of the post-genomic era

Prof. Jane Thomas-Oates, 30th November, 2005

Ultrafast excited-state processes of d6-metal carbonyl-diimine complexes: from excitation to photochemistry

Prof. A. Vicek, 11th January, 2006

Beyond nano - the chemistry of emergence

Prof. Stephen Mann, 1st March, 2006

3rd Year Postgraduate Poster Symposium

4th May, 2006

2nd Year Postgraduate Symposium

10th May, 2006

Precise synthesis and properties of organometallic dendrimers

Dr. Kiyotaka Onitsuka, 15th May, 2006

3rd Year Postgraduate Symposium

15th-16th May, 2006

Aspects of chemical biology: diversity based synthesis and oxidative stress

Dr. Richard Hartley, 14th June, 2006

A.4 Publications

Peláez, J. and Wilson, M. R.; Atomistic Simulations of a Thermotropic Biaxial Liquid Crystal; *Physical Review Letters*, 97 (26), 267801 - 267805 (2006)

Peláez, J. and Wilson, M. R.; Molecular Orientational and Dipolar Correlation in the Liquid Crystal Mixture E7: A Moleclar Dynamics Simulation Study at a Fully Atomistic Level.; *Physical Chemistry and Chemical Physics* (in press).